Exploring Methods to Determine Impactors' Origin Based on Crater Characteristics on Icy Moons

A numerical approach

Tim van Voorbergen

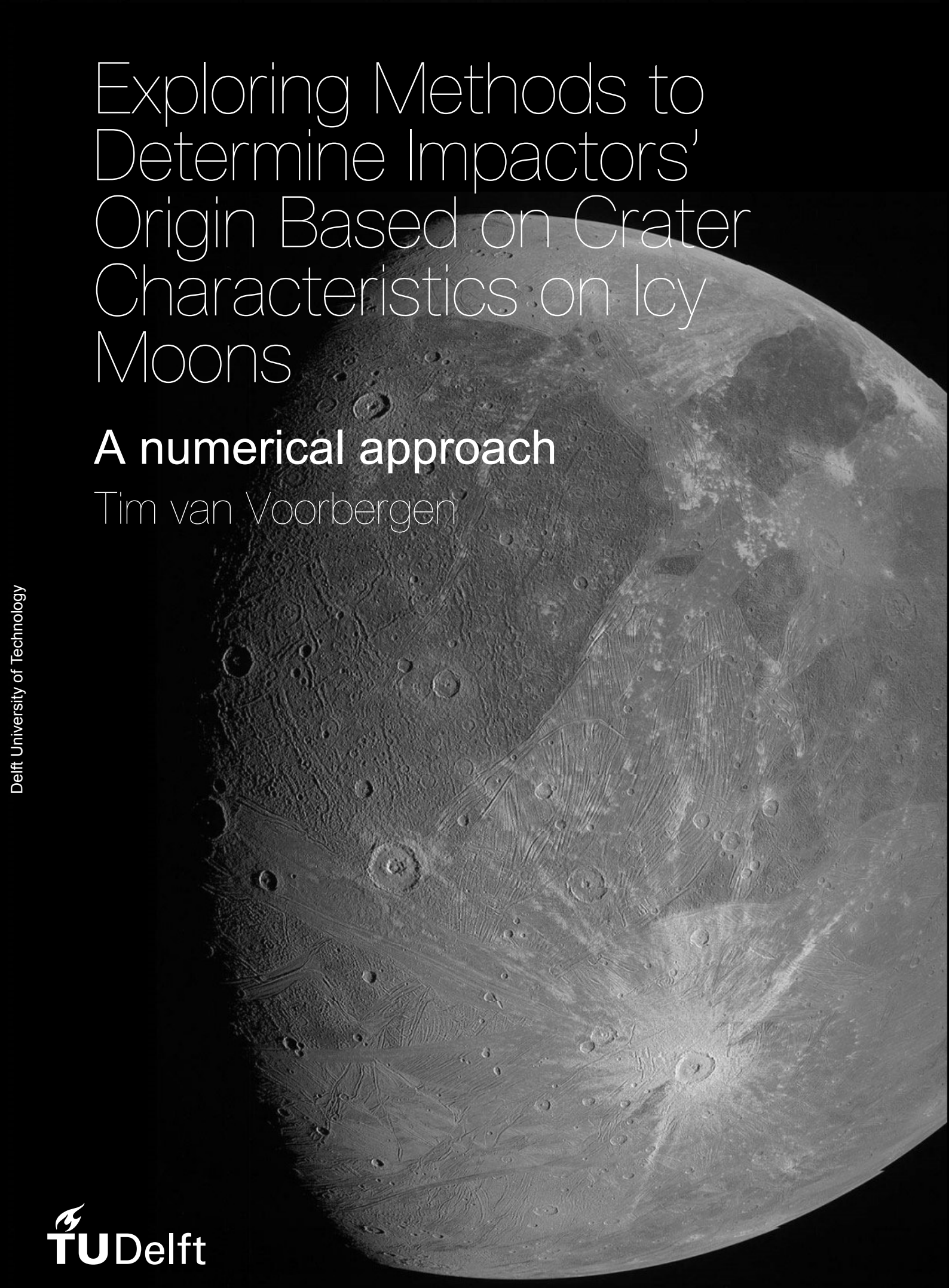

Delft University of Technology

TU Delft

Page left blank intentionally.

Exploring Methods to Determine Impactors' Origin Based on Crater Characteristics on Icy Moons

A numerical approach

by

Tim van Voorbergen

Student number: 4661915
Project duration: March 7, 2022 - October 14, 2025
Supervisors: Dr. Ir. Bart Root and Dr. Stéphanie Cazaux

TU Delft

Cover image retrieved from https://www.nasa.gov/image-feature/jpl/juno-s-ganymede-close-up

Page left blank intentionally.

Preface

When I was looking for a thesis topic, I had quite some difficulty trying to find one that sounded just right. When I was eventually presented with a topic related to simulating impacts on icy targets, I was intrigued. I first learned about impact craters, meteorites, and icy moons during a planetary sciences lecture, which already peaked my interest back then. So, I was enthusiastic about delving deeper into the theory and numerical simulation of impacts, and decided that this would be my thesis topic.

A long time has passed now, and looking back I feel like I have grown both professionally and personally as a result of this experience. It has been a long, yet fulfilling journey.

There are several people that I want to thank for their support during this thesis. First of all, this thesis would not have even existed without my supervisors Dr. Ir. Bart Root and Dr. Stéphanie Cazaux. I could not have asked for better supervisors. They have been nothing less than helpful, understanding, patient, and kind, and I want to thank them for their support and guidance. Also, I would sincerely like to thank Prof. Dr. Garreth Collins for granting access to the iSALE2D hydrocode, through which the simulations were run. In addition, Prof. Dr. Garreth Collins and Dr. Thomas Davidson have often helped clear up misconceptions and confusions I had about the code, for which I am grateful. A special thanks to Dr. Jordan Steckloff, who was willing to meet with me on zoom and help answering some questions I had about the equations of state, despite the inconveniences of living in different time zones. I also want to thank Dr. Sarah Stewart, for answering my questions about the equation of state, and providing me with very useful suggestions. To conclude, I thank my friends and family for their support, as well as anyone who is reading this, be it for an educational/professional purpose or just because it interested you. I hope that you will be able to gain a better understanding of impact cratering and impact simulations, and why they are crucial to understanding our solar system a little bit better.

Tim van Voorbergen
Rijnsburg, The Netherlands, October 14, 2025

Page left blank intentionally.

Abstract

Impact craters provide valuable insights into the formation and geological evolution of planetary bodies. However, the origin of the impactor often remains uncertain. Typically, two different origins are considered: a planetocentric origin, where impactors orbited a parent-planet, or a heliocentric origin, where impactors orbited the Sun. This distinction is crucial, because the velocity is different for planetocentric and heliocentric impactors, and using one model or the other can lead to significantly different outcomes. To address this issue, further research into this topic is required.

To help determine the origin of impactors, this report explores potential methods to distinguish heliocentric and planetocentric impactors based on crater characteristics on icy moons, using hydrocode impact simulations. While previous studies have examined cratering in ice, they primarily focused on crater diameter and depth. Here, additional characteristics are explored, including damage, temperature, and ice phases, to identify correlations between these crater properties, impact velocity, and impactor size. From these correlations, the probability that a crater was formed by a heliocentric or planetocentric impactor can be inferred.

This report focuses on impact simulations targeting a Ganymede-like surface, with velocities of 5 km/s and 15 km/s representing planetocentric and heliocentric impactors, respectively. Simulation results reveal distinct differences in crater morphology for the depth-to-diameter (d/D) ratio between 5 km/s and 15 km/s. Thus, an impact velocity can be inferred for a given crater diameter and depth by determining its position relative to these d/D curves. Fracturing was observed to be significantly more extensive in the 15 km/s simulations, although observations of actual craters often show limited fracturing due to freezing, post-impact relaxation, and tectonic movements. However, in larger craters, extensive fracturing can allow drainage of impact melt, forming central pits — a feature that could act as an indicator of high-velocity impacts, since fracturing is mostly prominent for the 15 km/s simulations. Temperature results show high-temperature crystalline ice forming on the crater floor and walls, with a surrounding layer of warm material, both more prominent in the 15 km/s simulations. Comparisons with observational data reveal that a 1000 m, 15 km/s simulation aligns well with craters showing low amorphous ice mass fractions and large ice grain sizes near the crater, suggesting that such craters could similarly result from high-velocity impactors.

Overall, the combined findings provide a good preliminary indication of the impactor origin based on observable crater properties. Nonetheless, uncertainties remain and adjustments and improvements could be made to attain a more concrete result. Future research should expand simulations to other icy moons to compare the response of differing environments, incorporate alternative viscosity models such as the PEIERLS model, and explore a wider range of impactor sizes and velocities thus increasing the number of simulations. Finally, introducing 3D simulations could provide new perspectives regarding oblique impacts, ejecta patterns, and central peaks.

Contents

List of Tables

List of Figures

Nomenclature

List of Abbreviations

ALE	Arbitrary Lagrange Eulerian
EOS	Equation of state
HDA	High-Density Amorphous
LDA	Low-Density Amorphous
NASA	National Aeronautics and Space Administration
OAT	One-at-a-time
SPH	Smooth Particle Hydrodynamic
SI	Sensitivity index
STP	South Polar Terrain
VHDA	Very High-Density Amorphous

List of Symbols

Latin symbols

A	Pre-exponential factor	[−]
	or Constant in Tillotson eos	[−]
	or Measure of asymmetry	[−]
a	Constant in Simon approximation	[−]
	or Constant in Tillotson eos	[−]
	or Slope of linear equation	[−]
B	Positive constant in damage model equation	[−]
	or Constant in Tillotson eos	[−]
b	Constant in Tillotson eos	[−]
	or Bias of linear equation	[−]
c	Speed of sound	[m/s]
	or Exponent in Simon approximation	[−]
c_b	Speed of sound in iSALE2D	[m/s]
D	Diameter	[m]
D_{cp}	Diameter of central peak	[m]
D_f	Diameter of crater floor	[m]
d	Crater depth	[m]
	or Impactor diameter	[m]
	or Size	[m]
E	Energy	[J]
	or Specific energy	[J/kg]
	or Energy density	[J/m^3]
E_a	Activation energy	[K]
E_c	Energy of cold part in Helmholtz free energy equations	[J]
E_{cv}	Energy of complete vaporization	[J]
E_e	Energy of electronic part in Helmholtz free energy equations	[J]

E_{iv}	Energy of incipient vaporization	[J]
E_k	Kinetic energy	[J]
E_t	Energy of thermal part in Helmholtz free energy equations	[J]
E_0	Energy close to vaporization energy	[J]
F	Helmholtz free energy	[J]
F_c	Helmholtz free energy: cold part	[J]
F_e	Helmholtz free energy: electronic part	[J]
F_t	Helmholtz free energy: thermal part	[J]
g	Surface gravity	[m/s^2]
H	Crater depth	[m]
H_{rim}	Crater rim height	[m]
h_{cp}	Height of central peak	[m]
i	Orbit inclination	[rad]
K	Scaling coefficient	[−]
L	Impactor diameter	[m]
m	Mass	[kg]
Nd	Number of density nodes	[−]
Nt	Number of temperature nodes	[−]
P	Pressure	[N/m^2]
	or Probability of comet passage	[−]
P_{EC}	Ecliptic comet impact probability relative to Jupiter	[−]
P_c	Pressure used in Tillotson eos for the compressed state	[N/m^2]
P_h	Pressure used in Tillotson eos for the expanded state	[N/m^2]
P_m	Pressure used in Tillotson eos during the transition between two forms	[N/m^2]
p_c	Pressure at which failure is always assumed compressional	[N/m^2]
	or Pressure of cold part in Helmholtz free energy equations	[N/m^2]
p_e	Pressure of electronic part in Helmholtz free energy equations	[N/m^2]
p_t	Pressure of thermal part in Helmholtz free energy equations	[N/m^2]
q	Perihelion distance	[m]
R	Radius	[m]
R_i	Radius of impactor	[m]
R_p	Radius of projectile	[m]
r	Distance	[m]
	or Radius	[m]
r_R	Roche limit	[m]
r_c	Distance where continuous regime starts	[m]
S	Entropy	[J/K]
	or Target radius	[m]
	or Sensitivity	[−]
SI	Sensitivity index	[−]
SI^*	Normalized sensitivity index	[−]
T	Temperature	[K]
T_{dec}	Decay time	[s]
T_m	Melting temperature	[K]

T_{m0}	Melting temperature at zero pressure	[K]
t	Time	[s]
	or Time for ice to crystallize	[s]
u	Specific internal energy	[J/kg]
U	Shockwave velocity	[m/s]
	or Relative velocity	[m/s]
U_x	Radial portion of relative velocity	[m/s]
V	Velocity	[m/s]
v	Velocity	[m/s]
	or Density scaling coefficient	[−]
v_i	Impact velocity	[m/s]
v_{lim}	Kinematic viscosity of the fluidized region	[m^2/s]
W_T	Width of terraced wall zone	[m]
x	Constant used in kinetic energy to crater diameter relation	[−]
	or Variable in linear equation	[−]
	or Tested sensitivity analysis parameter	[−]
Y	Yield strength	[N/m^2]
Y_c	Cold yield strength	[N/m^2]
Y_d	Yield strength of damaged material	[N/m^2]
$Y_{d,0}$	Yield strength of damaged material at zero pressure	[N/m^2]
Y_i	Yield strength of intact material	[N/m^2]
$Y_{i,0}$	Yield strength of intact material at zero pressure	[N/m^2]
y	Defines linear equation	[−]
	or Representation of sensitivity parameter result	[−]

Greek Symbols

α	Constant used in Tillotson eos to control rate of convergence	[−]
β	Constant used in Tillotson eos to control rate of convergence	[−]
γ_β	Dimensionless parameter for duration of vibrations	[−]
γ_η	Dimensionless parameter for strength of vibrations	[−]
Δ	Difference in distance	[m]
ϵ_f	Plastic strain at failure	[−]
ϵ_{fb}	Minimum failure strain for low pressures	[−]
ϵ_p	Accumulated plastic strain	[−]
η	Viscosity	[Ns/m^2]
	or Ratio between density and reference density	[−]
μ	Velocity scaling coefficient	[−]
	or Normalized planetary mass	[−]
μ_d	Coefficient of friction for damaged material	[−]
	or Mean molecular weight	[kg/kmol]
μ_i	Coefficient of friction for intact material	[−]
ξ	Thermal softening constant	[−]
π_D	Pi-group scaling: dimensionless measure of crater diameter	[−]
π_2	Pi-group scaling: dimensionless measure of gravity-scaled size	[−]

π_3	Pi-group scaling: influence of target strength	[−]
π_4	Pi-group scaling: ratio of target and projectile densities	[−]
ρ	Density	[kg/m^3]
ρ_p	Density of projectile	[kg/m^3]
ρ_t	Density of target	[kg/m^3]

1 Introduction

One of the most profound scientific questions concerns the possibility of life existing beyond Earth. For such life to exist, the presence of water is considered essential, making the icy moons in the solar system prime candidates for observation and exploration. The Saturnian moon Enceladus, along with the Jovian moons Ganymede and Europa, are particularly attractive in that regard, due to hypothesized subsurface oceans composed primarily of water. This makes gathering detailed information on these celestial bodies of crucial importance. Crater analysis offers here a useful input into the geological history of these bodies. Craters can provide estimates of the surface age and insights into the internal composition, geology, and formation processes of a celestial body. Craters form from external objects, or impactors, traveling at hypersonic speeds. The origin of these impactors is of importance, as it can significantly influence their characteristics. Currently, two models are employed for these origins: the heliocentric model, which assumes impactors are orbiting the Sun and impact at a very high velocity, and the planetocentric model, which assumes impactors are orbiting the body in question or a parent-body, and strike at lower velocities.

In real scenarios, both models are very likely involved in the creation of craters. As a result, this duality introduces uncertainties, which are highlighted in research by Bell [5]. Bell estimated ages on the Saturnian moons using these two models. Applying the heliocentric model showed that there should be a higher crater density for moons further away from Saturn, suggesting that Titan should have an old surface age, which contradicts the observations of youthful characteristics. Conversely the planetocentric model showed a uniformly young age for the Saturnian moons, but could not rule out the saturation effects on Titan. In essence, neither model sufficiently explains the data. Therefore, to improve the accuracy of surface analyses, a way to distinguish heliocentric and planetocentric craters is explored in this report by analyzing numerical simulations of crater impacts.

This report is structured into nine chapters. Chapter 2 introduces the scientific background by providing information on several theories on planetary formation, crater morphology, crater characteristics on icy moons, and hydrocode simulations, along with a summary of previous work, the knowledge gap, the research questions, and objectives. Chapter 3 focuses on the equation of state. The equation of state is paramount in the simulation of impacts, as it governs material behavior in impact simulations. Besides discussing and comparing the different equations of state available in iSALE2D, alternatives are explored as well. Chapter 4 provides an overview of the most relevant input and output parameters. In addition, the simulation procedure and post-processing is described. The verification and validation methods used are covered in Chapter 5. Through example problems and comparative studies, simulations are recreated to verify and validate iSALE2D and the methods used. A sensitivity analysis is performed in Chapter 6. Influential or sensitive parameters are identified by varying them one-at-a-time, and comparing the results with a control simulation. Chapter 7 presents the Ganymede simulation results, focusing on crater morphology, damage, and temperature, which are plotted for different impactor sizes and impact velocities. Chapter 8 interprets these results, compares them to previous work, and discusses limitations. Finally, Chapter 9 concludes with answers to the sub-questions and main research question. Additionally, recommendations are given for future studies.

2
Scientific Background

In this chapter, relevant background information on impact craters is discussed in order to obtain a fundamental understanding of the research performed in this report. First, Section 2.1 briefly describes popular theories on the formation of planets, moons and small bodies in the solar system. Then, the impact crater morphology and impact process are explained in Section 2.2. Section 2.3 includes information on the different types of craters found on the icy moons of Jupiter and Saturn. Section 2.4 briefly explains how to determine the age of a body based on the craters on its surface. Section 2.5 covers the phase diagram of water and the different variations of ice. Then, Section 2.6 describes how impacts are simulated using hydrocodes. In Section 2.7, work that has previously been done by other researchers is summarized. Finally, Section 2.8 states the knowledge gap, followed by the research question and objectives, which are derived accordingly.

2.1. Formation of Bodies in the Solar System

Generally, the formation of celestial bodies in any given planetary system is a consequence of the formation of a star. Figure 2.1 provides a brief visualization of this formation process [7]. As described by Lissauer and de Pater [8], and as shown in Figure 2.1a, the process starts with a large cloud of interstellar gas and dust. At some point, when dense parts in the cloud reach a critical density, it starts to collapse, forming a protostar, shown by Figure 2.1b and Figure 2.1c. Due to the centrifugal forces, material that has a high specific angular momentum cannot reach the protostar, and instead orbits it, thereby forming a disk, as shown by Figure 2.1d. When stellar winds and radiation eventually have blown away the surrounding shell of gas and dust, the star goes into the so-called T-Tauri phase, shown in Figure 2.1e [9]. After this phase, the star becomes a pre-main-sequence star, and eventually a main-sequence star. These stars will still have a surrounding remnant disk, and from this disk a planetary system can form, as shown by Figure 2.1f. Such a system could contain planets, moons and other small bodies such as asteroids and comets [8].

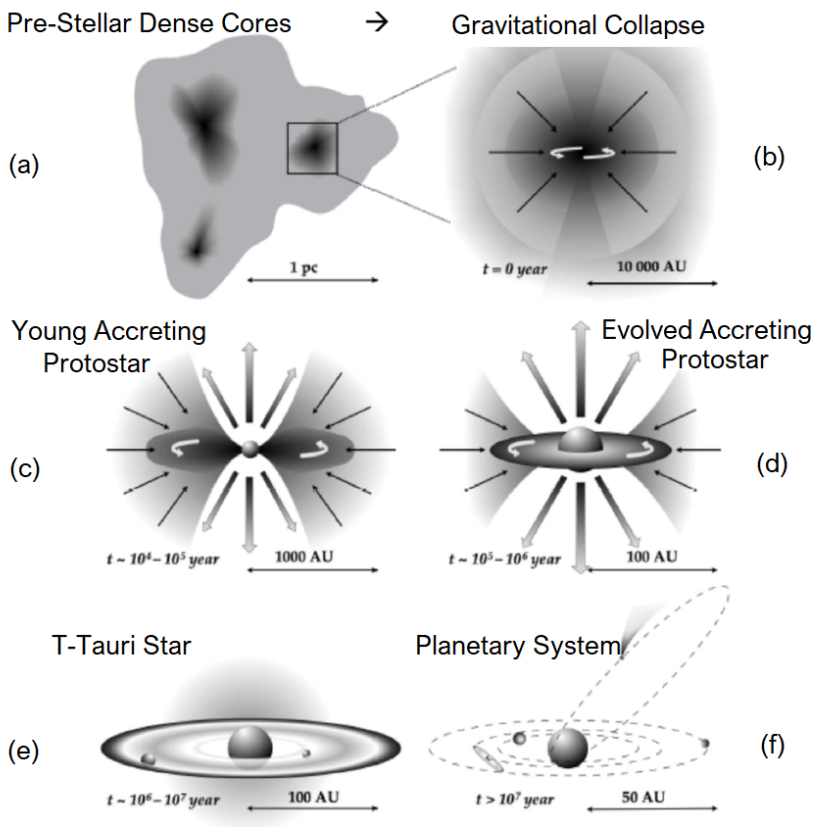

Figure 2.1: The formation of a star and a planetary system is visualized here in six images. Images (a) and (b) mainly visualize the formation of dense cores in the molecular cloud, followed by the eventual collapse due to gravity. Consequently, image (c) and (d) show the creation of a protostar and its disk, whereas image (e) and (f) show the formation of a main sequence star and finally a planetary system [6].

2.1.1. Planet Formation Theories

There are two main theories on the formation of planets: core accretion and gravitational instability. In the core accretion model, planetesimals accrete to produce a heavy element core. Once this core reaches a critical mass, its increasing gravity allows it to attract gas from the surrounding disk, forming a gas giant. This mechanism can also be used to explain the formation of terrestrial planets, but in that case solid material continues

to accrete, instead of gas. However, a constraint that remains for the core accretion model, is the timescale. The core and the gas accretion phases must be completed before the material in the disk dissipates, but the timescale for core and gas accretion phases have been estimated to be close to the upper limit of the disk depletion [10].

The alternative theory, gravitational instability, states that if a disk is sufficiently massive, it can break up due to its own gravity and fragment into dense clumps. These clumps can then contract and collapse to form gas giants, which would occur in a relatively short time period, overcoming the issue the core accretion model has with the timescale [11, 12]. However, there are also issues with the gravitational instability model. For example, the disks must be cool and dense. This can be derived from the equation for the Toomre parameter Q. Essentially, if $Q \lesssim 1$, self gravity of the disk becomes more important, which is very important for the initial fragmentation of the disk into clumps [13]. Other issues are related to observations. Jupiter and Saturn exhibit a heavy element interior, which can be recreated with the core accretion model, but not for the gravitational instability model, because gas is primarily accreted, resulting in a composition that is more similar to stars [14]. Moreover, gravitational instability is expected to occur at large distances, due to temperature conditions and the fact that newly formed clumps migrate inwards too quickly and get destroyed. But, observations show that gravitational instability is almost never observed at such distances [13].

Currently, the core accretion model is often considered the most appropriate model for planet formation, as there are too many issues, limitations, and conditions revolving around the gravitational instability model.

2.1.2. Formation of Moons in the Jovian and Saturnian System

Besides planets and gas giants, there are also numerous moons located in the solar system. In particular, the moons in the Jovian and Saturnian systems are interesting, because Jovian moons have similar characteristics to one another, whereas the Saturnian moons have little in common. As a result, many theories for both systems have been created over time.

For the Jovian system, a promising theory was developed by Canup and Ward [15]. It states that moons or satellites originated from the material found in the circumplanetary disks. Such disks can form if a gas giant accumulates sufficient gas [8]. Considering the facts that the moons in the Jovian system have similar masses, orbit in prograde and circular orbits, and are approximately coplanar, it suggests that they all formed within a shared circumplanetary disk. Their formation could have come from collisions that occurred in the disk, which would accumulate more material from the disk in order to grow. Over time, their orbits would become more circular and coplanar due to the gravitational interactions between the disk and the satellites, eventually forming the Jovian moons [15].

On the other hand, the moons in the Saturnian system are quite different. Asphaug and Reufer [16] hypothesized that Saturn used to have Galilean-like moons, but due to orbital instabilities they collided and merged, eventually forming Titan. The remnants of this collision would then clump together and form Saturn's so-called mid-sized moons: Enceladus, Mimas, Tethys, Dione, and Rhea. Another theory focuses on the compositional data. Anderson et al. [17] based their hypothesis on the building blocks of Titan. They looked at Saturn's circumplanetary disk, and investigated the icelines of several materials. Concluded was that Titan and Enceladus must have been formed between certain lower and upper limit icelines, in order for their compositional data to match. However, the simulations were relatively simple, and positions of icelines were only indicative and could differ with different initial temperatures of the circumplanetary disk. Hence, there is room for improvement.

For the smaller moons of Saturn, one of the most promising and widely accepted theories, proposed by Canup and Ward [19], suggests that these moons formed from Saturn's rings. The rings are located within the Roche limit or very close to it. The Roche limit is the maximum radius in which the tidal forces are larger than the self-gravity of any body, thus causing it to break apart if it lies within this limit. So, if material were located outside the Roche limit, it could grow in size by accumulating material directly from the ring, and by doing so potentially form a satellite. Canup and Ward [19] calls this first stage of satellite formation the "continuous regime", as visualized in Figure 2.2a. While the satellite is continuously growing by accreting material from the ring, it remains just outside the Roche limit and has less angular velocity than the rings. This means that the rings exert a positive torque on the satellite, resulting in an outwards migration of the satellite.

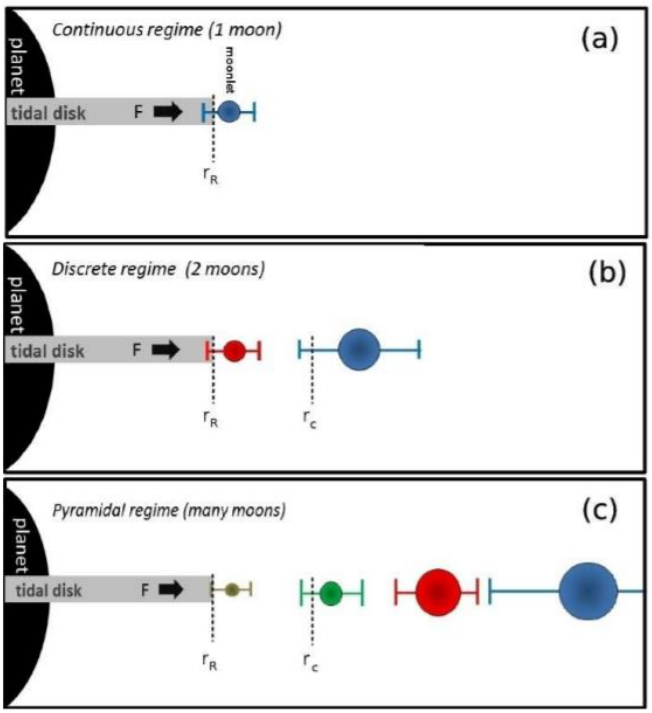

Figure 2.2: The three satellite formation regimes: a) Continuous regime, b) discrete regime and c) pyramidal regime. r_R represents the Roche limit and r_c represents the distance where the continuous regime takes place [18].

When the first satellite is too far away to attract material from the rings, a new satellite can form. This is the start of the second stage. Like the original satellite, the second satellite will slowly migrate outwards. Canup and Ward [19] call this the "discrete regime", and it is shown in Figure 2.2b. Eventually, the second satellite will catch up to the first satellite. At this point, they will merge, leaving one larger satellite. In the meantime, a third satellite forms at the edge of the Roche limit. The process described by the discrete regime will continue to occur numerous of times, with multiple smaller and larger satellites being formed and accreted. This is the third stage, called the "pyramidal regime", and is shown by Figure 2.2c. This process stops when the distances between the satellites become too large, so that they cannot affect each other anymore.

2.1.3. Formation of Small Bodies

The formation of small bodies, such as asteroids, in the Solar System can be divided into two main formation theories. The first theory states that, at the beginning of the solar system, dust particles bonded together in the protoplanetary disk through gravity and pebble accretion, forming planetesimals. After the formation of the solar system, the surviving planetsimals became primordial asteroids, often referred to as C-type or S-type asteroids, as they are abundant in Carbon (C) or Silicon (S) [8, 20, 21].

The second theory describes a process in which small bodies are created upon the collision of larger bodies, which can be planetesimals or even protoplanets. The resulting asteroids are often referred to as V-type or M-type asteroids. V-type asteroids are rich in basalt, and hypothesized to be the remnants of a larger asteroid called Vesta. M-type asteroids contain metals such as iron and nickel [8, 22, 23].

2.2. Impact Crater Morphology and Process

The aforementioned theories of planet and moon formation describe how solid bodies are created from the protoplanetary and circumplanetary disks. The small bodies that remain after the formation process play a crucial role in shaping the surfaces of these solid bodies through impacts. Some characteristics of these impactors are reflected by the observed crater morphologies and distributions, which allows for the interpretation on whether impacts were primarily heliocentric or planetocentric. Distinguishing between these two regimes is important, because it places limits on when and how moons are formed in relation to their parent planet, for

example. Thus, analyzing crater morphologies provides a link between formation theories and the geological records preserved on surfaces. In this section, the mechanics of the impact process and the resulting crater morphologies are examined in detail, with particular focus on the icy surface of Ganymede as a representative case.

Impact craters on planets and moons are formed when an object, typically traveling at a high velocity, strikes a target surface. Upon contact, the kinetic energy of the impactor is largely transferred to the target, resulting in a spectacular explosion that flings material in all directions. In this section, the crater morphology and the different types of craters are discussed in Subsection 2.2.1, and in Subsection 2.2.2 the impact process is explained step by step. Finally, in Subsection 2.2.3, an important impact crater scaling law is discussed.

2.2.1. Crater Morphology and Different Types of Craters

A crater can generally be identified by its large bowl-like or circular shape, and can be found on many planets and moons in the solar system. Depending on the initial conditions of the projectile, such as the velocity, mass, and impact angle, different types of craters can be created. Varying types of crater will be discussed in this section.

Simple Craters

The most basic crater shape is called the simple crater.In the case of a vertical impact, simple craters are typically formed by impactors with a low impact velocity, mass, or both. Simple craters can also result from ejecta falling back on the surface, which is often created as a result of a prior larger impact. The crater diameter of simple craters on Ganymede generally do not get larger than ~2 km, although this also depends on material characteristics [24] .

Simple craters are bowl-shaped, have smooth walls and have a small crater rim, which can be smooth or ragged. Depending on the impact conditions, molten impactor material can be found on the crater floor [25]. A good example of a simple crater is shown in Figure 2.3a. Multiple smaller simple craters can also be observed surrounding the main crater, which were likely formed by ejecta. A schematic of a typical simple crater is shown in Figure 2.3b, to provide a cross-section view, as well as to show some of the main crater parameters: the diameter (D), depth (H) and crater rim height (H_{rim}).

(a) The Moltke crater, located on the Moon, is a good example of a simple crater [26].

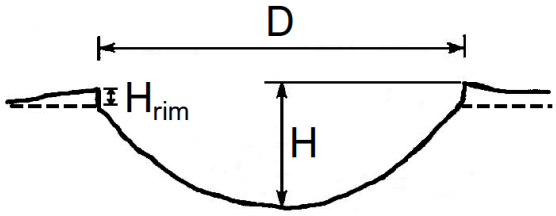

(b) A simple schematic of a simple crater, adjusted from Melosh [27].

Figure 2.3: The figure on the left shows an example of a simple crater called the Moltke crater on the Moon. Numerous smaller simple craters can be observed surrounding the crater. The figure on the right shows a schematic of a simple crater, displaying important parameters: D, H and H_{rim} represent the diameter, depth and crater rim height respectively. The dashed lines on the side of the crater represent the pre-impact surface.

Complex Craters

Increasing the impactor's kinetic energy can drastically change the crater's characteristics. When an impactor has far more kinetic energy than required to create a simple crater, a complex crater can form. A schematic can be seen in Figure 2.4, displaying the most important complex crater parameters. In addition to the rim height, rim-to-rim diameter, and the depth, complex craters have additional features of importance, such as the diameter (D_{cp}) and height (h_{cp}) of the central elevation. Other key parameters are the crater floor diameter (D_f), and the width of the terraced wall zone (W_T) [27].

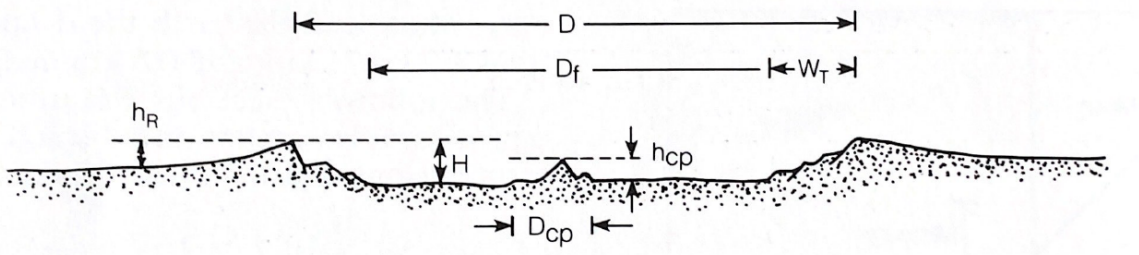

Figure 2.4: Schematic of a complex crater. Visible is the characteristic central peak in the center, abbreviated with cp. D is the rim-to-rim diameter of the crater, D_f is the diameter of the crater floor, h_R is the height of the rim with respect to the pre-impact surface, H is the depth of the crater, h_{cp} is the height of the central peak with respect to the crater floor, D_{cp} is the diameter of the central peak and W_T is the width of terraced wall zone [27].

Notable features of the typical complex crater shape, are the flat crater floor and the central elevation, which can also be seen in Figure 2.4, and a good example of a complex crater is the Euler crater, shown in Figure 2.5a. These features can form during the later stages of crater formation, where the crater collapses in on itself if it is sufficiently large. In essence, the material falls back into the crater and accumulates in the middle, creating a central peak. Consequently, complex craters typically have a lower depth-to-diameter ratio compared to simple craters, as their depths are shallower [27].

Transition Craters

Besides simple and complex craters, there are also transition craters. As the name suggests, these craters form under specific conditions, where the transition between simple and complex takes place. An example is the Bessel crater, shown in Figure 2.5b. As can be seen, it does not quite resemble a complex crater, but it cannot be classified as a simple crater either. A transition crater is therefore characterized by both simple crater and complex crater characteristics, which are relatively smooth walls, and a crater floor that is partly or completely covered by debris that slumped from the crater walls [28].

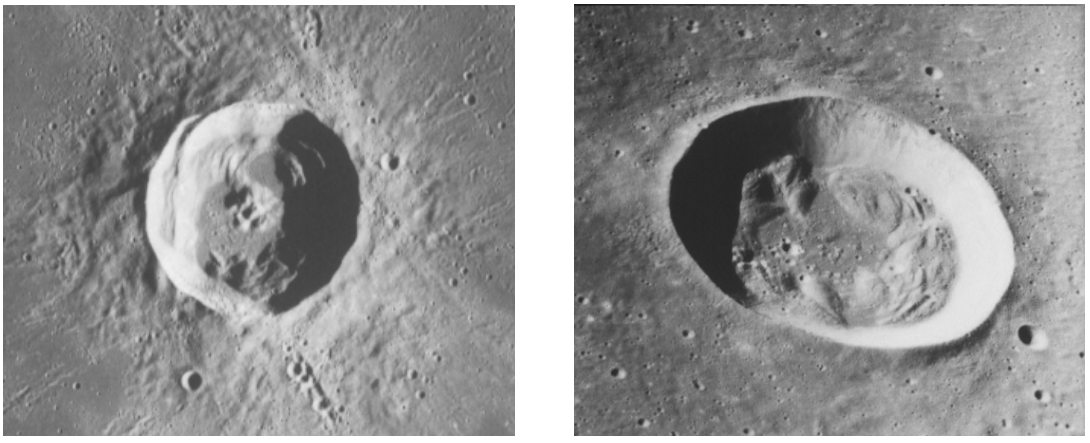

(a) The Euler complex crater on the Moon [26]. **(b) The Bessel transition crater on the Moon [26].**

Figure 2.5: Shown on the left is the Euler crater, which is a good representation of a typical complex crater. Noticeable is the characteristic central peak in the center. The Bessel crater can be seen on the right, and is an excellent example of a transition crater. It shows the relatively smooth walls reminiscent of a simple crater, as well as a partially filled crater floor that can often be seen for complex craters.

Dome Craters

In addition to typical complex craters, there is another rare type of complex crater, called a dome crater or simple dome. Instead of a central peak, dome craters have a dome-like shape in the center of the crater. They are formed as a result of icy material that was pushed up during the modification stage, and can be found on Ganymede and Callisto [29]. They are often surrounded by a trough, which is surrounded by a ring-like structure. An example of such a crater is the Melkart crater located on Ganymede, which can be seen in Figure 2.6a, where a dome-like shape in the center is clearly visible.

Penepalimpsets and Palimpsets

Penepalimpsets and palimpsets are circular high-albedo features found on Ganymede. The difference between these two is primarily related to their age, because palimpsets occur only on the dark terrain and penepalimpsets occur on all terrain types. Since the dark terrain is known to predate the bright terrain, it is used to separate the two types. A key characteristic of these features is related to viscous relaxation. Crater rims are often not visible for palimpsests, and only subtle concentric lineations and smooth central areas can sometimes be seen for only larger palimpsets. Penepalimpsests, on the other hand, have more expressed concentric features, and observable ejecta or secondary craters [31].

Multi-ringed Basins

Finally, craters resulting from extremely large impacts can form multi-ringed basins. These craters are very rare, and the Asgard crater, located on Callisto, is an example of such a crater, and can be seen in Figure 2.6b. From Figure 2.6b, the center of the crater stands out as it is lighter in color. Surrounding the center of such craters, numerous concentric rings can be seen. It is hypothesized that these rings formed, because the thin icy lithosphere fractured easily upon impact [30].

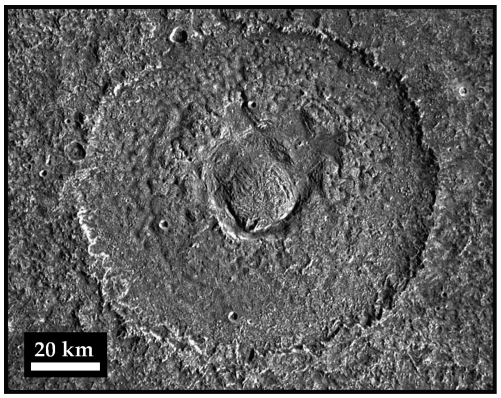

(a) The Melkart dome crater on Ganymede [29].

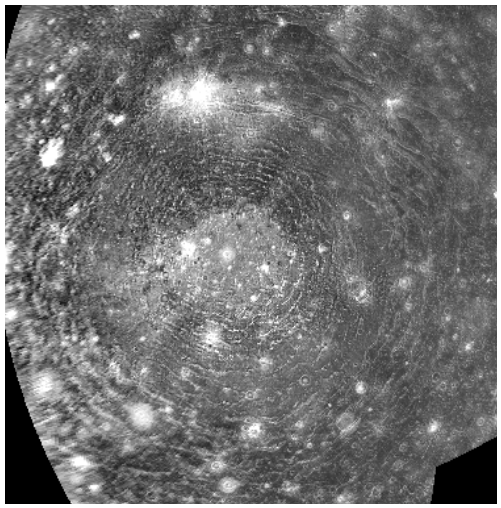

(b) The Valhalla multi-ringed basin structure on Callisto [30].

Figure 2.6: Examples of a dome crater (top) and multi-ringed basin (bottom) are given, where the dome is clearly visible in the middle of the crater, and multiple concentric rings can be seen, respectively.

Summary Crater Morphology

To summarize the different morphological variants of craters, and to provide some numerical information, Table 2.1 provides an overview of the general crater diameter and depth that can be expected. Additionally, the range of impact velocity and impactor size are provided as well. Note, however, that the impactor size is dependent on the impact velocity, and therefore conservative order-of-magnitude estimations are given.

Table 2.1: Typical crater diameters and crater depths are given for different crater morphologies on Ganymede. Additionally, a general velocity and impactor size range, that could result in the creation of the corresponding crater morphology, is given.

Morphology	Crater diameter [km]	Crater depth [km]	Impact velocity [km/s]	Impactor size [km]
Simple crater [1, 24, 32]	0.5 - 1.9	0.2 - 0.4	5 - 30	0.01 - 0.2
Transition crater [24, 31, 32]	∼2	∼0.4	5 - 30	0.2 - 0.4
Complex crater [24, 31–33]	2-60	0.34 - 1.65	5 - 30	0.5 - 10s
Dome crater [31, 32]	60 - 175	0.8 - 1.6	5 - 30	5 - 10s
(Pene)palimpset [31, 32]	60 - 355	∼0.5	5 - 30	10s - 100s
Multi-ringed basin [31, 32]	≥350	2 - 8	5 - 30	10s - 100s

2.2.2. Crater Formation Process

The crater formation process consists of three stages: the contact and compression stage, the excavation stage, and the modification stage [27]. This entire process is visualized by Figure 2.7.

The formation of a crater begins with the contact and compression stage, and typically lasts no longer than a few seconds, depending on the size of the impact. Upon contact, compression of material initiates and a strong pressure wave is sent through the target, which can be seen in Figure 2.7a. Simultaneously, a shock wave travels through the impactor, and when it reaches its end, it is reflected back as a release wave, which is shown Figure 2.7b alongside the expanding shock wave. Most of the impactor is then relieved of the high pressure, and this generally marks the end of the contact and compression stage [27].

The next stage is the excavation stage, which has a duration in the range of minutes. There are two main processes in this stage: the expansion of the shock wave through the target, and the excavation flow. Over time, the shock wave expands and propagates outward through the target and weakens in strength as it engulfs more material. Meanwhile, target material is set in motion. This creates a way for the excavation flow, which actually opens the crater, shown in Figure 2.7c [27]. The shock wave determines mainly the masses and temperatures of melted and vaporised material. The excavation flow on the other hand, is responsible for the size of the final crater and its shape. In the meantime, the ejecta rises above the surface, as depicted in Figure 2.7c and Figure 2.7d. It will continue to follow a ballistic trajectory until it either falls back onto the surface, or flies into space if its velocity is sufficiently high. Depending on the kinetic energy of the ejecta, they can sometimes create noticeable smaller craters around the main crater [27].

Finally, the last stage is the modification stage, which can last in the order of hours. Af-

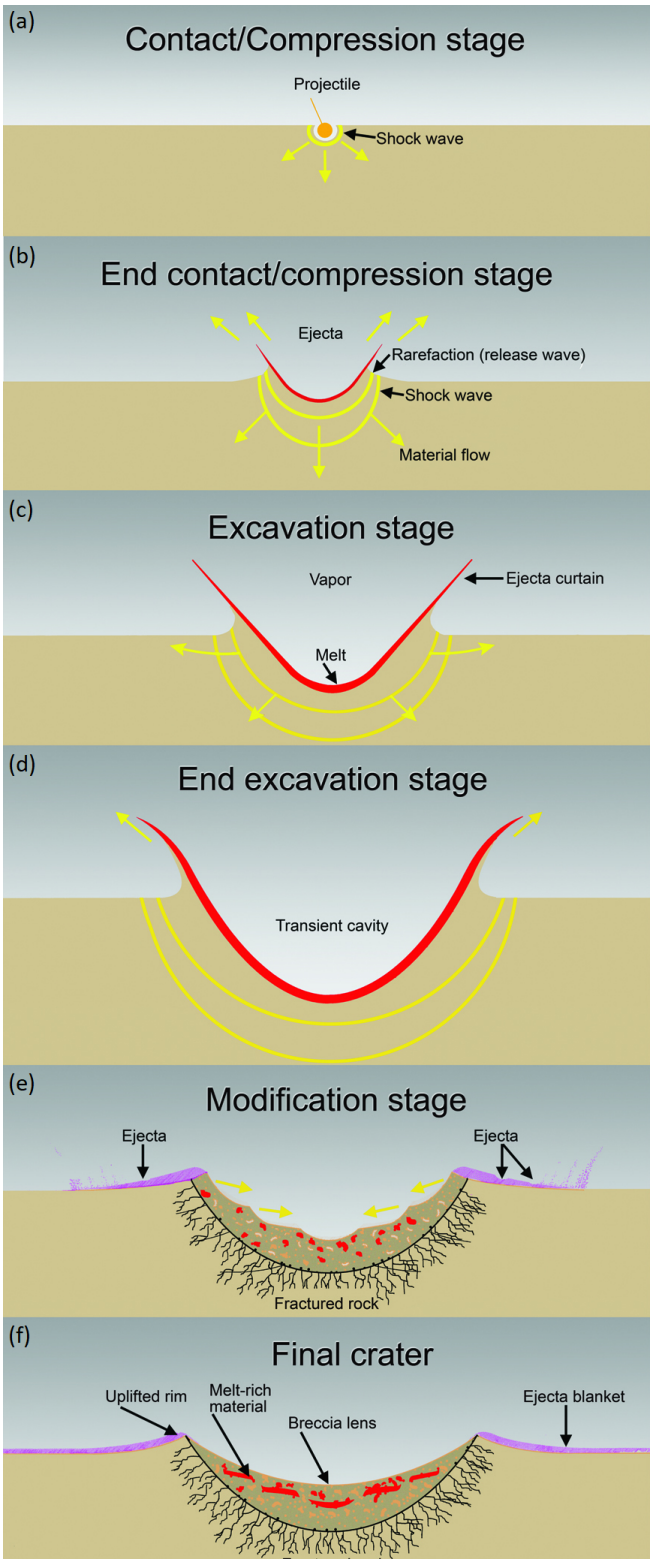

Figure 2.7: The different stages in the crater formation process are shown from top to bottom. The contact and compression stage is shown in (a) and (b). The excavation stage is depicted in (c) and (d). The transient cavity represents the crater shape right after the excavation stage and before it undergoes modification. In (e) and (f) the modification stage is shown, and breccia can be seen lying on the crater floor in (f). This is typically a mix of molten and shocked material [34].

ter the material has deformed and ejecta has been expelled from the crater, the motion of material will come to a short halt, whereafter it starts to fall back towards the center of the crater, as can be seen in Figure 2.7e and Figure 2.7f. Gravity is a major component causing this motion, though elastic rebound of underlying compressed material also plays a role. These collapse events can range from small amounts of debris sliding down into the crater, to whole crater shape alterations, such as the rise of the crater floor, appearance of central peaks, and the sinking of rims [27]. After the collapse of a crater, it is possible that over a long period of time, uplift or rebound of material is still happening. Though, this is generally in small amounts. Once the motion of material has largely come to a standstill, the modification stage can be considered completed, and a final crater has formed [27].

2.2.3. Pi-Group Scaling Law

A lot of research has been done in impact cratering. In order to scale the impact or to predict the diameter of a crater, scaling laws have been developed. A useful method is the dimensionless pi-group scaling approach. It uses dimensional analysis, in which relevant impact crater parameters are used, such as the ones given by Equation 2.1 [27, 35].

$$\pi_D = f\left(\pi_2, \pi_3, \pi_4\right) \qquad \pi_2 = 1.61\frac{gL}{v_i^2} \qquad \pi_3 = \frac{Y}{\rho_p v_i^2} \qquad \pi_4 = \frac{\rho_t}{\rho_p} \tag{2.1}$$

Where π_D is the dimensionless measure of the crater diameter, and π_2, π_3 and π_4 are dimensionless parameters. π_2 is the gravity-scaled size, equal to the ratio of gravitational and inertial stresses, where g is the surface gravity, L is the diameter of the impactor, and v_i is the impact velocity. π_3 measures the influence of target strength, where Y is the target material strength, and ρ_p is the projectile density. π_4 is the ratio of target and projectile densities, where ρ_t is the density of the target.

To obtain the complete form of π_D, that is including the terms for both the strength and gravity regime, Equation 2.2 can be used [35].

$$\pi_D = K_1\left[\pi_2{\pi_4}^{\frac{2+\mu-6\gamma}{-3\mu}} + \left(\pi_3{\pi_4}^{\frac{2-6\gamma}{-3\mu}}\right)^{\frac{2+\mu}{2}}\right]^{\frac{-\mu}{2+\mu}} \tag{2.2}$$

Where K_1 represents the scaling coefficient, μ is the velocity scaling exponent, and ν is the density scaling exponent [35]. Equation 2.2 can then be plotted, and an example is given by Figure 2.8. It shows curves for material 1 (M1) and material 2 (M2), where π_D is given on the y-axis, and π_2 on the x-axis.

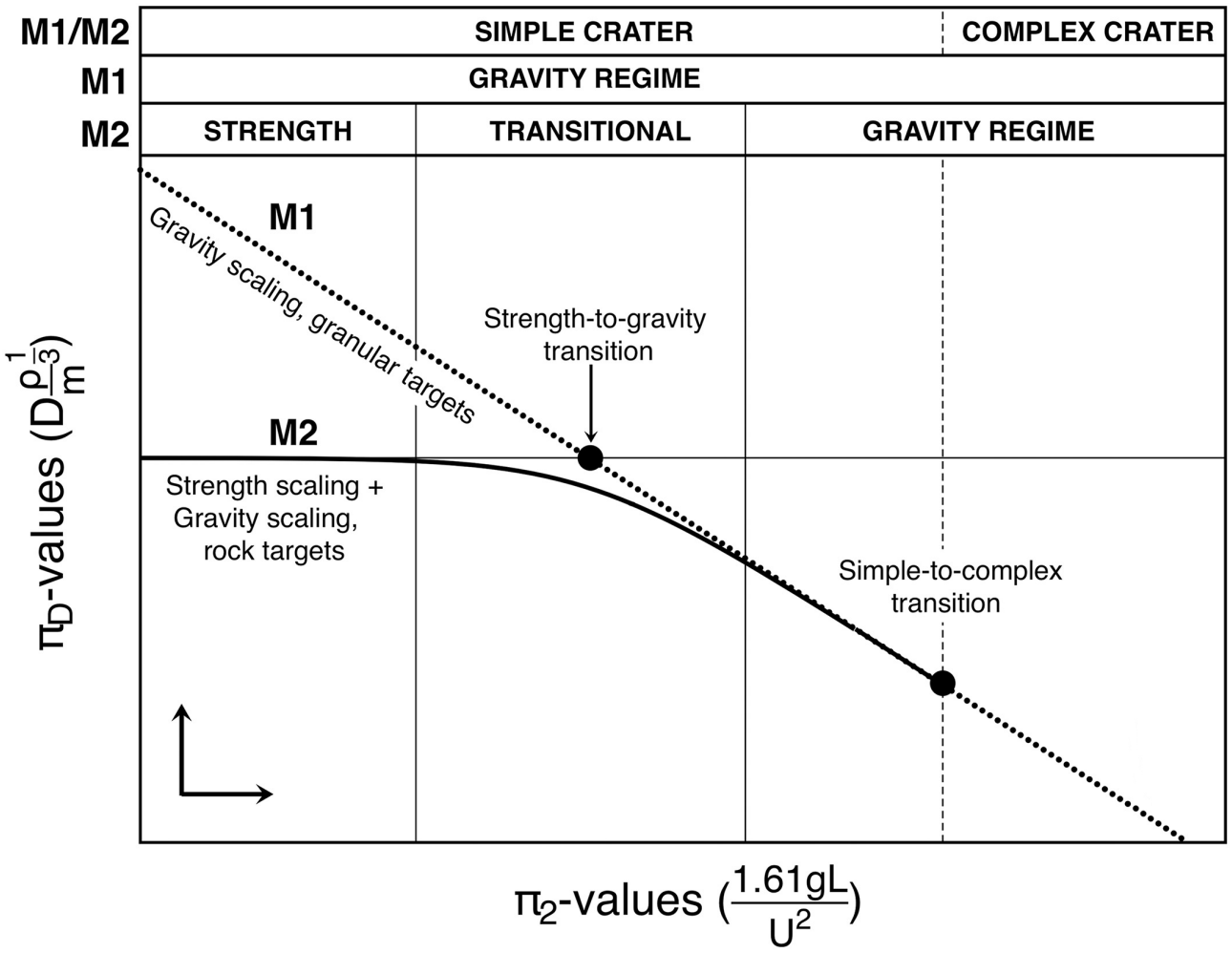

Figure 2.8: The gravity and strength regime in the pi-group scaling method. Parameter U in the x-axis represents velocity, and parameter D and m on the y-axis represent the transient crater diameter and impactor mass respectively. M1 is the curve used for granular target materials, and M2 is used for rocky target materials. It can be seen that the strength-to-gravity transition occurs before the simple-to-complex crater transition. Therefore, the strength regime is mainly dominant in smaller craters, whereas the gravity regime is dominant for larger crater [35].

Here, M1 shows the typical behavior of granular materials. Since granular materials have no effective strength, this leads to $Y = 0$ and thus $\pi_3 = 0$. This simplified Equation 2.2 to Equation 2.3. Essentially, it is a linear function of π_2, which can be seen in Figure 2.8 [35].

$$\pi_D = K_1 \left[\pi_2 \pi_4^{\frac{2+\mu-6\gamma}{-3\mu}} \right]^{\frac{-\mu}{2+\mu}}$$
$$\pi_D = K_{DG} \pi_2^{\frac{-\mu}{2+\mu}} \qquad K_{DG} = K_1 \pi_4^{\frac{2+\mu-6\nu}{-3\mu}\frac{-\mu}{2+\mu}} \tag{2.3}$$

As for M2, a rocky material, it has a finite strength and therefore $Y \neq 0$ and $\pi_3 \neq 0$. For sufficiently small values of π_2, π_3 will dominate, in essence, this is the strength regime, where strength determines the size of the crater more than gravity. So, for negligible values of π_2, Equation 2.2 can be rewritten to Equation 2.4 [35].

$$\pi_D = K_1 \left[\left(\pi_3 \pi_4^{\frac{2-6\gamma}{-3\mu}} \right)^{\frac{2+\mu}{2}} \right]^{\frac{-\mu}{2+\mu}}$$
$$\pi_D = K_{DS} \pi_3^{\frac{-\mu}{2}} \qquad K_{DS} = K_1 \pi_4^{\frac{1-3\nu}{3}} \tag{2.4}$$

Essentially, this equation is a straight horizontal line, due to its independence of gravity. This can also be seen in Figure 2.8, where the curve for M2 is practically horizontal for small values of π_2. However, the larger

the crater becomes, the greater the effect of gravity will become. This is also observable from Figure 2.8, where the effect of gravity slowly becomes greater for M2, until it eventually follows the trend of granular materials, in essence gravity nearly fully dominates crater diameter.

There are different regimes for craters: gravity-dominated or strength-dominated craters, as shown in Figure 2.8. For relatively small craters, size is mainly restricted by the strength of the material of the target surface, and so they are strength-dominated. On the other hand, as crater size increases, gravity becomes increasingly more important than strength, making them gravity-dominated [27].

One can determine whether a crater is in the strength or gravity regime by looking at the morphology. The strength-to-gravity regime transition is difficult to determine, however, it is known that it occurs before the simple to complex transition. Therefore, if a crater is complex, it will be in the gravity-dominated regime [27].

2.3. Impact Craters on Icy Moons in the Saturnian and Jovian System

There are many moons in the Saturnian and Jovian systems, and the ones that will be considered here are Titan and Enceladus for the Saturnian system, and Europa, Ganymede and Callisto for the Jovian system. Subsection 2.3.1 discusses the craters and surface features on the icy moons in the Jovian system, and Subsection 2.3.2 discusses the same for the icy moons in the Saturnian system.

2.3.1. Impact Craters on the Icy Moons of Jupiter

Among the three icy moons in the Jovian system, Europa is the only one that is rather scarce in craters compared to Ganymede and Callisto. Due to this scarcity, it is often estimated to be relatively young, perhaps even less than 10 million years according to McKinnon [36]. Contrarily, surface features that are in abundance are lineaments and ridges. These features are prominent, and can be seen all across Europa's surface, as shown in Figure 2.9a, and in close-up in Figure 2.9b. These features are hypothesized to result either from the ejection of material from beneath the icy shell, or crumpling of the ice shell itself due to tidal changes [37]. The surface composition is approximated to be 80% water ice and sulfuric acid and 20% hydrated salts [38].

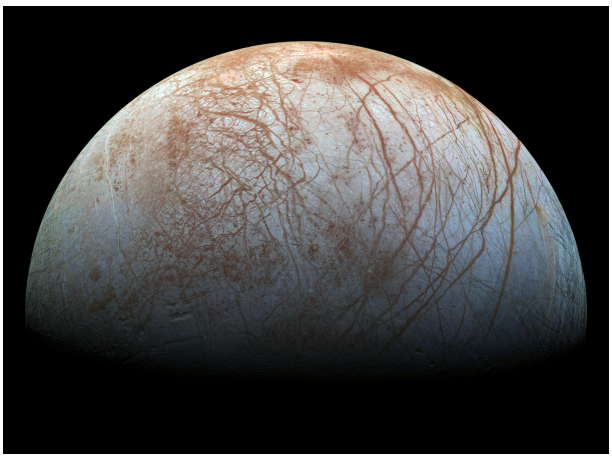

(a) Ridges and lineaments on Europa can be observed in orange- and brown-like colors [39].

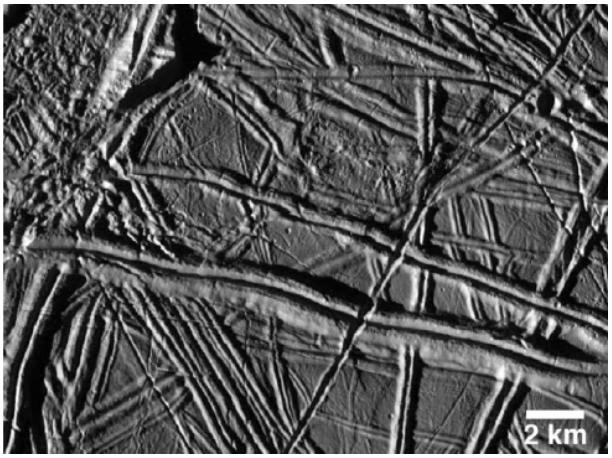

(b) Close up of the ridges and lineaments on Europa's surface [40].

Figure 2.9: In the figure on the left, the ridges across Europa's surface can clearly be seen. The figure on the right shows a close up of some of these ridges.

As for Ganymede, the largest and most massive moon in the Solar System, its surface is composed of 50% water ice and 50%, and can be divided into two surface types: dark and bright terrain [36, 41]. The dark terrain accounts for about one-third to half of the surface, and the rest is bright terrain [29, 42]. The bright terrain is noticeably less cratered than the dark terrain, and as a result the dark terrain is suggested to be Ganymede's oldest part. In Figure 2.10, the difference between terrains is shown, where the dark terrain can be seen on the bottom of the image and the bright terrain on the top.

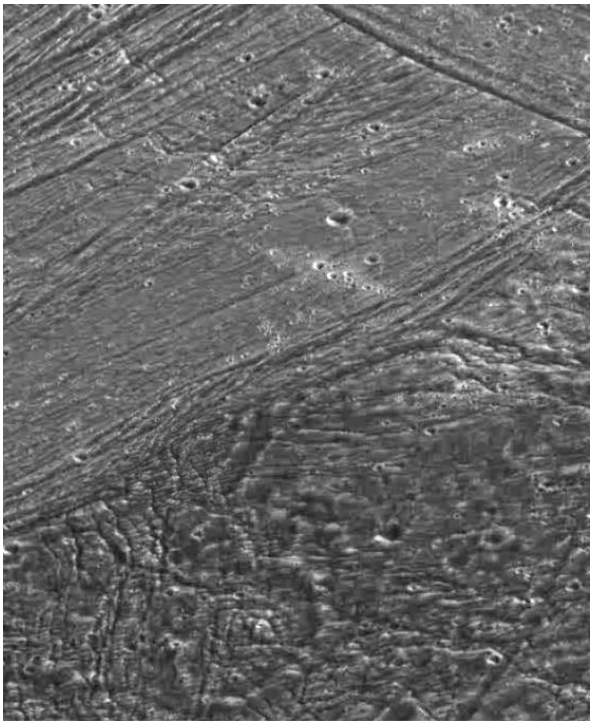

Figure 2.10: Image of Ganymede's surface, taken by the Galileo spacecraft. It shows the difference between the dark and bright terrain [36].

The dark terrain is geologically quite complex. Besides the many craters, it contains large fractures that sometimes reveal bright material beneath. Some of crater floors are also filled with material which could be assumed volcanic in nature. However, there also exist smooth dark areas. As for the bright terrain, there a large parts of crustal material, which are separated by faults. Grooves are common on bright terrain and are generally believed to result from surface extension. Suggested by Pappalardo et al. [43], is that the light material formed mainly through the modification of dark material by tectonic and cryovolcanic processes.

There are different types of craters that can be observed on the surface of Ganymede, which can be viewed in Figure A.1 in Appendix A. In short, every type of crater discussed in Subsection 2.2.1 can be found on Ganymede. The distribution of these craters and impact features are thought to be controlled by both the distribution of light and dark materials and a slight apex-antapex asymmetry in the light material crater density, meaning that there is an asymmetry in the crater density on Ganymede's leading edge (apex) and trailing edge (antapex) [29].

The last moon in the Jovian system that will be discussed here is Callisto. Callisto is slightly smaller in size than Mercury and has a low density, suggesting about a 50% water ice and 50% rock composition, similar to Ganymede [30, 41, 44]. The surface is very heavily cratered and therefore hypothesized to be ancient [36, 44]. A multitude of types of craters can be found, of which the most apparent are the vast multi-ringed basins, which can reach up to 4000 km in diameter, as shown in Figure 2.6b.

Besides large multi-ringed basins, simple craters were observed as well. They contain a range of degradation states, including fresh craters with ejecta and rays, circular rims, and walls with little or no evidence of slumping [44]. There are also complex craters that have similar characteristics to craters seen on the terrestrial planets and the Moon [44]. Some of the larger craters also show central domes [45]. Finally, a somewhat rare type of surface feature noticed on Callisto are the so-called catenae, or crater chains. As the name suggests, a crater chain consists of many craters that are aligned, thus creating a sort of chain. An example of a catanae can be seen in Figure 2.11, which includes about 25 craters. A potential theory on their formation revolves around the idea that the catenae formed due to an impact by a string of fragmented material, which was the result of a larger object that impacted the surface.

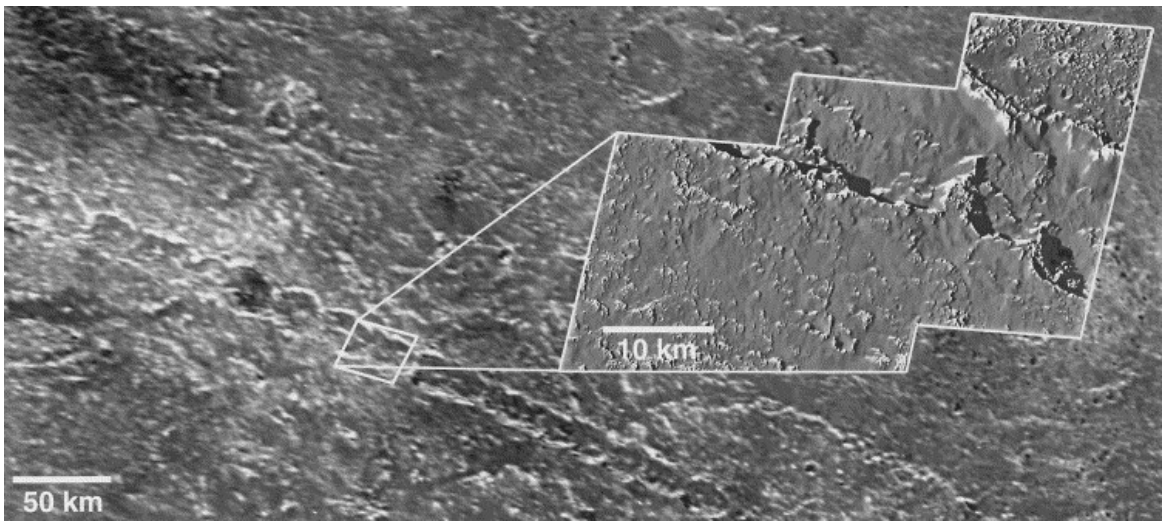

Figure 2.11: Image of the Gomul Catena (410 m/pixel) and inzoom of the white square (40 m/pixel) showing the degraded terrain on and around the catena [44].

2.3.2. Impact Craters on the Icy Moons of Saturn

The icy moons in the Saturnian system that are considered here are Titan and Enceladus. Titan is Saturn's largest moon, and the only moon in the solar system that has an atmosphere. From Cassini's radar imagery, about 59 probable craters were identified [5]. These were considered probable, because there were no obvious key crater characteristics observed.

Two examples of craters that were identified are the Ksa and Menrva crater. The Ksa crater displays characteristics of a complex crater, where a circular outline, raised rim, and a flat floor with a central peak can be seen. The Menrva crater is the biggest geological feature on Titan, being a multi-ringed impact basin. It is also one of the only impact basins found on Titan [46].

Some features on the surface of Titan are, however, not as clearly distinguishable as the previously mentioned craters. They might not necessarily look like craters, but still have some notable crater characteristics. These surface features are considered probable impact craters [46], and were either imaged with a low resolution, are significantly degraded/eroded, or both. For instance, some craters have a bright rim and are circular, but their their floors are partially cut or obscured by dunes. Wood et al. [46] noticed an unexpected low amount of small craters, which can amount to multiple theories. One example is the aforementioned limited resolution, or the erosion of the craters. Though, most likely for Titan, the atmosphere is the cause. Due to the thick atmosphere, most of the impactors would disintegrate before hitting the surface [46, 47].

Lastly, there is the relatively small moon Enceladus. Despite its size, it is a very geologically active moon [49]. At its crater-free south pole, Cassini detected plumes coming from fissures commonly known as tiger stripes.

In addition to the south pole, Bland et al. [49] state that there are two other regions of Enceladus' surface that have been geologically affected, which together accounts for about 50% of the total surface. Outside of these regions, the surface is dominated by craters, though they do not have a lot of typical crater-like features, as can be seen in Figure 2.12. They are mostly showing characteristics corresponding to viscous relaxation, such as shallow depths and up-domed floors. Bland et al. [49] suggests from simulations that viscous relaxation of Enceladus' largest craters is due to a relatively brief period of extreme heating that decayed quickly.

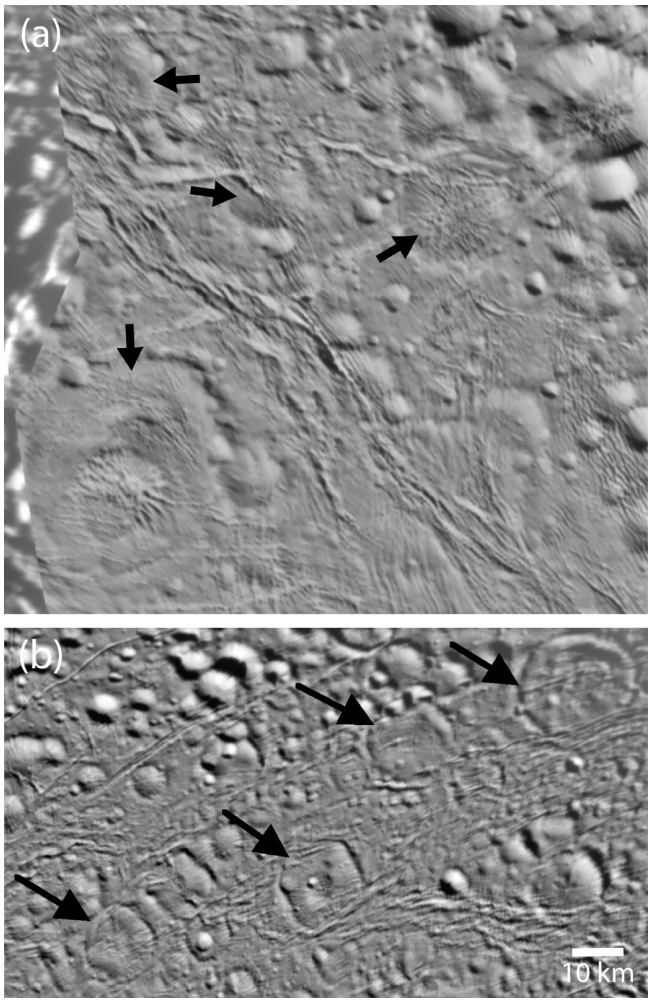

Figure 2.12: Image taken by Cassini, where the black arrows point out the remnants of relaxed craters. Such crater characteristics imply that there was once enough heat to make the icy crust flow viscously [48].

Other researchers such as Kirchoff and Schenk [48] and Schenk and Seddio [50] also think that the craters were affected by viscous relaxation. Schenk and Seddio [50] compared the images and data from Cassini with their own crater-size distributions, and noticed that the southern hemisphere had a much lower crater density than the northern hemisphere. Bray et al. [51] analysed the distribution of craters and indeed also found that more craters appeared relaxed in the southern hemisphere than in the northern hemisphere. Not only concluded Bray et al. [51] that the craters could have been affected by viscous relaxation, they also suggested that burial by material form the south polar plumes could have played a role. Kirchoff and Schenk [48] agree with this and concluded that such "missing" craters could have been removed by either viscous relaxation or burial by plume material or a combination of the two.

2.4. Age Determination Through Craters in the Solar System

The age of craters or terrains on celestial bodies can provide valuable insight into a body's geologic history, which can help explain how the solar system was created for instance. Essentially, they are a pool of knowledge.

One way to calculate the age is to obtain both the crater density and the cratering rate. The crater density is the number of craters of a specified size or larger, averaged over the entire surface of the body. For instance, if there are 100 craters with a size of ≥20 km on the entire surface of a body, then the crater density would be 100 divided by the total surface area of that body. The cratering rate is the number of impact events that occur each year on average, that would result in a crater with the specified size of ≥20 km mentioned earlier. Then, by dividing the crater density by the cratering rate, the age can be obtained. The crater density can be determined straightforward by looking at imagery gathered by flyby spacecraft. The cratering rate, however, is more difficult. It can be calculated in several ways. Zahnle et al. [52] determined cratering rates on synchronously rotating satellites in the solar system through Öpik's equations and Monte-Carlo simulations [53]. The Öpik equations are given by Equation 2.5 [54].

$$P = S^2 U/\pi \sin i|U_x| \qquad S^2 = R^2\left(1 + 2\mu/RU^2\right) \qquad U_x^2 = 3 - 2(2q)\cos i \qquad U^2 = 2(1-q) \tag{2.5}$$

Where P is the probability of passage within the target radius, per heliocentric revolution of the comet, S is

the aforementioned target radius, U is the relative velocity of the comet and planet near the orbit intersection point, normalize to the circular planetary orbital velocity, i is the comet orbit inclination, U_x is the radial portion of the relative velocity, R is the planet radius normalized to the mean planetary orbit distance, μ is the planetary mass normalized to the mass of the Sun, q is the comet perihelion distance normalized to the mean planetary orbit distance.

Öpik's equations calculate the probability of a specific projectile impacting a given body. Since many of these orbital parameters can have a wide range of values, and the fact that they are generally not known, a Monte-Carlo approach is commonly used in order to obtain the probability of an impact per impactor orbital revolution [53]. Another method described by Zahnle et al. [55] uses the current number of ecliptic comets. This number can be derived from three sources: 1) the number of small comets observed near Earth, 2) the historical record of small comets known to have closely encountered Jupiter, 3) the observed number of Centaurs in the more distant Solar System. Through models, simulations and observations, impactor distribution equations can be formed, and estimations for the cratering rates can be made.

The outcome of these estimations, however, may depend on the type of model used. One can use a heliocentric model, where the assumption is made that the impactors were originally orbiting the Sun, or a planetocentric model can be used, where the assumption is made that the impactors were originally orbiting a body. The main differences between these models are the velocity and the size of the impactors, which can affect the results.

2.5. Different Phases of Ice

The focus of this report is to study impacts in icy targets. Important here is to look at the different phases of ices that occur during the impact, since the heat and pressure will affect the ice on a molecular level. Ice is essentially water that is frozen into a solid state and based on its crystalline structure, proton ordering and density, it can be classified by different phases, which are shown in the phase diagram of water in Figure 2.13 [56]. Here, one can see how the different phases of water are connected, and what pressures and temperatures are required to get water into a certain phase. Typical phases of ice form in a crystalline structure, though there are other phases called amorphous ice, which can occur under different densities: low-density amorphous (LDA) and high-density amorphous (HDA) ice [57]. HDA is formed by compression of ordinary ice Ih or LDA at pressures in the order of a few hundred MPa. Very-high-density amorphous (VHDA) ice can form as well, which occurs when HDA is slightly warmed to 160 K under a pressure of 1.0 GPa-2.0 GPa. Contrary to crystalline ice, the water molecules in amorphous ice are arranged in a disordered state [57].

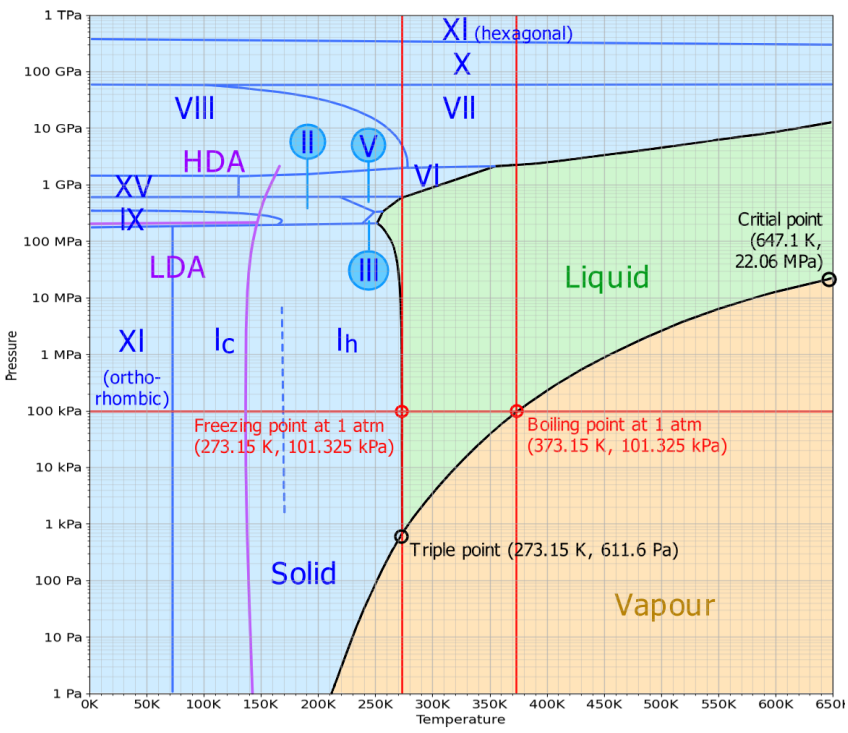

Figure 2.13: The phase diagram of water. Vapor, liquid and solid phases are present, as well as most of the different ice phases and the amorphous states (adjusted from Baez [56]).

As part of a study on Ganymede and Europa, Stewart and Ahrens [58] studied the ice phases that occur when varying the pressure of ice at initial conditions of 100 K and 263 K. They identified the main regions of the

shock Hugoniot to be elastic shocks in ice Ih, ice Ih deformation shocks, and shock transformation to ice VI, ice VII, and liquid water. Furthermore, they found that shock-induced ice VI may remain metastable upon release from shock pressures of about 1.0 GPa and below about 100 K. They conclude that shock-induced formation of high-pressure solid ice polymorphs should be relatively rare. Shock-induced melting of ice, however, will be widespread in impact events. Thus, one can expect that different ice phases can be created during an impact, where they will most likely change because of shock-induced melting.

2.6. Hydrocode Theory

A hydrocode is a piece of software that can be used to calculate and simulate phenomena regarding shocks, which makes them suitable for simulating planetary impacts [59]. The typical approach is to first generate a mesh or grid, where the impact will take place. Then, values for the input parameters and the different available options have to be selected. An important part of this, is the equation of state. The equation of state (EOS) is different for each material, because it is used to imitate the behavior of that specific material under different pressures and stresses. The equations that describe the conservation of mass, momentum and energy are then solved to determine the state of the material at a given point during the impact [59].

There are many different hydrocodes available [60]. Some of the main differences are related to their modeling approach and whether it is possible to simulate in multiple dimensions. Regarding the modeling approach, there are four different methods, as shown in Figure 2.14. The Eulerian approach uses a fixed coordinate system in space, which is a simple, yet adequate, method, but can be lacking in accuracy due to cell averaging. On the other side, a coordinate system that moves with the material is called the Lagrangian approach [60], and is more accurate than the Eulerian approach, but it is not useful for simulations where large deformations and distortions occur. Another approach combines the previously discussed approaches and is called the Arbitrary Lagrange-Eulerian approach (ALE), which partially solves the distortion issue, but has increased complexity due to geometrical calculations associated with handling an arbitrary mesh [61]. Lastly, another approach exists which is a meshless Lagrangian approach called Smooth Particle Hydrodynamic (SPH). It has the advantage of not having a fixed grid, but is limited in resolution and experiences problems with the implementation of strength models [62]. In essence, each approach has its advantages and disadvantages.

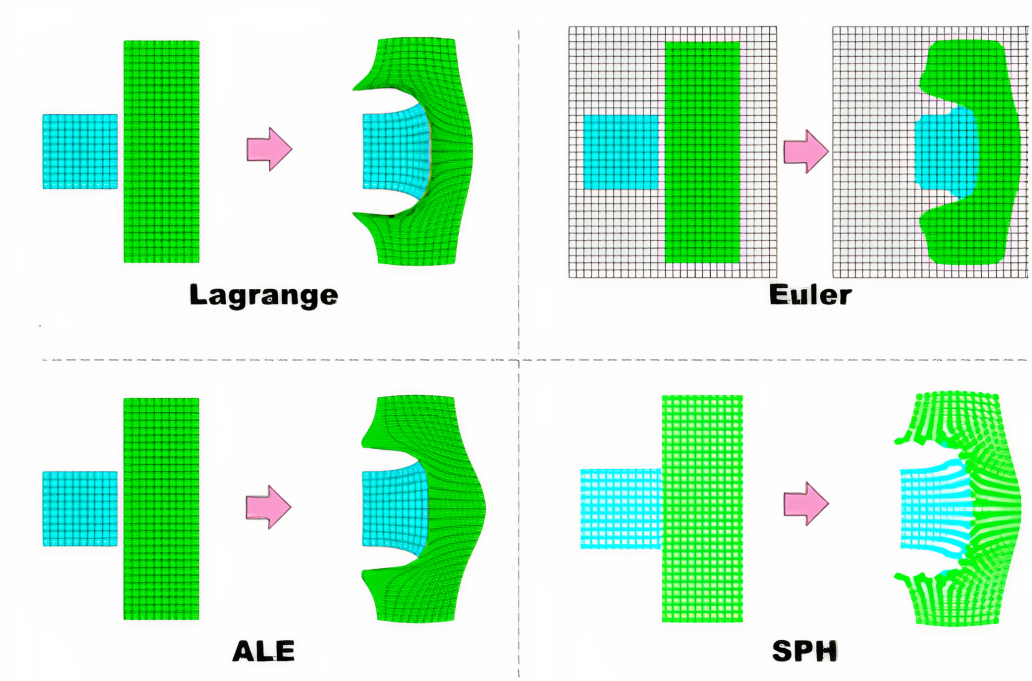

Figure 2.14: Visualization of the mesh for a Lagrangian, Eulerian, ALE and SPH meshing approach [63]. As shown in the upper left figure, the Lagrangian approach uses a coordinate system that moves with the material, where the Eulerian approach uses a coordinate system that is fixed, and encapsulates the area where the movement of material occurs. The ALE approach shown in the lower left figure combines the prior two approaches, and the SPH approach in the lower right figure uses a Lagrangian method but without a mesh. Each approach has its own advantages and disadvantages.

In order to determine the most appropriate hydrocode to use, previous research papers were investigated. Regarding papers that specifically study impacts in icy targets, most were found to utilize either the iSALE2D hydrocode, or the CTH hydrocode [1, 2, 64, 65]). It can be concluded then that both iSALE2D and CTH appear to be viable options for impact simulations in ice. The CTH hydrocode uses a Eulerian approach, and the iSALE2D hydrocode has options to use the Eulerian, Lagrangian or the ALE approach. Therefore, there is a slight preference to use the iSALE2D hydrocode, however, to decisively make a choice between the two, accessibility was also considered. As a matter of fact, to be able to use the CTH hydrocode, a license needs to be requested and a possible fee needs to be paid. On the other side, for iSALE2D only a simple questionnaire needs to be filled in to request access. Therefore, the decision was made to use the iSALE2D hydrocode.

2.7. Previous Work on Impact Simulations on Icy Moons

In this section, previous work related to impact simulations on icy moons is summarized. In Subsection 2.7.1, work related to impacts on icy moons in the Jovian system is discussed, and the same regarding the impacts on icy moons in the Saturnian system is addressed in Subsection 2.7.2.

2.7.1. Previous Work Regarding Impact Simulations on Icy Moons in the Jovian System

Some of the work regarding the simulating of impacts on icy Galilean moons has been done by Bray [66]. Bray used the iSALE2D hydrocode to simulate impacts on Ganymede and Europa, thereby studying the effect of different strength models and their parameter values, as well as testing and creating equations of state. The simulations on Ganymede were mainly used for experimenting with input values and models, whereas the actual simulations on Europa were related to applying these models in a layered target.

Another study, by Bjonnes et al. [1], simulated impacts in Ganymede and Callisto, where some of the results from the Ganymede simulations are shown in Figure 2.15. They studied the ice shell covering the moons by varying different parameters values such as the projectile radius and the thermal gradient of the ice shell. In Figure 2.15a, Figure 2.15b and Figure 2.15c, the projectile radius is 20 m, 50 m and 700 m respectively, and the thermal gradient is 10 K/m for all three simulations. Multiple runs were conducted to better understand the thermal structure of the ice shell. The results showed that the range of thermal profiles created craters ranging from shallower than observed to deeper than observed craters. It was recommended though, that impurities in the target should be considered, given the effect of material strength on the subsurface thermal structure.

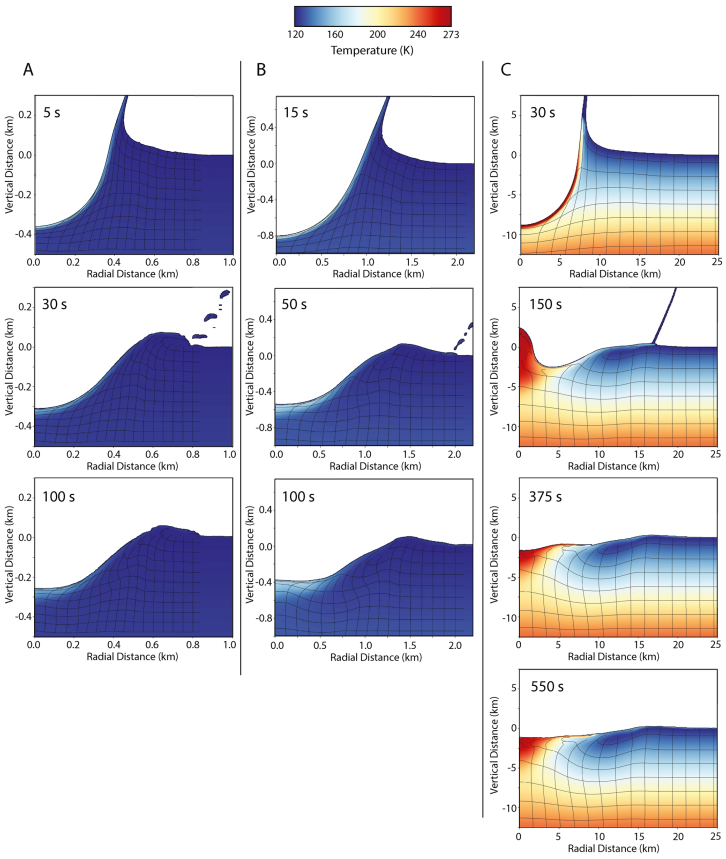

Figure 2.15: Simulation results for impacts in ice for three different situations. A 10 K/km conductive thermal gradient is used, overlying 250 K convective ice. The diameter of the impactor from left to right column is 40 m, 100 m, and 1.4 km, respectively. Tracer lines are visualized by thin black lines showing internal deformation [1].

Senft and Stewart [64] investigate the icy shell on Ganymede and Callisto through simulations, using a new EOS that includes more ice phases, the ”5-phase EOS”. Their simulations explored the effect of varying the impact conditions and target thermal gradient on impact crater formation on icy satellites. By using independently derived model parameters, they

can illustrate a diversity of cratering phenomena, including the discovery of discontinuous excavation and hot plug formation.

Silber and Johnson [2] studied the icy shell on Europa through impacts. They investigated the thickness and internal structure of the ice shell by varying parameters such as the thermal gradient and the gradient type (conductive, convective), and verified if they could reproduce the observed crater depth-to-diameter and crater morphologies.

2.7.2. Previous Work Regarding Impact Simulations on Icy Moons in the Saturnian System

Crósta et al. [67] simulated large impacts on Titan, investigating if a breach in Titan's icy shell could lead to an exchange of materials between Titan's layers, in particular between the surface and the subsurface ocean. Crósta et al. [67] used the iSALE2D hydrocode to study the formation of a Menrva-size impact crater, varying the assumed ice shell thickness from 50 km to 125 km and assumed a thermal structure. They analyzed the implications and potential contributions of impact cratering as a process that can facilitate the exchange of surface organics with liquid water.

In a paper by Bell [5], the age of the Saturnian moons was determined. Bell made a database of the craters on the moons, and employed the planetocentric model, instead of the often-assumed heliocentric model. Bell focused on the relative crater densities between moons, and calculated scaling relationships. The relative ages on the moons was consequently determined. Results showed that the usage of a planetocentric cratering model implies that the cratered plains of Mimas, Tethys, Dione, Rhea, and Iapetus are of broadly similar age, whereas the surface of Titan is definitely younger than the cratered plains of Rhea and Iapetus, if not much younger. However, due to lack of constraints on the planetocentric cratering rate and how it varies with time, this model provides very limited constraints in terms of absolute age, and it cannot rule out a surface of Titan that is very old and has a very slow erosion rate and negligible endogenic resurfacing.

Roberts and Stickle [68] studied impacts on Enceladus, specifically impacts in the South Polar Terrain (STP). Tides on Enceladus are recognized as observed thermal anamolies, however, measured heat flow patterns and activity cannot be explained by this alone, because tidal potential is symmetric about the equator, and no thermal anomaly is present in the north pole. Therefore, Roberts and Stickle [68] explore the possibility of a large icy impactor impacting the south pole and breaking through the ice shell that will eventually lead to the large thermal anomalies that are observed nowadays.

Results showed that an impact that is capable of creating a crater the size of what is currently the size of the STP, could punch through the 20 km ice shell, and excavate a cavity extending 30 km deep, exposing part of the ocean to space. They also find that the impact shock heating would be retained for a few Myr, and that local ice softens to allow for more tidal dissipation.

However, Roberts and Stickle [68] concluded that more work is needed to understand how a highly-fractured crater floor is able to be restored to only four huge fractures that are observed currently. Extensive fracture modeling is needed to quantify how the four tiger stripes could be sustained over geologic time scales. In addition, more evidence of the possibility that an impact crater breach in the STP could be the cause of the thermal anomalies needs to be conducted. The lack of craters suggests the SPT is young and any original impact structure would have been heavily modified by geologic activity.

2.8. Knowledge Gap

Based on previous studies, it can be concluded that many papers focus solely on the ice shell of a single icy moon, often Europa, or examine the effects of varying thermal profiles within the target or the ice shell. However, little research exists following up on what Bell [5] has done, which is to explore possible links between heliocentric and planetocentric impactors, and craters or ages of terrain. This, in combination with certain unexplored aspects in impact simulations, such as looking at different ice phases, could therefore be leveraged to create a research question. That is, investigating a possible method that can be used to determine whether the impactor had a heliocentric or planetocentric origin, based on the craters on icy moons and their characteristics. This could potentially be done by looking at the different types of ice in and around a crater, and looking at parameters such as the shape, size, damage, and temperature. Therefore, the research question will be: *"Can*

crater morphology, target damage, target temperature, and different ice phases be used to identify whether the impactor had a heliocentric or planetocentric origin in craters on icy moons?".

To address the main research question, multiple sub-questions have been established to systematically guide the analysis. These sub-questions cover essential aspects of the problem. First, it is necessary to assess the accuracy and applicability of the equations of state (EOS) of water/ice in iSALE2D, as this directly affects the reliability of the simulation results. Consequently, additional EOS that provide improved accuracy shall be researched and implemented if the pre-existing EOS are found lacking. Then, the robustness of the hydrocode is determined through verification and validation. A sensitivity analysis is also performed, which aims to evaluate the influence of the input parameters on the impact process and final crater. To quantify crater characteristics such as diameter and depth, a reliable method is determined for the extraction of these properties. Finally, the focus shifts back to the main research question and the parameters of interest — impact velocity and impactor size — and their influence on key aspects of crater formation. These include the resulting crater morphology, the extent and depth of damage and fracturing, and the thermal response of the target, including changes in ice phases.

1. Is the resolution of the different equations of state in iSALE2D high enough to be able to distinguish different ice phases)?
2. Are there other promising equations of state outside of the ones present in iSALE2D?
3. How can the iSALE2D hydrocode be verified and validated?
4. How can the diameter and depth be determined from the simulations?
5. What are the effects of a sensitivity analysis of the input parameters on the final crater and the impact process?
6. What is the influence of impact velocity and impactor size on the resulting crater morphology in impact simulations under Ganymede-like conditions?
7. What is the influence of impact velocity and impactor size on the resulting crater damage in impact simulations under Ganymede-like conditions?
8. What is the influence of impact velocity and impactor size on the resulting crater temperature and ice phases in impact simulations under Ganymede-like conditions?

3
Equation of State

In this chapter, the focus is shifted to the EOS. The EOS plays an important part in the simulation of impacts, as it describes the state of the material based on the pressure, temperature and density encountered. In Section 3.1, the different types of EOSs are discussed, as well as the ones that are already implemented in iSALE2D. In Section 3.2, the relevant iSALE2D EOSs are studied through phase diagrams to explore their differences. Then, in Section 3.3, EOSs that are not available in iSALE2D are investigated. Finally, the performance and usability of the EOSs is discussed and compared in Section 3.4.

3.1. Different Equations of State in iSALE2D

iSALE2D supports the usage of different EOS, with ANEOS and Tillotson being among the most frequently used. The reason for this being that planetary impacts require an EOS that is capable of accurately determining material states across a wide range of pressures, densities, and temperatures. In addition, shock states need to be captured, which are essential to impacts. Therefore, more advanced EOS such as ANEOS and Tillotson are used [69].

The Tillotson EOS is relatively straightforward and popular for its simplicity. It is an analytical EOS, hence it only uses equations to calculate the state of the material, which for further interest can be viewed in Appendix C [70]. In iSALE2D, it is required to define input parameters such as the reference density, specific heat capacity and some constants that are specific to the Tillotson EOS. During the simulation, the program then uses those values and calculates the state of the material at each time step.

The ANEOS EOS is, compared to the Tillotson EOS, highly complex due to its explicit treatment of the different phases of the material. It is a semi-analytical EOS, which uses both equations and tables to determine the state. In iSALE2D, one can either choose to use a pre-existing ANEOS EOS file - a large table with parameter values - or create a customized ANEOS table by redefining several input parameters. Creating an ANEOS table is quite challenging though, because a lot of very specific information about a material is needed [71]. As for the pre-existing ANEOS files, these are already accessible from the start, and can be used directly by writing down their file name in the input file.

As mentioned before, the ANEOS EOS is a large datafile with numbers. These numbers correspond to certain parameters or characteristics of the material. These parameters form a multi-dimensional table, and typically include pressure, density, sound speed, temperature, and specific internal energy. Of these, density and temperature are commonly used as input parameters in the columns and rows of the table, respectively. Since ANEOS is a semi-analytical EOS, it uses both the large table and equations to determine the state of the material at any given time step [72].

This is also how the system works in iSALE2D, however, there is barely any documentation on the ANEOS datafile. Despite the lack of clarity, the structure and meaning of the numbers was discovered after thorough investigation, and aid of co-creator of iSALE2D Professor Gareth Collins. Essentially, the data in the ANEOS datafile can be translated to a 2D table as shown in Table 3.1. The input parameters here are the density (ρ) and either the temperature (T) or the specific internal energy (u), although temperature is most commonly used. Then, for each combination of density and temperature, there is a corresponding group of values for the specific internal energy (or temperature if specific internal energy is an input), pressure (P), and sound speed (c).

Table 3.1: Example of the table structure corresponding to an ANEOS datafile. For each value of temperature (T) and density (ρ), there exists a corresponding group of specific internal energy (u), pressure (P), and sound speed (c) values. There are a finite number of nodes or points for temperature and density, represented by (Nt) and (Nd) respectively. Temperature and density are typically spaced non-uniformly.

	ρ_1	ρ_2	ρ_3	...	ρ_{Nd}
T_1	$(u,P,c)_{1,1}$	$(u,P,c)_{1,2}$	$(u,P,c)_{1,3}$	...	$(u,P,c)_{1,Nd}$
T_2	$(u,P,c)_{2,1}$	$(u,P,c)_{2,2}$	$(u,P,c)_{2,3}$	...	$(u,P,c)_{2,Nd}$
T_3	$(u,P,c)_{3,1}$	$(u,P,c)_{3,2}$	$(u,P,c)_{3,3}$	...	$(u,P,c)_{3,Nd}$
...	...	...	...	...	...
T_{Nt}	$(u,P,c)_{Nt,1}$	$(u,P,c)_{Nt,2}$	$(u,P,c)_{Nt,3}$	...	$(u,P,c)_{Nt,Nd}$

Next, to understand how the numbers in the ANEOS datafile are connected to the parameters from Table 3.1, Table 3.1 is given that uses numbers taken from an example EOS. The ANEOS data file systematically cycles through specific internal energy, pressure, and sound speed values for each density in the first row, then proceeds to the next temperature (or row) and repeats this process. This looping continues until all the temperature and density combinations are covered.

Table 3.2: Example of how the values in the ANEOS table are connected to the parameters from Table 3.1. On the left side, example values are given similarly as they would in an ANEOS file. On the right, parameters from Table 3.1 are displayed, and it can be seen which values correspond to which parameters, and how. As an example, 120 density nodes have been used here, meaning that after every 90 rows in the ANEOS file, the next row in Table 3.1 starts, which is indicated by the first number in the subscript of the parameters on the right side.

ANEOS file					→	Parameters from Table 3.1			
Row	Col 1	Col 2	Col 3	Col 4		Col 1	Col 2	Col 3	Col 4
1	1.59E+03	8.32E+03	2.47E+08	1.67E+03	→	$u_{1,1}$	$P_{1,1}$	$c_{1,1}$	$u_{1,2}$
2	2.90E+03	1.55E+08	1.75E+03	2.27E+02	→	$P_{1,2}$	$c_{1,2}$	$u_{1,3}$	$P_{1,3}$
3	5.46E+07	1.82E+03	1.97E+02	5.48E+07	→	$c_{1,3}$	$u_{1,4}$	$P_{1,4}$	$c_{1,4}$
4	1.90E+03	2.77E+03	1.77E+08	2.04E+03	→	$u_{1,5}$	$P_{1,5}$	$c_{1,5}$	$u_{1,6}$
...	...	...	...	...		...	...	...	...
90	8.44E+11	2.19E+04	8.06E+07	1.05E+12	→	$c_{1,Nd-1}$	$u_{1,Nd}$	$P_{1,Nd}$	$c_{1,Nd}$
91	3.41E+04	3.23E+08	5.98E+12	3.56E+04	→	$u_{2,1}$	$P_{2,1}$	$c_{2,1}$	$u_{2,2}$
...	...	...	...	...		...	...	...	...
5400	3.76E+04	6.01E+08	7.63E+12	3.90E+04	→	$c_{Nt,Nd-1}$	$u_{Nt,Nd}$	$P_{Nt,Nd}$	$c_{Nt,Nd}$

3.2. Study of the Pre-existing Equations of State in iSALE2D

This report focuses on impacts on icy targets, which means EOSs for water are essential. As mentioned before, there are already several EOSs available in iSALE2D for water, however, only one EOS can be used, and so a choice must be made. In order to make that decision, it is important to understand how the EOSs are different from each other. To do so, a phase diagram is created by plotting the pressure, temperature, and density in a heatmap. The process of creating this phase diagram is explained in Subsection 3.2.1. Then, in Subsection 3.2.2 and Subsection 3.2.3, phase diagrams are made for the water_ice EOS and h2o_ice EOS respectively, which are the two most relevant EOS for water that are already available in iSALE2D.

3.2.1. Creation of the Phase Diagram

To plot the phase diagram, temperature, pressure and density are required, with temperature on the x-axis and pressure on the y-axis. However, the table in the ANEOS file is structured in such a way that only temperature and density can be used on the x-axis and y-axis. Hence, the density and pressure need to switch places, which can be achieved by interpolation.

In the ANEOS file, the density is given as a single array, with a length equal to the number of density nodes. To switch density with the pressure, density has to become a function of both temperature and pressure. For the EOSs in iSALE2D, the density typically consists of 120 nodes or numbers. In order to switch the density and the pressure, it means that 120 nodes are also needed for the pressure. This can be achieved in a simple way by selecting a minimum and maximum value using Python functions such as linspace or logspace, which automatically calculate these 120 points. Important is to select appropriate minimum and maximum values. This is best explained with an example. Let the 120 pressure points be represented by $[P_1 \;\; P_2 \;\; P_3 \;\; \dots \;\; P_{120}]$, and assume that the ANEOS tabular data is structured the same way as shown in Table 3.1. When using interpolation, three points are required: a point of interest that needs to be interpolated, which is taken from $[P_1 \;\; P_2 \;\; P_3 \;\; \dots \;\; P_{120}]$, and two neighboring points from Table 3.1, where one is just below the point of interest, and one above the point of interest. However, if pressure values in the original ANEOS table like $\left[P_{1,1} \;\; P_{2,1} \;\; P_{3,1} \;\; \dots \;\; P_{Nt,1}\right]$ exceed P_1, or if values like $\left[P_{1,Nd} \;\; P_{2,Nd} \;\; P_{3,Nd} \;\; \dots \;\; P_{Nt,Nd}\right]$ fall below P_{120}, interpolation cannot be performed because no values would exist below or above the point of interest. Therefore, P_1 and P_{120} must be chosen such that they encompass the range of all pressures, in essence, see Equation 3.1.

$$P_1 \geq \max\left(\left[P_{1,1} \;\; P_{2,1} \;\; P_{3,1} \;\; \dots \;\; P_{Nt,1}\right]\right) \qquad P_{120} \leq \min\left(\left[P_{1,Nd} \;\; P_{2,Nd} \;\; P_{3,Nd} \;\; \dots \;\; P_{Nt,Nd}\right]\right) \tag{3.1}$$

Once the pressure list is appropriately created, the process of switching the pressure and density is next. Interpolation is used for this process and essentially has to be done for each row in Table 3.1. There are multiple ways to perform interpolation, but the method used here is the simple linear interpolation method. Linear interpolation has its disadvantages, such as its arguable accuracy, however, it is a very simple method, and when used for data that does not fluctuate significantly, and is not far apart, it can be sufficiently accurate. To ensure that linear interpolation is a suitable option, a test was performed. The reader is referred to Appendix C for more information regarding the theory of linear interpolation.

In order to check whether linear interpolation provides sufficient accuracy, a 2D plot was created of pressure and density from data from the water_ice EOS. Note that the data for only a few temperature nodes is shown, mainly to ensure the clarity of the plot. Figure 3.1 shows different pressure-density curves for temperatures in the range of 35000-86700 K. Note that these temperatures were only used for the sake of visualizing the interpolation method. An arrow is displayed to show the position the curves would move to for lower temperatures. The orange curves represent the original data, and the blue dots and lines represent the interpolated data points. An enhanced plot closer to the origin can be found in Figure A.2 in Appendix A.

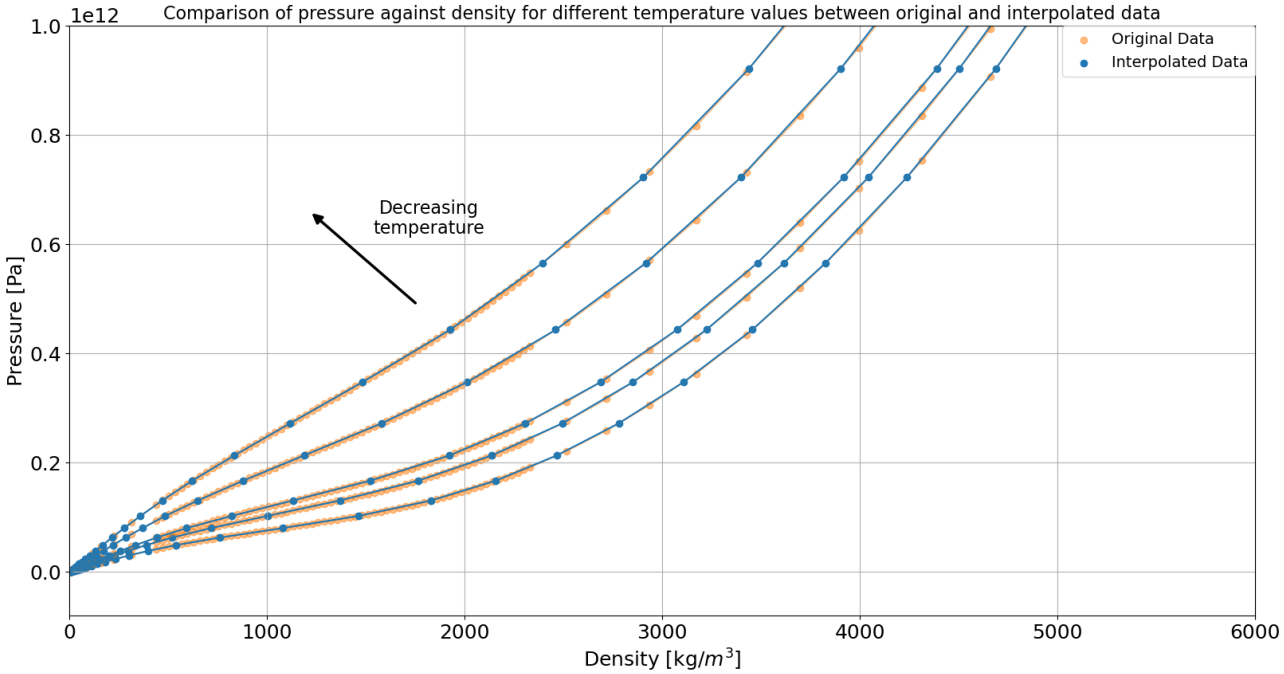

Figure 3.1: Pressure against density for different temperatures. The original data is displayed by the orange colored dots, and the interpolated data is given by blue dots and lines. It can be seen that the interpolated data follows the original data very well. Also shown is the direction of decreasing temperature, displaying the direction the pressure-density curve would move in for decreasing temperatures.

It can be seen from Figure 3.1, that with the same number of nodes, the individual linear segments follow the original data very well. Moreover, since the pressure list is created using the Numpy function logspace, the number of nodes can easily be increased for enhanced accuracy. Therefore, it was concluded that the use of linear interpolation is a sufficiently viable approach to create the phase diagram.

3.2.2. Phase Diagram of the water_ice Equation of State

The first EOS that is analysed is the ”water_ice.aneos” EOS. This EOS uses temperature and density as inputs, with 60 temperature nodes and 120 density nodes. The temperature ranges from 1 K to 8.67×10^4 K and the density ranges from 1.0×10^{-1} kg/m^3 to 1.09×10^4 kg/m^3. As mentioned in Subsection 3.2.1, in order to switch the density and pressure, an appropriate minimum and maximum pressure value is required for the new pressure list. By quickly finding the highest minimum pressure value and lowest maximum pressure value, a list was created that uses logarithmically spaced points between a pressure value of 1 Pa and 5.8×10^{12} Pa.

When running the code, an unexpected error was returned, and further investigation of the ANEOS table showed that some pressures were stored as negative values. This was confirmed after plotting the pressure against the density for the first few temperature nodes, which can be found in Appendix A in Figure A.2. After the temperature value of 200 K, the issue of the negative pressures disappears. The reason for these negative pressures remains unknown, but since it affected only a few nodes, a decision was made to exclude them. However, the data becomes incomplete through these measures, and so nonphysical behavior in the phase diagram is expected around the affected regions. This region is located around temperatures between and 0 K and 200 K, and pressures around 10 MPa.

With the problem solved, the phase diagram that was made is given by Figure 3.2. Note the limits on both axes, which were used for a better comparison to the actual phase diagram given by Figure 2.13.

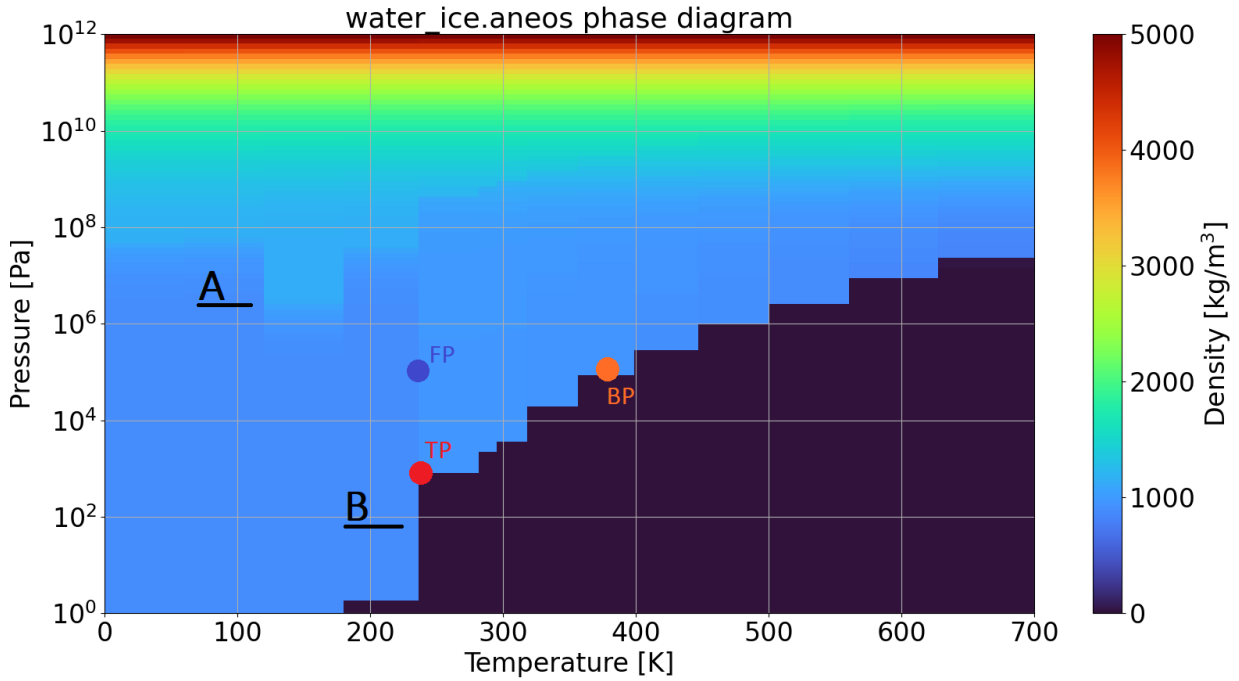

Figure 3.2: Phase diagram of the water_ice EOS. The figure has been enhanced to show the phase diagram between the temperatures 0-700 K, pressures 1-1.0 × 10^{12} Pa, as well as densities 0-5000 kg/m^3. The letters A and B are used to indicate unexpected behavior. Three points are also shown: TP, FP, and BP, which represent the triple point, freezing point, and boiling point, respectively.

Comparing Figure 3.2 to Figure 2.13, a few significant differences can be seen. Immediately noticeable is that the phase diagram looks rough or jagged, which is likely indicative of a low resolution in both temperature and density, though mainly temperature. Besides this, there are a few other noticeable differences. The region indicated by the letter A is unusual, as the horizontal line at 6.0 × 10^7 Pa, that is created by the difference in density, is suddenly interrupted at ∼120 K. This difference could be explained though by the negative pressures found previously. It was predicted then, that the effect of removing the negative pressure would likely impact the same region in the phase diagram.

A second region of interest is the vertical line shown at the letter B, where the natural curve of the boundary between the dark and light blue areas is disrupted, which is likely due to a low resolution. Looking closer at Figure A.4 at around 200 K, it shows that the density increases substantially, while the pressure remains at a very low value. This means that a color difference should be expected for a low pressure value, which can indeed be seen. Nevertheless, the difference in quality between Figure 3.2 and Figure 2.13 remains evident.

Next, the phase diagram is studied in more detail. Figure 3.2 shows that there is a relatively noticeable distinction between the vapor, liquid and solid phases, effectively due to the changes in density which is visualized by the colors, similar as shown in Figure 2.13. Unfortunately, the solid water phases cannot be distinguished. The parts that are somewhat distinguishable are the areas between 1 Pa-1.0 × 10^7 Pa and 0 K-250 K, which corresponds to the ice Ih and Ic phases, and between 1.0 × 10^7 Pa-1.0 × 10^9 Pa and 0 K-250 K, which corresponds to the ice phases ice II, ice III, ice V, ice VI, ice IX and ice XV, but are too hard to tell apart. This is also the case for the phases at the top of the figure at a pressure higher than 1.0 × 10^9 Pa, which constitutes of ice VII, VIII, X and XI. Although, this is partially due to the limit of the density, which was put on the lower side to enhance the visibility and distinguishability of the other areas.

Key points here are the freezing point, boiling point and the triple point, which are essential to the phase diagram. Although, not only the freezing or boiling point is checked, but rather the entire boundary. Looking at the freezing boundary, the diagram should show a clear change in phase at 273.15 K and between 700 Pa-1.0 × 10^8 Pa, and around a pressure of 1.0 × 10^9 Pa and temperatures equal or larger than 273.15 K. From Figure 3.2, it can be seen that there is a difference in density, however, it is around 235 K and starts at a much lower pressure of 30 Pa. As for the other boundary, the change looks similar to the actual phase diagram. The boiling boundary can be found along the curve made between the dark blue and light blue colors, at atmospheric

pressure and at a temperature of 373.15 K and higher. Despite the low resolution, Figure 3.2 shows a curve that is similar in shape and resembles the expected curve from Figure 2.13. Lastly, the triple point, located at ~611 Pa and 273.15 K [73], is where all three phases come together. Due to the low resolution, the triple point in Figure 3.2 is located in a different place, around 700 Pa and 235 K.

3.2.3. Phase Diagram of the h2o_ice ANEOS Equation of State

The other ANEOS EOS for water is called ”h2o_ice.aneos”, and differs from the water_ice EOS, because it uses specific internal energy as an input instead of temperature. This complicates the creation of the phase diagram, as both temperature and pressure have to be switched with specific internal energy and density respectively. Moreover, this EOS uses a different number of nodes, which is 200 for the specific internal energy and 270 for the density.

Despite the complication of switching both temperature and pressure with the specific internal energy and density, it remains feasible. Initially, the process is similar as before, with one parameter swapped for another using linear interpolation. For instance, temperature is replaced by specific internal energy through interpolation. Then, the pressure and density need to be swapped. However, at this moment, the pressure values are tied to the original specific internal energy values rather than the interpolated temperature. Hence, this requires an additional interpolation step to align the pressures with the new temperature values. For a visual aid, see Table 3.3. The left side with the blue letters represent the original values taken directly from the h2o_ice data, whereas the red letters on the right side are used to show the parameters that were changed due to interpolation, and have different values now. So first, a simple interpolation is performed where the temperature and the specific internal energy are switched.

Table 3.3: The table structure of the h2o_ice EOS is given on the left side, where specific internal energy and density are in the rows and columns, respectively. On the right side, the same table, but specific internal energy and temperature switched, is given. The parameters highlighted in blue represent the original data, whereas those in red are used to show that those parameters have been interpolated.

Original table structure					Table structure after interpolation			
	ρ_1	...	ρ_{270}			ρ_1	...	ρ_{270}
u_1	$(T,P,c)_{1,1}$	...	$(T,P,c)_{1,270}$	$\longrightarrow$	T_1	$(u,P,c)_{1,1}$	...	$(u,P,c)_{1,270}$
u_2	$(T,P,c)_{2,1}$	...	$(T,P,c)_{2,270}$	$\longrightarrow$	T_1	$(u,P,c)_{2,1}$	...	$(u,P,c)_{2,270}$
...	...	...	...		...	...	...	
u_{200}	$(T,P,c)_{200,1}$	...	$(T,P,c)_{200,270}$	$\longrightarrow$	T_1	$(u,P,c)_{200,1}$	...	$(u,P,c)_{200,270}$

As can be seen from Table 3.3, the pressure values on the right side still correspond to the original specific internal energy values. Since specific internal energy has now been replaced by temperature, the associated pressure values must be recalculated to match the updated specific internal energy values. Since the density values have not changed, and the original specific internal energy values are known, they can be used together with the new specific internal energy values to linearly interpolate the updated pressure values. A visualization of an example of this is given by Figure 3.3, which shows pressure against specific internal energy for a given density value. Essentially, one would be looking at data from a single column from Table 3.3. The blue dots represent the specific internal energy and pressure values from the left side in Table 3.3, which can be used to create linear equations between the points. Then, using the specific internal energy values from the right side of Table 3.3, giving the x-coordinates, one can obtain the new pressure values. By doing this for all density nodes, the correct pressure values are obtained.

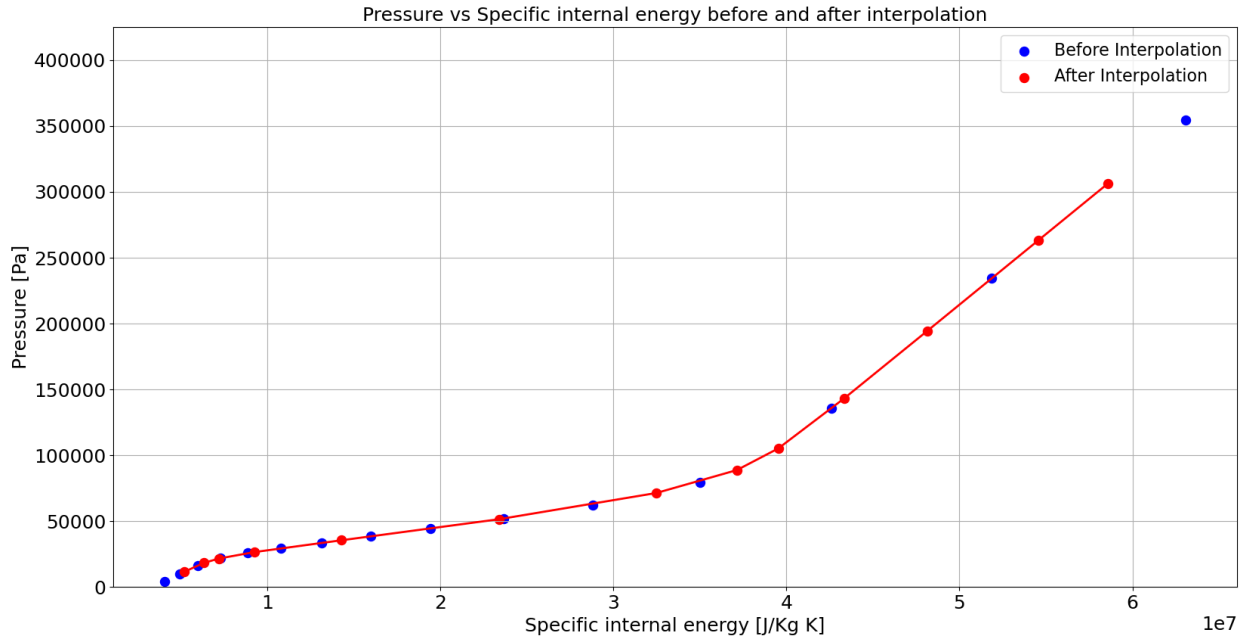

Figure 3.3: Example plot of pressure against specific internal energy, where the blue dots represent the original data, and the red dots represent the new specific internal energy values. The x-values of the red dots are known, and through linear interpolation based on the data from the blue dots, the y-values of the red dots could be calculated. The data after interpolation shows to be a good fit of the data before interpolation. The letters A and B are used to indicated areas of interest.

With the correct pressure values, the last step is to simply switch the pressure and density through linear interpolation, as done before. With the data on temperature, density, and pressure now available, the phase diagram is plotted and shown in Figure 3.4.

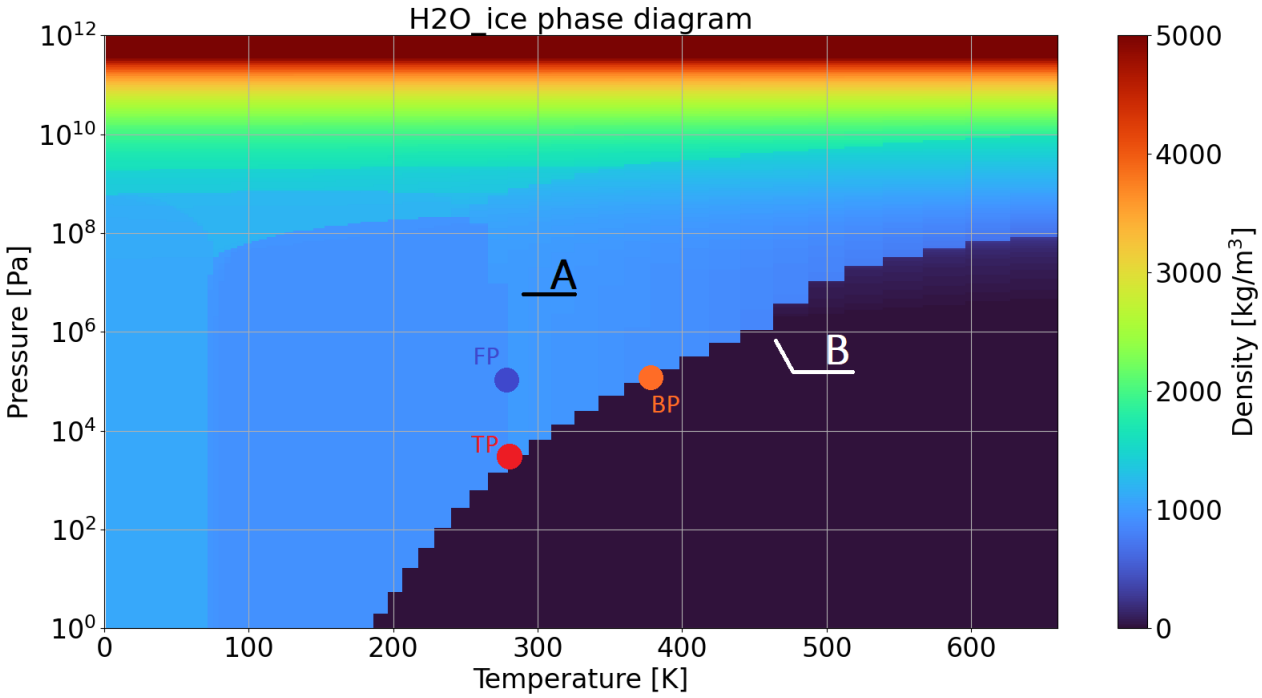

Figure 3.4: Phase diagram of the h2o_ice EOS. The figure has been enhanced to show the phase diagram between the temperatures 0-700 K, pressures 1-1.0 × 10^{12} Pa, as well as densities 0-5000 kg/m^3. The letters A and B are used here to indicate unexpected behavior. Three points are also shown: TP, FP, and BP, which represent the triple point, freezing point, and boiling point, respectively.

As can be seen from Figure 3.4, the phase diagram appears much smoother compared to the water_ice EOS shown in Figure 3.2. Immediately noticeable are the more refined curves, and more distinguishable ar-

eas of different density, which is likely due to the increased resolution. At first glance, only two areas appear unusual. Though hard to see, there is a slight difference in density, creating a boundary which is indicated by the letter ”A” in the plot. Here, a minor shift of the vertical boundary between the two shades of blue can be observed, which is likely due to the resolution, as the shift is rectangular in shape. The second area is displayed by the letter ”B”. Following the natural curve of the boundary, it shows a slight unexpected shift upwards. This should not occur, and despite the improvement of the resolution in comparison with Figure 3.2, this could still be an issue regarding the resolution in this particular area.

To assess the accuracy of Figure 3.4, specific areas and boundaries are compared to Figure 2.13. Starting with the freezing boundary, Figure 3.4 shows that there is a distinguishable difference in density at the correct values. There is subtle distinction in density at around 270 K from 600 Pa to 1.0×10^9 Pa, and the upper boundary at 1.0×10^9 Pa and $\geq$273.15 K. Moreover, the actual shape of these areas are similar to Figure 2.13. However, for the higher temperatures it seems that the boundary between the light blue and green/yellow color is more horizontal compared to Figure 2.13, where it continues to increase gradually with temperature. This could be a resolution issue, or it could simply be related to the data itself. The boiling boundary, which is the boundary between vapor and liquid, looks in Figure 3.4 correct. Despite the roughness, and the strange shift at location B mentioned before, the boundary is obvious and follows the one from Figure 2.13 quite well. Finally, the triple point, located at ~611 Pa and 273.15 K, looks in Figure 3.4 to be slightly off, as its location is around twice the normal pressure and at a temperature that is marginally higher. Overall, the differences are quite small, and compared to the water_ice EOS, this one is notably more accurate.

The EOSs discussed in Subsection 3.2.2 and Subsection 3.2.3 show to be very different from each other. It is obvious that h2o_ice shows much more potential with its higher resolution and is therefore the preferred choice. However, its resolution is arguably still on the lower side. Since iSALE2D offers only a handful of available EOSs, exploring additional and potentially higher-resolution EOSs may be beneficial.

3.3. Other Equations of State

In addition to the existing water/ice EOS options in iSALE2D, there are other research groups that have developed EOSs of their own.

One example is the SESAME water EOS. This EOS is essentially an extensive table containing all the data needed to compute the state given the required inputs. The SESAME EOSs are created by the Los Alamos National Laboratory[a]. However, gaining access to these EOSs involves putting forth a formal request and an agreement to certain conditions and terms, which complicates things. Alternatively, Senft and Stewart [74] created the 5-phase water EOS. This ANEOS EOS includes numerous ice phases and can be used for impact simulations.

When consulting with Professor Sarah Stewart, a co-creator of the 5-phase EOS, they mentioned that while the 5-phase EOS works well for small-scale and low-pressure impacts, it has its limitations at higher pressures[b]. For such cases, the AQUA EOS by Haldemann et al. [3] was suggested. This EOS includes multiple ice phases and is suitable to be used for planetary models and high pressure simulations. It shows great potential, and will therefore be further investigated in the upcoming sections.

3.3.1. AQUA Equation of State

The AQUA EOS provides several tables that are readily available on the internet, and were downloaded from Github[c]. AQUA includes numerous phases of water, and uses a large number of nodes for temperature and density, which could be indicative of a higher resolution compared to the h2o_ice.aneos EOS. First, verification of the data from AQUA, as well as verification of the Python code used to read the data, is performed. Then, the phase diagram of AQUA is created and compared to the actual phase diagram of water.

Verification of AQUA

First, in order to verify the data from the AQUA EOS file, a plot is made and compared to a reference. This is important, since both the Python code that reads the data, and the data itself, can be tested through this

[a] https://www.lanl.gov/org/ddste/aldsc/theoretical/physics-chemistry-materials/sesame-database.php (Accessed August 7, 2023)
[b] Personal communication by e-mail, July 11, 2023
[c] https://github.com/mnijh/AQUA (Accessed September 8, 2022)

method. Fortunately, the AQUA data is well organized, so extracting the values for the pressure, temperature, and other parameters can be done directly without interpolation. Figure 4 from Haldemann et al. [3] is used as reference. In fact, this figure is similar to the phase diagrams that have been created thus far, making it a suitable plot for verification. Figure 3.5a shows the figure from Haldemann et al. [3], and the plot that was created using the Python code can be seen in Figure 3.5b. Note that extra information is given in the reference plot. Thin black lines are used to mark the phase transition between the solid, liquid, and gaseous phase. The black dashed lines are adiabats calculated for a sphere with a mass 5 times that of Earth consisting of pure water for surface temperatures of 200 K, 300 K and 1000 K. The white dashed lines are the density contours.

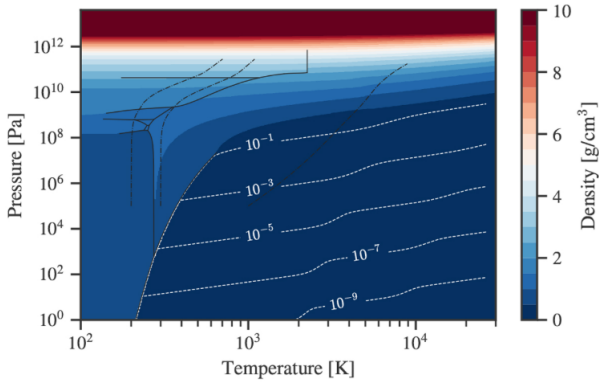

(a) Pressure against temperature plot for varying densities, taken from Haldemann et al. [3].

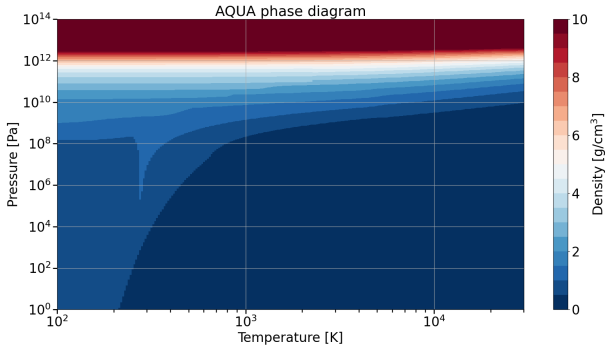

(b) Pressure against temperature plot for varying densities, created from a written Python script.

Figure 3.5: Comparison between the pressure against temperature plot taken from Haldemann et al. [3] (left), and the plot created in Python (right). Note in the plot on the left that the thin black lines are used to mark the phase transition between the solid, liquid, and gaseous phase. The black dashed lines are calculated for a sphere with a mass 5 times that of Earth consisting of pure water for surface temperatures of 200 K, 300 K and 1000 K. The white dashed lines are the density contours. No differences were found between the plots, therefore verifying the AQUA data and the capability of the Python code to correctly read and process the data.

As shown in Figure 3.5, the two figures are identical. The colors, the boundaries, and the lines/curves all match up, and therefore the Python code used to read the data, and the data itself, are considered to be verified. Now, the AQUA phase diagram can be compared with the actual phase diagram to assess its suitability as an EOS option. Based on the results, it could be implemented and used in iSALE2D.

Phase Diagram of the AQUA Equation of State

Technically, the phase diagram has already been plotted in Figure 3.5b, however, this specific section is dedicated to creating and studying the phase diagram in more detail. To remain consistent with the phase diagrams of water_ice and h2o_ice, the phase diagram for AQUA is plotted once more in a similar fashion. To do so, the pressure, temperature, and density must be extracted from the data. The structure of the AQUA table is different from the structure of water_ice and h2o_ice. Instead, AQUA's structure is much clearer and easier to understand, with headers that display the labels, parameters and their numbers. Also, the units used, their format, and a short but understandable description of the EOS are provided. There are multiple columns, which are allocated to different parameters, and a large number of rows. AQUA has three different files, which differ by the input parameters used. One file contains inputs for pressure and temperature, another where density and temperature are inputs (similar to the iSALE2D EOS files), and a third where density and specific internal energy are inputs.

To create a phase diagram, the pressure and temperature are required to be the inputs, and density should be an output. For the iSALE2D EOSs, linear interpolation was needed to achieve this, however, for AQUA simply the pressure and temperature file can be read, and the necessary parameters can be extracted directly without the need for interpolation. To be consistent with the phase diagrams of water_ice and h2o_ice, a similar plot is created for AQUA, given by Figure 3.6.

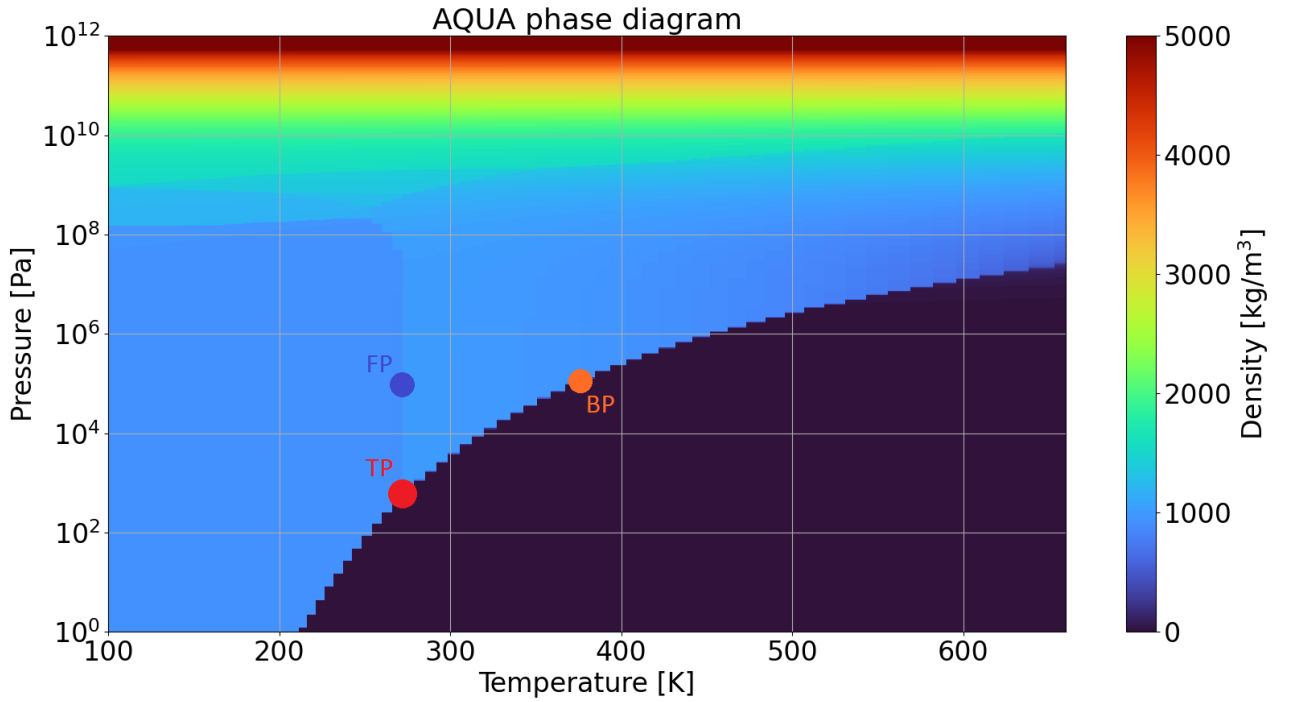

Figure 3.6: Phase diagram of the AQUA EOS, obtained by using the pressure-temperature datafile. The figure has been enhanced to show the phase diagram between the temperatures 100-700 K, pressures 1-1.0 × 10^{12} Pa, as well as densities 0-5000 kg/m^3. Three points are also shown: TP, FP, and BP, which represent the triple point, freezing point, and boiling point, respectively.

From the datafile, and the plot in Figure 3.6, it was immediately noticed that the lower limit for the temperature is 100 K, which is higher compared to the water_ice and h2o_ice EOSs. Nevertheless, it is apparent that AQUA's resolution is extremely high, which can be seen by the smooth boundaries created by the different areas of density. There is also considerable detail in the different regions that represents the different ice phases.

As with the previous comparisons, certain boundaries and points of interest are examined next, to see how closely Figure 3.6 aligns with Figure 2.13. The freezing boundary corresponds well to the actual phase diagram. Compared to the water_ice EOS and the h2o_ice EOS, there is no unexpected behavior in the plot, and a rather smooth curve is separating the solid and liquid phases. The other distinctions are clear too and seem to follow the boundaries shown by Figure 2.13 accurately. The boiling boundary looks from Figure 3.6 to be aligned with Figure 2.13, with only minimal roughness of the data. The curve made by the boundary is smooth and there are no sudden interruptions or discontinuities of any sort. Finally, the triple point was determined at around 270 K and 700 Pa, which compared to the theoretical values of 273.15 K and 611 Pa, comes very close.

Another interesting feature to study is the distinction between the ice phases. Since a very high resolution is used for AQUA, the distinction between different ice phases becomes more clear. One can see in Figure 3.6 that there are boundaries between some smaller areas due to their different densities, hence different colors. However, since the colors for the ice phases and the liquid phase are very similar, it can be difficult to clearly observe these boundaries. Fortunately, the AQUA ANEOS file includes the precise phase of the material in the data, which allows for easy plotting of these phases in a pressure-temperature plot. This plot is given in Figure 3.7, and ensures a clear view of all the different phases that are included in the EOS, and their location in the phase diagram.

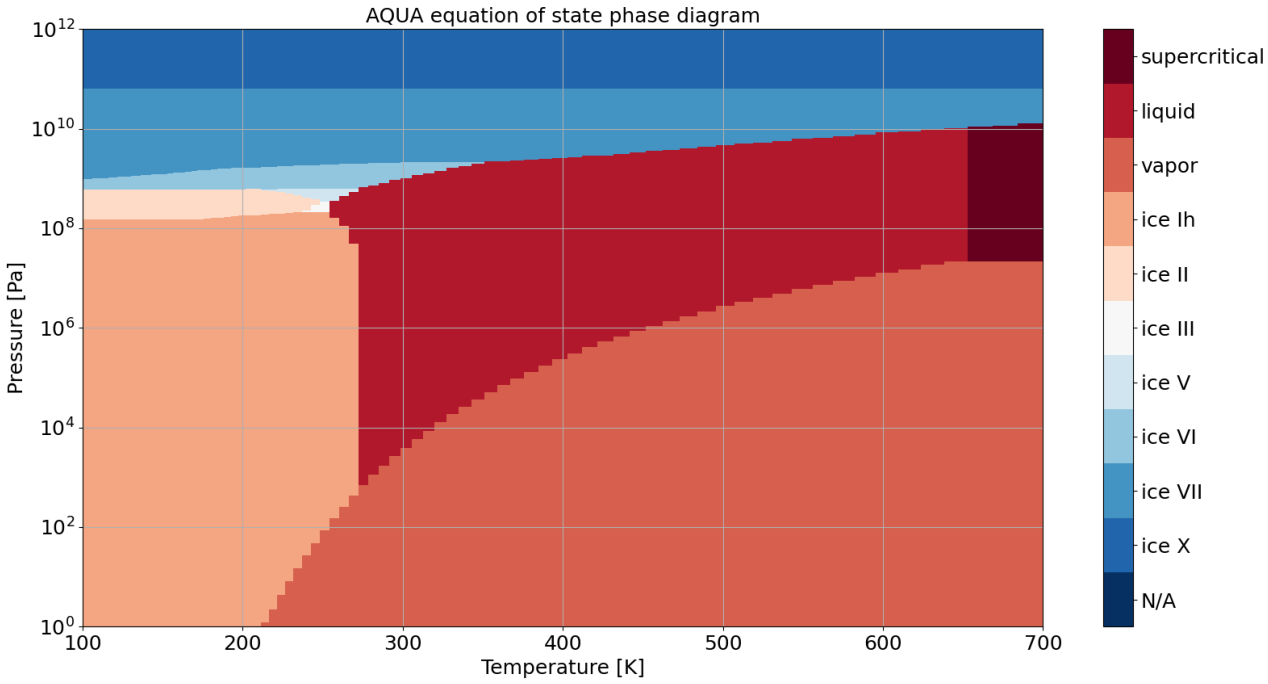

Figure 3.7: Phase diagram of the AQUA EOS displaying the different phases of water. Note that some phases have been merged and are not present in the diagram. However, due to the high resolution of AQUA, most of the ice phases can be distinguished, even small regions such as ice III which is located at roughly 250 K and 1.0×10^8 Pa.

Comparing Figure 3.7 and Figure 2.13, the different phases of water appear to match almost perfectly. Although, note that some of the phases in Figure 3.7 have been merged. For instance, ice IX and ice II are separate phases in Figure 2.13, however, it appears as ice II in Figure 3.7. Similarly, ice VIII is typically to the left of ice VII, but in Figure 3.7 only ice VII is represented.

3.3.2. AQUA Equation of State for Different Number of Nodes

Since the AQUA EOS has a very high resolution, this can raise the question whether the phase diagram can still be accurately represented with fewer nodes. Using fewer nodes could potentially improve the simulation runtime, as the program would have to process a smaller EOS file. However, the resolution should still be sufficient to distinguish the ice phases. Therefore, in this section, different numbers of nodes are explored to see how this affects the phase diagram and the simulation. First, phase diagrams are created to investigate the effects of varying resolution. Then, simulations are performed with the same EOS, but for different number of nodes, to see their direct influence on the impact process.

Phase Diagram of AQUA for Different Number of Nodes

To adjust the number of nodes, interpolation is applied. Through the use of the Numpy module function ”logspace”, the number of nodes can easily be modified, as this is one of the function’s inputs. With a given start value and end value, interpolation can be performed as described in Subsection 3.2.1. This allows for multiple EOSs, each with a different number of nodes. Multiple phase diagrams can then be made, and are shown in Figure 3.8. For consistency, the same temperature-to-density node ratio as in the original AQUA file is used, which is 1:5.

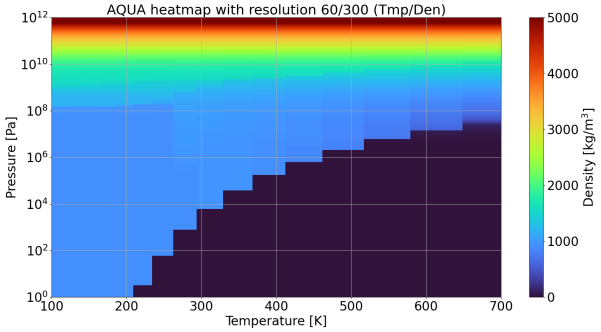

(a) Phase diagram with 60 temperature nodes and 300 density nodes

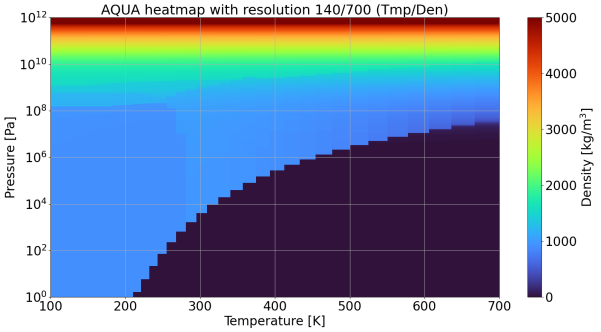

(b) Phase diagram with 140 temperature nodes and 700 density nodes

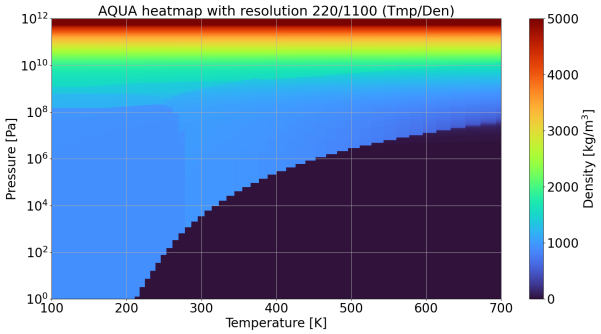

(c) Phase diagram with 220 temperature nodes and 1100 density nodes

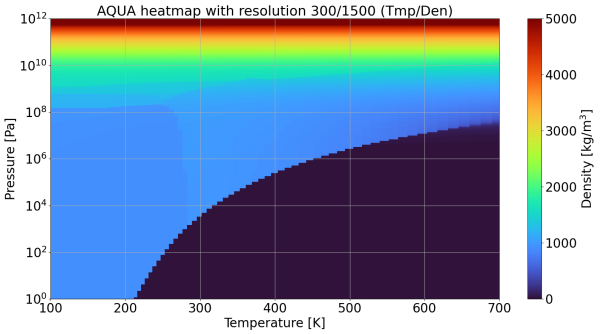

(d) Phase diagram with 300 temperature nodes and 1500 density nodes

Figure 3.8: Multiple phase diagrams of the AQUA EOS, each using different number of temperature and pressure nodes. The progressive increase in resolution is clearly visible for the first two to three plots. However, the third and fourth plots are practically indistinguishable, with only small differences.

Logically, it is expected that for a higher amount of nodes, the phase diagram will become more refined. This is clearly noticeable from Figure 3.8. Comparing Figure 3.8a and Figure 3.8d, there is quite a difference. Despite having the lowest number of nodes, Figure 3.8a still shows a phase diagram with a decent resolution. Much of the ice phases can still be distinguished, and the phase transitions appear relatively smooth considering the low amount of nodes. Beyond Figure 3.8c, it can be argued that the phase diagram does not change notably anymore. Therefore, it can be concluded that AQUA with 220 temperature nodes and 1100 density nodes could already provide enough accuracy. However, the phase diagram does not necessarily directly relate to the simulation results. Therefore, simple simulations should be run with these varying node counts to evaluate their effects.

Simulations of AQUA for Different Number of Nodes

The simulation consists of a simple setup with a granite impactor with a diameter of 500 m, striking an icy target at 10 km/s. The result for several different time steps is given by Figure 3.9. Note that the number of temperature/density nodes is given in the top left for each plot. An additional plot showing the temperature is provided in Figure A.5 in Appendix A.

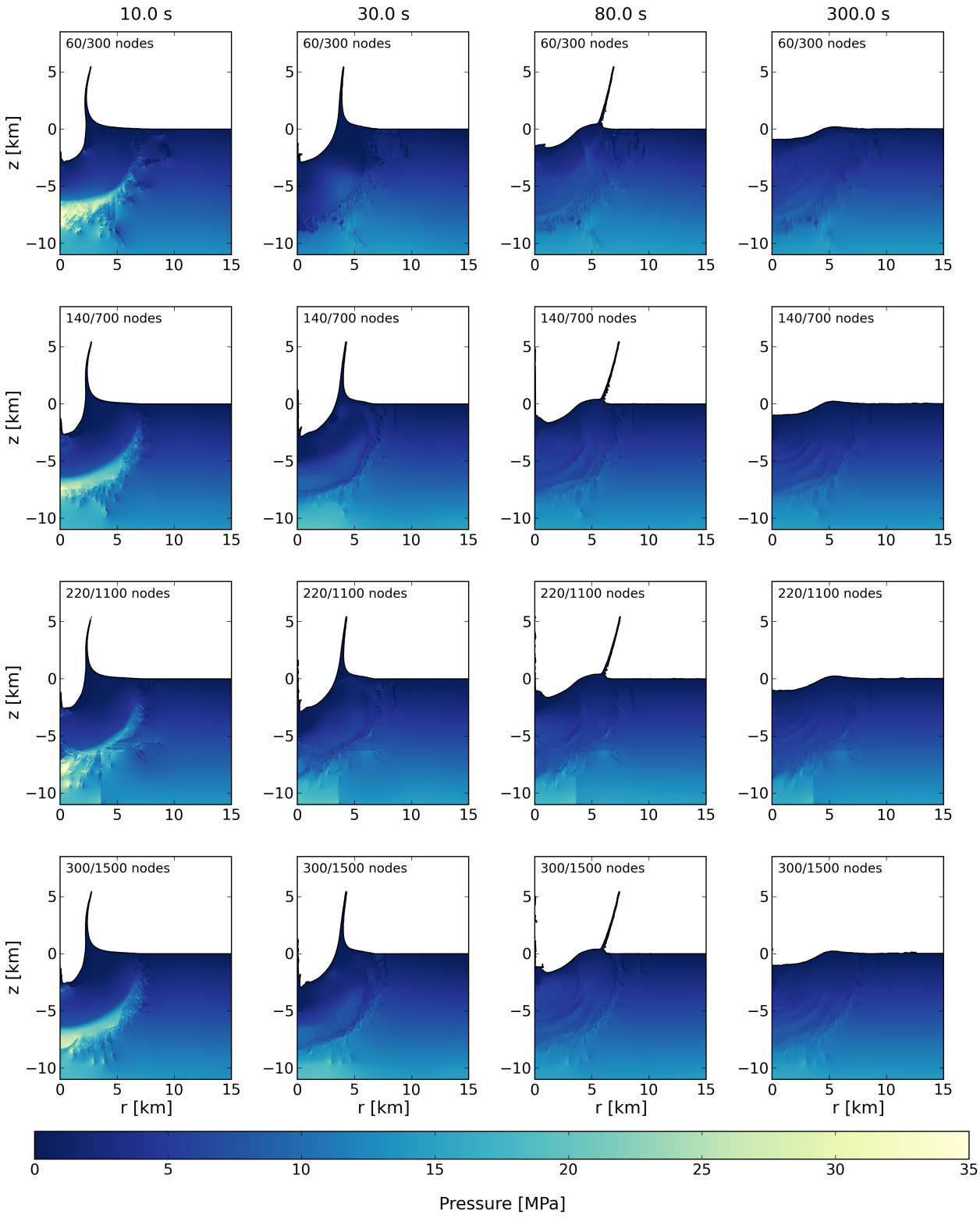

Figure 3.9: The simulation results of the different AQUA EOS that employ different number of temperature and density nodes. Note that the temperature and density nodes are given in each plot in the top left, where the first number represents the temperature nodes, and the second number the number of density nodes. The simulation is of a granite impactor with a size of 500 m in diameter, impacting an icy target surface at 10 km/s.

Figure 3.9 shows that the simulations are slightly different from each other, mainly visible through the damage in the target. Since a logspace function is used to generate the node values, lists with a different number of nodes (e.g., 60 vs. 120) will not contain identical values. In that case, two points that are used for interpolation might be closer or further apart in some scenarios, leading to differences in the corresponding temperature and pressure, and therefore differences in Figure 3.9.

On the other hand, the impact process remains relatively consistent for all simulations. Even for the final

time step, the crater diameter and depth are almost identical. Though, this is likely due to the fact that fundamentally the same EOS is used. During the majority of the impact process, the temperatures and pressures encountered range from approximately 120 - 350 K, and 0 - 50.0 × 10^6 Pa. Based on Figure 3.8, the phase diagrams besides Figure 3.8a remain similar to each other in these areas.

To see how the runtime compares with the increase in number of nodes, a simple plot was made, which can be seen in Figure 3.10. It is expected that a higher number of nodes results in a higher runtime.

As shown in Figure 3.10, there is an almost linear increase in runtime for an increase in the number of nodes. Comparing the runtime for the simulation using the highest number of nodes with the simulation using the lowest number of nodes, there is a 20% difference. Between the highest number of nodes and the second highest number of nodes, this difference decreases to only 6%. This increase in runtime is relatively small, making the higher resolution of the full AQUA EOS an acceptable trade-off. So, amongst the different number of nodes, the full AQUA EOS is considered the best option.

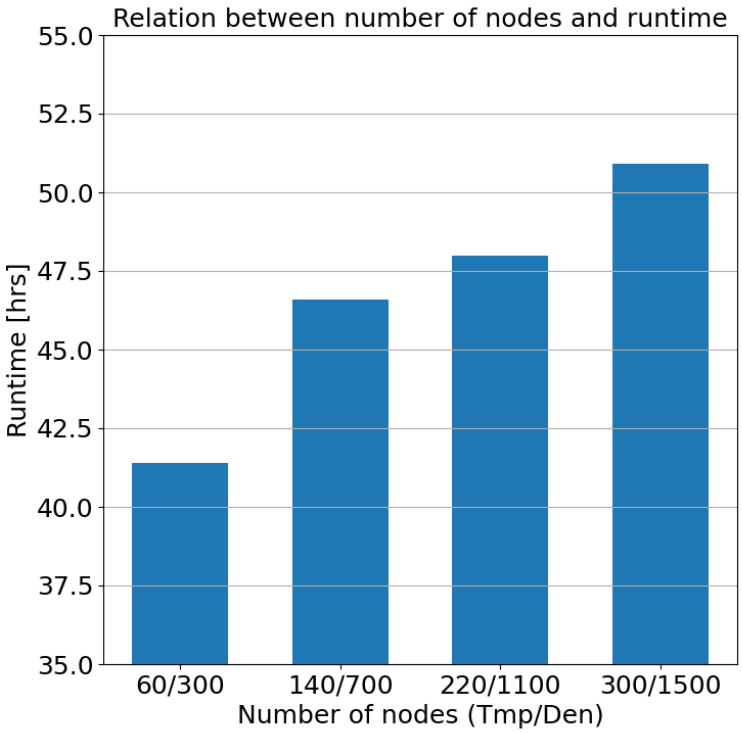

Figure 3.10: Runtime in hours against the number of temperature and density nodes for different AQUA EOSs. The increase in runtime is almost linear, with only small differences between the three rightmost histograms.

3.4. Comparison of the Equations of State

From Section 3.3, it seems that aqua is superior compared to the iSALE2D EOS, but to truly compared them to each other, the AQUA phase diagram should be plotted by using the exact same values for the temperature and density nodes as water_ice and h2o_ice. This will show a true comparison, as AQUA originally has a higher resolution. Since a high resolution can only be altered to a low resolution, h2o_ice and AQUA are changed to the format of the water_ice EOS.

This process is relatively simple on paper, but becomes very tedious in practice. This is due to the many linear interpolations that are required, and the fact that the temperature for AQUA does not go lower than 100 K, while the other two EOS do. For AQUA, this means that the first 5 temperature nodes have to be omitted. The remaining 55 temperature nodes, however, should preferably be divisible by 4 due to the nature of the iSALE2D ANEOS format. Hence, only 52 nodes are used for the AQUA phase diagram. This was achieved by removing the two highest temperature nodes, since these values are so high that it is unlikely they will be relevant. Then, using the water_ice temperature and density values, linear interpolation was performed for AQUA and h2o_ice. The result is a lower resolution EOS for AQUA and h2o_ice. The phase diagrams for AQUA and h2o_ice can be seen in Figure 3.11a and Figure 3.11b respectively, and the water_ice phase diagram is displayed once more in Figure 3.11c.

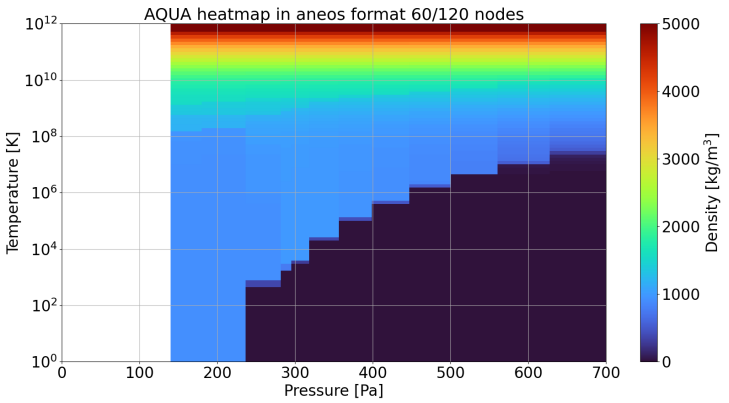

(a) AQUA phase diagram

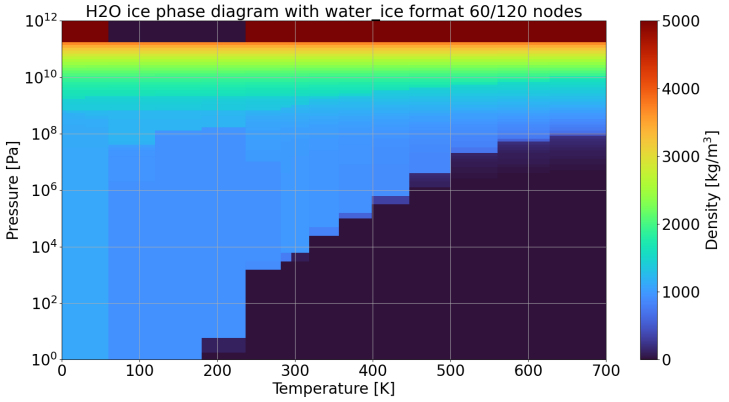

(b) h2o ice phase diagram

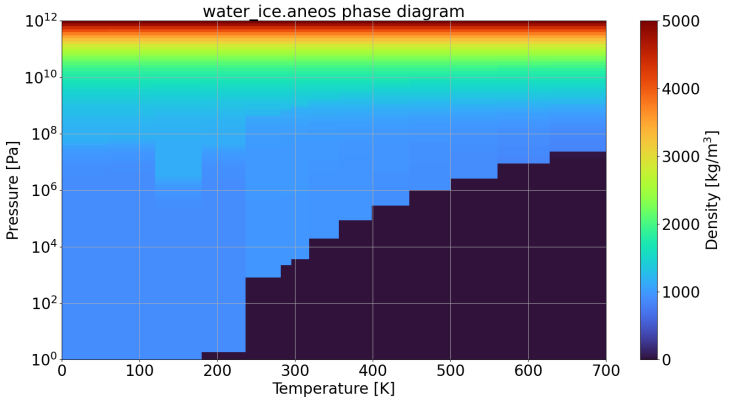

(c) Water ice phase diagram

Figure 3.11: Phase diagram of the AQUA, h2o_ice and water_ice EOS, all with the same amount of temperature and pressure nodes, and the same values for nodes, for as far as possible.

As can be seen from Figure 3.11, there are some similarities between the plots regarding the general areas of different density, as well as the boundaries and their roughness. The main difference can be seen around 175 K and 1.0×10^7 Pa, which was also an area of prior interest. For AQUA and h2o_ice, this area looks more natural and similar to the actual phase diagram than it does for the water_ice EOS, confirming that the anomaly that was noticed in Subsection 3.2.2 was specific for the water_ice EOS. Furthermore, h2o_ice, and especially AQUA, appear more detailed and refined around 190 K and 5.0×10^8 Pa. This is an area that includes multiple states of ice, and some can be distinguished in AQUA and h2o_ice, but not in water_ice. Thus, it can be concluded that even with the same number of nodes or less, and with the same node values, the water_ice EOS is inferior compared to the AQUA and h2o_ice EOS.

Since the AQUA and h2o_ice EOS show a strong similarity, they are examined in more detail. Since the h2o_ice normally has 200 temperature nodes and 270 density nodes, it is useful to compare both EOS using that format. The AQUA EOS will therefore be adjusted to use the exact same values as much as possible. The resulting reduced phase diagram of AQUA and the phase diagram of h2o_ice can be seen in Figure 3.12a and Figure 3.12b respectively.

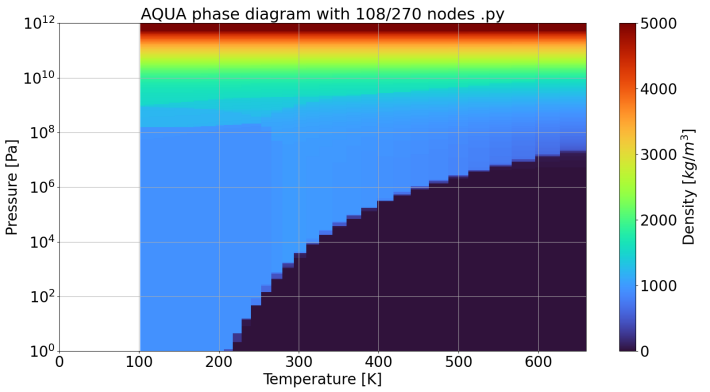

(a) AQUA phase diagram using 108 temperature nodes and 270 density nodes.

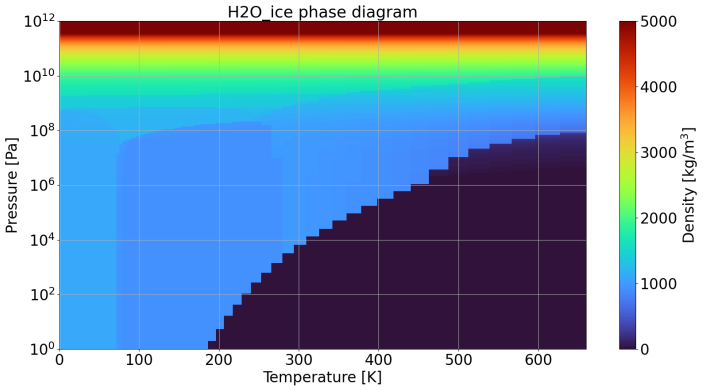

(b) The original h2o_ice phase diagram using all data available.

Figure 3.12: Difference between the AQUA and h2o_ice EOS. Both use the same temperature and pressure node values.

From Figure 3.12, it is evident that the two EOS are quite similar, even with identical nodes. Compared to the h2o_ice EOS, AQUA does not seem to have any irregularities in terms of its boundaries and the roughness, whereas h2o_ice still exhibits some irregularities, such as the boundary between vapor and liquid at 500 K and 1.0×10^7 Pa in Figure 3.12b, which is not present in Figure 3.12a.

The h2o_ice and AQUA EOS are comparably accurate to the actual phase diagram, though h2o_ice has some irregularities and a much lower resolution than AQUA. Since these EOSs demonstrate a similar accuracy, it can be interesting to use them in a simple impact simulation setting, and compare the results with both EOS are at their maximum potential. By examining any differences during the cratering process and the final crater shape, it may be easier to determine which EOS is better suited. The results are shown in Figure 3.13.

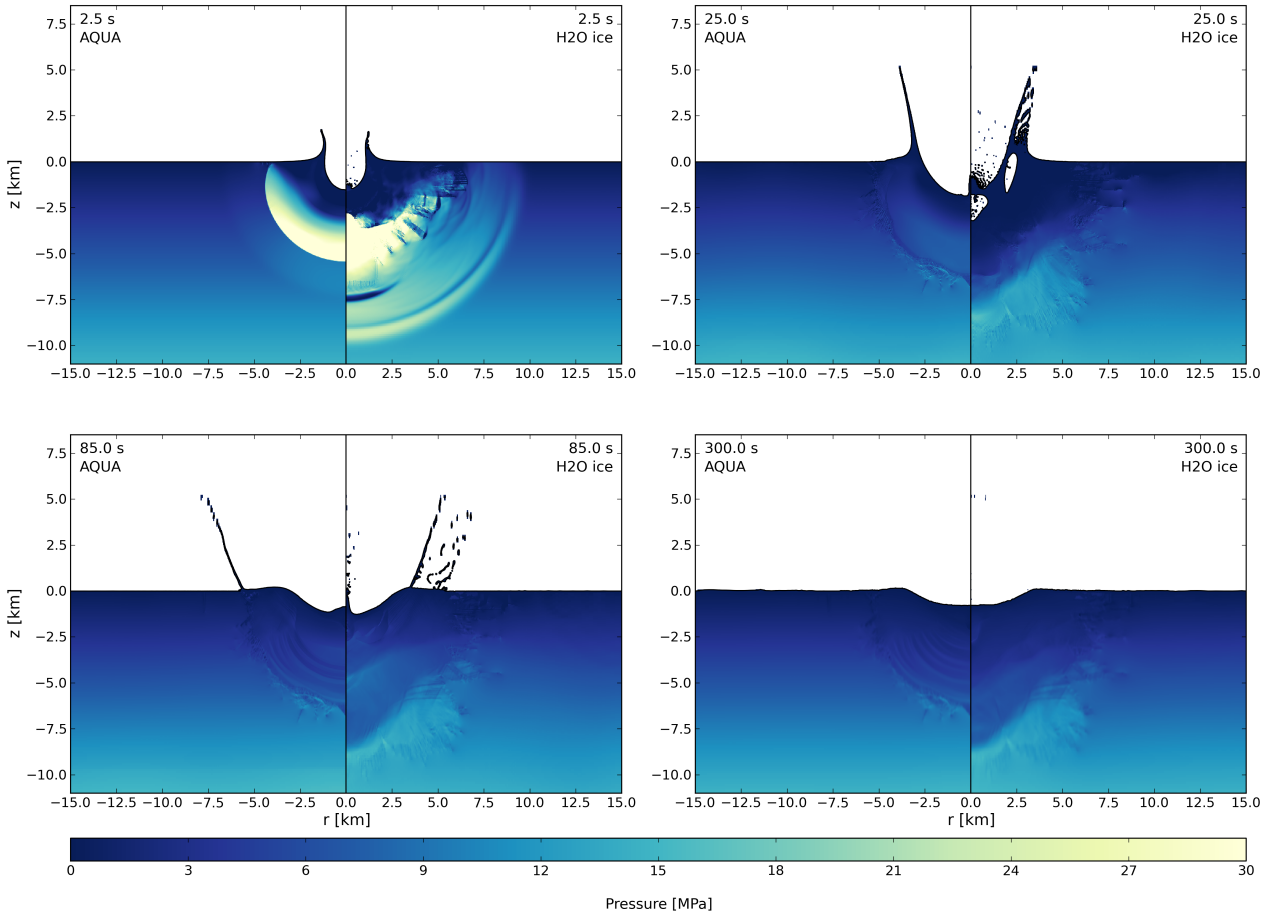

Figure 3.13: Results between the AQUA and h2o_ice EOS simulations at four different time steps. The results for the AQUA EOS simulations are given on the left side of each plot, and on the right side the simulation results for the h2o_ice EOS are displayed.

Figure 3.13 shows obvious differences between the AQUA and h2o_ice EOS. At 2.5 seconds, the shockwave propagating through the target of the h2o_ice simulation is nearly twice as fast. At 25 seconds, the h2o_ice EOS appears to create a much more violent reaction to the impact, as more particles and material are ejected or lifted up compared to AQUA. This remains the case at 85 seconds, where more ejecta is launched for the h2o_ice EOS. Moreover, the fractured area in the target is larger for the h2o_ice EOS. Surprisingly, despite these differences, the final crater shape is quite similar. It appears that the rim height is slightly higher for the AQUA EOS, while the diameter and depth are practically equal.

Ultimately, h2o_ice does not appear to be least effective EOS, however, the violent and unexpected behavior of material during the cratering process has not been observed in previous research papers, and can be considered concerning as its effect on the cratering process cannot be determined by a simple simulation example. Since the end results are very similar, and with AQUA not showing any unexpected or irregular behavior, it is decided to use the AQUA EOS for further simulations.

4

Method and Experimental Setup

Before a simulation can be started in iSALE2D, numerous input parameters have to be defined that are catered to the preferences of the user. Then, after the simulation is finished, the resulting data needs to be post-processed in order to be able to interpret the outcome. This chapter will focus on these aspects of the simulation process. First, Section 4.1 and Section 4.2 will cover the important inputs and outputs of the simulation, respectively. Then, Section 4.3 will focus on how simulations are performed, and describe the post-processing procedure.

4.1. Input Parameters of iSALE2D

The input parameters in iSALE2D are specified in two separate input files the asteroid input file and the material input file. The parameters in the asteroid file are focused on the key impact parameters, such as surface gravity, impact velocity, size of the grid, and more. As the name suggests, the material file includes parameters related to the materials used, such as the type of EOS and the strength model. Given the wide range of models and parameters available, the most relevant ones are briefly given in Subsection 4.1.1 and Subsection 4.1.2.

4.1.1. Asteroid Input Parameters

Most of the input parameters are located in the asteroid file. An overview of the parameters is given in Table 4.1, after which a select few parameters are described in more detail to provide a better understanding [71].

Table 4.1: Description of relevant parameters in the asteroid input file [71].

Parameter	Description
	Grid Parameters
GRIDH	The number of cells in the horizontal direction in the grid.
GRIDV	The number of cells in the vertical direction in the grid.
GRIDSPC	The spacing between the cells in the high-resolution zone in the grid.
GRIDSPCM	The maximum spacing between cells that can be attained.
GRIDEXT	The factor by which the grid spacing is increased after each cell in the extension zone.
	Global Parameters
S_TYPE	The type of impact (airburst, landslide, planet-size impact, vertical impact, meso-scale modeling experiments).
TSURF	The temperature on the surface of the target.
GRAV_V	The magnitude of the gravity in vertical direction.
R_PLANET	The radius of the body in question (if applicable).
DTDZSURF	The gradient of the thermal profile (i.e. the change in temperature due to a change in depth).
D_LITH	Thickness of the lithosphere.
	Impactor Parameters
OBJVEL	The velocity of the impactor upon contact with the target.
OBJRESH	The number of cells that make up the radius of the impactor.
OBJMAT	The material of the impactor.
	Target Parameters
LAYMAT	The material of the target layer(s).
LAYNUM	The number of layers of different material in the target.

Table 4.1: continued from previous page

Parameter	Description
LAYPOS	The vertical position of the top layer in the simulation grid, as measured from the bottom of the grid.
LAYTPROF	The thermal profile in each layer.
	Time and Saving Parameters
DT	Initial time step.
DTMAX	Maximum time increment.
TEND	The time after which the simulation will stop.
DTSAVE	The time interval when data will be saved.
VARLIST	List of input parameters that will be saved during a simulation.

To provide additional context, some terms are discussed here in more detail. Beginning with the high-resolution and extension zones mentioned under the grid parameters. These are the two primary zones in the grid. The high-resolution zone is located close to the site of impact, and preferably encompasses most of the target area that will be affected by the impact, to ensure that the area of interest has the highest resolution. Everything outside of the high-resolution zone is referred to as the extension zone. Additional plots of these zones and further information can be found in Section A.3 in Appendix A.

The LAYTPROF parameter provides several options. The most simple option is the constant thermal profile, where the entire target has one uniform and constant temperature, equal to the surface temperature defined under TSURF. For a conductive thermal profile, temperature varies linearly with depth. For convection, a conductive and convective thermal profile option can be chosen, with an additional option to also include a cap on the temperature equal to the melting temperature of the specified material. Lastly, a user defined custom thermal profile can be used.

4.1.2. Material Input Parameters

The inputs in the material file focus solely on the material of the impactor and the target. Similar to Table 4.1, a concise description for the most relevant models and parameters is given in Table 4.2 [71], followed by additional information to provide a better understanding. Note that numerous damage parameters are stated, since each damage model requires the definition of its own set of parameters.

Table 4.2: Description of relevant parameters in the material input file [71].

Parameter	Description
	Equation of State Parameters
EOSNAME	The name or identifier for the EOS file of the material as given in iSALE2D.
EOSTYPE	The type of EOS (Tillotson or ANEOS).
STRMOD	The strength model.
DAMMOD	The damage model.
ACFL	The acoustic fluizidation model.
THSOFT	The thermal softening model.
	General Parameter
POIS	Poisson ratio. Ratio between the transverse and axial strain of the material [75].
	Thermal Parameters
TMELT0	Melting temperature of the material at zero pressure.
ASIMON	Constant in the Simon approximation for melting temperature of the material.
CSIMON	Exponent in the Simon approximation for melting temperature of the material.

Table 4.2: continued from previous page

Parameter	Description
TFRAC	Thermal softening parameter.
	Strength Parameters
YINT0	Yield strength of intact material at zero pressure.
FRICINT	Coefficient of internal friction of intact material.
YLIMINT	Limiting strength of intact material at high pressures.
YDAM0	Yield strength of damaged material at zero pressure.
FRICDAM	Coefficient of internal friction of damaged material.
YLIMDAM	Limiting strength of damaged material at high pressures.
	Damage Parameters
	In case the IVANOV damage model is selected
IVANOV_A	Minimum failure strain for low pressure states.
IVANOV_B	A positive constant (increase in failure strain with pressure).
IVANVO_C	Pressure above which failure is assumed compressional.
	In case the COLLINS damage model is selected
BPTPRES	Brittle-plastic transition pressure.
BDTPRES	Brittle-ductile transition pressure.
YTENS0	Tensile strength of intact material.
	In case the SIMPLE damage model is selected
FAILSTRN	Constant plastic strain at failure.
	Acoustic Fluidization Parameters
GAMBETA	Dimensionless duration of the vibrations.
GAMETA	Dimensionless strength of the vibrations.

There are various models that can be chosen for the strength model, damage model, thermal softening model and acoustic fluidization model. For the strength model, there are options for liquids (LIQU/HYDRO), rocky materials (ROCK, LUNDD, LUNDI), metals (JNCK), granular materials (DRPR), ductile materials (VNMS), and ice (ICE). Depending on the model, either the strength parameters for intact material, damaged material, both or neither are applied. The thermal softening models available are the OHNAKA and JNCK models. The OHNAKA model uses the TFRAC parameter from Table 4.2, which is used to calculate the shear strength. The JNCK model is to be used only in combination with the JNCK strength model. The ACFL models available are the BLOCK and MELOSH models [71].

4.2. Outputs of iSALE2D

iSALE2D generates many output files, though only a few are important. One of these key files is simply called the output file, which tracks the progress of the simulation, and also provides a brief overview, including details such as the start date and time, grid and impact setup, and current time step. The most important output file, however, is the jdata file. This is a large file that contains all the data that has been saved during the simulation, which consists of the values of the parameters defined under VARLIST. The information in the jdata file can be plotted by using the Matplotlib plotting library from Python [76]. This allows for the creation of various plots at different time steps, which help visualize how parameters change over time during the impact.

4.3. Simulation and Post-Processing

Before a simulation is started, it is essential to ensure that the appropriate input parameters, models, and values are selected and defined in both the asteroid and material input files. After starting the simulation, iSALE2D will first initialize and provide an overview of the simulation settings, which can be seen in Figure A.7 in Appendix A

for more information. After this overview has been given, and no errors are detected, it automatically starts the simulation and will either run until the specified end time, or until the simulation is terminated or interrupted. If an error occurs, a dedicated text file is generated that describes the error in more detail and how to solve it.

For post-processing, different approaches can used to plot the results. Most useful is to plot a heatmap or colormap in Python, as this will display the impact and corresponding parameter values, such as the pressure or temperature, as shown in Figure 3.9 for example. To plot the data, the jdata file has to be read. When examining the structure of the jdata file, it appears as a large matrix with values that correspond to certain cells in the grid. However, alternatively of having each row in the jdata file correspond to a row of cells in the grid, the structure of this matrix is transposed, and the columns are read from bottom to top. Fortunately, iSALE2D has built-in functions that can directly obtain the necessary parameter values from the jdata file. The general structure of the plotting script is given by Algorithm 1.

Algorithm 1 Python code to plot jdata

```
Load jdata file
Set up figure (size, axes, titles, fontsize, ...)
for step = 1, 2, ..., nsteps do
    Read jdata file
    Plot desired parameters using Matplotlib function pcolormesh
    Add the colorbar (colormap, ticks, size, location, ...)
    Save the plot in a dedicated folder
    Clear the figure to plot the next time step
end for
```

Although plots are useful, analyzing and reviewing numerous plots from multiple simulations can be inefficient. Therefore, a small Python script was written that creates a short video out of these plots. The script works by first opening the folder containing the plots. Then, the desired size of the window is defined, as well as the frames per second. Next, a for loop is used, which cycles through all the files inside the aforementioned folder, and saves them in an array. Through the function cv2.VideoWriter from the module cv2 or opencv, the images are written to a video file format [77]. This approach makes analyzing and interpreting the simulation results much more accessible by allowing quick video playback.

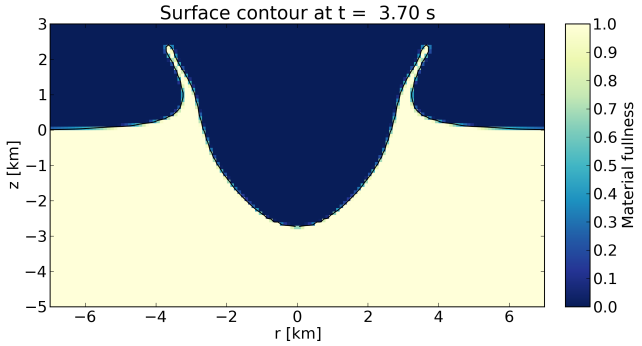

(a) The amount of material in each cell can be seen, where a white-yellow color indicates material is present in a cell, and dark blue indicates no material is present.

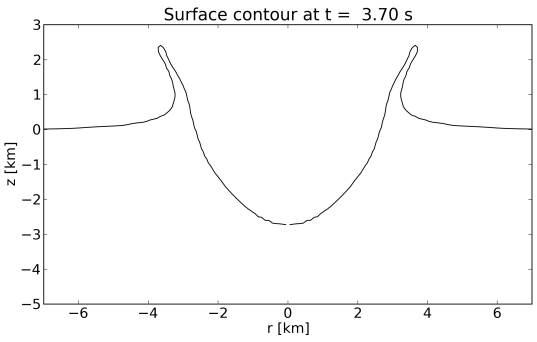

(b) Plot of only the surface contour, which is based on the plot shown in Figure 4.1a.

Figure 4.1: A colormap of the amount of material in each cell is shown in the figure on the top. Through changes in the plotting script, solely the surface contour can be obtained and plotted, as shown in the bottom figure.

This essentially concludes the post-processing part. However, there are still two important parameters that are not directly given by iSALE2D. These are the diameter and depth of the crater. After creating the plots, the depth and diameter could simply be estimated by visually inspecting the figures, this method is prone to inaccuracies due to Python's plot resolution, and human error. A solution for this is to calculate the diameter and depth from the output file directly. Besides the parameters that are saved during the simulation, iSALE2D also saves additional data on the cells, which can be accessed by "step". For example, using step.cmc[0] returns a 2D list containing zeros, floats and ones, which represent the amount of material in each cell in the grid. When

plotted in a colormap, cells that contain a 1 are full with material, and the cells that do not contain material all have a value of 0. However, more importantly is that the cells containing floats are all located along the surface of the target. An example can be seen in Figure 4.1, where Figure 4.1a shows the amount of material present in each cell in a colormap, and Figure 4.1b plots solely the contour containing the floats. This proves that the floats are the surface contour. This data is important, as it can be used to easily find the diameter and depth of the crater.

To determine the diameter and depth, the locations of the cells that make up the surface contour in Figure 4.1b are required. These can be found in step.cmc[0]. First, the location of the rim has to be found, which can be achieved by finding the highest cell containing a float. The coordinates of this cell give the location of the rim, and the radius is then equal to the value of the r-coordinate, as this gives the distance from the symmetry line in cells. The depth is determined by simply finding the lowest cell containing a float, and adding the rim height to get the total depth. The Python script for this process is described in Algorithm 2.

Algorithm 2 Python code to determine diameter and depth of the crater

```
Load jdata file
if step = nsteps − 1 then
    Read jdata file
    Read step.cmc[0]
    for i = 1, 2, ..., len(step.cmc[0]) do
        Determine first occurrence of 0 in each column and subtract those numbers by 1
        Save the numbers in a list
    end for
    Determine index where maximum value is located in the list
    Convert the index, which is cell number measured from the symmetry line, to meters
    To get the diameter, multiply by 2

    Determine the minimum value that occurs in the saved list
    Add the rim height to the number above
    To get the depth, convert to meters
end if
```

When determining the diameter, caution is required, as there might be scenarios where the diameter returned by the code could be incorrect. For example, if the simulation has not finished yet. In such cases, ejecta may still be in the air, or material is in the process of falling back, and when connected to the surface, the code could misinterpret this as the rim, which will affect the results and provide incorrect values for the diameter. Therefore, the final plot should always be consulted in case the depth and diameter need to be determined. Additionally, in the special case where the rim is relatively flat and several cells wide, the r-coordinate will be taken as the midpoint of those cells.

5
Verification and Validation

In this section, the iSALE2D hydrocode will be verified and validated. Even though iSALE2D is an already verified and validated tool, the tests used here are used to ensure iSALE2D has been correctly installed and if the code is calculating the states accurately. To test this, the example problems provided by iSALE2D are simulated and verified, of which the results are discussed in Section 5.1. Then, in Section 5.2, results from papers that simulated impacts in ice are recreated. This is done, because these studies use their own inputs, and the simulations performed are of a similar caliber as the ones that are performed later in this report. Therefore, to confirm that these different inputs work properly, it is important to see if their results can be correctly recreated.

5.1. iSALE2D Example problems

After installing iSALE2D on the TU Delft servers, the ”demo2D” simulation was run first, as per suggestion by iSALE2D. It is a basic and low-resolution simulation of a 1.6 km diameter sized granite impactor, striking a granite target at 6.5 km/s [71]. To verify the outcome, simulation results were plotted and compared to a few plots provided by iSALE2D on their Github [78]. A side-by-side comparison can be seen in Figure 5.1, where the plots from the iSALE2D Github can be seen on the left side, and the recreated simulation results on the right side.

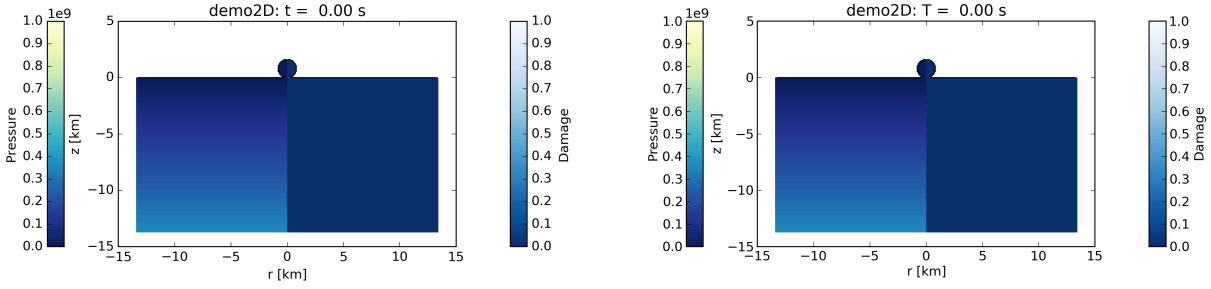

(a) Plot from iSALE2D Github at t = 0 s

(b) Recreated plot from simulation at t = 0 s

(c) Plot from iSALE2D Github at t = 1.23 s

(d) Recreated plot from simulation at t = 1.23 s

(e) Plot from iSALE2D Github at t = 2.46 s

(f) Recreated plot from simulation at t = 2.46 s

Figure 5.1: Comparison of the demo2D example problem results between the iSALE2D Github and the outcome obtained from running the simulation. A simple impact is shown, where a 1.6 km diameter granite projectile impacts a granite target at 6.5 km/s.

As can be seen from Figure 5.1, the figures are identical, indicating that the processes and calculations necessary to run this particular example work as intended. However, many more examples are available, all using different models, materials, and even forms of impact. To be absolutely sure that everything works properly, the other examples were run as well.

When comparing the results from the additional example problems with the iSALE2D Github plots, it was noticed that for most the results were identical. However, slight differences were observed for the ”dilatancy”, ”Planet2D”, ”planetesimal2D” and ”MesoParticles2D” examples. For the ”Mesoparticles2D” problem, which simulates a simple planar impact experiment, it was noticed that the particle’s positions and sizes are determined randomly, which would explain the differences between the plots. Figure 5.2 shows these plots, which confirms the differences of random particle positions and sizes. However, even though the initial positions and sizes are different, the simulation does converge to a comparable endpoint, as the final plot is similar to the one form the iSALE2D Github. Therefore, the processes performed by iSALE2D can still be considered verified for this example.

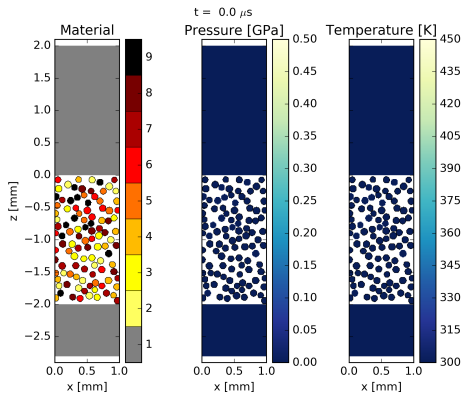

(a) Plot from iSALE2D Github at t = 0 μs

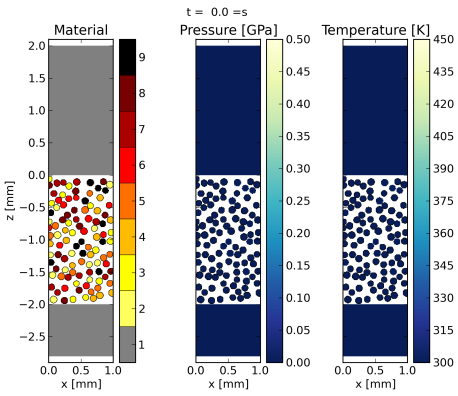

(b) Recreated plot from simulation at t = 0 μs

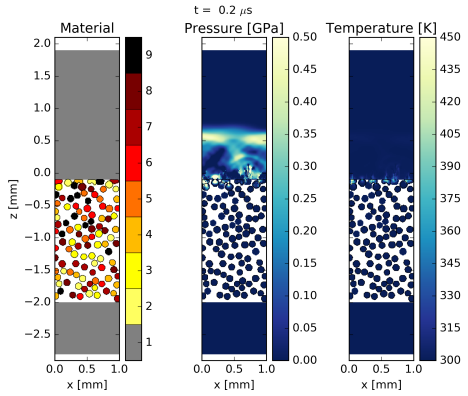

(c) Plot from iSALE2D Github at t = 0.2 μs

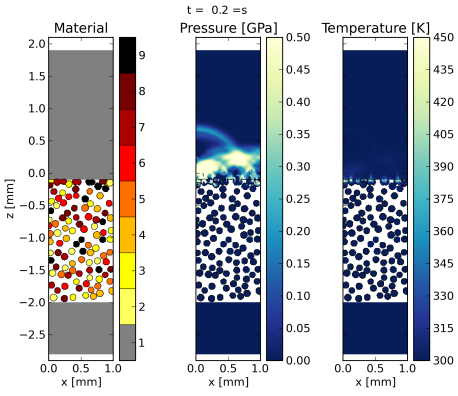

(d) Recreated plot from simulation at t = 0.2 μs

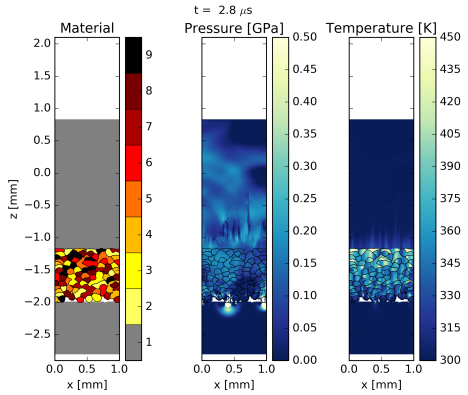

(e) Plot from iSALE2D Github at t = 2.8 μs

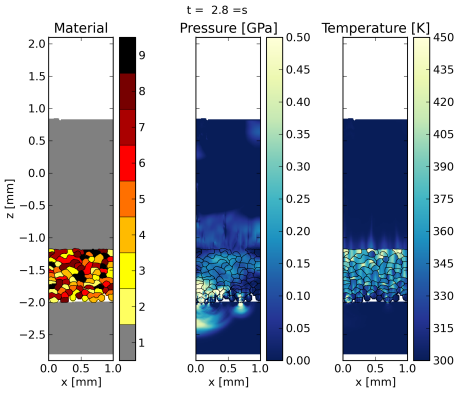

(f) Recreated plot from simulation at t = 2.8 μs

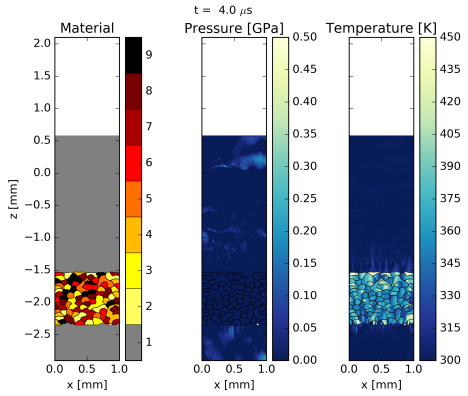

(g) Plot from iSALE2D Github at t = 4.0 μs

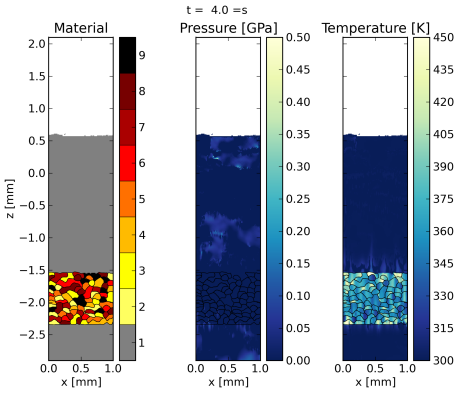

(h) Recreated plot from simulation at t = 4.0 μs

Figure 5.2: Comparison of the results from the Mesoparticles2D example problem between the plots from iSALE2D Github and the outcome obtained from running the simulation. The plots show a simulation of a simple planar impact experiment with granular materials at four different time steps, where a plate impactor strikes the particles at 500 m/s. The particles, pressure and temperature are shown at each time step.

As for the planet2D, dilatency and planetsimal2D example problems, slight differences were noticed in the shape and location of material when compared to the plots from Github. A possible reason for these differences could be explained by the computer hardware used to run the simulations. Different system specifications can lead to differences in rounding for instance, which can persist over time and produce noticeable changes in the plots for large, violent or chaotic impact simulations. However, the differences are minor, and do not affect the end result in a significant way. Therefore, these examples are also considered verified. To view the plots from the planet2D, dilatency and planetsimal2D problems, as well as the other example problems, refer to Figure A.8 through Figure A.15 in Section A.4.

5.2. Studies Simulating Impacts in Ice

To run simulations accustomed to user needs, the input files have to be changed accordingly. To verify that these custom inputs and material models function properly, results from two papers are recreated here.

However, it has to be stated though that a different version of iSALE2D was used to recreate the simulations. This was discoverd through a discussion with iSALE2D co-creator Professor Gareth Collins. Specifically, the studies referenced here utilized a developer version of iSALE2D, which is capable of implementing the PEIERLS viscosity model[a]. The PEIERLS model is not covered in the iSALE2D manual, however, it being a viscosity model, it is expected to affect the crater morphology [79]. This will be considered when interpreting the results in later sections.

The simulations performed by Bjonnes et al. [1] are focused on Ganymede and Callisto, which makes it suitable for verification and validation. They researched the effects that varying projectile radius and thermal gradient of the ice shell had on the ice shell. A small overview of some of the input parameters and their values is provided in Table 5.1.

Table 5.1: Parameter values utilized by Bjonnes et al. [1].

Parameter	Value
Surface temperature	120 K
Surface gravity	1.428 m/s^2
Planetary radius	2631 km
Melt temperature at zero pressure	273 K
Thermal softening parameter	1.2
Cohesion, intact	10.0×10^6 Pa
Coefficient of internal friction, intact	2
Limiting strength at high pressure, intact	1.1×10^8 Pa
Cohesion, damaged	10.0×10^3 Pa
Coefficient of internal friction, damaged	0.6
Limiting strength at high pressure, damaged	1.1×10^8 Pa
Equation of state	Tillotson (Ih)
Impact velocity	15 km/s

The figure that will be recreated from Bjonnes et al. [1] is Figure 4C. In addition to the information given by Table 5.1, it is mentioned that the projectile used has a 700 m radius, the target has a conductive thermal gradient of 10 K/km overlying 250 K convective ice, and the temperatures are capped at 273 K. Figure 4C is given, after some adjustment, together with the plot of the recreated results, by Figure 5.3. Since the input files were made public, the exact same inputs were used. Normally, identical results would be expected, however, since a different version of iSALE2D is used, some differences are anticipated.

[a] Personal communication via email, July 7, 2023

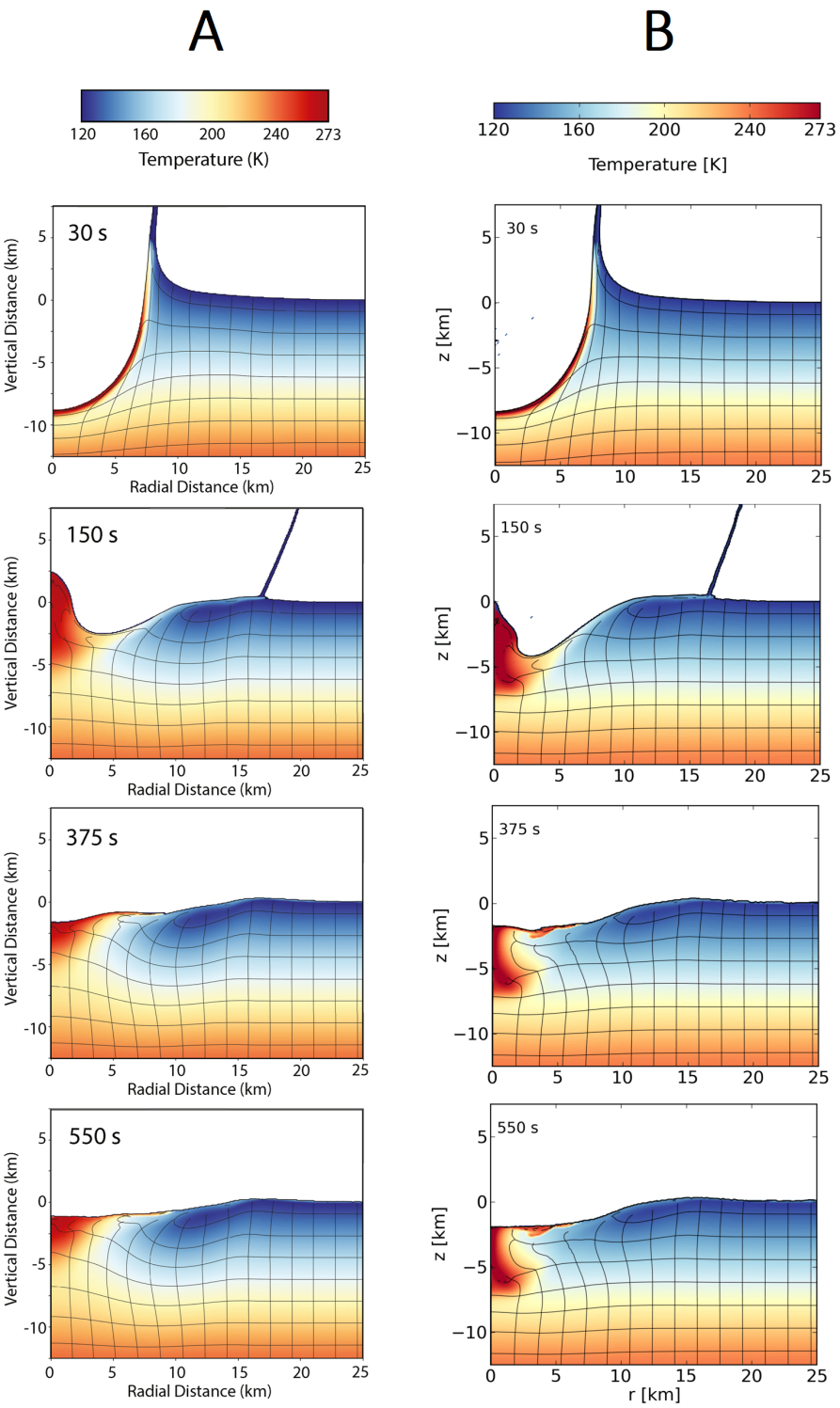

Figure 5.3: The plots made by Bjonnes et al. [1] are shown on the left side (A). The recreated results are given on the right side (B). The plots show the result of a simulation where a 1.4 km diameter icy projectile impacts an icy target at 15 km/s. The target layer has a conductive and convective thermal gradient, and the temperatures in the layer are capped at 273 K.

Comparing Figure 5.3A and Figure 5.3B, it is noticed that the results have some similarities, but are not identical. At t = 30 seconds, the plots are nearly identical, however, differences emerge at t = 150 seconds. A sphere-like rebound of material appears in Figure 5.3A, whereas in Figure 5.3B the shape is more pointed. Furthermore, the temperature in this area is higher compared to Figure 5.3A. These differences persist, in the subsequent plots. Due to the difference in iSALE2D version, such changes were expected. These temperature differences should be taken into account, as due to the higher temperatures near the site of impact, and especially deeper in the target, it can affect the interpretation of the ice phases encountered during the impact at these locations. As for the crater morphology, the final crater resembles the original plot quite well, with only

minor differences in the diameter, slightly steeper crater walls, and a slightly greater depth.

The second paper that is considered here is from Silber and Johnson [2]. Their research is centered around studying the impact crater morphology and the structure of Europa's ice shell. Simulations were performed using different impactor sizes, different ice sheet thicknesses and different thermal gradients. Since Europa is similar to Ganymede in a few ways, such as surface gravity, surface temperature and composition, it was considered suitable for verification and validation [65]. The input values given by Silber and Johnson [2] are also shown in Table 5.2.

Table 5.2: Parameter values utilized by Silber and Johnson [2].

Parameter	Value
Surface temperature	100 K
Melt temperature at zero pressure	273 K
Thermal softening parameter	1.2
Cohesion, intact	10.0×10^6 Pa
Coefficient of internal friction, intact	2
Limiting strength at high pressure, intact	1.1×10^8 Pa
Cohesion, damaged	10.0×10^3 Pa
Coefficient of internal friction, damaged	0.6
Limiting strength at high pressure, damaged	1.1×10^8 Pa
Equation of state	Tillotson (Ih)
Impact velocity	15 km/s

From the figures presented by Silber and Johnson [2], Figure 10 was selected for comparison, as it shows the result of a single impact at nine different time intervals, allowing for a detailed comparison. Figure 5.4 shows the aforementioned Figure 10, and the recreated results are given by Figure 5.5.

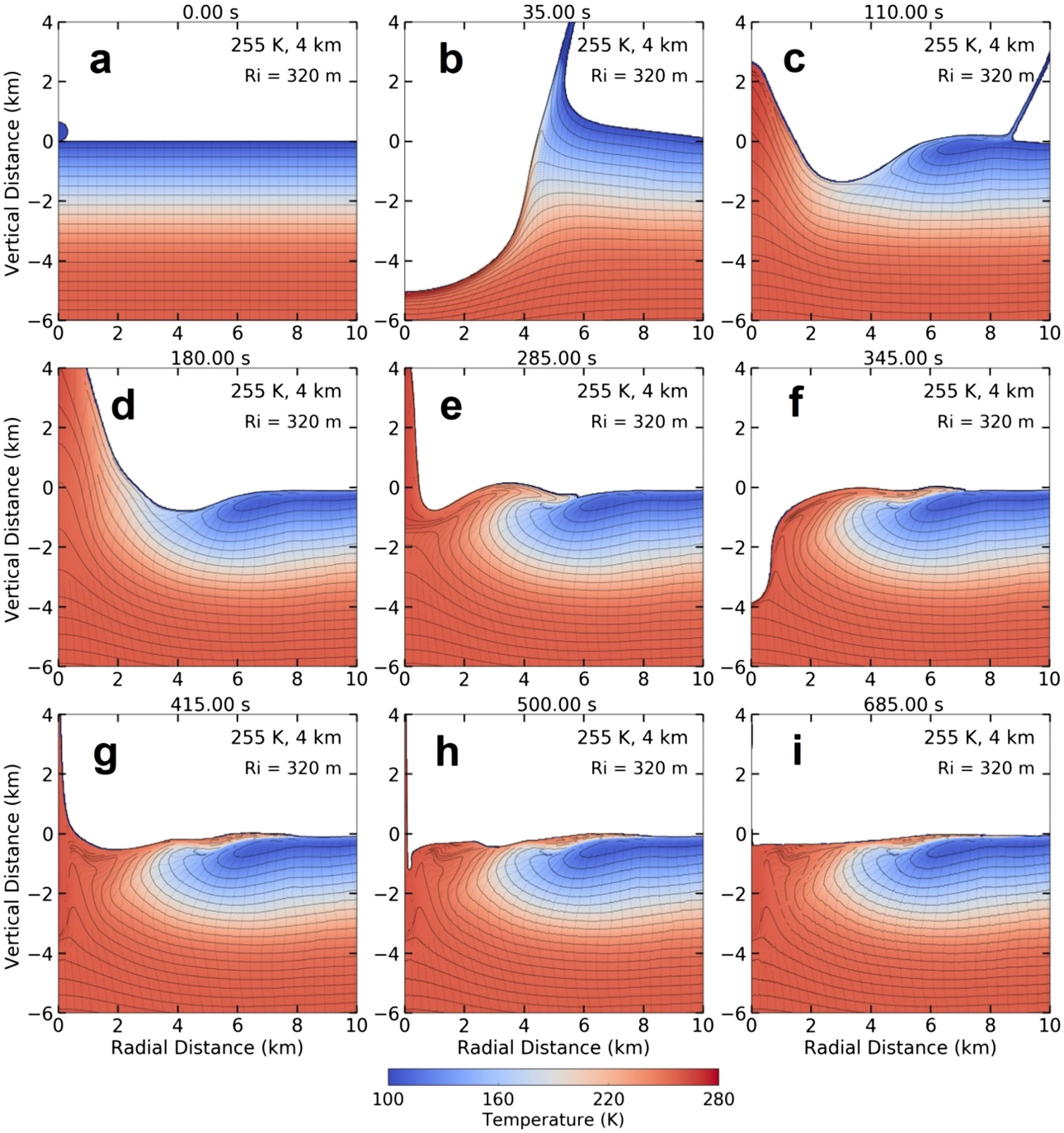

Figure 5.4: Simulation results from Figure 10 from Silber and Johnson [2]. Shown are the simulation results of a 640 m diameter icy projectile impacting a Europa-like target at 15 km/s, at nine different time intervals.

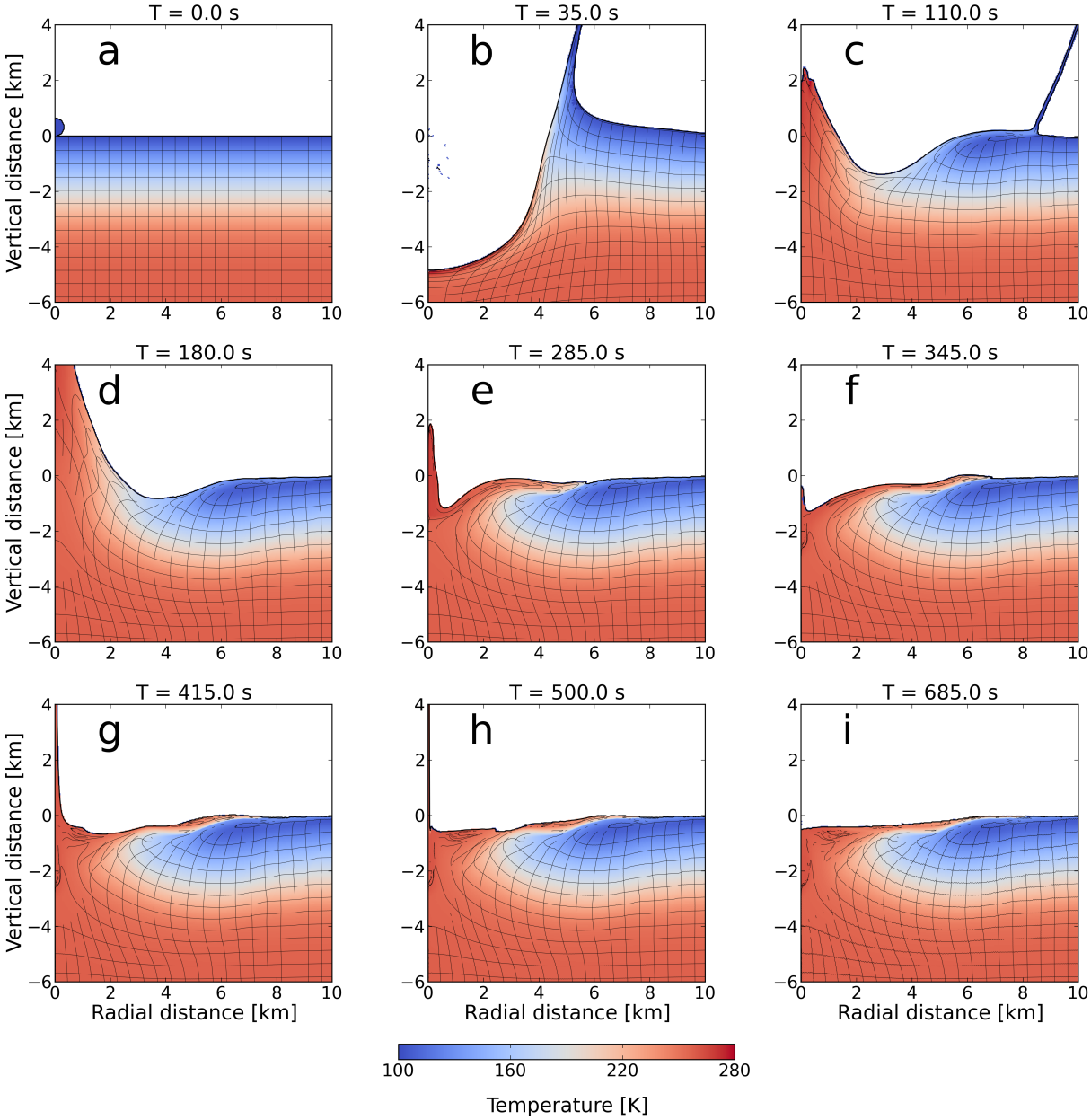

Figure 5.5: Recreation of Figure 10 from Silber and Johnson [2] using the iSALE2D hydrocode and the same input parameters, models and values.

Comparing Figure 5.4 and Figure 5.5, the plots are a bit different, similar to those noted for the previous paper. The simulation from panels a to d appear almost indistinguishable, but small changes emerge in panel e, where the placement and temperature of the material simply do not match up in certain areas. This persists, and the differences remain noticeable for the remaining panels. However, the final crater shape does not appear to be significantly different from the original, again similar to what was observed in Figure 5.3.

This is basically the same pattern as seen in Figure 5.3, and the type of differences are the similar as well. In both cases, the material behavior suggests a slightly more fluid-like response, which could indicate a lower viscosity compared to the original results, likely due to the absence of the PEIERLS viscosity model. Upon consulting Professor Collins, this is indeed the case. Moving forward, the inability to use the PEIERLS viscosity model will therefore be taken into account when interpreting the results.

6
Sensitivity Analysis

In this chapter, a sensitivity analysis is performed. Input parameters and their values are modified to investigate the robustness of the simulation and their effect on the cratering process and final crater morphology. This analysis will provide insights into the sensitivity of the input parameters. A control simulation is run first, which acts as a baseline. The inputs used for the control simulation are given in Section 6.1. Additionally, simulation plots for the pressure, temperature, and yield strength are given to provide a visual of the baseline impact. Then, parameters are changed one-at-a-time (OAT). Section 6.2 and Section 6.3 focus mainly on the simulation results from varying the general and environmental simulation parameters, and the material parameters, respectively, whereas quantifying the sensitivity of these parameters is performed in Section 6.4. Finally, an overview of the results is given in Section 6.5.

6.1. The Control Simulation

A control simulation is crucial when performing a sensitivity analysis, as it serves as a benchmark for comparison with other simulations. For the control simulation, a relatively small impact was simulated. The main reason for this choice is related to the runtime, since many simulations will be conducted, hence reducing the runtime is beneficial. However, it should still reflect a realistic scenario, meaning that the diameter and velocity should not be extremely high or low. Based on the impactor size and velocity used by previous research such as Bjonnes et al. [1], Bray et al. [65], and Silber and Johnson [2], a velocity of 10 km/s and a projectile diameter of 500 m were chosen.

Most material models used for the control simulation are based on the models used by previous research. For instance, papers such as Bjonnes et al. [1] and Bray et al. [65], utilize the ICE strength model, the BLOCK acoustic fluidization model, the OHNAKA thermal softening model, the IVANOV damage model, and the POLY low-density weakening model.

In Table 6.1, an overview of the most relevant input parameters and their values is given. For a full list of the values and the models, please refer to Table B.1 in Appendix B. The values for the surface temperature and gravity are based of those on Ganymede. Since the values for the dimensionless duration parameter and the strength of vibrations parameter were found to be inconsistent across different research, values from an example simulation from iSALE2D were used.

Table 6.1: Summary of the most relevant input parameters and their values used for the control simulation.

Parameter	Value	Unit
Asteroid Input File Parameters		
Surface temperature [80]	120	[K]
Surface gravity [80]	1.428	[m/s^2]
Impactor velocity	10	[km/s]
Impactor size (diameter)	500	[m]
Target thermal profile	Constant	
Material Input File Parameters		
Cohesion of intact material at zero pressure [1, 65, 66]	1.0×10^7	[Pa]
Coefficient of internal friction of intact material [1, 65, 66]	2.0	[−]
Limiting strength of intact material at high pressure [1, 65, 66]	1.1×10^8	[Pa]
Cohesion of damaged material at zero pressure [1, 65, 66]	1.0×10^4	[Pa]

Table 6.1: continued from previous page

Parameter	Value	Unit
Coefficient of internal friction of damaged material [1, 65, 66]	0.6	[−]
Limiting strength of damaged material at high pressure [1, 65, 66]	1.1×10^{8}	[Pa]
Minimum failure strain for low pressure states [1, 2]	1.0×10^{-4}	[−]
Positive constant (increase in failure strain with pressure) [1, 2]	1.0×10^{-11}	[−]
Pressure above which failure is always compressional [1, 2]	3.0×10^{8}	[Pa]
Dimensionless duration of vibrations	6.92×10^{-2}	[−]
Dimensionless strength of vibrations	1.1×10^{3}	[−]

In addition to the input parameters given in Table 6.1, Figure 6.1 is provided where the results of the control simulation are given at three different time steps. This provides a short overview of pressure, temperature, and yield strength of the control simulation.

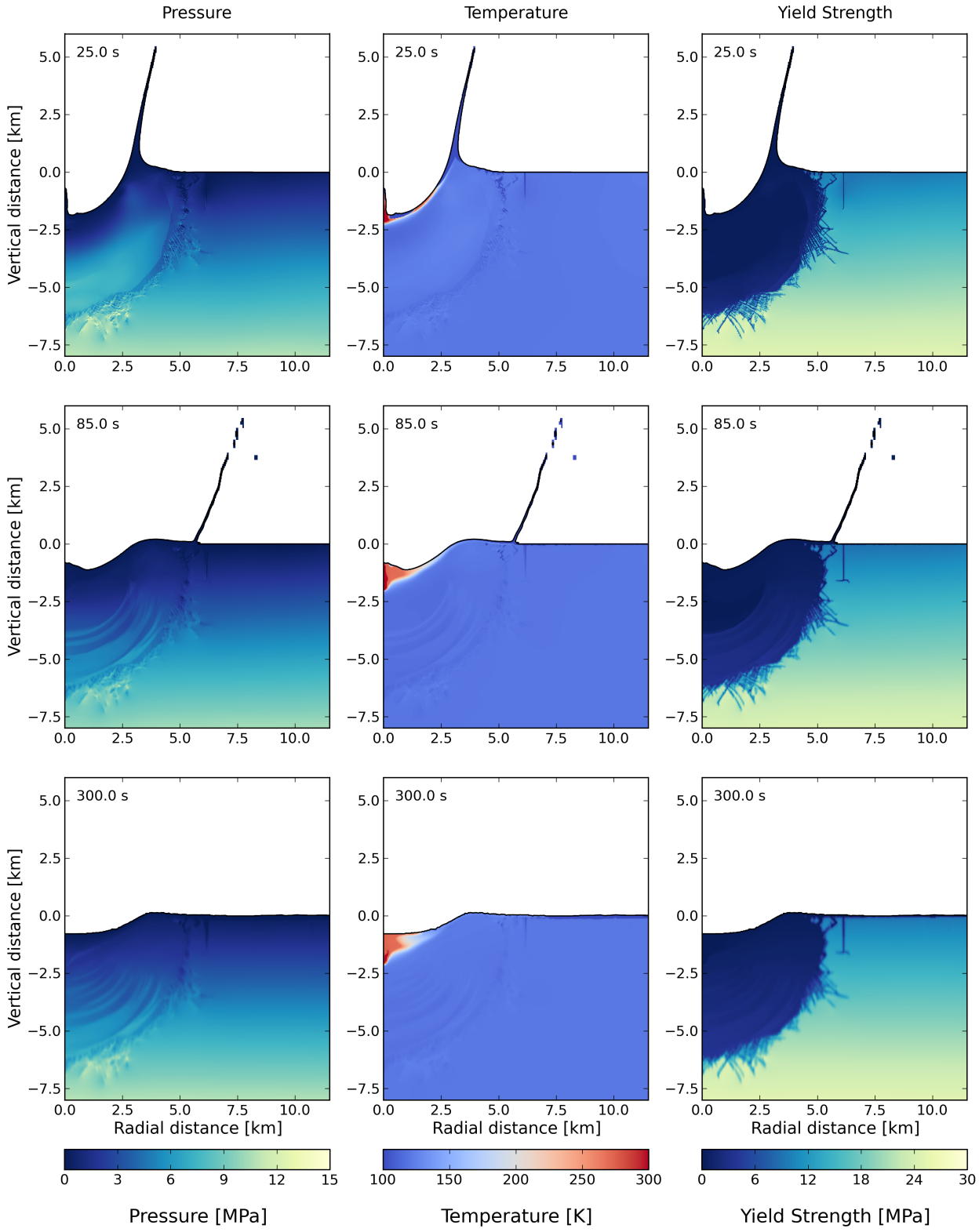

Figure 6.1: Overview of the pressure, temperature and yield strength of the control simulation at three different time steps. The impactor and target are both made of ice (AQUA EOS) at a surface temperature of 120 K. The impact velocity is 10 km/s and the impactor size is 500 m in diameter.

6.2. Simulation Results of Varying the Impact Parameters

The choice of input parameters directly affects the kind of impact simulated. Even small variations in these parameters could lead to significant differences, making it essential to systematically test their influence. This section focuses on six key parameters from the asteroid input file: surface temperature, surface gravity, impact velocity, impactor size, impactor material, and the thermal profile of the target.

Varying these parameters will provide insight into which factors dominate under Ganymede-like conditions and which have additional effects. It will highlight the parameter ranges that require more attention when interpreting simulation results.

6.2.1. Surface Temperature

The first parameter that is changed is the surface temperature. In reality, the surface temperature is not a constant value across the surface of a celestial body, as one side is typically exposed to sunlight, while the other side remains in the shadow. However, since the simulation takes place on a relatively small scale, it is assumed that the surface temperature of the area is constant. The surface temperature is varied from the control simulation by $\pm$20 K. This range was chosen, because the minimum temperature that the EOS can handle is 100 K. For consistency, the temperature will then also be increased by 20 K.

According to Zhang et al. [81], icy material will become stronger when temperature decreases. Therefore, it is expected that a lower temperature will result in a smaller crater in terms of both diameter and depth. Conversely, a higher surface temperature is expected to create larger craters. However, given the relatively small change in surface temperature, only slight differences are expected compared to the control simulation.

As anticipated, this is reflected by the results after running the simulations. A histogram of the differences between the crater diameter and the depth, compared to the control simulation, is given by Figure 6.2.

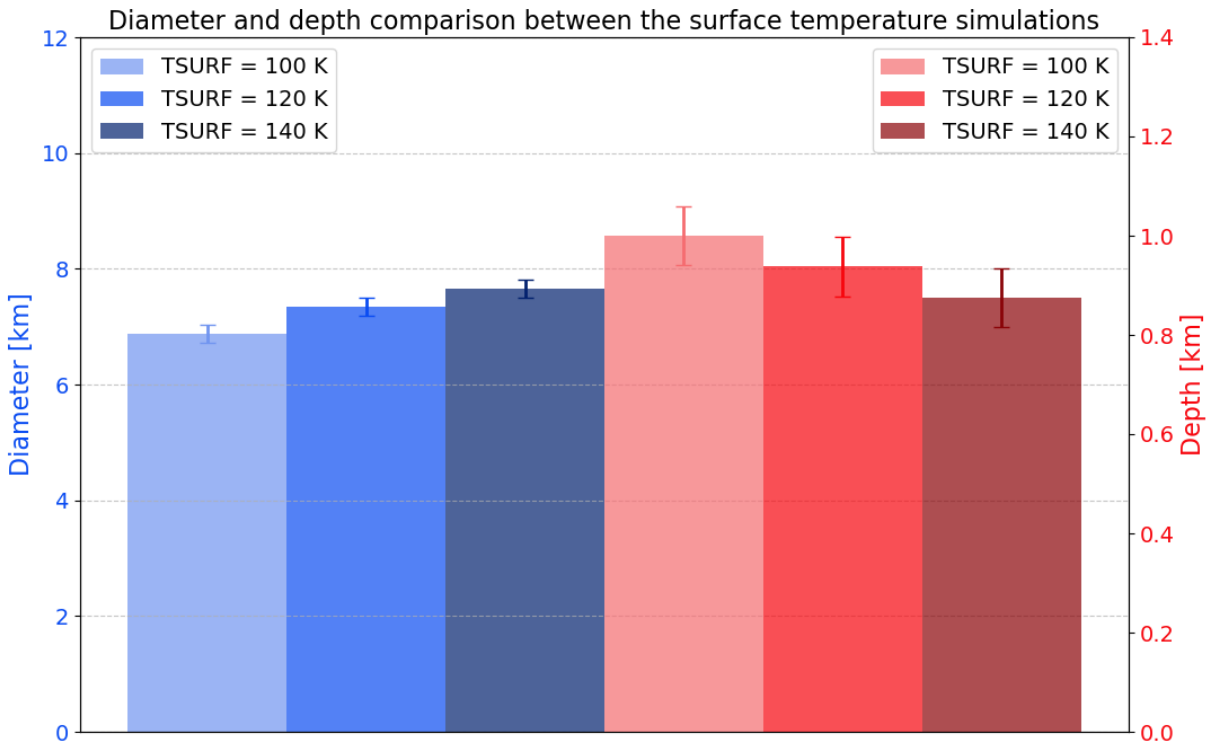

Figure 6.2: Comparison between the crater diameter (blue) and the crater depth (red) for the different surface temperature simulations. Both diameter and depth deviate only slightly from the control simulation. For the depth especially, the deviation even falls within the determined error.

Figure 6.2 visualizes the aforementioned small differences well. As mentioned before, the implemented change of $\pm$20 K might simply not have been substantial to notably influence the simulation and thus the final

crater shape. As for the diameter and depth values, it can be seen that the depth decreases for increasing surface temperature, which is contrary to expectations set earlier. This could be related to the fact that higher temperatures causes the material to become more relaxed, leading to a greater rebound of the crater floor. Additionally, it could effect the amount of material sliding back into the crater, which can change the depth. On the other side, the diameter does show expected behavior, with a decreased diameter for lower surface temperatures. Additional plots of the simulation at different time steps can be seen in Appendix A in Section A.5.

6.2.2. Surface Gravity

The surface gravity can be an important factor that influences the crater shape as mentioned in Subsection 2.2.3. Gravity plays a particularly crucial part during the modification stage. Key processes that are affected by gravity include the amount of material that is excavated, the amount of ejecta and its travel distance, the amount of material that will rebound, and the amount of material that will fall back into the crater.

For the control simulation, the surface gravity is set to $1.428\,\mathrm{m/s^2}$, equivalent to the surface gravity on Ganymede. For the other two simulations, this value is changed by $\pm 1\ \mathrm{m/s^2}$. This range was chosen to ensure a sufficiently large difference would occur, as smaller differences, such as $0.1\,\mathrm{m/s^2}$, are unlikely to result in any noticeable differences. At the same time, the deviation should not be too large, such that lower limit would reach near $0\ \mathrm{m/s^2}$.

With a lower gravity, it is expected that the crater diameter and depth will increase. The main reason for this is that gravity affects the fallback of material near the end of the cratering process. With a lower gravity, less material will fall back into the crater, leading to a larger and deeper crater. Additionally, the rebound of material in the crater floor is also affected by gravity, and a lower gravity may cause a larger rebound effect. So, a larger and in general a deeper crater for a lower gravity can be expected, but a peak or dome-like shape in the center on the crater floor should not be surprising. The results of the simulations are presented in Figure 6.3.

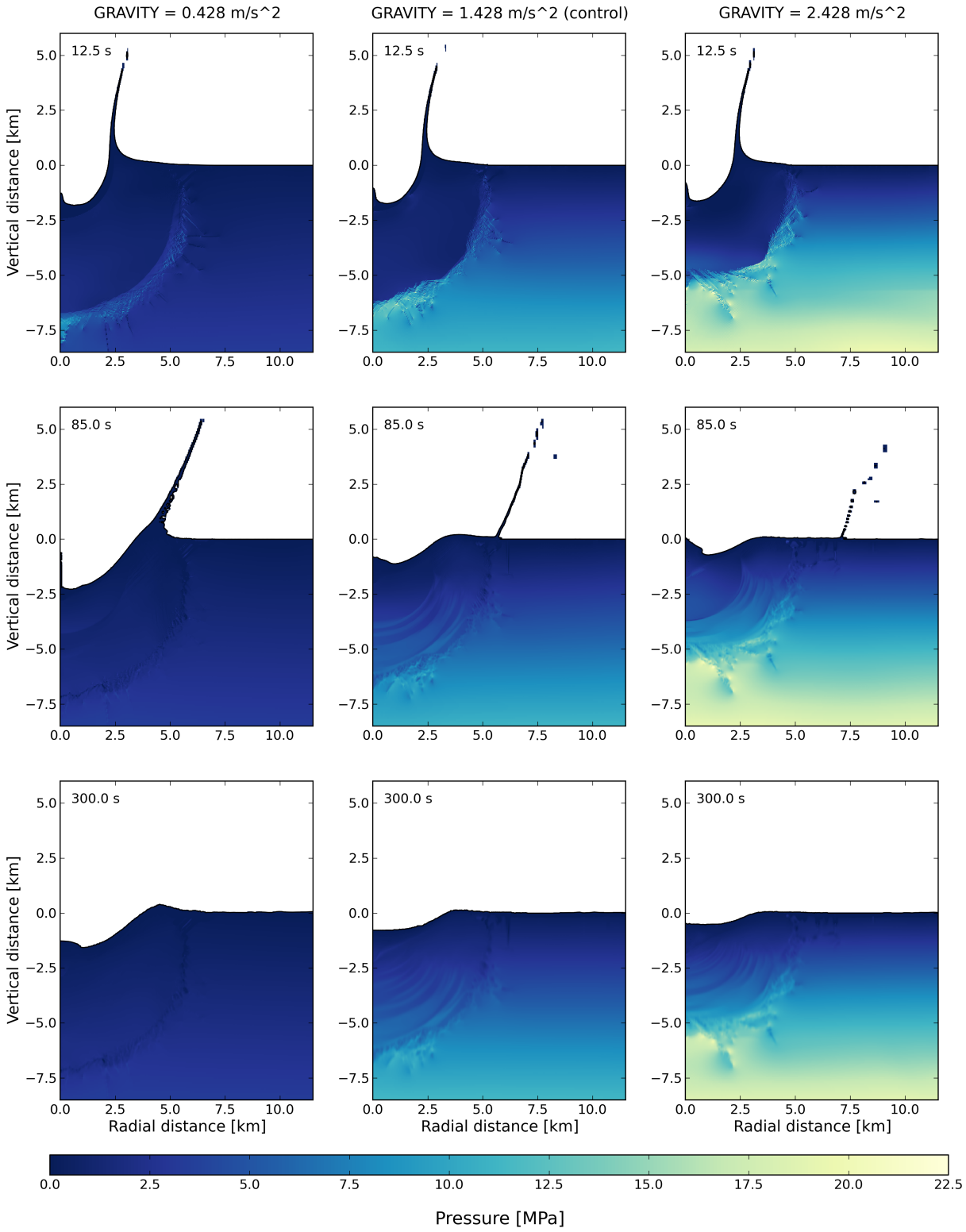

Figure 6.3: Sensitivity simulation results of the surface gravity. The differences between the plots is considerable, as depicted by the crater diameter and depth, as well as the damage in the target.

The first noticeable feature from Figure 6.3 is the difference in pressure gradient in the target. This is only a natural result from increasing or decreasing the surface gravity though, which can be explained by the hydrostatic equation [82]. This equation states that the pressure at a certain height or depth is proportional to the weight of the overlying material. The weight, in turn, is affected by the density and the gravity. Hence, changes in gravity result in a different pressure gradient in the target, as shown in Figure 6.3. Regarding the crater shape, the simulation with a lower gravity resulted in a deeper and larger crater, as expected. Especially the depth is larger in comparison to the other simulations. Moreover, a small peak or dome can be seen, which

aligns with previously stated predictions about the rebound affect for the lower gravity simulation. Noticeable is that the region of damage is different across the three simulations. This, approximately hemispherically shaped, region is where the most damage occurs, and is best observed in the top row in Figure 6.3. It has a radius of about 6 km for the higher gravity simulation, where for the low gravity simulation this is about 7.5 km. A reason for this difference could be attributed to the compression effects of gravity on the material. For a higher gravity, material resistance to movement and penetration is increased, thereby reducing the damage compared to the lower gravity simulations.

6.2.3. Impact Velocity

The impact velocity is one of the most important parameters in simulating impacts. It is a major component in the determination of the initial kinetic energy of the impactor, which is determined by Equation 6.1 [83]. Where m is the mass of the object, and v is the velocity of the object.

$$E_k = \frac{1}{2}mv^2 \tag{6.1}$$

Upon contact, the impactor transfers its kinetic energy to the target. Since kinetic energy increases quadratically with velocity, it is expected that the crater will become larger in size for larger impact velocities. Conversely, lower impact velocities should result in smaller craters. Furthermore, larger impact velocities are expected to increase the damaged area, due to more energy being transferred to the target, resulting in a more devastating impact. For the sensitivity simulations, the impact velocity used for the control simulation is changed by $\pm$25%. This range was chosen as the deviation is not too little and not too much. Moreover, as previously stated, even a small change in velocity leads to a much larger change in kinetic energy due to the quadratic scaling. The results of the simulations can be seen in Figure 6.4.

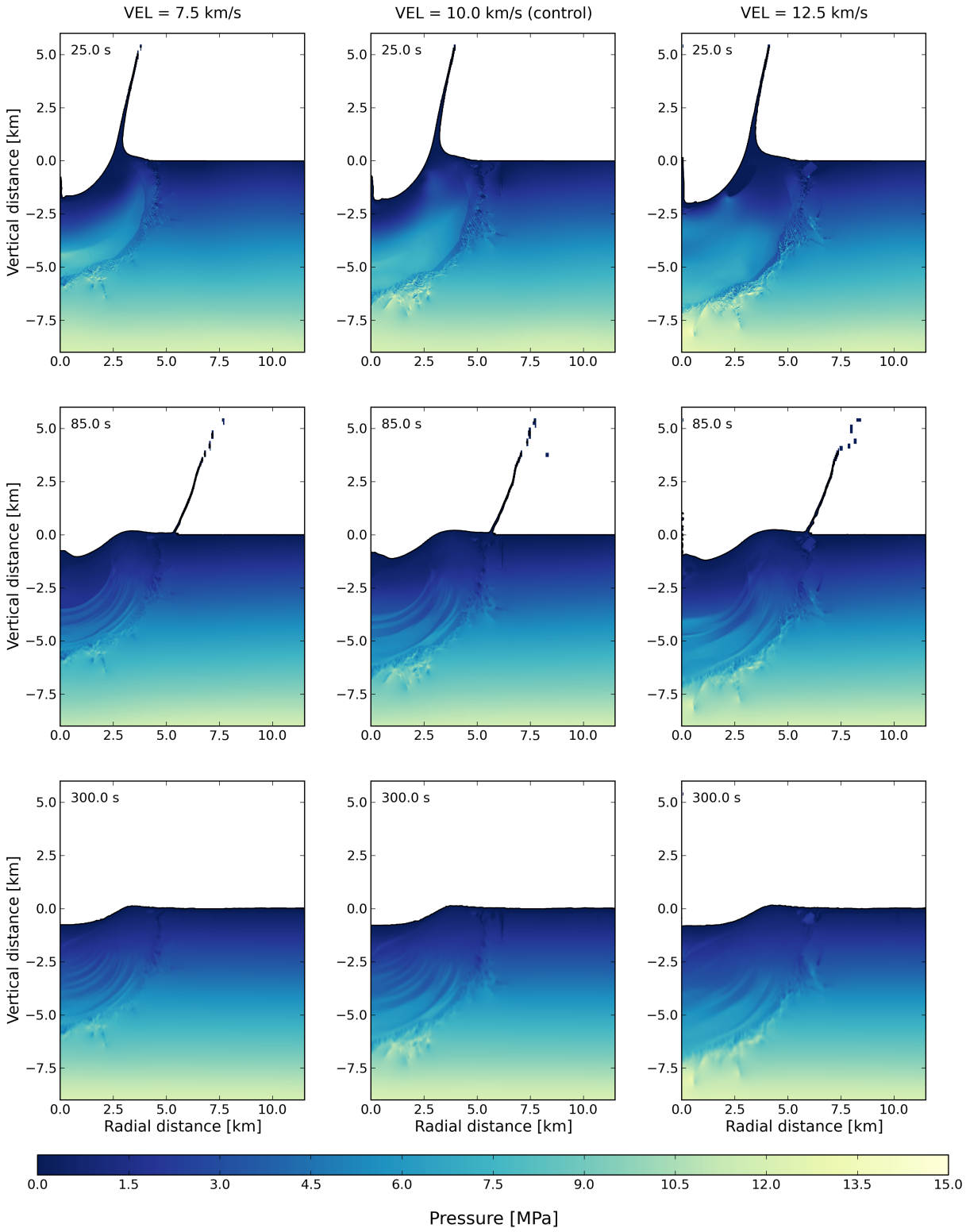

Figure 6.4: Sensitivity simulation results of the impact velocity. Only relatively small differences are visible in crater diameter and depth, though damage appear more extensive for higher velocities.

From Figure 6.4, it can be seen that the effect is unexpectedly on the smaller side. Even though a 10 km/s impact has 77.7% more energy than a 7.5 km/s impact, and a 12.5 km/s impact 56.25% more energy than a 10 km/s impact, the change in final crater shape remains modest. The depth changes only slightly across the three simulations. Although the crater shape appears similar, the diameter decreases by about 14% for the lower velocity and increases by approximately 9% for a higher velocity. These percentages are lower than expected, however, should not go unnoticed. The relationship between kinetic energy and the diameter of a crater might help explain these results. Many relationships between kinetic energy and the crater diameter

have been determined in the past, which are all slightly different, however, the majority can be simplified into the form shown in Equation 6.2. The values of x are based of Hughes [84], which were found through different research in terrestrial targets. While these targets differ from icy bodies, the general impact processes and crater shapes are comparable.

$$E_k \propto D^x \ , \ \text{for } 2.59 < x < 3.89 \tag{6.2}$$

Equation 6.1 and Equation 6.2 can then be rewritten to Equation 6.3, so that the ratio between two craters can be determined.

$$\frac{E_{k_2}}{E_{k_1}} \propto \frac{D_2^x}{D_1^x} \rightarrow \frac{v_2^2}{v_1^2} \propto \frac{D_2^x}{D_2^x} \rightarrow \left(\frac{v_2}{v_1}\right)^2 \propto \left(\frac{D_2}{D_1}\right)^x \rightarrow \frac{D_2}{D_1} \propto \sqrt[x]{\left(\frac{v_2}{v_1}\right)^2} \tag{6.3}$$

By considering different values of x, the theoretical difference in crater diameter can be determined. The increase in diameter that can be calculated from the 7.5 km/s to the 10 km/s impact is about 16%-24.9%, and from 10 km/s to 12.5 km/s about 12.1%-18.8%. When looking at Figure 6.4, the crater diameter increase from 7.5 km/s to 10 km/s can be found equal to 16.4%, and from 10 km/s to 12.5 km/s 11.5%. These fall on the lower end of the predicted range, however, they are close. In short, the increase in crater diameter with increasing impact velocity should not be entirely unexpected.

A clearly noticeable difference in Figure 6.4 though, is the damaged area in the target. Logically, it is largest for the simulation of a higher velocity impact. This observation suggests that the shockwave propagating through the target becomes significantly stronger at higher impact velocities, thus leading to a larger region of damage.

6.2.4. Impactor Size

Besides the impact velocity, the size of the impactor also affects the kinetic energy, as it is directly related to the mass m in Equation 6.1. A smaller impactor has less kinetic energy, and logically should result in a smaller crater, while a larger impactor would create a larger crater. To evaluate the influence of impactor size on the crater shape, simulations are run with diameters equal to 500 m $\pm$100 m. This range was chosen to maintain consistent with Subsection 6.2.3, and to ensure a similar initial kinetic energy. The results are given in Figure 6.5.

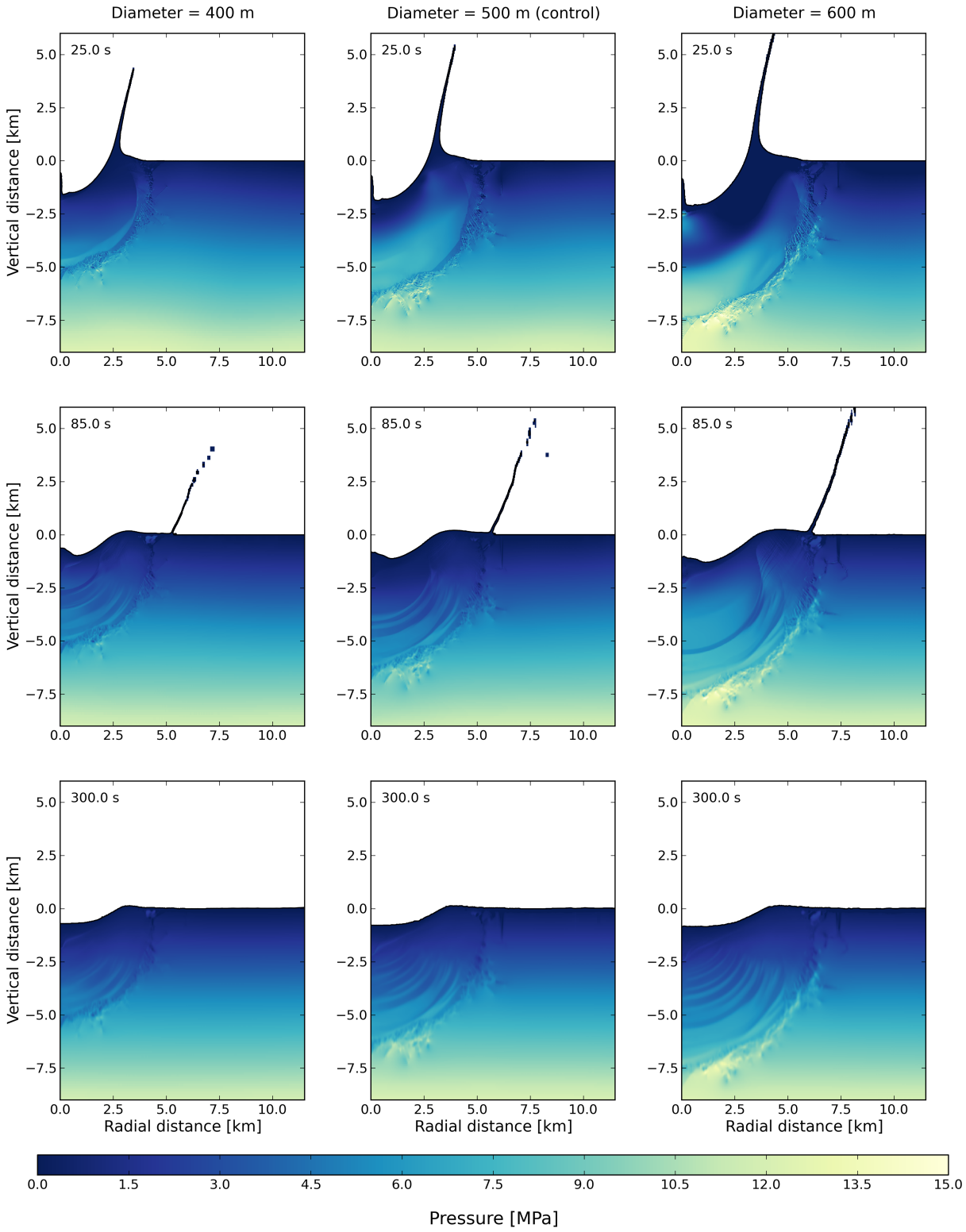

Figure 6.5: Sensitivity simulation results of the impactor size. Crater diameter and depth appear relatively similar at a first glance. However, the damage in the target is much more extensive for the larger impactor sizes.

Figure 6.5 shows that the crater depth changes only slightly, while the diameter changes more noticeably. Interestingly, the results are quite similar to those observed in Figure 6.4. To explain the results, Equation 6.1 is once more rewritten in terms of mass, similarly as done in Equation 6.3, and is given in Equation 6.4.

$$\frac{E_{k_2}}{E_{k_1}} \propto \frac{D_2^x}{D_1^x} \longrightarrow \frac{m_2}{m_1} \propto \frac{D_2^x}{D_2^x} \longrightarrow \frac{m_2}{m_1} \propto \left(\frac{D_2}{D_1}\right)^x \longrightarrow \frac{\frac{4}{3}\pi R_2^3}{\frac{4}{3}\pi R_1^3} \propto \left(\frac{D_2}{D_1}\right)^x \longrightarrow \frac{D_2}{D_1} \propto \sqrt[x]{\left(\frac{R_2}{R_1}\right)^3} \tag{6.4}$$

Using Equation 6.4, it can be calculated that the increase in crater diameter from a 400 m impactor size to

500 m is 18.8%-29.5%, and for 500 to 600 m it is 15.1%-23.5%. From Figure 6.5, the increase from the 400 m diameter simulation to the control simulation is 21.3%, and from the control simulation to the 600 m diameter simulation by 15.2%. These values are within, or close to, the theoretical range calculated using Equation 6.4, confirming that the results from Figure 6.5 are reasonable. Similar to the results from Subsection 6.2.3, the area of damage increases with impactor size. This aligns with the logic applied to impact velocity, as a larger impactor will transfer more energy to the target, generating a more devastating shockwave and causing greater damage to the target.

6.2.5. Impactor Material

The material of impactors can vary, comprising of water, silicates, and metals for example. Thus far, pure water ice has been used as the impactor material. To explore the effect of using an alternative material, granite is selected. To ensure the kinetic energy of the impact is consistent, the same mass is used for both simulations. This means that the size of the granite impactor is adjusted to account for its higher density compared to ice. It is expected that the granite impactor will produce a larger crater and cause more damage. Granite is denser and stronger than ice, making it more difficult to break apart. This allows for deeper penetration into the target, thus causing more damage in the process. In Figure 6.6 the simulation results are shown.

From Figure 6.6, it can be observed that the differences are relatively small, but noticeable. The granite impactor creates a 17.5% larger crater diameter and the depth is 22.6% greater compared to the control simulation, which are considerable changes. Additionally, the damage is slightly larger for the granite impactor. These observations align with the expectations established earlier. Logically, using different materials for the impactor will produce different impacts and crater shapes, however, even when using approximately the same kinetic energy, the differences especially in crater diameter and depth are not to be ignored.

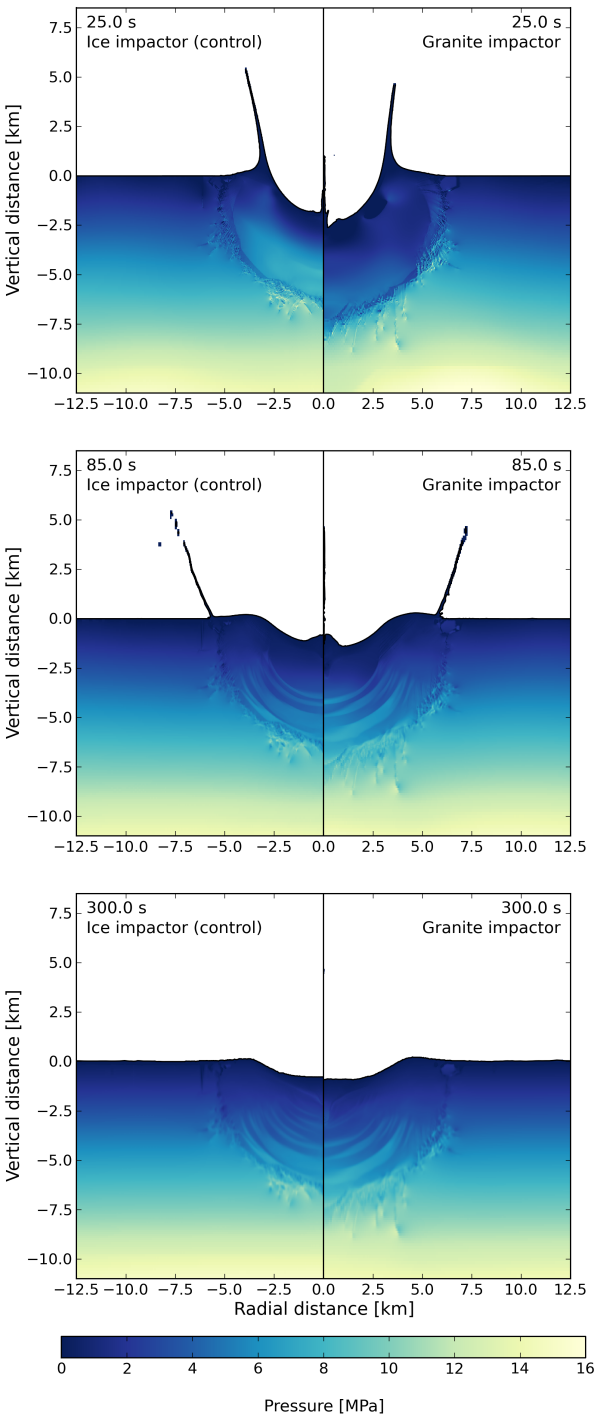

Figure 6.6: Sensitivity simulation results of the impactor material, comparing a granite impactor to an ice impactor using the same mass. Noticeable differences can be seen in crater diameter and depth, though the damage appear approximately equal.

6.2.6. Thermal Profile of the Target Layer

Depending on the celestial body in question, selecting an appropriate thermal profile is essential. This is especially relevant for larger impacts where a lot of material is excavated, as deeper layers in the target will have higher temperatures, which can have an effect on the crater formation. The available options for the thermal profile are constant (CONST), which is set by default; conductive (COND); conductive and convective (COND-CONV); and conductive and convective, with the temperature capped at the melting temperature of the material (CONDCONVCAP). Expected is that the different thermal profiles will have a limited effect on the cratering process, mainly because the impact is relatively small, meaning that not enough material is excavated for the effect of the thermal profile to become visible in the final crater shape.

Upon plotting the results, noticeable differences in the crater shape were observed, while the temperature practically did not change. As mentioned before, this is probably due to the impact not being large enough for the effect of different thermal profiles to become visible. Nevertheless, closer analysis of the crater shape shows that the measured differences amount to about 15%, which is arguably not negligible. Therefore, the usage of various thermal profiles should be taken into account, especially for even larger impacts. Readers can view the simulation results in Figure A.17 in Figure A.5.

6.3. Simulation Results of Varying the Material Models and Parameters

Similarly to Section 6.2, this section examines the effects of varying material parameters and values on the simulation and crater formation. Several material models are available, each with their own set of specific input parameters. However, there are a few models in iSALE2D that will not be considered here though, specifically the viscosity models, porosity models and the low-density weakening models. Regarding the viscosity models, the iSALE2D manual states that these should only be used for liquid EOSs. Even though in Chapter 5 the PEIERLS viscosity model was discussed, which was used for similar ice-on-ice impacts, it was also mentioned that the currently used version of iSALE2D cannot utilize this model. Hence, viscosity models are not considered here. Porosity models are excluded for the simple reason that they are not relevant to the simulation. No porosity models are needed for the upcoming simulations, hence they are not examined. Finally, the low-density weakening model offers only two options: using no model or the POLY model. Based on previous research, the POLY model is consistently applied, and therefore it will be used here as well. Since the low-density weakening model also has no additional parameters to investigated, there is no need to study it in detail.

6.3.1. General Material Parameters

There are a few material parameters that are not linked to any specific material model. Nevertheless, they are important enough that they have to be specified in the material input file. The ones that are discussed here are the poisson ratio (POIS), the melting temperature at zero pressure (TMELT0), and two parameters from the Simon approximation for temperature: the constant a (ASIMON), and the exponent c (CSIMON).

Poisson Ratio

First, the poisson ratio is examined. This parameter is used for the calculation of the shear modulus, and the iSALE2D code assumes its value to be independent of temperature and pressure. Looking at the calculation for the shear modulus given by iSALE2D, lowering the poisson ratio will increase the shear modulus [71]. Hence, it is expected that a lower poisson ratio will result in a smaller crater, since a higher shear modulus translates to a more rigid material, meaning that a higher force is necessary to deform the material. So, the crater should be smaller for a lower poisson ratio, and for a higher poisson ratio larger. The simulations used poisson ratios of 0.33 $\pm$0.03. The value for the poisson ratio used in the control simulation was chosen based on previous research [1, 2]. The value of the deviation was based on research by Sinha [85], which provided an overview of different dynamic poisson values, which ultimately ranging from 0.29 to 0.37. Hence, a deviation of $\pm$0.03 was decided.

After plotting the results, minimal differences were observed in the crater shape and size between the three simulations. However, the damage in the target were are slightly higher for higher values of the poisson ratio.

This observation aligns with the expectations set earlier, as a higher value of the poisson ratio relates to a lower shear modulus, making the target more prone to damage. However, this should also result in a larger crater. The reason why the effects in crater shape might be so small, could be that the shear modulus influences the cratering process to a lesser degree than parameters like gravity, which might overshadow the impact of varying the poisson ratio. To view the simulation results of the poisson ratio, refer to Figure A.5 in Appendix A.

Melting Temperature at Zero Pressure

The melting temperature at zero pressure is also investigated. Together with the ASIMON and CSIMON parameters, it is considered a general thermal parameter, and it is used in an equation which calculates the melting temperature of the material, given by Equation 6.5.

$$T_m = T_{m0}\left(\frac{p}{a} + 1\right)^{1/c} \tag{6.5}$$

Where T_{m0} is the melting temperature at zero pressure, p is the pressure, and a and c are the constants ASIMON and CSIMON respectively.

The melting temperature at zero pressure is considered first, and a deviation from the control simulation equal to $\pm$27 K, or roughly 10%, was applied. Logically, for a lower value it is expected that more of the target will melt, since melting of material will occur faster compared to the higher melting temperature simulations. Since more material should melt, it is expected that the final crater becomes larger due to the excavation of more material, but shallower due to potential backflow of melted material. Conversely, a higher melting temperature at zero pressure is predicted to result in a smaller crater, with a greater depth.

Unexpectedly, the plotted results showed that the changes in melting temperature at zero pressure practically had a negligible effect on the final crater. It could be that the effect of melting temperature at zero pressure is simply being overshadowed by other influences. To investigate further, Equation 6.5 was plotted with melting temperature on the y-axis and pressure on the x-axis, given in Figure 6.7.

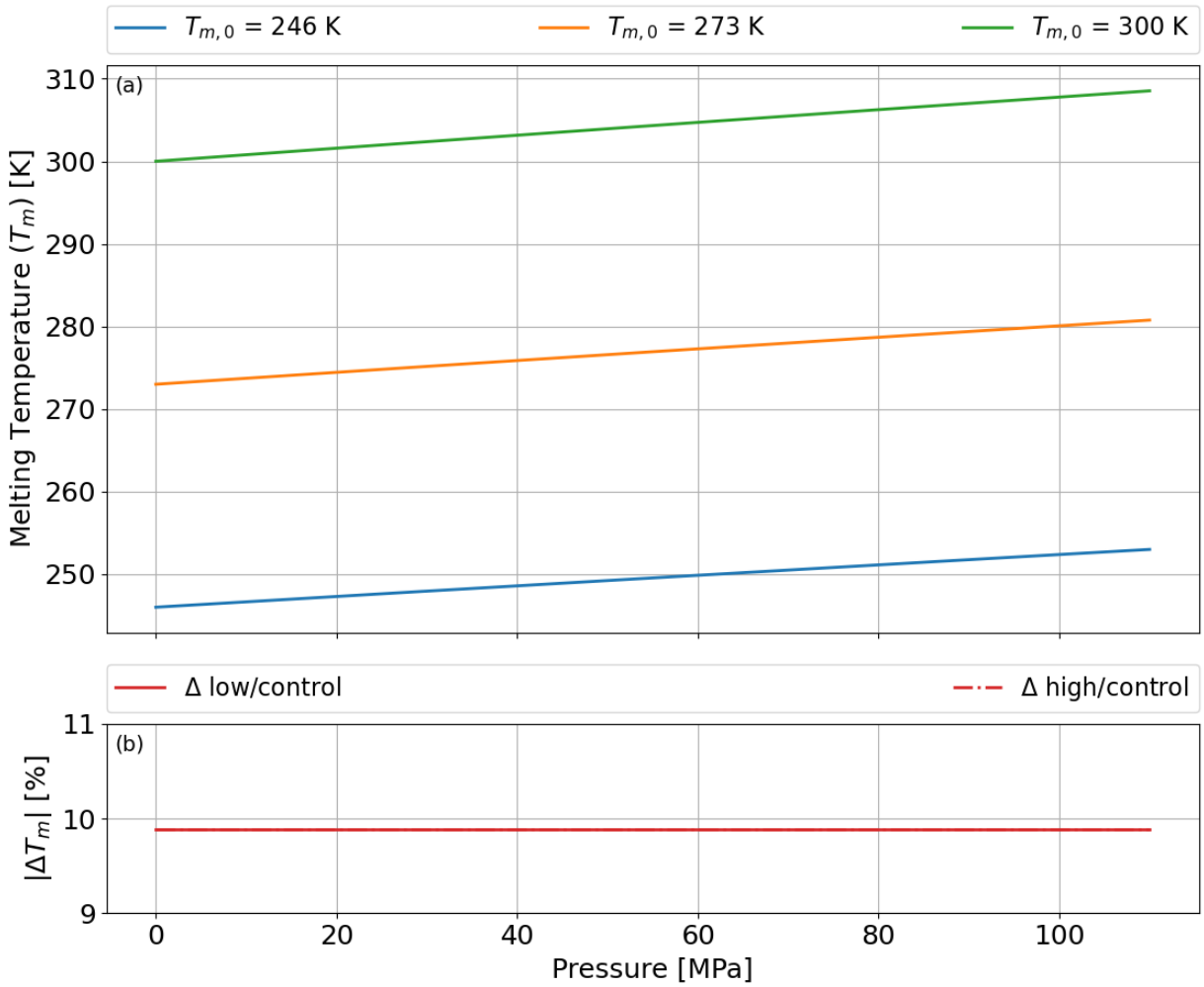

Figure 6.7: Plot of the melting temperature against pressure for different TMELT0 parameter values (a). In addition, a plot with the differences between the curves is given underneath (b).

From Figure 6.7, it becomes apparent that the variation in melting temperature is minimal, which can explain the negligible differences observed in the simulation results. Additional plots on the melting temperature can be found in Appendix A in Figure A.5.

ASIMON Parameter

The ASIMON parameter, a constant in Equation 6.5, is adjusted next. Since ASIMON is just a constant value, expectations were derived based on how changing the ASIMON parameter would affect the melting temperature in Equation 6.5. It shows that a decrease in ASIMON increases the melting temperature, mirroring the effects that increasing TMELT0 has on the melting temperature. Hence, a lower ASIMON value is expected to result in a smaller crater, and conversely a higher ASIMON value should result in a larger crater. The ASIMON parameter is changed by $\pm$25%, which was considered to be an sufficient deviation from the control simulation.

The plots reveal no significant changes in the cratering process due to adjustments of the ASIMON parameter. Since the ASIMON parameter is just a constant value with no description given by iSALE2D, it is difficult to find a reason for the lack of variation across the simulations. Therefore, similar to TMELT0, a plot was made of Equation 6.5 for more insight, which can be seen in Figure 6.8.

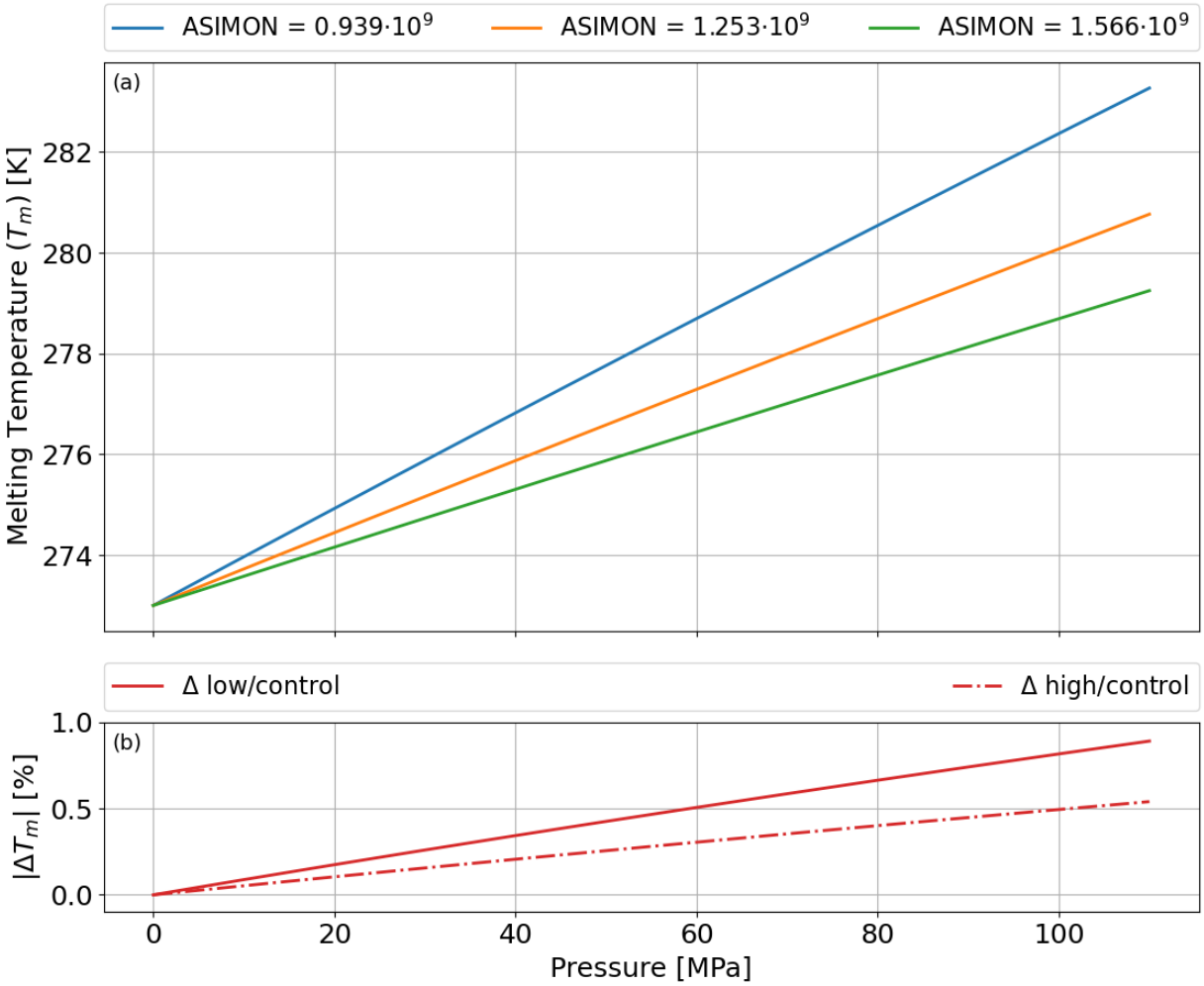

Figure 6.8: Plot of the melting temperature against pressure for different ASIMON parameter values (a). In addition, a plot with the differences between the curves is given underneath (b).

Figure 6.8 shows that the differences between the three curves are minor, less than one percent in fact. Therefore, it is reasonable to accept that there is virtually no difference between the three simulations. To view the plot of the ASIMON simulation, see Figure A.5 in Appendix A.

CSIMON Parameter

Finally, the CSIMON parameter is addressed. Similar to ASIMON, the CSIMON parameter lacks a clear definition, so expectations are again derived from Equation 6.5. Based on Equation 6.5, a decrease in CSIMON results in a higher melting temperature, mirroring the effect of a decrease in ASIMON or an increase in TMELT0, which would result in a smaller crater. Conversely, a higher value of CSIMON should result in a larger crater. The CSIMON parameter is changed by $\pm 16.67\%$, which was deemed reasonable as the value of CSIMON is already quite small.

The simulation results show that, like with the ASIMON parameter, there are practically no differences in the plots. Therefore, a plot was made again between the melting temperature and the pressure for varying CSIMON values, which can be seen in Figure 6.9.

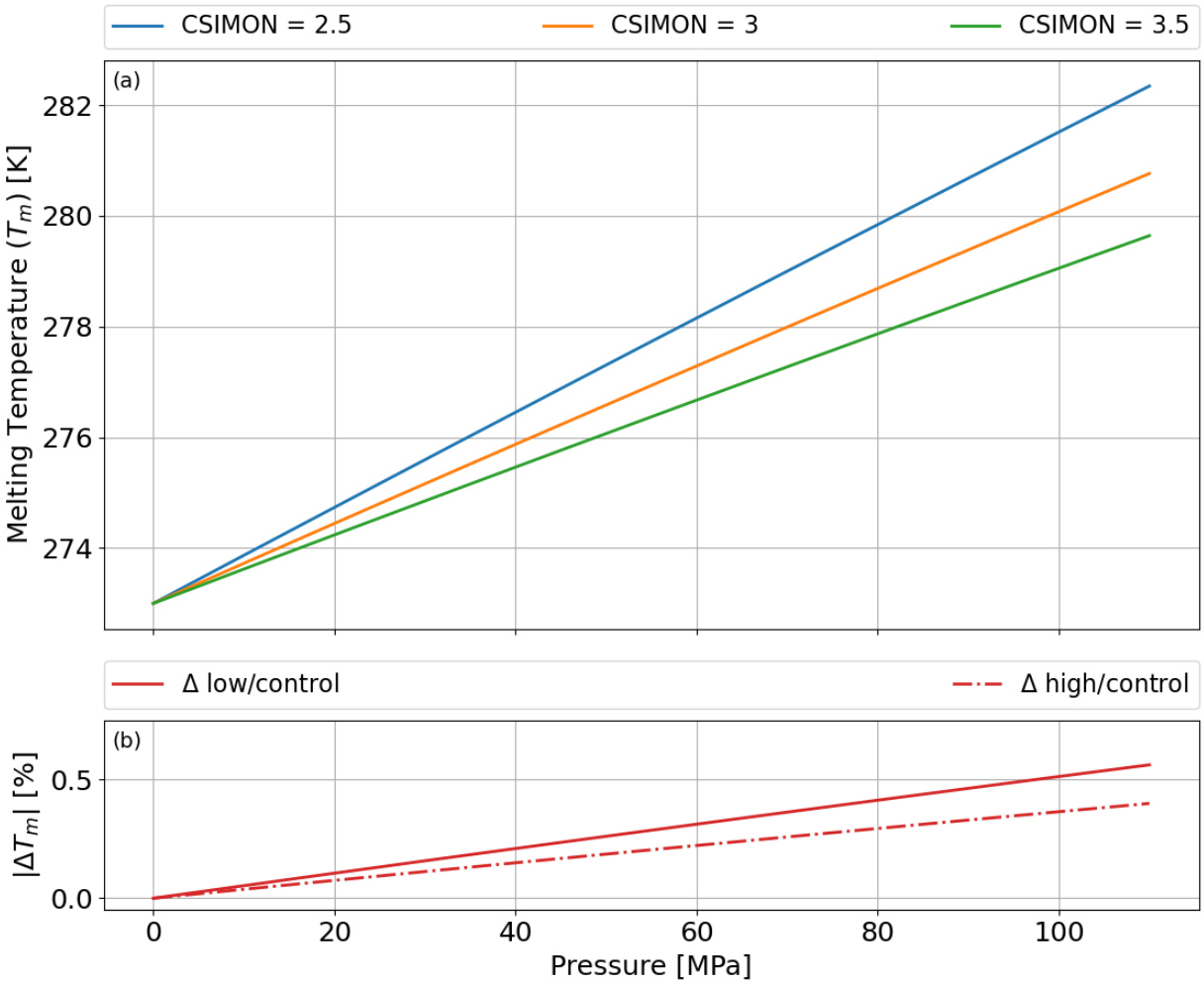

Figure 6.9: Plot of the melting temperature against pressure for different CSIMON parameter values (a). In addition, a plot with the differences between the curves is given underneath (b).

From Figure 6.9, it can be seen that the curves resemble those from Figure 6.8, however, the differences here are even smaller compared to the control simulation. This suggests that CSIMON, like ASIMON, has little effect on the cratering process. Additional plots of the CSIMON simulation results are shown in Figure A.5 in Appendix A.

In summary, the poisson ratio, melting temperature at zero pressure, ASIMON, and CSIMON parameter show minimal to no observable differences from the control simulation.

6.3.2. Strength Models

There are numerous strength models in iSALE2D, each designed for a specific material type. For example, the ”JNCK” model is a strain and strain-rate dependent strength model for metals, whereas the ”HYDRO” model is a inviscid fluid model. Given that the impactor and target material of the simulated impacts are made of ice, it is only logical to utilize the ”ICE” strength model. This model requires six input parameters to be able to calculate the stresses generated during the impact process. To calculate these stresses, Equation 6.6 is given.

$$Y_{(i,d)} = Y_{(i,d)0} + \frac{\mu_{(i,d)} P}{1 + \frac{\mu_{(i,d)} P}{Y_m - Y_{(i,d)0}}} \tag{6.6}$$

In Equation 6.6, the subscript ”i” and ”d” refer to intact or damaged material, respectively. $Y_{i,d}$ is the cohesion or yield strength of the material, $Y_{(i,d)0}$ is the yield strength of the material at zero pressure, $\mu_{(i,d)}$ is the coefficient of friction of the material, P is the pressure, and Y_m is the limiting strength of the material at high pressures.

Yield Strength of Intact Material

First, the yield strength of intact material at zero pressure is varied. The control simulation uses a value of 1.0×10^7 Pa, which has been widely used in previous studies, as referenced in Table 6.1. Therefore, a moderate deviation of $\pm$25% was decided. Logically, for a lower value, it is expected that the damage in the target increases, as well as the crater size. This can also be deduced from Equation 6.6, where lowering the value for $(Y_i)_0$ will decrease Y_i. With a lower yield strength, deforming and displacing the material will become easier. However, once the material becomes damaged, the yield strength of intact material is no longer relevant, as the dedicated damaged material parameters become dominant.

The resulting plots displayed minor differences across the simulations, which can be viewed in Figure A.5 in Appendix A. Among the three simulations, damage was slightly higher in the simulations with lower cohesion, which aligns with previously stated expectations. However, the diameter and depth practically remained unchanged. This can likely be attributed to reasons mentioned before, the fact that intact material parameters are primarily relevant right before deformation of material occurs, which is a brief period of time. Instead, the damaged material parameters become the controlling factor, which could account for the minimal differences observed between simulations.

Friction Coefficient of Intact Material

Next is the friction coefficient of intact material. This value is changed by $\pm$25% compared to the value used for the control simulation. With a higher coefficient of internal friction, it is expected that the strength of the material increases, as a higher friction coefficient results in a higher resistance to particle movement within the material. The opposite would be true for a lower coefficient of internal friction. This prediction is also supported by Equation 6.6, which shows that an increase in μ leads to an increase in Y.

The results, however, show insignificant differences between the plots, and are therefore not displayed here; instead, they are shown in Figure A.5 in Appendix A. The only observable difference was a slight increase of yield strength in the target for simulations using a higher value of the friction coefficient. However, it does not influence the final crater in any way. This situation can be explained by the same reasoning as with the yield strength of intact material discussed previously: once the material is damaged, the intact strength parameters lose their influence on the simulation.

Limiting Yield Strength of Intact Material

Next, a change was made to the parameter that corresponds to the yield strength at high pressures. Variations equal to $\pm$30.0 MPa from the control simulation were chosen. For a lower value, it is expected that the crater shape is larger, since the reduction in strength would allow material to break apart faster, resulting in a larger crater. The opposite can be expected for a higher limiting strength.

However, once again, the results of the simulations showed a different outcome than predicted. Barely any major differences were observed, and similar to the previous two parameters, the same reasoning is applicable. To view the simulation plots, see Figure A.24 in Figure A.5.

Yield Strength of Damaged Material

Next, the same three parameters are changed again, but for damaged material. Starting with the cohesion at zero pressure, this value was adjusted by $\pm$25%. As with YINT0, it is expected that a lower value of YDAM0 will result in more damage and a larger crater, because the lower the yield strength allows the material to deform more easily. This can also be seen from Equation 6.6, where a lower value of $Y_{(d)0}$ results in a lower value of Y_d. In these simulations, a larger difference in final crater shape is expected compared to the intact material parameters, as Equation 6.6 will primarily be dependent on the damaged material parameters during the impact, given that the material remains in a damaged state for a longer duration.

However, unexpectedly, the results for the YDAM0 parameter show no noticeable differences between the plots, which can be seen in Figure A.5 in Appendix A. One possible explanation is that the stress generated during the impact was much higher than the value used for YDAM0, and so any difference in YDAM0 would not have changed in the cratering process. To investigate further, the yield strength is plotted against the pressure, to see the effects of the various YDAM0 values, which can be seen in Figure 6.10.

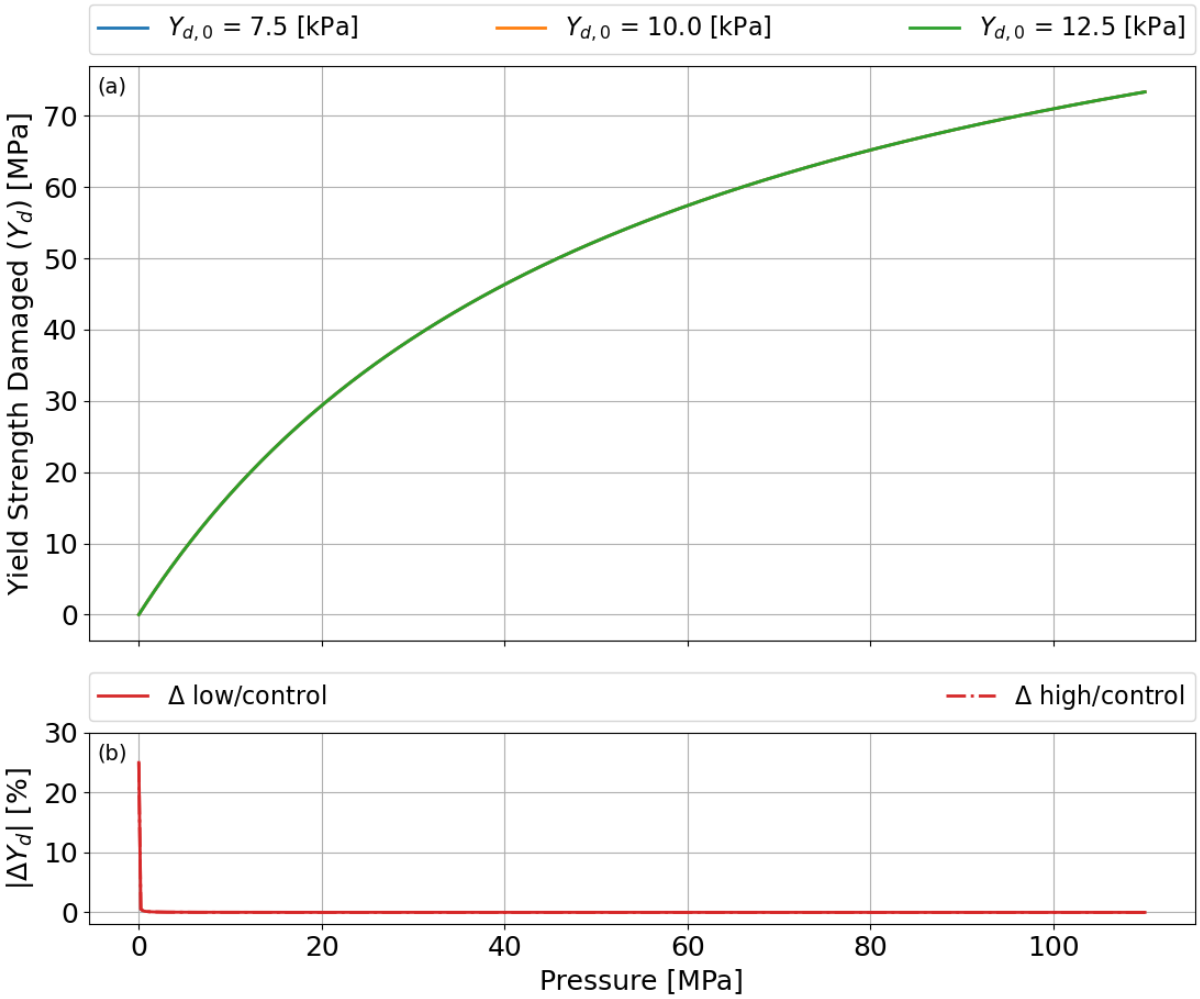

Figure 6.10: Yield strength against pressure, plotted for different values of cohesion for damaged material at zero pressure. The curves are very close, if not on top of each other, and are therefore hard to distinguish (a). In addition, underneath is shown a plot of the differences between the curves in percentages, and it shows here practically no differences between the curves either, or at least the differences are near zero (b).

From Figure 6.10, it can be seen that the three curves are nearly identical, which is proven by the subplot underneath which shows the differences between the curves and the control curve. Apart from the anomaly at zero pressure, the differences with the control are near zero for both lower and higher values of $Y_{d,0}$. Hence, they have an insignificant effect on the overall yield strength of the material, and, consequently, on the cratering process.

Friction Coefficient of Damaged Material

For the coefficient of internal friction of damaged material, the value was moderately changed by $\pm$25%. A lower value of FRICDAM is expected to decrease the yield strength based on Equation 6.6. So, for a lower value of FRICDAM it is predicted that the crater will be larger in diameter and depth, with more damage or a larger damaged area, and vice versa for higher FRICDAM values. The simulation results are shown in Figure 6.11.

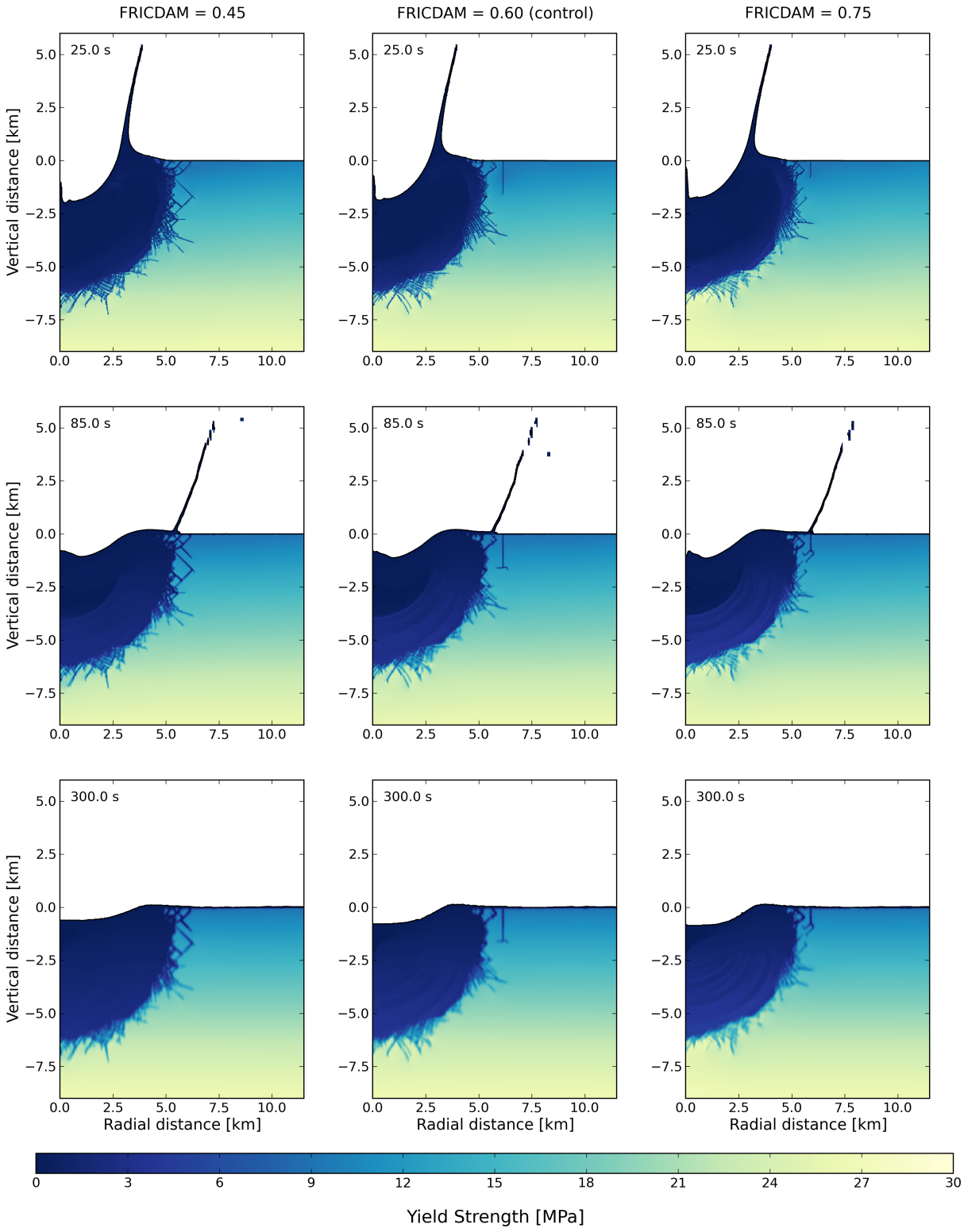

Figure 6.11: Sensitivity simulation results of the coefficient of internal friction of damaged material. In the left column results are shown using a lower coefficient, in the middle is given the control simulation, and to the right the results using a higher coefficient.

This time, some noticeable differences can be observed in Figure 6.11. As expected, the area of damage is smaller for a higher FRICDAM. Additionally, the crater shape is noticeably different: in the simulation using a FRICDAM value of 0.45, the crater is more shallow, but larger in diameter, while in the simulation with a higher FRICDAM value, the crater is deeper and the diameter is smaller. This is only partially in line with predictions set earlier, as the depth differs from expectations. This discrepancy might be the result from material rebound on the crater floor. With a lower yield strength, the rebound may be greater, due to a decreased resistance to

bounce back.

Limiting Yield Strength of Damaged Material

Finally, the limiting strength of damaged material at high pressures, YLIMDAM, was varied. These changes are similar to those made for YLIMINT, since they share the same values in the control simulation. As their effects will be similar as well, based on Equation 6.6, the expectations for YLIMDAM are identical to those set for YLIMINT.

The results show, similar to YLIMINT, no visible differences between the simulation plots, which can be viewed in Figure A.5 in Appendix A. Similar reasoning can be used to explain these results, as used for the YLIMINT parameter.

To conclude, aside from the FRICDAM parameter, the damaged parameters do not substantially influence the simulation. The FRICDAM showed a relatively large difference in crater depth, which should not be overlooked.

6.3.3. Damage Models

The main parameters in the damage models are the invariant measure of the accumulated plastic strain (ϵ_p), and the plastic strain at failure (ϵ_f). The former is a variable that changes during the simulation and is always positive, while the latter can be calculated by an equation. For the IVANOV damage model, damage is determined through Equation 6.7 [71].

$$D = \min\left(\frac{\epsilon_p}{\epsilon_f}, 1\right) \tag{6.7}$$

Here, ϵ_f is an increasing function of pressure, defined by Equation 6.8, where ϵ_{fb} is a minimum failure strain for low pressure states, p_c is a pressure above which failure is assumed compressional and B is a positive constant. This simple function allows for rapid brittle failure in tensile and low-pressure modes and semi-brittle failure at higher pressures [71].

$$\epsilon_f = \max(\epsilon_{fb}, B(p - p_c)) \tag{6.8}$$

In iSALE2D, there are three parameter values that need to be defined when using the IVANOV damage model: IVANOV_A, IVANOV_B, and IVANOV_C, which are represented by ϵ_{fb}, B, and p_c, respectively [71]. These three parameters are varied to see their effect on the cratering process and the damaged sustained by the target.

IVANOV_A Parameter

First, IVANOV_A is changed from the value used in the control simulation by $\pm$25%. Expectations are that a smaller value of IVANOV_A will result in more damage in the target material, thus yielding a larger crater. This makes sense when thinking about what lowering the value for the minimum failure strain for low pressure states means. If this value decreases, it means that the failure strain for low pressure states is reached for even lower stress values. This should result in more damage and consequently a larger crater. This is confirmed by looking at Equation 6.8, where a lower value of ϵ_{fb} results in a lower value of ϵ_f, which in turn results in a larger value for the damage in Equation 6.7.

Upon examining the simulation results, it became clear that the differences between the plots were practically negligible, as shown in Figure A.5 in Appendix A. To investigate the reason for this, ϵ_f is plotted against the pressure for varying values of IVANOV_A, as shown in Figure 6.12.

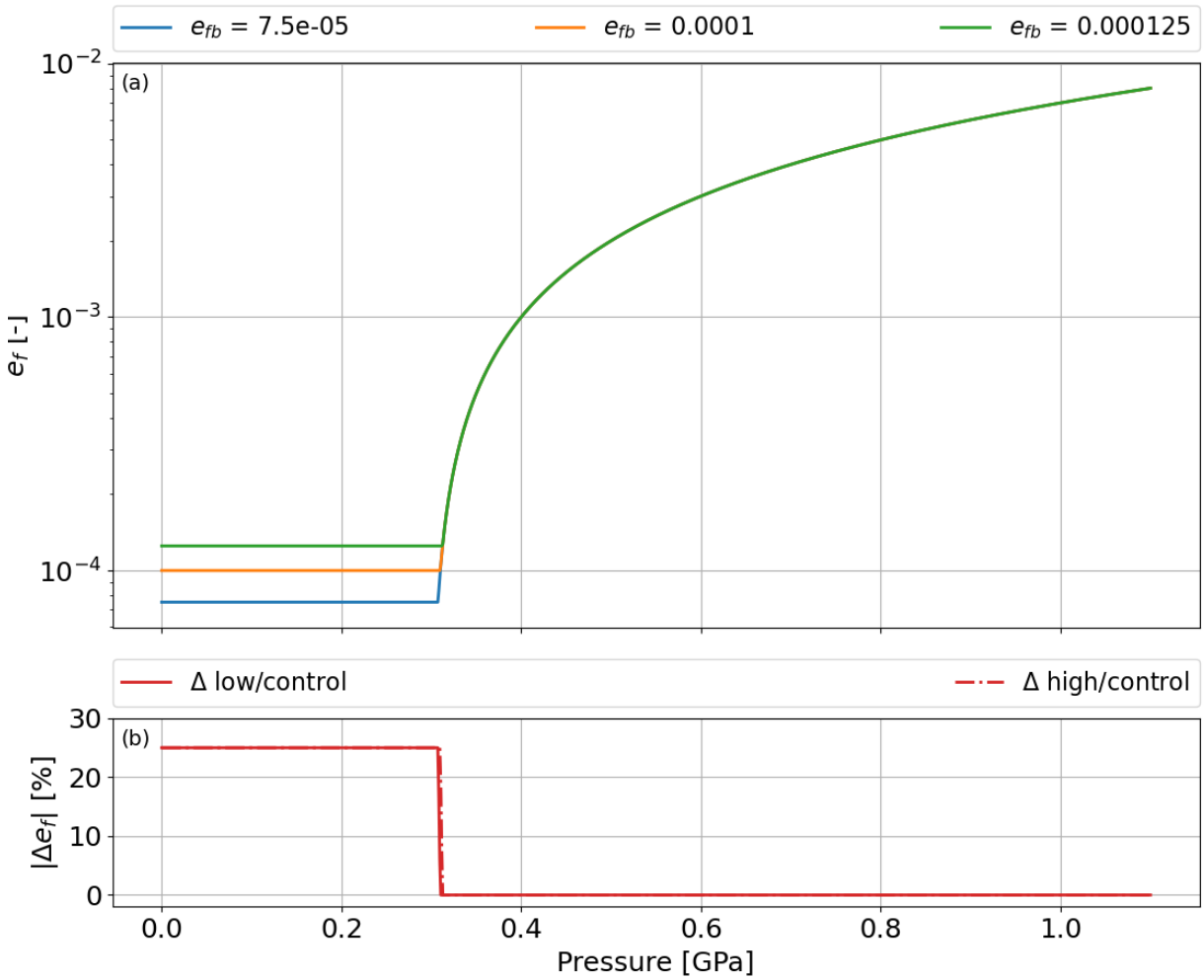

Figure 6.12: Plot of the ε_f (e_f) parameter against pressure for different values of ε_{fb} (e_{fb}) or IVANOV_A (a). In addition, a plot with the differences between the curves is given underneath (b).

In Figure 6.12, it can be seen that the changes in IVANOV_A results in very little difference in ϵ_f. Only for lower pressure values there is a clear distinction between the curves, with the values differing by an amount equal to the initial change of $\pm$25% compared to the control simulation, which can be seen in the subplot. These changes appear insufficient to produce enough of a noticeable difference in the cratering process.

IVANOV_B Parameter

Secondly, the IVANOV_B parameter is changed by $\pm$25%. Referring back to Equation 6.7 and Equation 6.8, and using a similar reasoning as used for IVANOV_A, it can be expected that a lower value of IVANOV_B results in a lower value for ϵ_f, and thus more damage and a larger crater.

Upon plotting the results, however, it was noticed that the differences between the plots were minimal, which can be found in Figure A.5 in Appendix A. To investigate the reason for this, ϵ_f was again plotted against the pressure, shown in Figure 6.13.

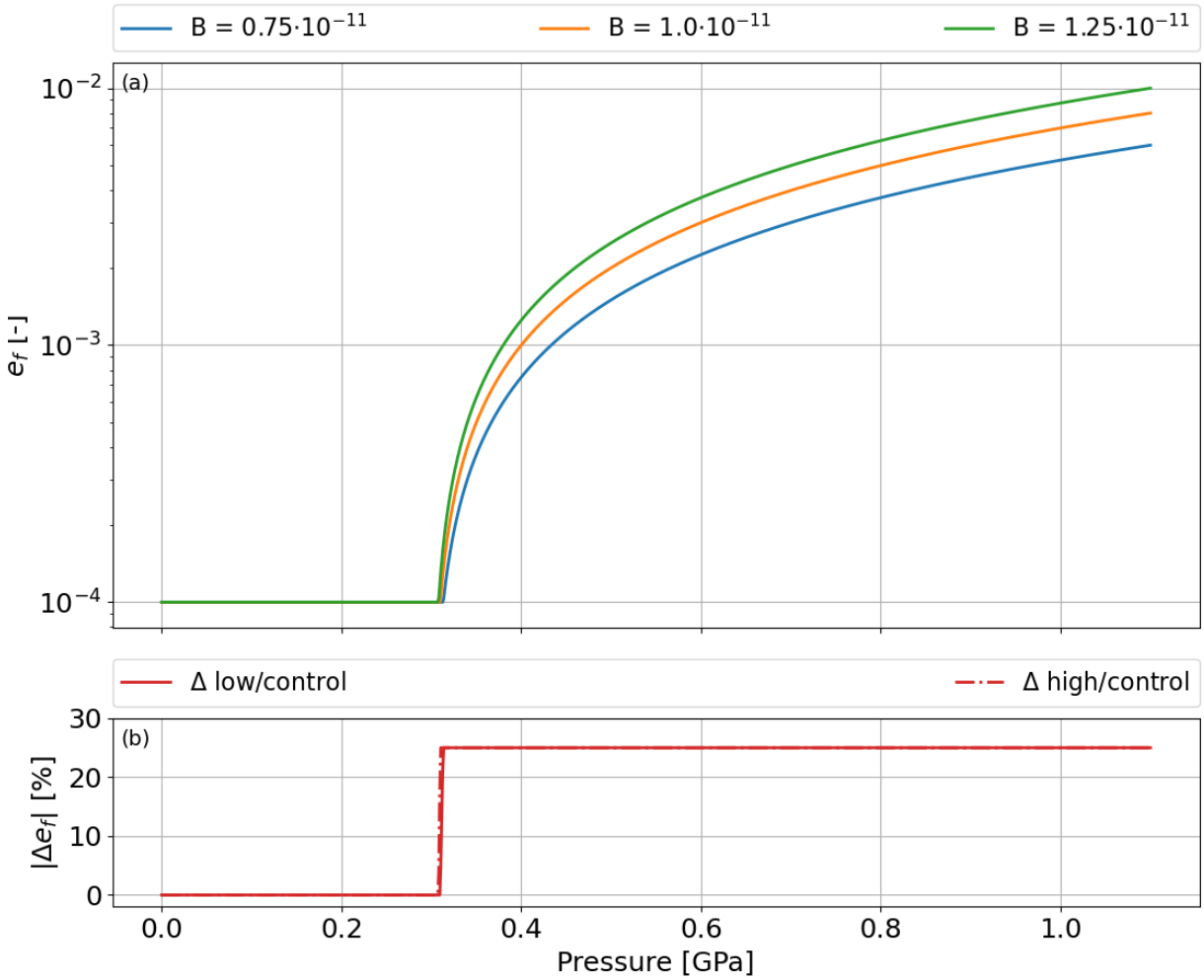

Figure 6.13: Plot of the ε_f (e_f) parameter against pressure for different values of B or IVANOV_B (a). In addition, a plot with the differences between the curves is given underneath (b).

From Figure 6.13, it can be seen that the curves are virtually identical until a pressure of approximately 0.32×10^8 Pa. Beyond this point, the differences become noticeable, however, the difference is constant and is equal to only $\pm$25% compared to the values of the control curve. In addition, the pressures at which this difference occurs is only at the contact and compression stage. In this extremely short period of time, there is not enough of an effect of this parameter on the cratering process to make a noticeable difference. Since the pressure in the target remains relatively low after this stage, the parameter appears to have no further major influence.

IVANOV_C Parameter

Finally, the IVANOV_C parameter is discussed. Based on Equation 6.8 and Equation 6.7, it can be determined that a smaller value of IVANOV_C will result in a larger value of ϵ_f, and thus less damage; a higher IVANOV_C value would have the opposite effect. The other two simulations will once again differ from the control simulation by $\pm$25%.

The resulting plots, however, show that changing the IVANOV_C parameter by 25% has virtually no effect on the damage and crater, which can be seen in Figure A.5 in Appendix A. The ϵ_f is then plotted against pressure again to find a possible explanation, which can be seen in Figure 6.14.

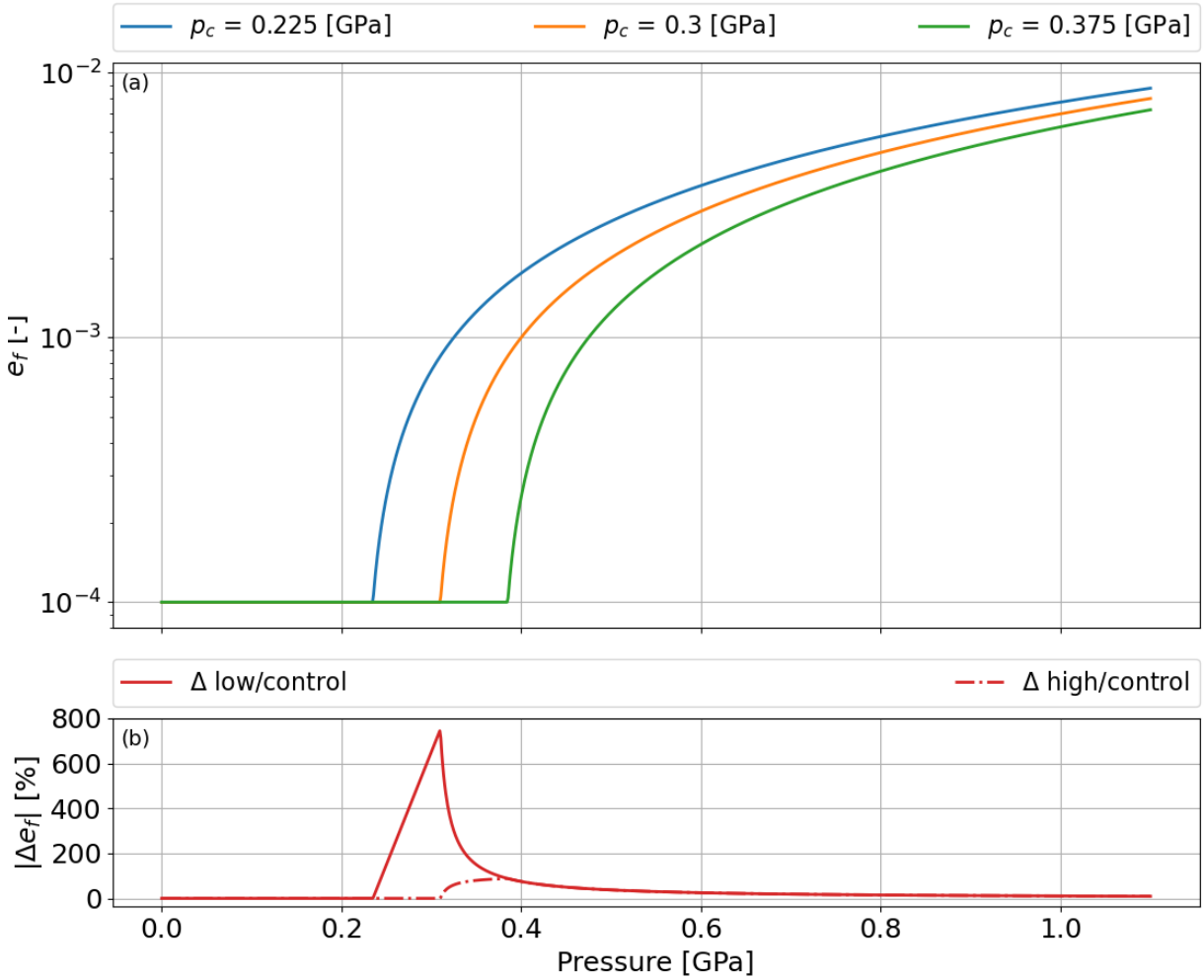

Figure 6.14: Plot of the ε_f (e_f) parameter against pressure for different values of p_c or IVANOV_C (a). In addition, a plot with the differences between the curves is given underneath (b).

It can be observed that there is practically no difference until 0.25×10^9 Pa, which is also shown in Figure 6.14b. After that, there is quite a large difference between the lower and control curve, until a pressure of 0.32×10^8 Pa. However, as mentioned before, a reason why this does not translate to noticeable changes in the cratering process, could be due to the fact that these high pressures are only reached for a very small amount of time, which is not enough to invoke apparent changes in the crater or target.

6.3.4. Thermal Softening Model

The thermal softening model approximates the shear strength of the material, which depends on temperature, using a simple relationship given by Equation 6.9.

$$Y = Y_c \tanh\left(\xi\left(\frac{T_m}{T} - 1\right)\right) \tag{6.9}$$

Where Y_c is the cold yield strength, ξ is a constant in thermal softening law, which is a material constant, T_m is the melting temperature of the material and T is the current temperature of the material.

The only input parameter for the thermal softening model is the thermal softening parameter, ξ, from Equation 6.9. This parameter is varied slightly to observe its effect on the cratering process, with the control value of 1.2 modified by ± 0.2. Expected is that an increase in the thermal softening parameter will result in a smaller crater with less damage. The reason is based on Equation 6.9, where an increase in ξ results in a higher value for the yield strength, making the material more resistant to deformation.

From the simulation results, minor differences between the plots were observed, which can be found in Figure A.5 in Appendix A. As expected, noticeable is the yield strength in the target that is higher for the

simulations with a higher ξ value. However, the effects on the crater size and damage are marginal. The size of the crater is slightly larger for the simulation utilizing a lower value of ξ, and vice versa for simulation with a higher ξ. In addition, the damage is also slightly larger for the simulations with a lower ξ. Nevertheless, these differences are in the order of a few percent, which is considered as negligible.

6.3.5. Acoustic Fluidization Model

Of the few available models for acoustic fluidization, the BLOCK model has been used on several occasions in previous research, and is utilized in this study. This model includes two main input parameters, γ_η and γ_β, where the former represents the strength of the vibrations during the impact, and the latter represents the duration of the vibrations.

As mentioned in Section 6.1, γ_η and γ_β were found to vary considerably across previous research, making it challenging to find suitable values. While values could be taken from research papers, such as Bjonnes et al. [1] and Silber and Johnson [2], using them directly without having a clear understanding of their influence would be unwise. Through private consultations with Professor Gareth Collins, and reviewing papers from Bray et al. [65], Silber et al. [86], Rae et al. [87] and Wünnemann and Ivanov [88], it became evident that there are no fixed values for γ_η and γ_β. However, Bray et al. [65] identified empirical relationships between γ_η, γ_β, and projectile diameter for Ganymede-like conditions, which were derived from simulations that closely matched observed crater shapes. If the projectile radius is known, these relations will then return the value for γ_η and γ_β that results in a final crater that resembles observations.

To link the projectile radius and the γ_η and γ_β parameters, Bray et al. [65] first determined the decay time ($\mathrm{T_{dec}}$) and limiting viscosity ($\mathrm{v_{lim}}$) for craters on Ganymede that are 4-25 km in diameter, by matching modeled crater depths, wall slopes, and widths of central peaks and pits to observations, and linked them to the projectile radius. The equations that followed are given by Equation 6.10 and Equation 6.11 [65].

$$\mathrm{T_{dec}} = 4.86 R_p^{0.46} \tag{6.10}$$

$$\mathrm{v_{lim}} = 55.48 R_p^{1.32} \tag{6.11}$$

Where $\mathrm{T_{dec}}$ is the duration of the vibrations, R_p is the radius of the projectile and $\mathrm{v_{lim}}$ is the strength and the vibrations.

To express γ_η and γ_β in terms of the projectile radius, additional relations that are able to link $\mathrm{T_{dec}}$, $\mathrm{v_{lim}}$, γ_η, and γ_β, are required. These relations were found in an article by Wünnemann and Ivanov [88], and are shown in Equation 6.12 and Equation 6.13 [88].

$$\gamma_\beta = \frac{\mathrm{T_{dec}} c_b}{R_i} \tag{6.12}$$

$$\gamma_\eta = \frac{\mathrm{v_{lim}}}{R_i c_b} \tag{6.13}$$

Where R_i is again the radius of the impactor, c_b is the sound speed of the material, which is a constant, and equal to 500 m/s, in iSALE2D [71].

Combining Equation 6.10, Equation 6.11, Equation 6.12, and Equation 6.12, equations for γ_β and γ_η can be obtained as functions of projectile size. These equations are shown in Equation 6.14 and Equation 6.15, and will be used to calculate the γ_β and γ_η for the Ganymede simulations in the upcoming section.

$$\gamma_\eta = \frac{55.48 \mathrm{R_p^{1.32}}}{R_i c_b} \tag{6.14}$$

$$\gamma_\beta = \frac{4.86 \mathrm{R_p^{0.46}} c_b}{R_i} \tag{6.15}$$

Thus, Equation 6.14 and Equation 6.15 can be used to find the value of γ_η and γ_β, that will result in a final crater that matches observations closely. However, these equations apply only under the specific Ganymede conditions set by Bray et al. [65].

Since these findings were discovered in retrospect, the values of γ_η and γ_β used in the sensitivity simulations and the control simulation were taken from an example in iSALE2D, rather than calculated from Equation 6.14 and Equation 6.15. However, this does not significantly affect the results, as the purpose of the sensitivity analysis is to examine how changes in γ_η and γ_β influence the cratering process.

Compared to the value used in the control simulation, γ_η is changed here by factors of 10, resulting in values of 6.92×10^{-3} and 6.92×10^{-1}. Based on the definition of γ_η given in the iSALE2D manual, it is derived that lower values of γ_η increase vibration strength during the impact [71]. Therefore, it is expected that for lower values of γ_η, the crater will become shallower and wider, as a stronger shaking induces a tendency of the material to distribute itself across the surface, and move towards a horizontal equilibrium due to gravity. Conversely, higher values of γ_η should result in narrower and deeper craters. An analogy would be to imagine shaking a pile of dirt or sand on a flat surface; with stronger or prolonged shaking, the pile tends to fall apart and flatten due to gravity. The simulation results from varying γ_η can be seen in Figure 6.15.

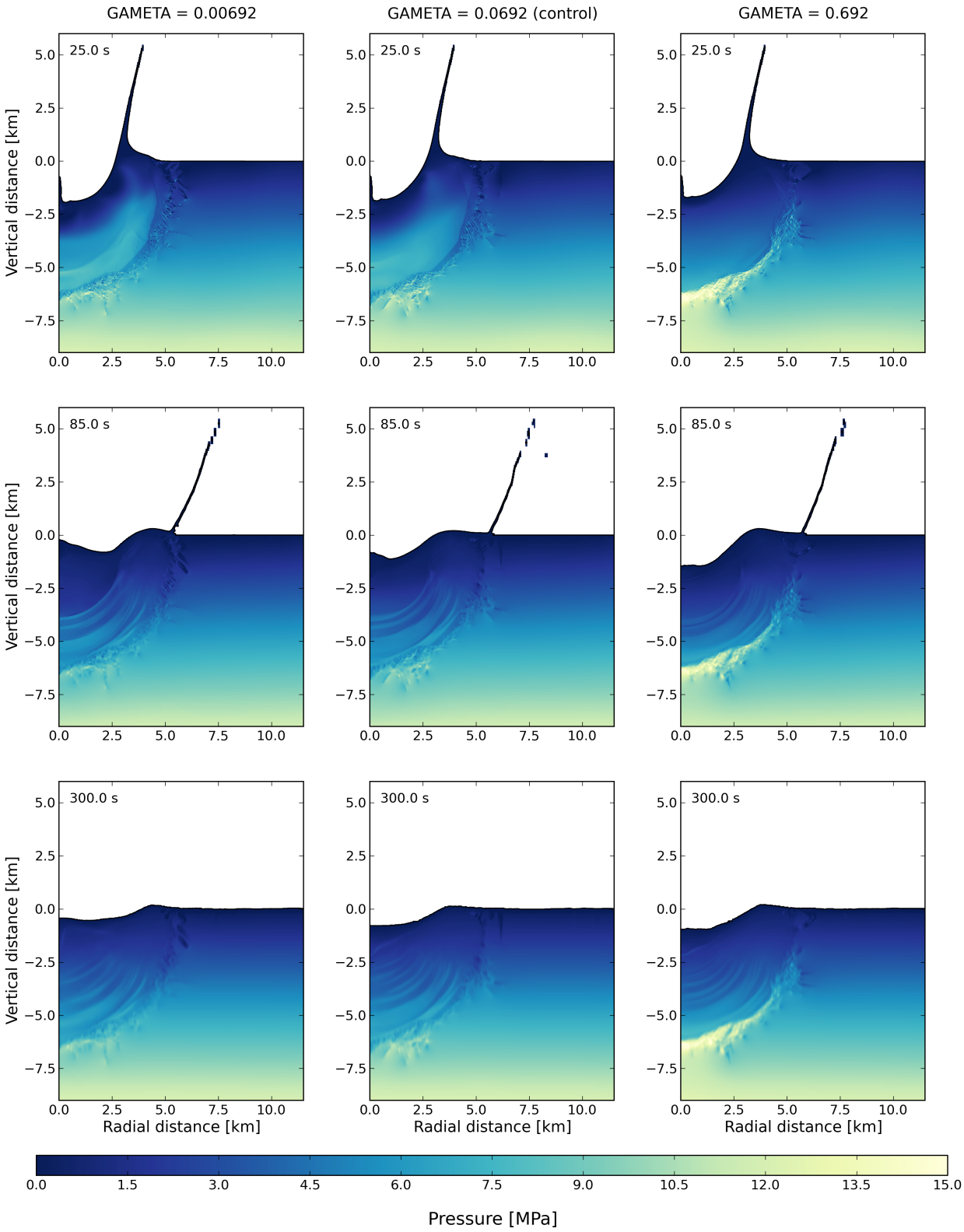

Figure 6.15: Sensitivity simulation results of varying the γ_η parameter. Quite a large difference can be seen between the three different simulations. Especially the crater depth varies notably. The damage in the target appears equal in range across simulations, which is indicated by the transition of 'distorted' material to smooth at around a depth of 7 km. However, it does appear that material is shocked to higher pressures for the simulation using a large value of γ_η.

Figure 6.15 shows that for lower values of γ_η, the crater becomes shallower and slightly wider compared to higher values, which is in accordance with the expectations mentioned earlier. Additionally, the damage region is slightly larger for lower values of γ_η. This is logical, as lower values of γ_η induce stronger shaking upon impact, which would naturally result in more damage in the target.

For γ_β, values were changed to 0.1×10^3 and 5.1×10^3. According to the iSALE2D manual, γ_β is defined as the duration of the vibrations. Hence, it is expected that higher values of γ_β will result in a shallower and wider crater, due to the increased duration of the vibrations. Conversely, lower values of γ_β should result in deeper and narrower craters. The simulation results can be seen in Figure 6.16.

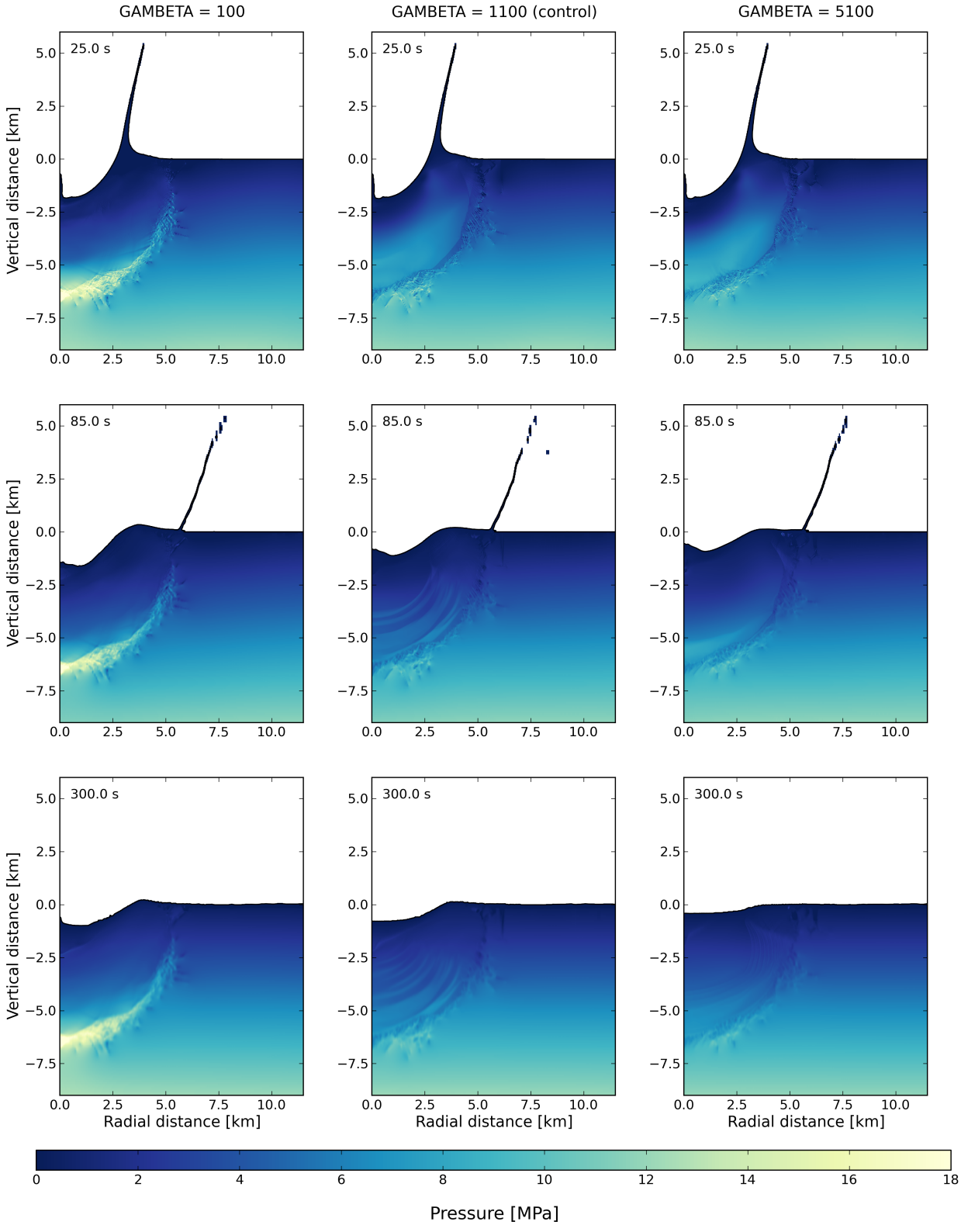

Figure 6.16: Sensitivity simulation results of varying the γ_β parameter. A considerable difference can be observed from the plots. The main distinction is the crater depth, similar to γ_η. Also similar to γ_η, is that for γ_β, the damage in the target seems to reach approximately the same depth for all three simulations, but for a lower value of γ_β, the material at the edge of the damaged region is shocked to higher pressures.

It can be noticed from Figure 6.16, that the results differ significantly from the control simulation. For larger values of γ_β, the craters become more shallow, and conversely with smaller values the crater becomes deeper, which matches expectations set previously. However, the diameter stays approximately equal across all simulations. Generally, an increase in γ_β appears to have an opposite effect to an increase in γ_η. This is in line with the hypothesis that a longer vibration duration, due to an increase in γ_β, results in similar effects to stronger vibrations, due to a decrease of γ_η. The damage regions remain relatively comparable in size, though less compressed material is present for higher values of γ_β. This can be explained by the fact that the simulations with a higher γ_β value experience a longer vibration duration, which over time relieves the compressed material of the high pressures.

6.4. Quantifying Sensitivity

Several methods can be utilized to quantify the sensitivity of parameters. Some of these methods will briefly be covered in Subsection 6.4.1, including the ones that will be used throughout this section. Then Subsection 6.4.2 focuses on the theory and equations to calculate the required quantities. Finally, in Subsection 6.4.3 the equations are applied to the simulation results from Section 6.2 and Section 6.3, and the sensitivity of the parameters will be determined.

6.4.1. Sensitivity Analysis Methods

There are numerous methods available to assess the sensitivity of parameters. One example is Sobol' indices. Here, all parameters are varied simultaneously across their full range. After obtaining the results, two parameters can be calculated, the first-order and total-order sensitivity indices, where the former measures direct effects, and the latter includes effects of interactions. Essentially, it can provide information on how much each individual parameter influences the output variance, and how much through of the influence is caused due to a combination of parameters. This is a solid method, as it works across large parameter ranges, and identifies both direct and interaction effects. However, a downside is that it requires hundreds to thousands of simulations, making it computationally extremely intensive, as well as time consuming [89].

An alternative is Morris' method. Here, parameters are varied one at a time over a grid of random base points. The change in output for a change in input is then measured. Then, a statistical distribution is made of the effects, where the mean value is linked to the overall influence (or global trend), and the standard deviation to non-linearity or interactions. This method captures global sensitivity with less simulations than Sobol (10-20x less), and it can also handle large variations in parameters [90].

These two methods provide quantitative measures of each parameter's contribution to the overall output variance, including nonlinear interactions. However, they require a large number of model evaluations, which was not computationally feasible for this study and given the time constraints. Therefore, simpler sensitivity analysis methods were investigated.

First, is the normalized sensitivity. This method basically assesses the relative change in output per relative change in input, providing a local value for the sensitivity. This makes it more useful for points close to the control value. Nevertheless, it is a simple method that can provide a practical, dimensionless measure of proportional influence [91].

To account for any possible non-linear or asymmetric behavior, the normalized sensitivity can be complemented by the sensitivity index (SI) method, which expresses the total output span across the tested range. Contrary to the normalized sensitivity, the sensitivity index is a global measure of sensitivity. Additionally, the measure of non-linearity can further be measured through the asymmetry index (A) [91].

These three methods together will be used to quantify the sensitivity. However, it must be stated that because of these simpler methods, the purpose of this sensitivity analysis is to evaluate the relative influence of input parameters on the output (crater diameter and crater depth), rather than to perform a full probabilistic or variance-based sensitivity analysis. Full more full-fledged sensitivity analysis, the Sobol' indices or Morris method is advised.

6.4.2. Theory for Quantifying Sensitivity

The sensitivity analysis performed in this section follows the one-at-a-time (OAT) method. As the name suggests, parameters are varied one-by-one by a certain value with respect to the control or baseline, in both the positive and negative direction. To quantify the sensitivity of these parameters, three complementary measures are utilized which have been mentioned in Subsection 6.4.1.

The first method is the normalized sensitivity coefficient, which can be calculated according to Equation 6.16 [91].

$$S = \frac{\Delta y/y}{\Delta x/x} \qquad \Delta y/y = \frac{y_{parameter} - y_{control}}{y_{control}} \qquad \Delta x/x = \frac{x_{parameter} - x_{control}}{x_{control}} \tag{6.16}$$

Where x is the tested parameter, ΔX is the fractional different of the change in the tested parameter with respect to the control, y is the parameter that is used to check sensitivity (crater diameter or crater depth), and Δy is the difference in the result with respect to the control.

However, the results of the simulations that have been performed contain uncertainties, which should be taken into account. Equation 6.16 alone cannot be used for this, thus additional equations and changes to Equation 6.16 are required. Equation 6.17 shows the altered equations that will be used to account for the uncertainties in the results.

$$\begin{aligned}
S^-_{min} &= \frac{\frac{\left(y^-_{low} - y_{0,high}\right)}{y_{0,high}}}{\Delta x^-} & S^-_{max} &= \frac{\frac{\left(y^-_{high} - y_{0,low}\right)}{y_{0,low}}}{\Delta x^-} \\
S^+_{min} &= \frac{\frac{\left(y^+_{low} - y_{0,high}\right)}{y_{0,high}}}{\Delta x^+} & S^+_{max} &= \frac{\frac{\left(y^+_{high} - y_{0,low}\right)}{y_{0,low}}}{\Delta x^+} \\
\Delta x^+ &= \frac{x_+ - x_0}{x_0} & \Delta x^- &= \frac{x_- - x_0}{x_0} \\
S_{mean,min} &= \frac{S^-_{min}\Delta x^- + S^+_{min}\Delta x^+}{\Delta x^+ + \Delta x^-} & S_{mean,max} &= \frac{S^-_{max}\Delta x^{-]} + S^+_{max}\Delta x^+}{\Delta x^+ + \Delta x^-} \\
S_{mean} &= \frac{1}{2}\left(S_{mean,min} + S_{mean,max}\right) & \Delta S_{mean} &= \frac{1}{2}\left|S_{mean,max} - S_{mean,min}\right| \\
|S_{mean}| &= \frac{1}{2}\left|S_{mean,min} + S_{mean,max}\right| & |\Delta S_{mean}| &= \frac{1}{2}\left|S_{mean,max} - S_{mean,min}\right|
\end{aligned} \tag{6.17}$$

Where the superscript $+$ is equal to the value corresponding to the point with respect to the control in the positive direction, and $-$ in the negative direction. For example, if a parameter changes by $\pm$ 20%, then the results for the point that changed by +20% corresponds to $+$, and -20$ corresponds to $-$. The subscripts ”low” and ”high” represent the lower and upper bound of the uncertainties or error bar values, respectively. The subscript ”0” corresponds to the values from the control.

Essentially, Equation 6.16 is adjusted and calculated for ”worst-case” scenarios based on the uncertainties provided, which are represented by $S^{\pm}_{min}$ and $S^{\pm}_{max}$. Then, the mean is taken for the minimum and maximum values, after which the mean of those two values to obtain the final value for the normalized sensitivity. Then, the magnitude of this value can be calculated, which is useful for determining which parameter exhibits the largest value of S_{mean}.

Then, the numerical values of S_{mean} are linked to the sensitivity as follows.

- S_{mean} < 0 - Parameter is sensitive in negative direction with respect to the control.
- S_{mean} > 0 - Parameter is sensitive in positive direction, with respect to the control.
- $|S_{mean}|$ < 0.1 - Negligible sensitivity.
- 0.1 $\leq |S_{mean}|$ < 0.5 - Weak sensitivity.
- 0.5 $\leq |S_{mean}|$ < 1.0 - Moderate sensitivity.
- $|S_{mean}| \geq$ 1.0 - Strong sensitivity.

The second measure is the calculation of the sensitivity index (SI). This quantifies the total relative variation across the range of the tested parameter values. Basically, it provides a global measure of the sensitivity. When accounting for the uncertainties, it can be computed according to Equation 6.18 [91]. Essentially, it takes the minimum and maximum difference in y-values, including the uncertainties, and normalizes it to the control value.

$$\begin{aligned} SI_{min} &= \frac{\left|y^{+}_{low} - y^{-}_{high}\right|}{y_{0,high}} & SI_{max} &= \frac{\left|y^{+}_{low} - y^{-}_{high}\right|}{y_{0,high}} \\ SI_{mean} &= \frac{1}{2}\left(SI_{min} + SI_{max}\right) & \Delta SI_{mean} &= \frac{1}{2}\left|SI_{max} - SI_{min}\right| \end{aligned} \tag{6.18}$$

Again, y is the result used to test sensitivity (crater diameter or crater depth). The superscripts ”+” and ”−” indicate the positively and negatively perturbed points with respect to the control, respectively. The subscripts ”low” and ”high” are used to indicate the lower and upper bounds of the uncertainty. The sensitivity is quantified here as follows.

- SI_{mean} < 0.05 - Output hardly changes. The parameter is practically insensitive.
- SI_{mean} 0.05-0.2 - Parameter is weakly sensitive.
- SI_{mean} 0.2-0.5 - Moderately sensitive.
- $SI_{mean} \gtrsim$ 0.5 - Output is strongly sensitive.

However, note that there is no dependence on the amount by which the parameter is changed, meaning that the result provides information for the entire range for which the simulations were performed.

SI can also be normalized to provide information related to the change in input parameter. This can be done according to Equation 6.19.

$$\begin{aligned} \Delta x &= \frac{|x^{+} - x^{-}|}{x_0} \\ SI^{*}_{min} &= \frac{SI_{min}}{\Delta x} & SI^{*}_{max} &= \frac{SI_{max}}{\Delta x} \\ SI^{*}_{mean} &= \frac{1}{2}\left(SI^{*}_{min} + SI^{*}_{max}\right) & \Delta SI^{*}_{mean} &= \frac{1}{2}\left|SI^{*}_{max} + SI^{*}_{min}\right| \end{aligned} \tag{6.19}$$

The sensitivity of SI^{*} is quantified here as follows.

- $SI^{*}_{mean} \sim 0$ - Parameter is insensitive.
- SI^{*}_{mean} < 1 - Weak sensitivity.
- $SI^{*}_{mean} \sim 1$ - Proportional sensitivity.
- SI^{*}_{mean} > 1 - Strong sensitivity.

Finally, a measure for the asymmetry index (A) is introduced, which is used to evaluate the linearity, and which direction induces a stronger response. This is done by comparing the sensitivities of the tested parameter. When including uncertainties, Equation 6.20 is used to compute the mean value of the asymmetry [91].

$$\begin{aligned} A_{min} &= \frac{S^{+}_{min} - S^{-}_{max}}{S^{+}_{min} + S^{-}_{max}} & A_{max} &= \frac{S^{+}_{max} - S^{-}_{min}}{S^{+}_{max} + S^{-}_{min}} \\ A_{mean} &= \frac{1}{2}(A_{min} + A_{max}) & \Delta A_{mean} &= \frac{1}{2}|A_{max} - A_{min}| \end{aligned} \tag{6.20}$$

The values of A_{mean} can be used to reach the following conclusions.

- $A_{mean} \sim 0$ - Symmetric (linear) response, there is an equal effect in both directions from the control.
- A_{mean} > 0 - Response is more sensitive in the positive direction. Essentially, increasing the parameter compared to the control value, causes a stronger change in output than decreasing it.
- A_{mean} < 0 - Response is more sensitive in the negative direction. Decreasing a parameter with respect to the control will cause a stronger change in output than increasing it.
- $|A_{mean}|$ < 0.1 - (Near) perfect symmetry.

- $0.1 \leq |A_{mean}| < 0.3$ - Slight asymmetry and non-linear behavior.
- $0.3 \leq |A_{mean}| < 0.6$ - Moderate asymmetry and non-linearity.
- $|A_{mean}| \geq 0.6$ - Strong asymmetry and clear nonlinear or one-sided behavior.
- $|A_{mean}| \longrightarrow 1$ - Extreme asymmetry, one direction dominates completely.

These three methods together characterize not only the magnitude but also the directionality and non-linearity of the parameter sensitivities.

However, there are a few parameters, or rather models, that were changed in Section 6.2 where the aforementioned equations do not work. This is for the impactor material and thermal profiles. Since full model changes were performed here, and not a numerical difference, a different method needs to be used to determine sensitivity.

The normalized sensitivity (Equation 6.16) can still be used here, but the value of Δx has to be set to 1, as there is no numerical difference with the control. Note that the equation then becomes similar to Equation 6.18. Basically, in order to assess the sensitivity of changing the models, only the fractional difference between the adjusted model and the control can be determined in this scenario. Since uncertainties are present, a minimum and maximum sensitivity value can be calculated. The mean of this value will then be used to quantify the sensitivity. The equations are given by Equation 6.21 [91].

$$\begin{aligned} S_{min,mod} &= \frac{\left(y_{i,low} - y_{0,high}\right)}{y_{0,high}} & S_{max,mod} &= \frac{\left(y_{i,high} - y_{0,low}\right)}{y_{0,low}} \\ S_{mean,mod} &= 0.5 \cdot \left(S_{min,mod} + S_{max,mod}\right) & \Delta S_{mean,mod} &= 0.5 \cdot \left|S_{max,mod} - S_{min,mod}\right| \end{aligned} \tag{6.21}$$

Where y_i represents the results of the changed models, the subscripts ”low” and ”high” represent the lower and upper bounds of the uncertainties, and the subscript ”mod” represents ”"model”, which is used here to distinguish from the aforementioned S_{mean} value. Note that the asymmetry is also not computed here, as there are only individual changes with respect to the control.

Values for $S_{mean,mod}$ are then linked to the sensitivity as follows.

- $S_{mean,mod} \approx 0$ - No sensitivity.
- $S_{mean,mod} < 0.1$ - Weak sensitivity.
- $0.1 \leq S_{mean,mod} < 0.5$ - Moderate sensitivity.
- $0.5 \leq S_{mean,mod} < 1.0$ - Strong sensitivity.
- $S_{mean,mod} \geq 1.0$ - Very strong sensitivity.

6.4.3. Application of Theory to Sensitivity Simulation Results

The theory and equations from Subsection 6.4.2 can be applied to the data obtained from the simulations in Section 6.2 and Section 6.3 to quantify the sensitivity. However, this has to be done for both the crater diameter and crater depth. Thus, results are split in two parts. For the crater diameter, the sensitivity analysis results are given by a plot in Figure 6.17. Similarly, for the crater depth, a plot is given by Figure 6.18.

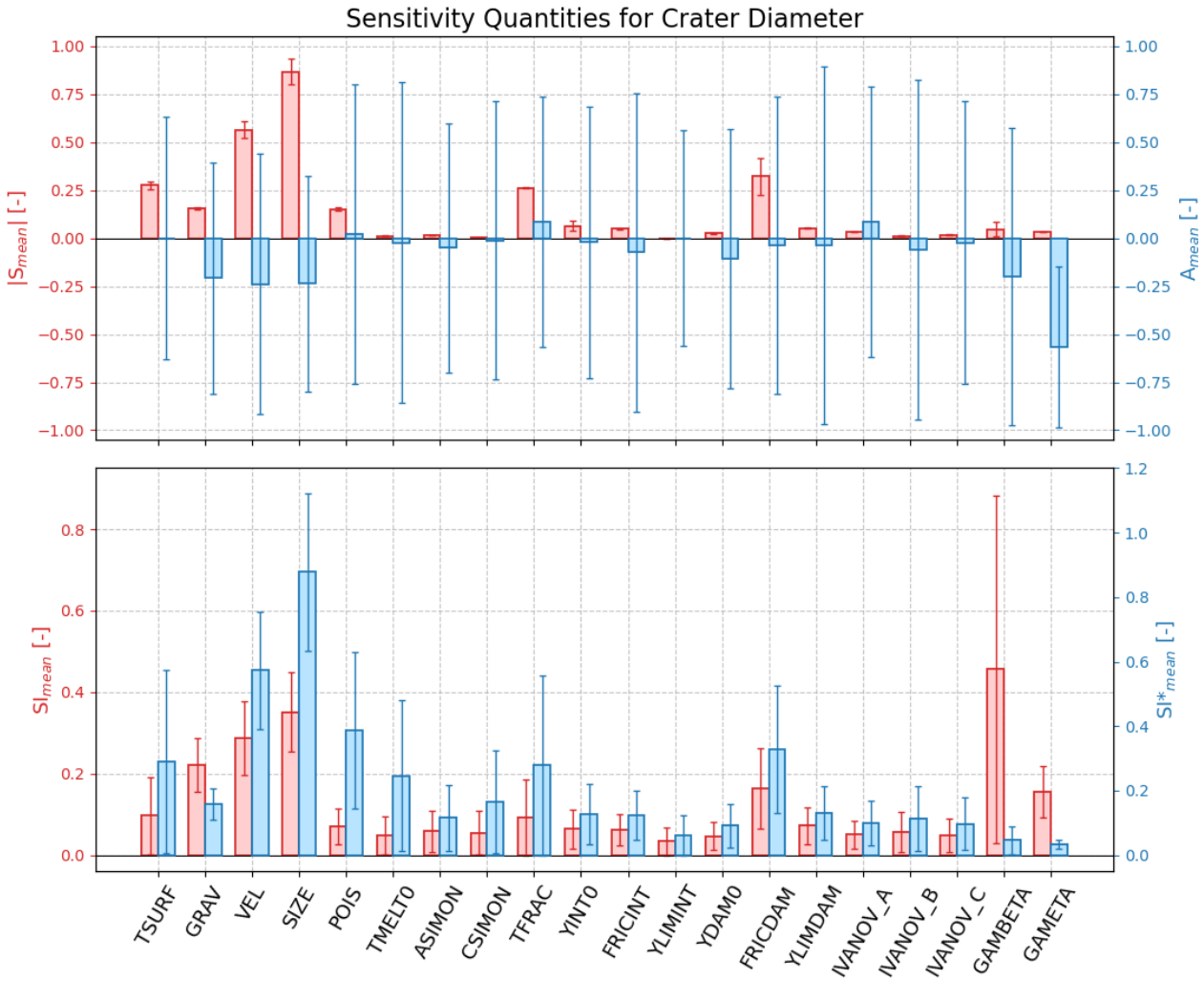

(a) Sensitivity quantities are plotted for the parameters with numerical differences compared to the control. The plots show the sensitivity of the changed parameter to the crater diameter specifically. The top plot shows the magnitude of the mean normalized sensitivity and the asymmetry. The lower plot displays the global sensitivity index and a normalized version.

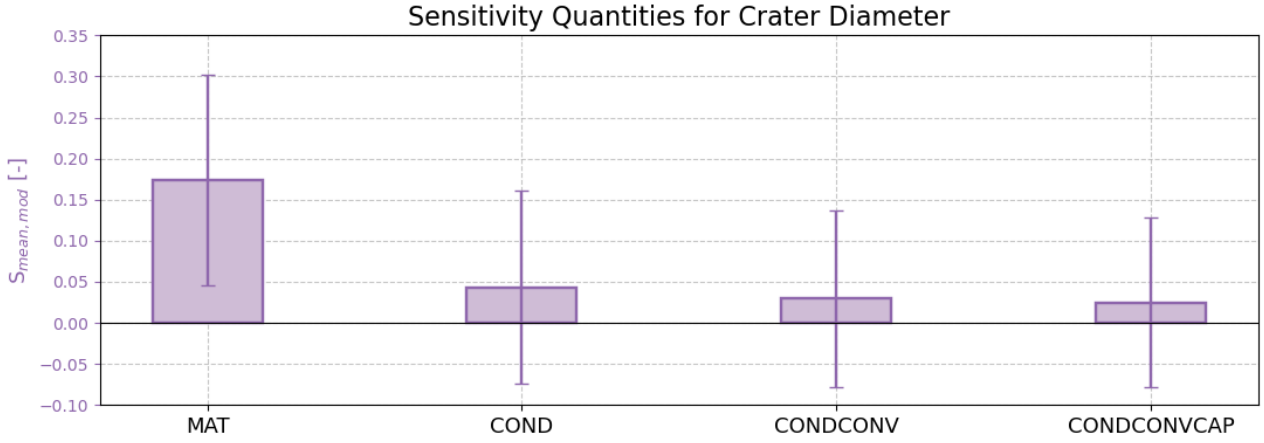

(b) Sensitivity quantities are plotted for the parameters where the change is related to a change in model. The plot shows the mean sensitivity, and its magnitude, of the changed model to the crater diameter specifically.

Figure 6.17: Quantitative results of the sensitivity analysis, measuring the change in parameter for the resulting crater diameter.

From Figure 6.17, a lot of information can be gathered. Firstly, it confirms the insensitivity of most of the strength and damage parameters, which is indicated by the low values of $|S_{mean}|$, SI_{mean} and SI^*_{mean}. As was already noted in Section 6.3, only the FRICDAM parameter showed a distinct difference in crater shape, and this is reflected here by a clear increase in $|S_{mean}|$, SI_{mean}, and SI^*_{mean} with respect to the other strength and

damage parameters. It shows a weak sensitivity to crater diameter. Noticeable, are the huge uncertainties for many parameters in A_{mean}. Although, this can be explained by the fact that only slight changes in crater diameter could be observed for many of these parameters, and the uncertainties in crater diameter exceed these differences. As a result, the direction of asymmetry cannot be resolved, leading to large uncertainties. Only for the GAMETA parameter can a clear negative asymmetry be resolved. As for the parameters that exhibit notable signs of sensitivity, TSURF, GRAV, VEL, SIZE, TFRAC, and FRICDAM show relatively high values. However, besides VEL and SIZE, these parameters exhibit mainly a weak to moderate sensitivity. As for VEL and SIZE, they show large values for $|S_{mean}|$, SI_{mean} and SI^*_{mean}, displaying a moderate to strong sensitivity. Looking at the results of the different models in Figure 6.17b, basically only the change in material is weak to moderately sensitivity to crater diameter, though this was observed in Section 6.2, where the different LAYTPROF models barely affected the crater diameter.

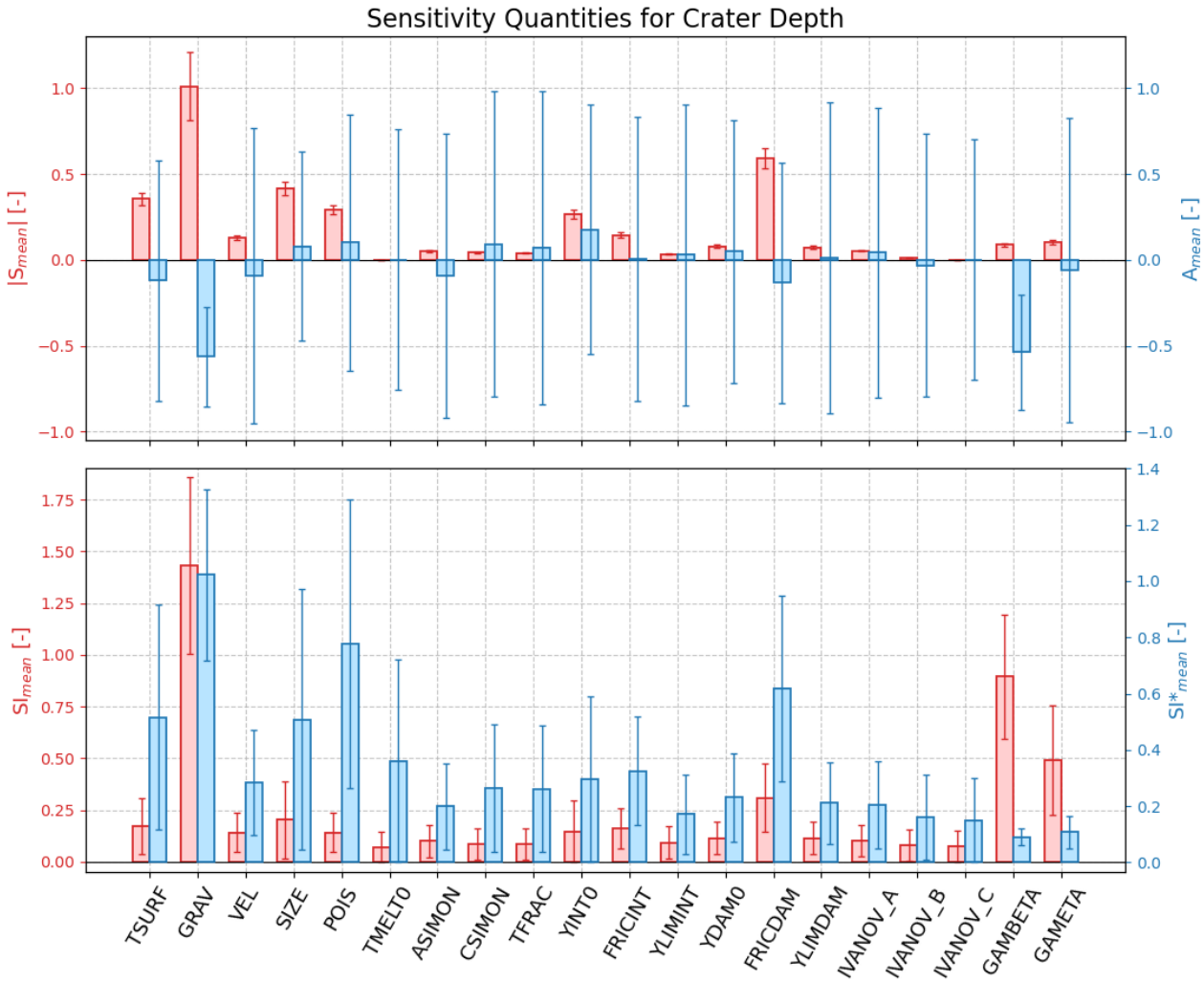

(a) Sensitivity quantities are plotted for the parameters with numerical differences compared to the control. The plots show the sensitivity of the changed parameter to the crater diameter specifically. The top plot shows the magnitude of the mean normalized sensitivity and the asymmetry. The lower plot displays the global sensitivity index and a normalized version.

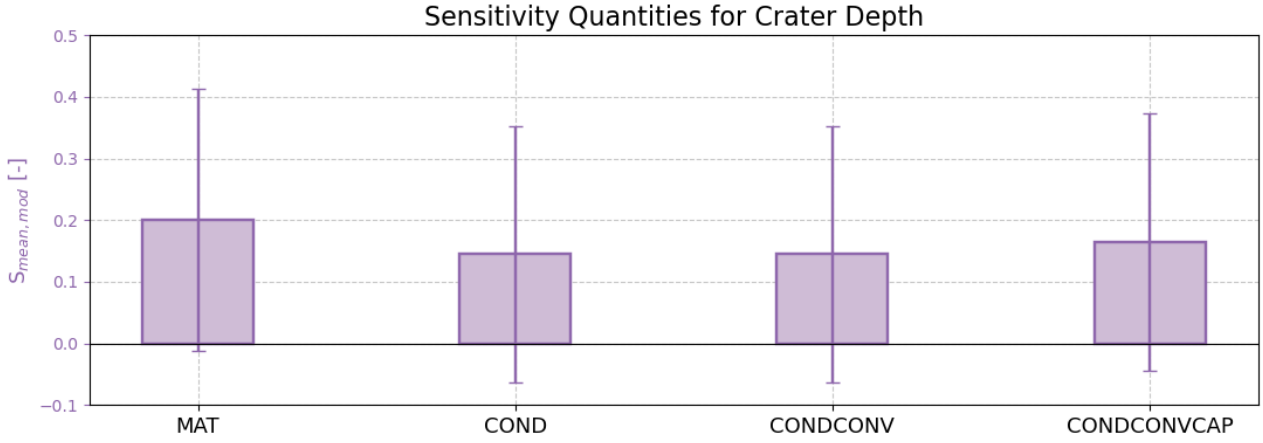

(b) Sensitivity quantities are plotted for the parameters where the change is related to a change in model. The plot shows the mean sensitivity, and its magnitude, of the changed model to the crater depth specifically.

Figure 6.18: Quantitative results of the sensitivity analysis, measuring the change in parameter for the resulting crater depth.

Noticeable from Figure 6.18 is that the majority of the parameters that displayed some sensitivity for the crater diameter, are also sensitive for the crater depth. Especially obvious is the GRAV parameter here, which already showed large deviations from the control simulation in Section 6.2, and exhibits here a high value for $|S_{mean}|$, SI_{mean}, and SI^*_{mean}, making it moderately to strongly sensitive. Also noticeable is the asymmetry,

which shows a stronger material response in crater depth for a decrease in gravity rather than an increase. Also apparent are the contributions of TSURF, SIZE, POIS and FRICDAM again, which show relative large values for $|S_{mean}|$ and SI^*_{mean}, making them weak to moderately sensitive. GAMBETA is an outlier as well, showing a clear asymmetry and a large value for SI_{mean}, meaning a large difference in outcome from the simulation results, with a stronger response for the lower values. As for the different models, they all show similar behavior. Even though $S_{mean,mod}$ shows a weak-to-moderate positive sensitivity, the uncertainty in these values are quite large, meaning that the response is not statistically significant. Essentially, they may be only weakly dependent on this parameter instead. Thus, they are treated as weakly sensitive to the crater depth.

6.5. Summary of the Sensitivity Analysis Results

In this section the findings from this chapter are summarized. Figure 6.19 is presented here to provide an overview of the results from Section 6.2 and Section 6.3, that is the crater diameter and crater depth as a function of the difference in input parameter with respect to the control. These plots will allow for easy comparison between the sensitivity simulation results, and the identification of outliers regarding crater diameter and crater depth. The reason for grouping the results was primarily to improve readability. The subplots are divided into impact parameters (Figure 6.19a), general thermal material parameters (Figure 6.19b), strength model parameters (Figure 6.19c), damage model parameters (Figure 6.19d), ACFL parameters (Figure 6.19e), and the different LAYTPROF models and impactor material (Figure 6.19f). The LAYTPROF and impactor material simulations are grouped together here, as they do not vary from the control simulation by a quantitative measured compared to the rest. Additionally, a table with the numerical values is given in Table 6.2.

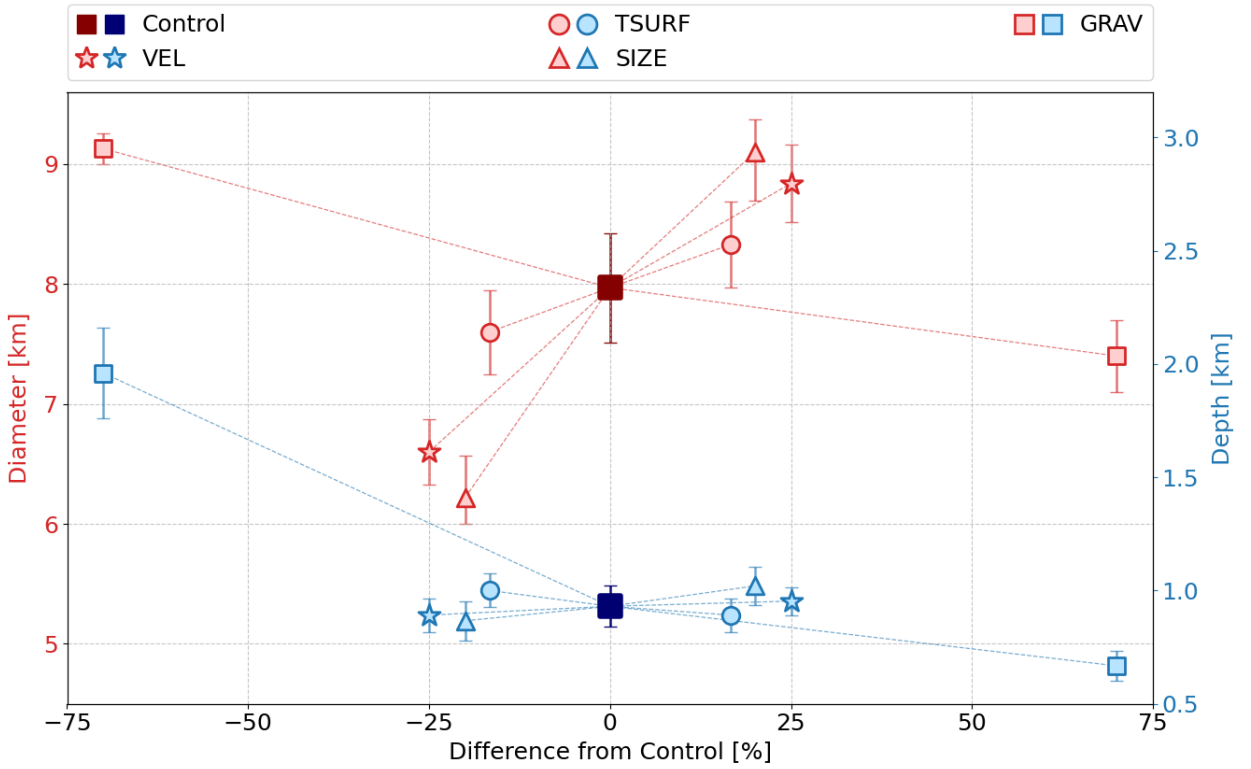

(a) Crater diameter and depth for varying input parameter of the asteroid input file.

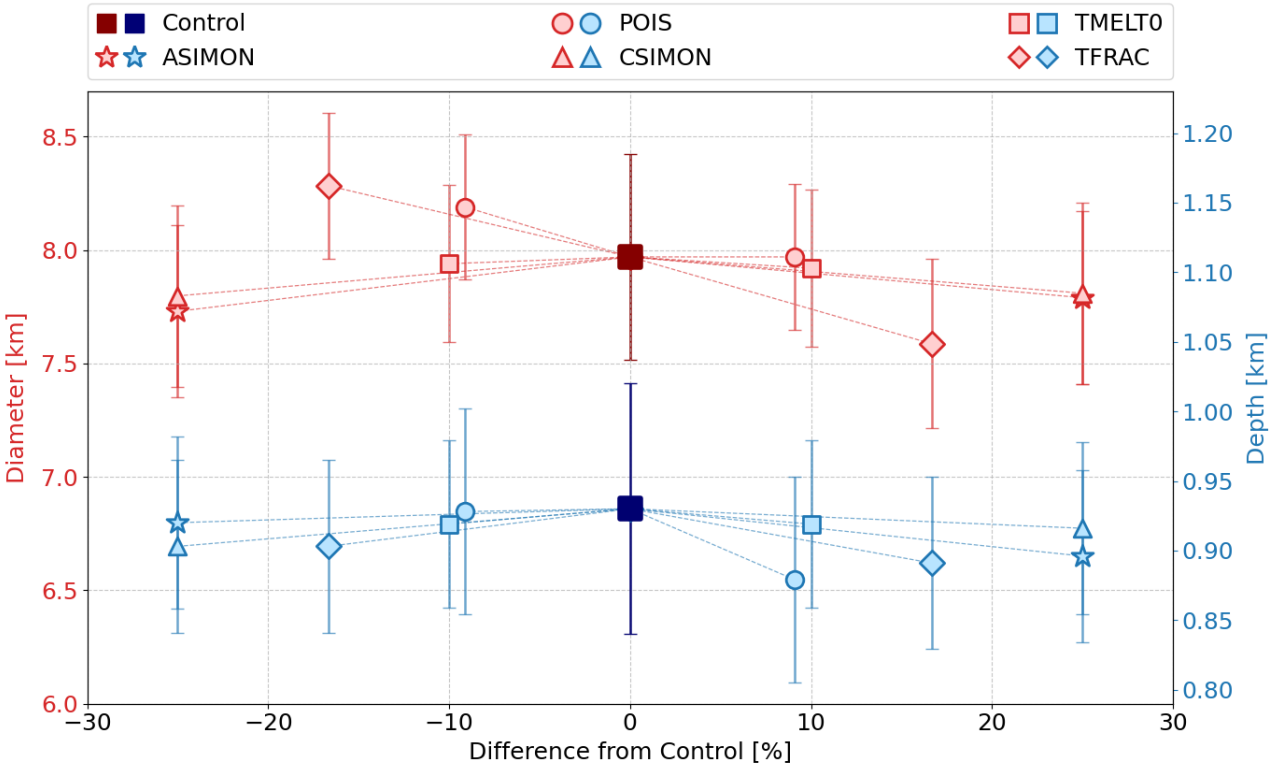

(b) Crater diameter and depth for varying general material parameters.

Figure 6.19: Crater diameter and crater depth for each simulation performed during the sensitivity analysis. Figure 6.19a shows the results from the impact parameters from Section 6.2. Figure 6.19b gives the results from the general material parameters discussed in Subsection 6.3.1.

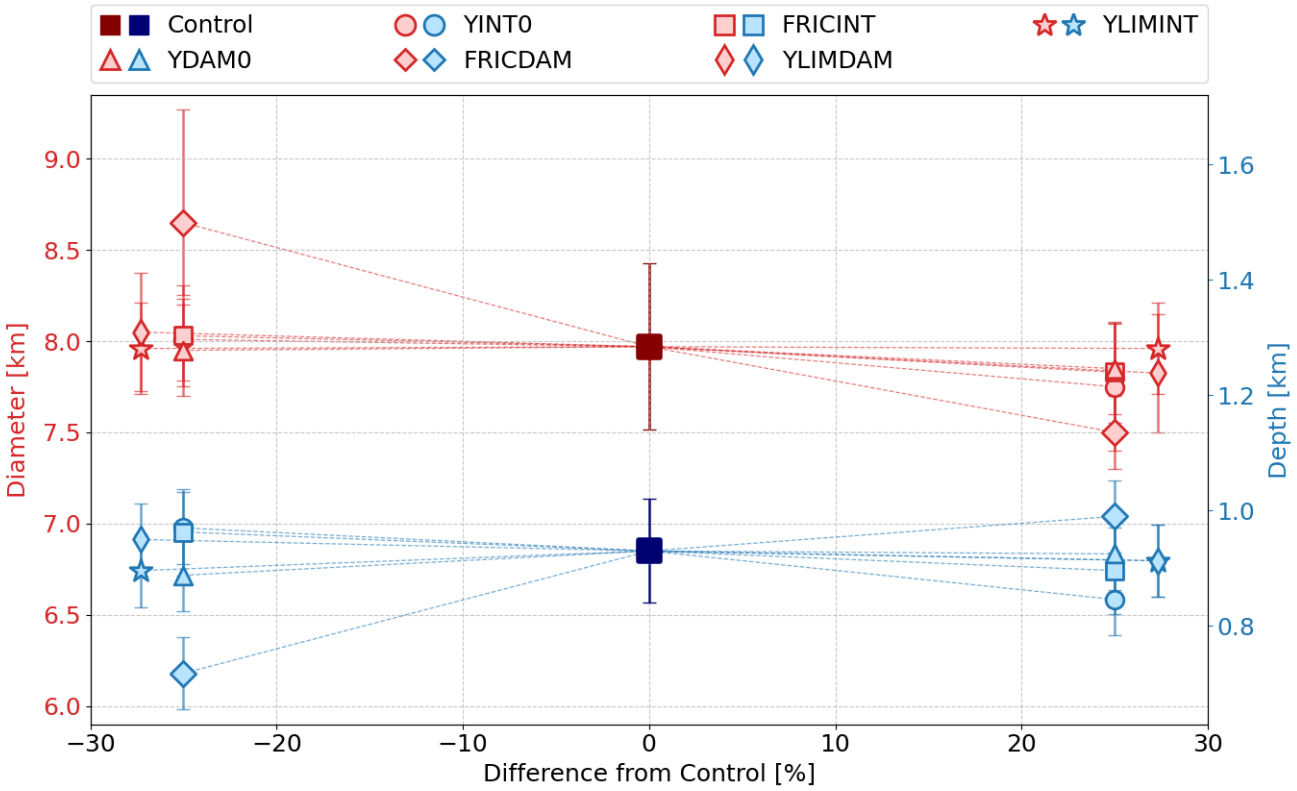

(c) Crater diameter and depth for varying material strength parameters.

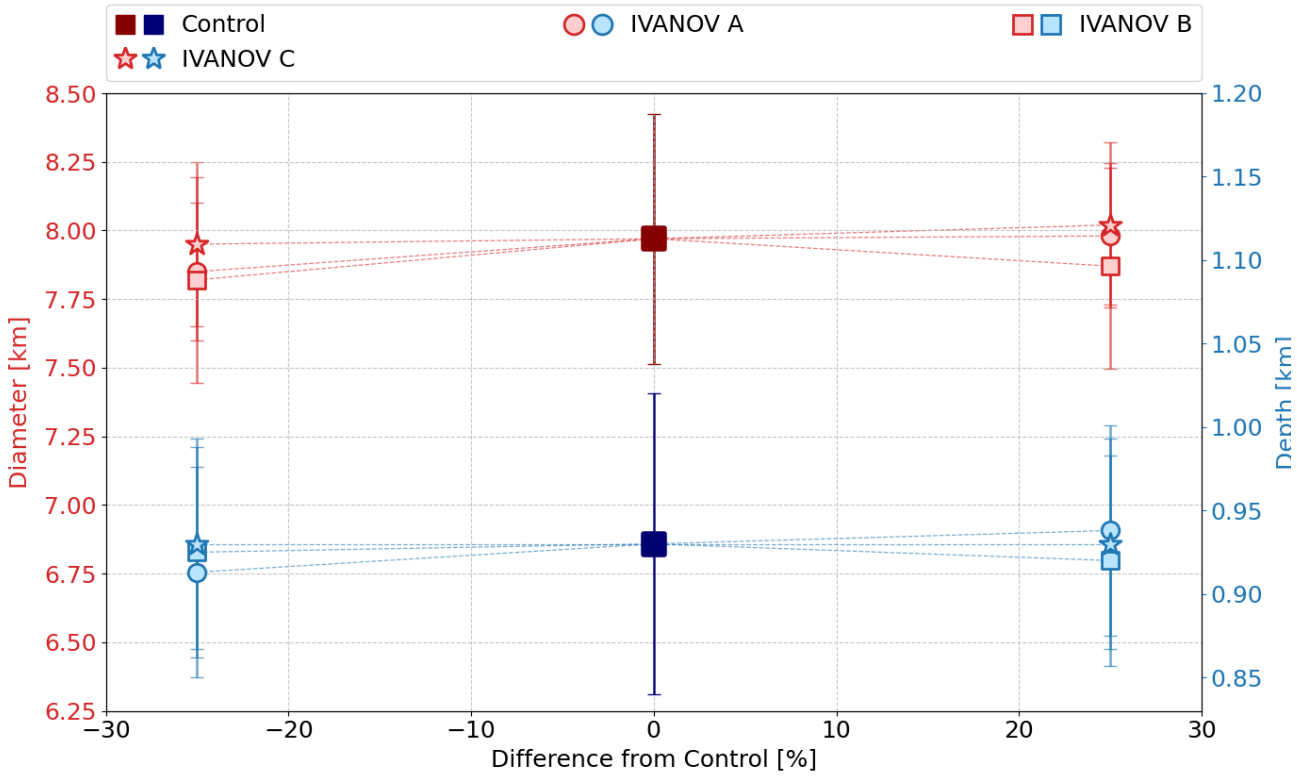

(d) Crater diameter and depth for varying damage model parameters.

Figure 6.19: Crater diameter and depth for varying strength model parameters is given by Figure 6.19c, and for the damage input parameters it is given by Figure 6.19d.

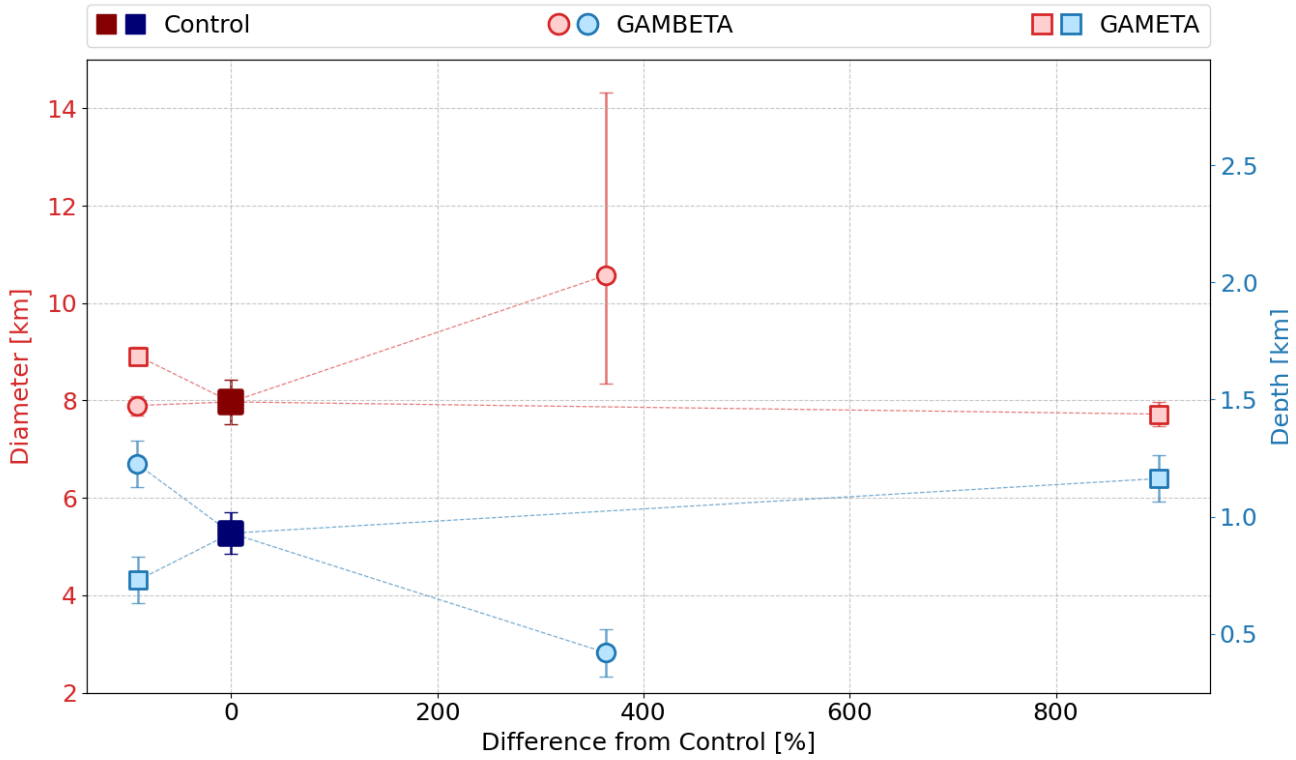

(e) Crater diameter and depth for varying ACFL input parameters.

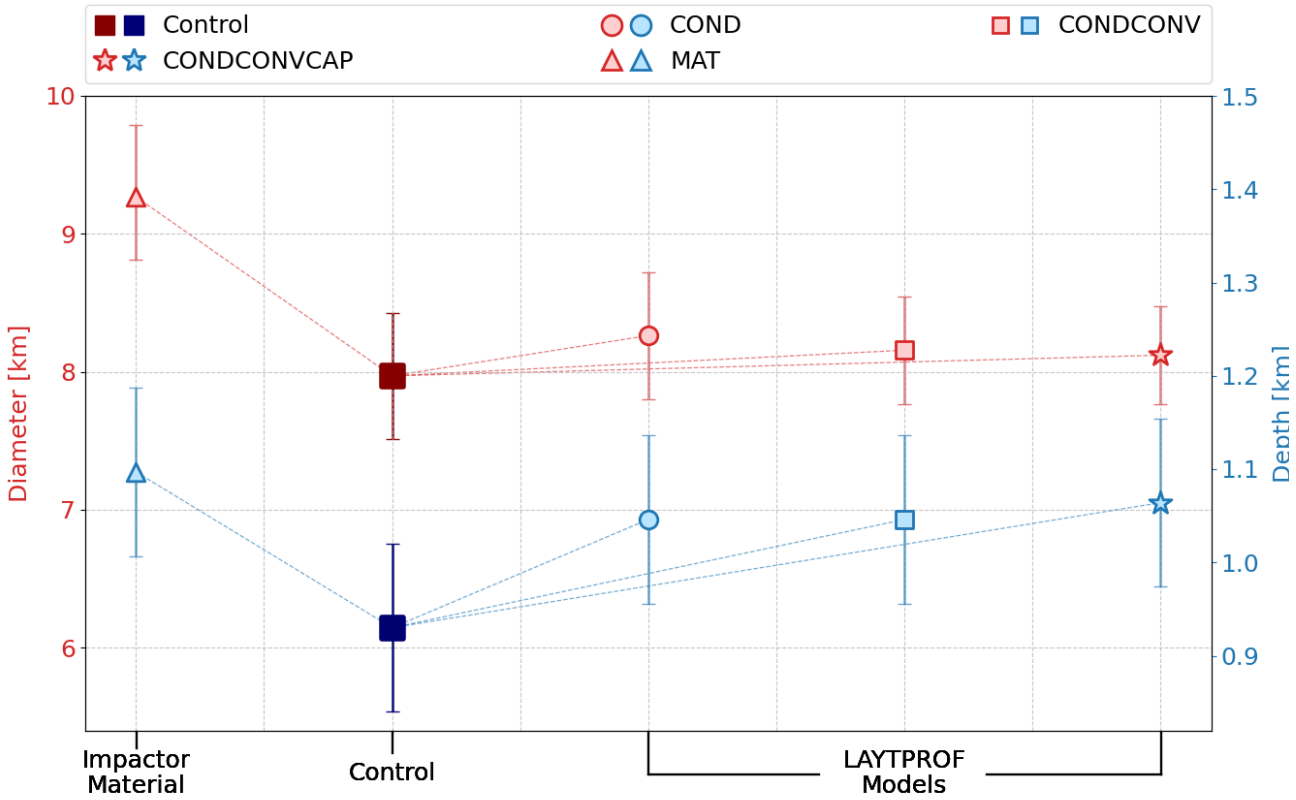

(f) Crater diameter and depth for different impactor material, and for different thermal profiles.

Figure 6.19: The ACFL parameters are given in Figure 6.19e. Finally, Figure 6.19f shows the results from varying the LAYTPROF model and the results from using a different impactor material are shown. Note that the data for "MAT" represents the different materials used from Subsection 6.2.5. The x-axis here displays the different simulations performed. Essentially, on the far left is the result from changing the impactor material, and on the right of the control simulation are the results from varying thermal profile models.

Table 6.2: Overview of the crater diameter and depth values for the sensitivity simulation results. The differences with respect to the control simulation are given, as well as the corresponding crater diameter and depth including uncertainties.

Parameter	Change w.r.t. Control	Crater Diameter [km]	Crater Depth [km]
Control	N/A	7.97 ± 0.46	0.93 ± 0.09
TSURF	+16.67%	8.33 ± 0.36	0.891 ± 0.074
	-16.67%	7.60 ± 0.35	1.00 ± 0.074
GRAV	+70%	7.40 ± 0.3	0.67 ± 0.067
	-70%	9.13 ± 0.13	1.96 ± 0.2
VEL	+25%	8.84 ± 0.322	0.95 ± 0.062
	-25%	6.60 ± 0.27	0.89 ± 0.074
SIZE	+20%	$9.10^{+0.272}_{-0.40}$	1.02 ± 0.086
	-20%	$6.22^{+0.347}_{-0.223}$	0.866 ± 0.086
MAT	Granite	$9.268^{+0.518}_{-0.457}$	1.097 ± 0.09
LAYTPROF	COND	8.262 ± 0.46	1.046 ± 0.09
	CONDCONV	8.156 ± 0.39	1.046 ± 0.09
	CONDCONVCAP	8.12 ± 0.355	1.064 ± 0.09
POIS	+9.1%	7.97 ± 0.32	0.879 ± 0.074
	-9.1%	8.19 ± 0.32	0.928 ± 0.074
TMELT0	+10%	7.92 ± 0.347	0.919 ± 0.06
	-10%	7.94 ± 0.347	0.919 ± 0.06
ASIMON	+25%	7.79 ± 0.38	0.896 ± 0.062
	-25%	7.73 ± 0.38	0.920 ± 0.062
CSIMON	+25%	7.81 ± 0.4	0.916 ± 0.062
	-25%	7.798 ± 0.4	0.903 ± 0.062
YINT0	+25%	7.75 ± 0.348	0.846 ± 0.062
	-25%	8.01 ± 0.224	0.97 ± 0.062
FRICINT	+25%	7.83 ± 0.275	0.896 ± 0.075
	-25%	8.03 ± 0.275	0.963 ± 0.075
YLIMINT	+27.3%	7.96 ± 0.25	0.913 ± 0.063
	-27.3%	7.96 ± 0.25	0.896 ± 0.063
YDAM0	+25%	7.85 ± 0.25	0.925 ± 0.063
	-25%	7.95 ± 0.25	0.888 ± 0.063
FRICDAM	+25%	7.5 ± 0.2	0.99 ± 0.063
	-25%	$8.65^{+0.62}_{-0.396}$	0.718 ± 0.063
YLIMDAM	+27.3%	7.825 ± 0.325	0.913 ± 0.063
	-27.3%	8.05 ± 0.325	0.95 ± 0.063
IVANOV_A	+25%	7.98 ± 0.25	0.938 ± 0.063
	-25%	7.85 ± 0.25	0.913 ± 0.063

Table 6.2: continued from previous page

Parameter	Change w.r.t. Control	Crater Diameter [km]	Crater Depth [km]
IVANOV_B	+25%	7.87 ± 0.375	0.92 ± 0.063
	-25%	7.82 ± 0.375	0.925 ± 0.063
IVANOV_C	+25%	8.02 ± 0.3	0.93 ± 0.063
	-25%	7.95 ± 0.3	0.93 ± 0.063
TFRAC	+16.67%	7.587 ± 0.373	0.891 ± 0.062
	-16.67%	8.284 ± 0.323	0.903 ± 0.062
GAMETA	+900%	7.72 ± 0.248	1.163 ± 0.1
	-90%	$8.91^{+0.193}_{-0.164}$	0.73 ± 0.1
GAMBETA	+363.64%	$10.57^{+3.76}_{-2.23}$	0.42 ± 0.1
	-90.91%	7.896 ± 0.198	1.225 ± 0.1

In Figure 6.19, it can be seen that the surface gravity has the largest effect on both the crater diameter and depth. Even though the deviations in percent are larger than for the other parameters, combining the results from the sensitivity analysis in Subsection 6.4.3, it proves to be sensitive parameter, especially for the crater depth. While crater diameter also varies moderately with changes in impact velocity and impactor size, the depth remains practically unaffected, which is also reflected by the sensitivity analysis showing a more pronounced sensitivity towards the crater diameter. Nevertheless, velocity differences result in diameter changes of approximately 16.4% for a lower value and 11.5% for a higher value. Similarly, the impactor size shows a difference of 21.3% for a lower value and 15.2% for a higher value. Despite the limited effect on the crater depth, these differences in diameter are noteworthy. In combination with the results from the sensitivity analysis, both impact velocity and impactor size are considered sensitive parameters.

The parameter that appears to have the least influence here is the surface temperature. It does have a slightly more pronounced effect in the crater depth compared to impact velocity and size, which can also be seen in sensitivity analysis, however, the differences here are small to begin with. Thus, it is considered weakly sensitive.

For the general material parameters, the biggest outliers are the poisson ratio and the thermal softening constant. The largest deviations for these parameters are observed in crater diameter, with differences of approximately 5.0% for TFRAC and 2.8% for POIS. Although these represent the largest changes, the variations are slight, and in combination with the results from the sensitivity analysis, they are considered weakly sensitive.

As concluded from Subsection 6.3.2, the strength model parameters have a minimal impact on crater characteristics, with the exception of the FRICDAM parameter, as was also concluded in Subsection 6.4.3. Especially for a lower value, the FRICDAM parameter shows relatively substantial differences, in particular regarding the crater depth, which deviates from the control simulation by approximately 23.2%. Its effect on the crater depth was also particularly apparent in the sensitivity analysis. As for the crater diameter, despite the moderate change of roughly 8.5%, it should not go unnoticed. Based on these findings, the FRICDAM parameter can be considered moderately sensitive.

As can be seen from Figure 6.19d, the damage parameters do not have a meaningful effect on the crater size. Deviations from the control simulation are under 2% for the crater diameter, and under 5% for the crater depth. Unsurprisingly, the sensitivity analysis also showed practically no sensitivity from these parameters.

The GAMBETA and GAMETA parameters, shown here in Figure 6.19e, are interesting. Subsection 6.4.3 shows low values of $|S_{mean}|$ and SI_{mean}, but large values of asymmetry and SI_{mean}, though for the latter this is due to the big differences in input parameter value. Essentially, these parameters exhibit only a weak sensitivity, but important is to remember the fact that there are no correct values for GAMBETA and GAMETA. Without the relations determined in Subsection 6.3.5, a guess for GAMBETA and GAMETA would have to be

made, and as Figure 6.19e and Subsection 6.4.3 show, this could lead to very different final craters. In short, GAMBETA and GAMETA might not be sensitive, but they are still important.

Finally, the change in impactor material and the different thermal profiles are plotted in Figure 6.19f. The plot shows a relatively large difference in crater diameter of approximately 17.5%, and difference in crater depth of roughly 22.6%, highlighting the importance of carefully selecting the appropriate materials, though the sensitivity analysis shows only a weak sensitivity. As for the thermal profiles, even though the differences in crater depth are decent, the diameter remains largely unaffected, and the analysis shows only a weak sensitivity.

7

Ganymede Simulations

Based on the knowledge and experience obtained with iSALE2D throughout this report, simulations can be performed under Ganymede-like conditions following the methods described in Chapter 4. First, Section 7.1 briefly addresses the experimental setup that is used here, which includes relevant input parameters and values, and the assumptions under which the simulations are performed. Then, the results from the simulations are shown in Section 7.2. Crater characteristics that will be studied are the size and shape, the damage or the amount of fractured material through density, and the temperature.

7.1. Experimental Setup of Ganymede Simulations

This section will explain the setup used for the simulations. First, the input parameter values are given in Subsection 7.1.1. In addition, a reasoning for the models and values is given. Then, in Subsection 7.1.2, some relevant assumptions are given, which were both created, and imposed by how iSALE2D fundamentally operates.

7.1.1. Simulation Setup and Parameter Inputs

From Chapter 6, it was determined that surface gravity, impact velocity, impactor size, friction coefficient of damaged material, TFRAC, and POIS are the most sensitive parameters. GAMETA and GAMBETA are not as sensitive, but are also of importance. Therefore, their values must be determined or chosen accurately. Surface gravity can be readily obtained from JPL [80]. The impact velocity and impactor size are simply chosen. The value for the friction coefficient of damaged material was based on previous research [1, 2], as well as TFRAC and POIS. GAMETA and GAMBETA were computed using Equation 6.14 and Equation 6.15, as detailed in Subsection 6.3.5.

The input parameters are summarized in Table 7.1. Below, a brief explanation of the decisions made for the other parameters and their values is provided, apart from the ones mentioned above. Note that two impact velocities and four impactor sizes are specified, essentially a total of eight simulations will be performed. Additionally, since there are four different impactor sizes, there are also four different values for GAMETA and GAMBETA.

Table 7.1: Models and parameter values used for the Ganymede simulations. Given under the asteroid input parameters are a few important general parameters, and underneath that are the material parameters. At the bottom are the ACFL parameters. Since they are calculated with equations that are proportional to the projectile size, values are given for each impactor diameter.

Asteroid input parameters				
Parameter				Value
Impact velocity				5 km/s and 15 km/s
Impactor diameter				100 m, 250 m, 500 m, and 1000 m
Surface temperature				120 K
Surface gravity				1.428 m/s^2
Thermal profile				Conductive and Convective, capped at 255 K
				Thermal gradient is 10 K/km, and lithosphere thickness is 13.5 km
Material input parameters				
Parameter				Value
Equation of state				water/ice (AQUA)
Melt temperature at zero pressure				273.0 K
Thermal softening parameter				1.2
Cohesion of intact material				10 MPa
Coefficient of internal friction of intact material				2.0
Limiting strength at high pressure of intact materia				0.11 GPa
Cohesion of damaged material				10 kPa
Coefficient of internal friction of damaged material				0.6
Limiting strength at high pressure of damaged material				0.11 GPa
	D = 100 m	D = 250 m	D = 500m	D = 1000 m
Dimensionless strength of vibrations, γ_η	0.0388	0.0520	0.0649	0.0811
Dimensionless duration of vibrations, γ_β	2938.7	1791.7	1232.3	847.54

Two impact velocities are used in the simulations. These values are based on the impact velocity for planetocentric and heliocentric impactors. For planetocentric impactors, a velocity of 5 km/s is used [55], while for heliocentric impactors, a velocity of 15 km/s is applied [1, 2, 65].

Regarding the impactor size, a range of 100 m to 1000 m in diameter was selected. There were multiple reasons for this decision. First, from a numerical perspective, both small and large impactors pose challenges. Small impacts require a fine grid due to a obligatory decreased cell spacing, which was found to increase the runtime dramatically. Conversely, large impactors result in extensive material motion and crater excavation, which is computationally intensive to model. The 100 m to 1000 m range provides a balance between these extremes.

Another reason is related to the provided range of crater sizes and impactor diameters in Table 2.1. The chosen range of projectile sizes correspond to crater morphologies of simple, transition, and complex craters. These craters are abundant on Ganymede, which make them a suitable for studying representative simulation impacts, whereas large crater such as palimpsets and multi-ringed basins are less common, and require the simulation of very large impacts. Finally, the selected range of projectile sizes corresponds well with data from previous research, which have used diameters ranging from 52 m to 1.4 km [1, 2]. This ensures comparability with the work performed in this report.

The mean surface temperature utilized by different research was found to be inconsistent, and so a value of 120 K was decided based on JPL [80] and Bjonnes et al. [1]. For the thermal profile, a conductive and convective model with a cap on the temperature equal to 255 K was applied. A cap on the temperature is included, as McKinnon [92] predicts that the ice below the conductive part is convecting between temperatures equal to 243 K and 263 K. For that reason, Bray et al. [65] use temperatures between 255 K and 273 K, and Bjonnes

et al. [1] between 240 K and 260 K. Based on these ranges, a temperature cap of 255 K was selected. A thermal gradient of 10 K/km was chosen, as Bjonnes et al. [1] found it resulted in better agreements with crater observations. Then, by taking the surface temperature of the target and assuming a linear thermal gradient from the surface to the end of the thermal profile, the thickness of the lithosphere was calculated to be 13.5 km.

Finally, the strength and damage parameters were simply derived from previous research on impacts in icy targets [1, 2, 65]. As mentioned earlier, the values for GAMETA and GAMBETA were calculated through Equation 6.14 and Equation 6.15. Although these equations were originally determined from 15 km/s simulations, it is assumed they can also be applied to 5 km/s simulations without significant discrepancies. However, as a consequence, this might lead to an unexpected crater shape, as Subsection 6.4.3 has shown that the ACFL parameters exhibit a relatively strong asymmetry, and incorrect values on the side of this asymmetry might affect the resulting crater more than initially expected.

7.1.2. Simulation Assumptions

Appropriate assumptions are essential for simulations and experiments. While it is practically impossible to simulate a perfectly realistic impact, proper assumptions simplify the problem and ensure a sufficiently accurate outcome. Below is a list of the assumptions that apply to the simulations.

1. 90-degree impact angle. The impact angle is fixed at 90 degrees, measured from the horizontal x-y surface plane. This translates to a perfectly vertical impact, which simplifies the simulation significantly due to the inherent symmetry.
2. Undifferentiated materials. Realistically, most projectiles and targets have a mixed composition. However, EOSs for such materials are unavailable. Therefore, it is assumed that both the projectile and target are composed of one primary material, ice.
3. Perfect shapes. The impactor is assumed to be perfectly spherical. While there are some asteroids that are nearly spherical, most are irregularly shaped [93]. Spherical projectiles are simpler and easier the simulate, and do not require a 3D simulation tool, which would otherwise be necessary. Additionally, the surface of the target is assumed to be perfectly smooth and flat, which is rarely the case in reality. Faults, pre-existing craters, mountains, ridges, and other surface features could affect the outcome, but are excluded here for simplicity.
4. Linear thermal gradient. Temperature typically increases with depth, but the rate can vary depending on the location or depth. To simplify the thermal profile, a linear gradient is assumed.

7.2. Ganymede Simulations

In this section, results from the simulations are shown and discussed. In Subsection 7.2.1, the crater shape is observed by looking at the geometry of the final craters. Then, in Subsection 7.2.2 the damage and the amount of fractured material is focused on. Finally, in Subsection 7.2.3 the temperature in the target is studied.

7.2.1. Shape of the Crater

The crater shape and size are crucial indicators of the impact energy, as larger impacts typically result in larger craters. In this section, the shape and size of the final craters are compared between the 5 km/s and 15 km/s simulations, as well as across the four different impactor sizes. The simulation results are presented in Figure 7.1, while more detailed plots of all the individual simulations can be found Section A.6 in Appendix A.

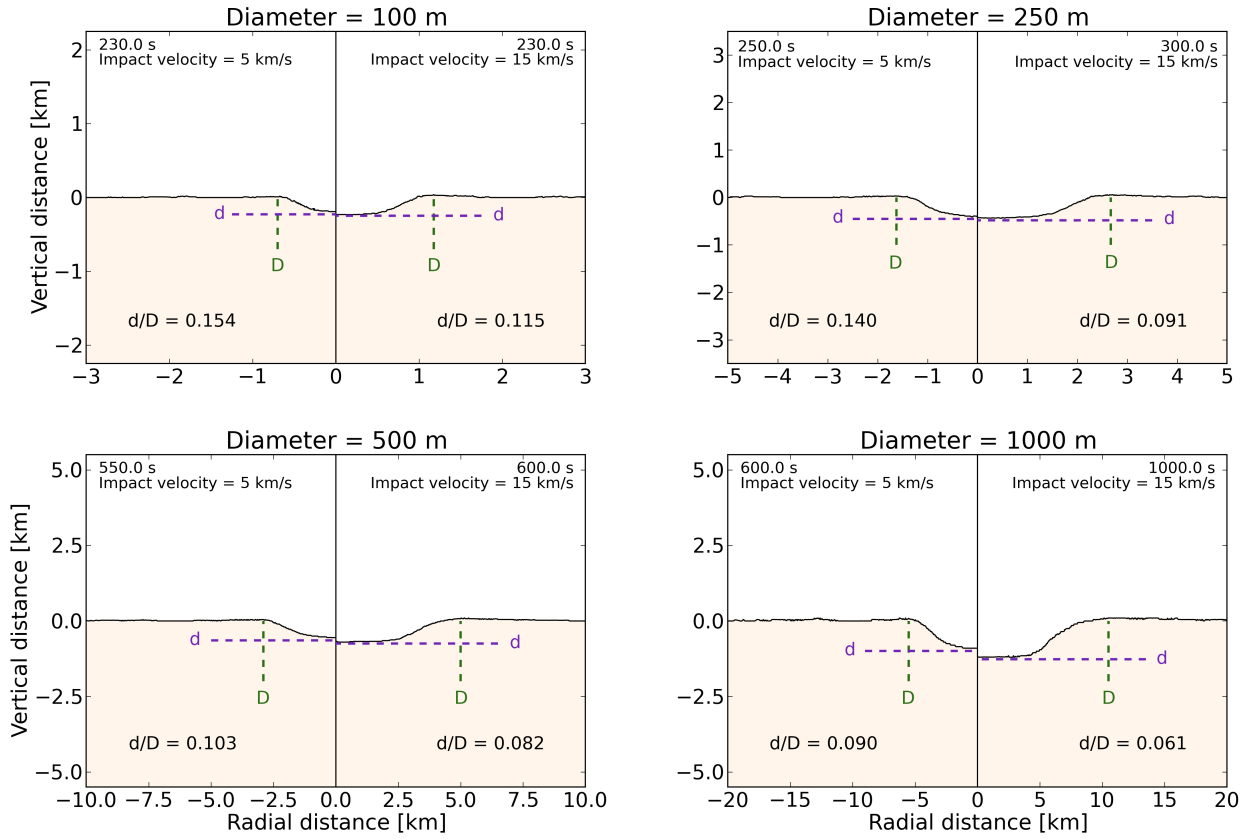

Figure 7.1: Plots of the final crater resulting from the Ganymede simulations. In the top left and top right of each plot the time and the impact velocity are given. Note that different times are reported. These time intervals were chosen such that no movement of the material was detected anymore. In each plot, the diameter (D) and depth (d) are given by green and purple dashed lines respectively. In addition, the depth-to-diameter ratio (d/D) is given. The depth was measured from crater floor to rim height, and the diameter was measured from rim-to-rim.

As expected, Figure 7.1 demonstrates that both the diameter and depth of the craters are larger for the 15 km/s simulations. Noticeable though, is that the crater depth across all simulations remains relatively small. Additionally, the crater floors are quite flat - features that are partially intentional and anticipated due to the values of γ_β and γ_η used, which ensured that the crater defaults to such a shape. The depth-to-diameter ratio is also given and it shows a decline with increasing impact energy, indicating that the diameter increases more than the depth for higher-energy impacts.

To further investigate the effect of the impactor size and velocity on the crater shape, the diameters and depths from all simulations were plotted. These values were obtained by using the Python script described in Section 4.3, and the results are presented in a histogram, which is shown in Figure 7.2. It displays the diameter on the left y-axis in green, and the depth on the right y-axis in purple. To differentiate the data, darker colors are used for the 5 km/s data, and lighter colors for the 15 km/s data.

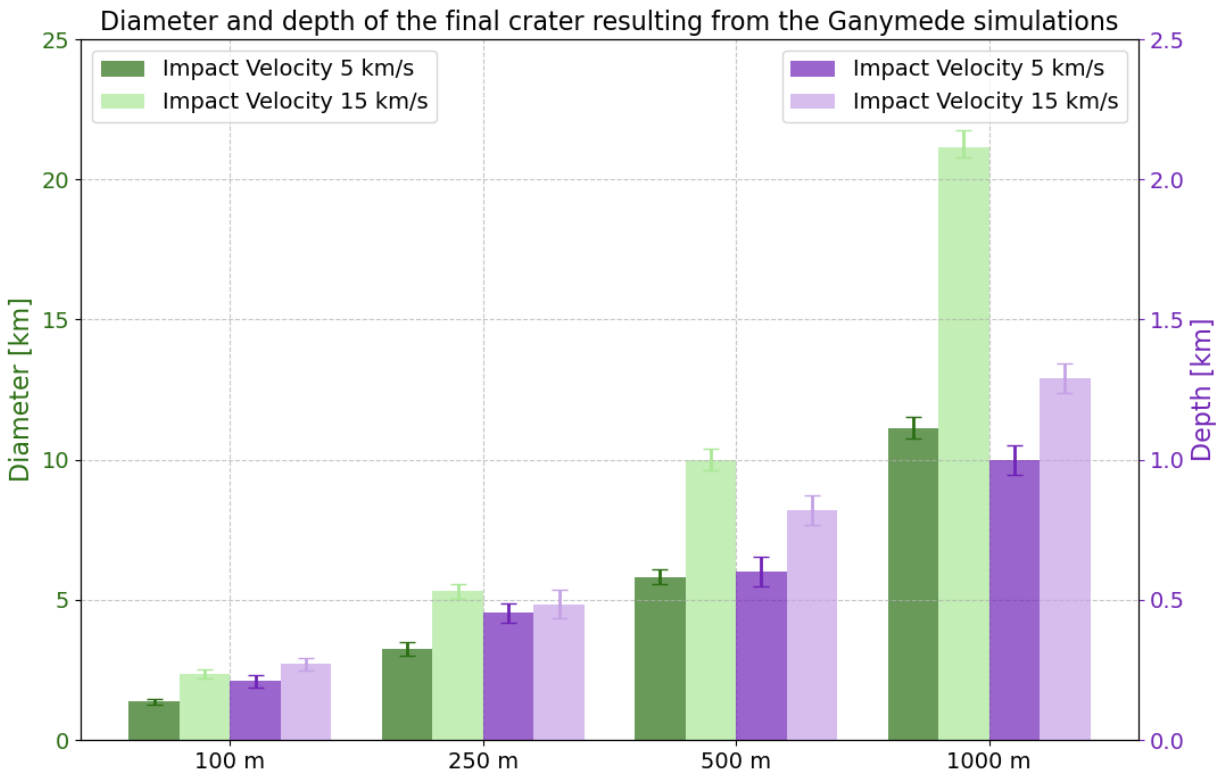

Figure 7.2: Diameter and depth of the Ganymede simulations. The left y-axis displays the diameter in kilometers, whereas the y-axis on the right shows the depth in kilometers. The diameter and depth of the simulations using an impact velocity of 5 km/s are shown in a dark green and dark purple color, and for the simulations using an impact velocity of 15 km/s a light green and light purple color are used. Errorbars are also provided, where the green colors correspond to the error in diameter, and the purple colors correspond to the error in depth.

The results reveal that the diameter increases more rapidly for the 15 km/s simulations compared to the 5 km/s simulations. On the other hand, the depth for both velocities increases at a relatively steady and similar rate. This consistent increase in depth, coupled with the faster growth in diameter, also explains the declining d/D ratio for larger impacts. This trend is likely influenced by the ACFL parameters values used, which tend to the flatten the craters, thereby reducing the depth while the diameter is not as much affected, resulting in a decreasing d/D ratio.

7.2.2. Damage and Fractured Material in the Crater

The damage sustained by the target during the impact can give valuable insights into the cratering process. For instance, by observing at the fractures in the crater and surrounding the crater, an indication on the amount of energy involved can be made. The simulation plots displaying the damage are given by Figure 7.3. Note that different times are reported. These time intervals were chosen such that no movement of the material was detected anymore.

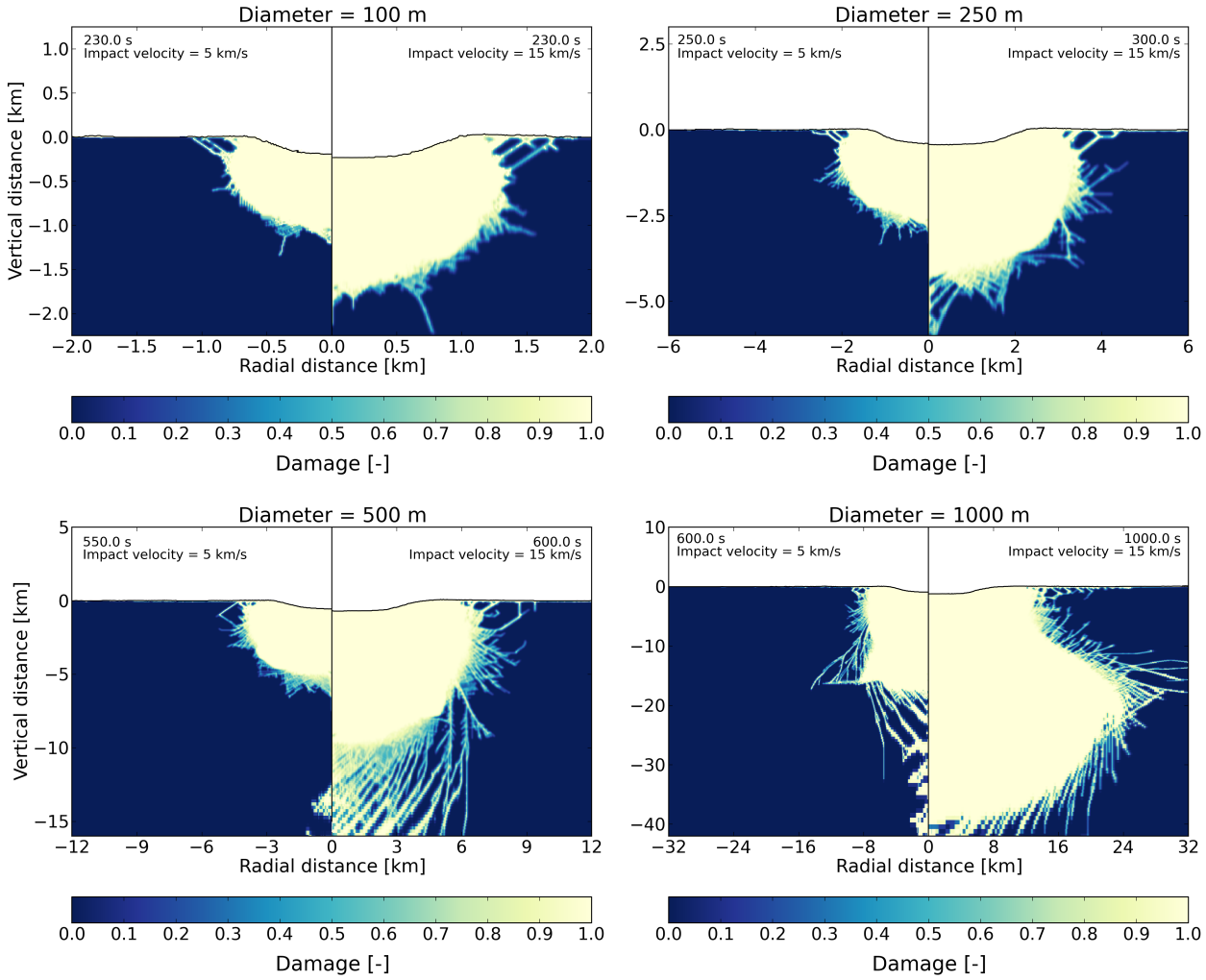

Figure 7.3: Plots of the final crater damage resulting from the Ganymede simulations. In the top left and top right of each plot the time and the impact velocity are given. The time intervals were chosen such that no movement of material was detected. The damage is indicated by a fraction, where 0 indicates there is no damage in the cell, and 1 indicates the whole cell contains damaged material. Anything in between is partially fractured material, which can generally be found in between the fully damaged and intact material.

From Figure 7.3, it can be seen that the extent of the damage caused by impacts is strongly influenced by both impact velocity and impactor size. For the 100 m diameter impactor at 5 km/s, it can be seen that the damage is concentrated near the surface and confined to a depth of less than 1 km. Increasing the velocity to 15 km/s shows a significant broadening and deepening of the damage zone, with high damage levels around the crater and moderate damage extending further into the target material. For the 250 m diameter impactor simulations, the 5 km/s case exhibits a larger damage zone compared to the 100 m diameter impactor, with high damage levels near the crater and damage reaching depths of over 2.5 km, and lateral distances reaching slightly higher than 2 km. At 15 km/s, the damage continues to extend much deeper and laterally to more than 3 km in radius. The simulation of the 500 m diameter impactor shows that the damage becomes far more extensive, with significant damage reaching about 6 km deep and moderate damage extending beyond an equal amount in radius for the 5 km/s case. At 15 km/s, the damage zone grows dramatically, not only extends the damage laterally and vertically, fracturing of material occurs as well, which is indicated by the stripes of damage deepest in the target. This effect can also be observed in the other plots, however, for the first time it is most prominent and apparent in this situation. The largest impactor, 1000 m in diameter, produces an immense damage zone. At 5 km/s, significant damage penetrates to depths of approximately 20 km, and reaches about 10 km in radial distance. At 15 km/s, the damage zone reaches its maximum extent, with severe damage encompassing the crater and damage spreading to depths exceeding 35 km and radii over 24 km.

Note that the damage reaches beyond the lithosphere thickness of 13.5 km. This can have several consequences for the subsequent crater development, because material at depths greater the material exhibits a relatively warm temperature. Warmer material can conduct and advect heat upward along the fractures, which

can cause local temperature rise, reducing ice strength and viscosity, leading to enhanced crater wall collapse and an increased relaxation rate of topography [94–96].

In general, higher impact velocities produce significantly broader and deeper regions of damage, due to greater energy transfer, while larger impactors exponentially increase the extent of both complete and moderate damage. Although complete damage is localized near the crater, moderate damage extends beyond the crater boundaries and is expressed by fractures for larger impacts.

7.2.3. Temperature and Ice Phases in the Crater

The temperature of the crater is important to investigate. When exposed to sunlight, icy moons are subjected to the UV-radiation, which gradually transforms the crystalline ice layer on the surface into a thin layer of amorphous ice [97]. The conditions under which crystalline ice transitions to amorphous ice depends on the duration and intensity of heating. This phenomena has been researched by Boshuizen [98], and an equation relating the time to crystallize and the temperature was found, and is given by Equation 7.1.

$$t_{cryst} = A \cdot \exp\left(E_a/T\right) \tag{7.1}$$

Here, A is the pre-exponential factor equal to 9.54×10^{-14} s, E_a is the activation energy equal to 5370 K for pure water ice, and T is the temperature in Kelvin. Using Equation 7.1, a plot can be created that shows the timescale against the temperature for crystalline and amorphous ice, and is given by Figure 7.4. Note that the curve represents the boundary between crystalline and amorphous ice, which if crossed, would transform amorphous ice into crystalline.

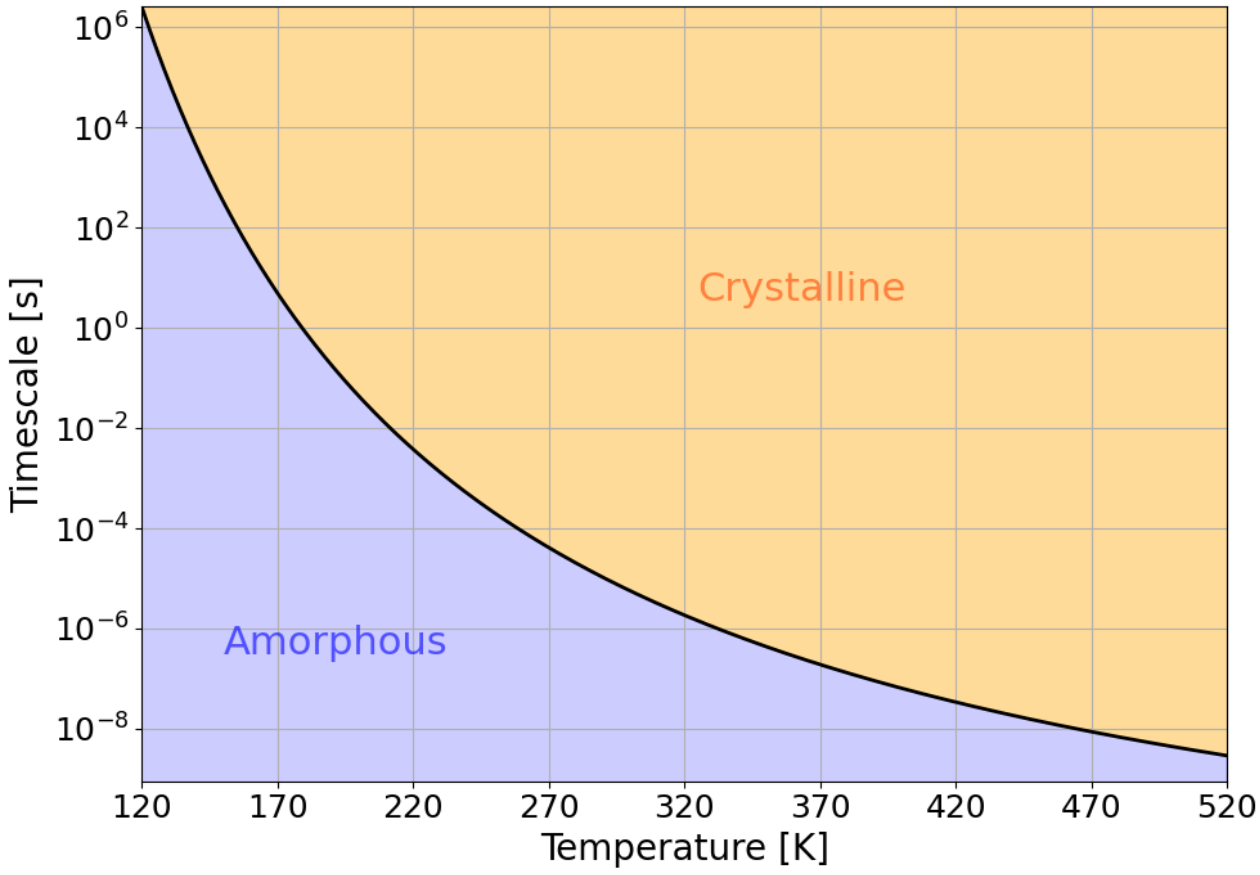

Figure 7.4: Crystallization time for different temperatures based on Boshuizen [98]. The shaded area underneath the curve displays the area where the material is in an amorphous state. The shaded area above the curve represents material in a crystalline phase state. Under certain conditions, icy material can transform from an amorphous to a crystalline state.

The information that Figure 7.4 shows can be useful for understanding the thermal effects of impacts. Heat that is generated during impacts causes ice to transition into its crystalline state. By analyzing the temperatures from the Ganymede simulations, a plot can be generated to indicate regions where the ice transitions. The maximum temperature on the colorbar can be set to the transition temperature of amorphous to crystalline ice,

so that regions at or above this temperature will represent crystalline ice, and have a distinct color. The peak temperature occurs practically directly after the impact, so the value of the timescale would be approximately equal to the initial time step used in the simulation, which is 1.0×10^{-4} s. From Figure 7.4, a transition temperature of about 255 K can be derived, and was used as the maximum temperature in the colorbar. Though keep in mind that the actual temperature could be higher because of this temperature cap. A plot of the peak temperature was then created, and is presented in Figure 7.5.

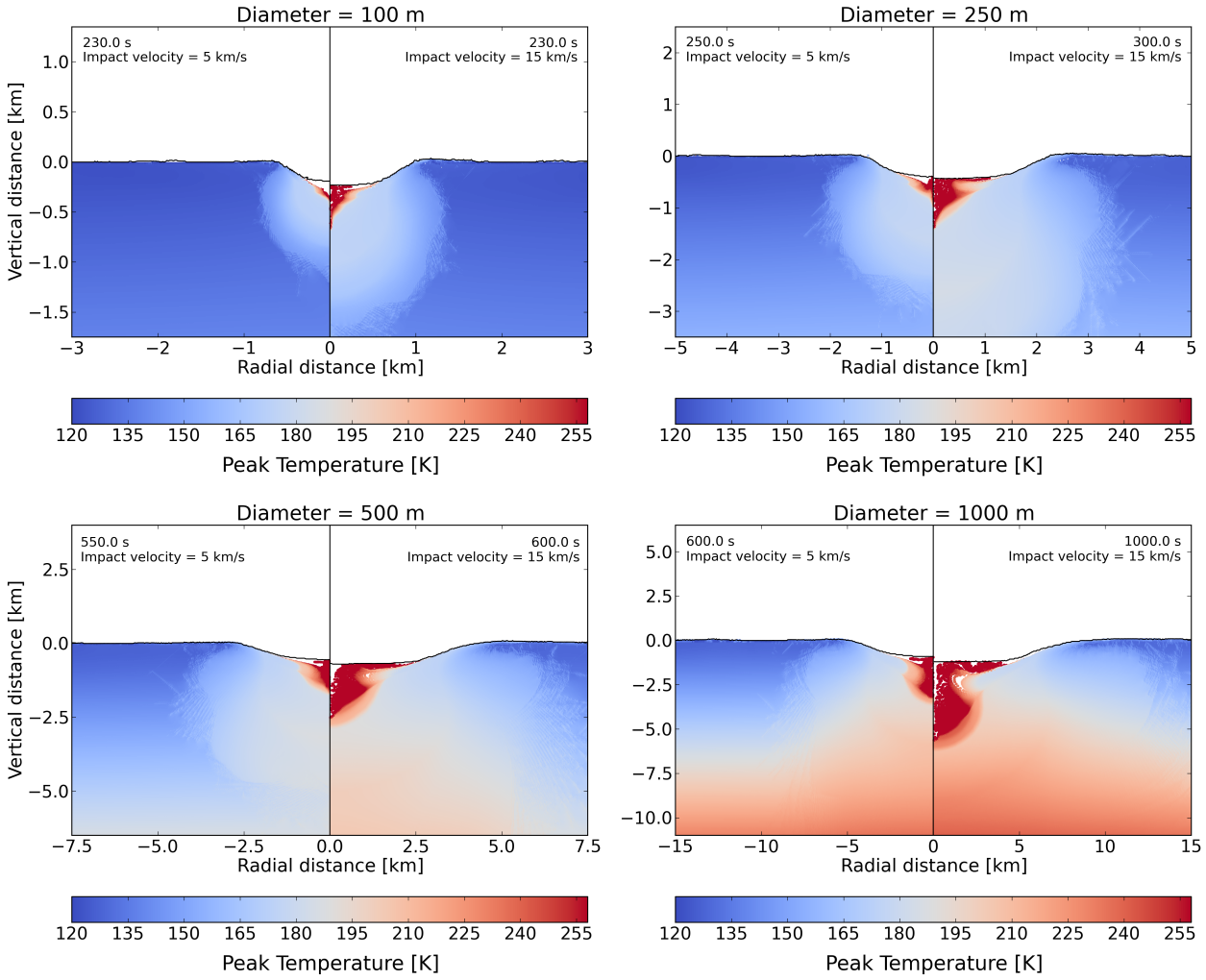

Figure 7.5: Peak temperature plots for the Ganymede simulations. Note that the maximum temperature is set to 255 K. As mentioned before, this allows for the identification of crystalline ice, however, note that due to the cap of 255 K, the actual temperature could be (much) higher. In the top left and top right of each plot the time and the impact velocity are given. Note that different times are reported. These time intervals were chosen such that no movement of the material was detected anymore.

First, note that some regions near the impact site appear as white or empty spaces. This is due to the behavior of the tracers used to monitor peak temperatures. Tracers are points floating within the simulation grid, connected by horizontal and vertical lines that deform with the material during impact. When deformation becomes extreme, the spacing between tracers may grow excessively large, leaving gaps. These gaps appear as the white spaces in the plot. Ideally, tracers should fully cover the grid, but here, the tracer spacing might have been set too high. Nonetheless, the white spaces are small and can be reasonably assumed to have temperatures similar to adjacent tracers. For instance, the white space near the symmetry line in the 500 m and 15 km/s simulation likely has tracers with temperatures at or above 255 K, which can be based on surrounding tracers and the fact that heat is concentrated at the impact site.

Figure 7.5 show that both impact velocity and impactor size significantly affect the temperature distribution and thermal penetration into the target. For the 100 m diameter impactor at 5 km/s, the temperature increase is mainly located near the impact site and the immediate surface, and temperatures remaining between 120

K and 180 K in most of the target. At 15 km/s, the high-temperature zone expands slightly, though the heat penetration remains shallow with most of the material below the crater floor still exhibiting temperatures below 180 K. For the 250 m diameter impactor, the 5 km/s simulation shows a larger high-temperature region, but the effects are still shallow and deeper regions remaining below 180 K. At 15 km/s, the high-temperature region extends deeper into the target and temperatures above 200 K are now spreading well below the crater floor. With the 500 m diameter impactor, the high-temperature region at 5 km/s is notably larger, and temperatures exceeding 200 K penetrate deeper into the target. At 15 km/s, the high-temperature zone significantly expands, with temperatures above 200 K now reaching several kilometers beneath the crater floor. Finally, for the 1000 m diameter impactor, the 5 km/s simulation shows a broader temperature distribution with high temperatures extending deep into the target. At 15 km/s, this effect is most pronounced, and temperatures above 200 K are spreading extensively both laterally and vertically.

Overall, the 5 km/s simulations have their high-temperature effects mainly confined to the impact site and right below the surface and crater floor, while the high-temperature material in the 15 km/s simulations demonstrate substantial penetration into the target. Additionally, larger impactors aid in extending the temperature distributions, with the 1000 m impactor causing the most widespread heating effects, where heat penetrates several kilometers below the crater floor, with temperatures exceeding 200 K.

Investigating the ice phases in more detail, based on the temperatures obtained in this section, and data on the pressures, the corresponding ice phases can be determined from the AQUA EOS data. Figure 7.6 provides a plot similar to Figure 7.5, where the different ice phases are displayed.

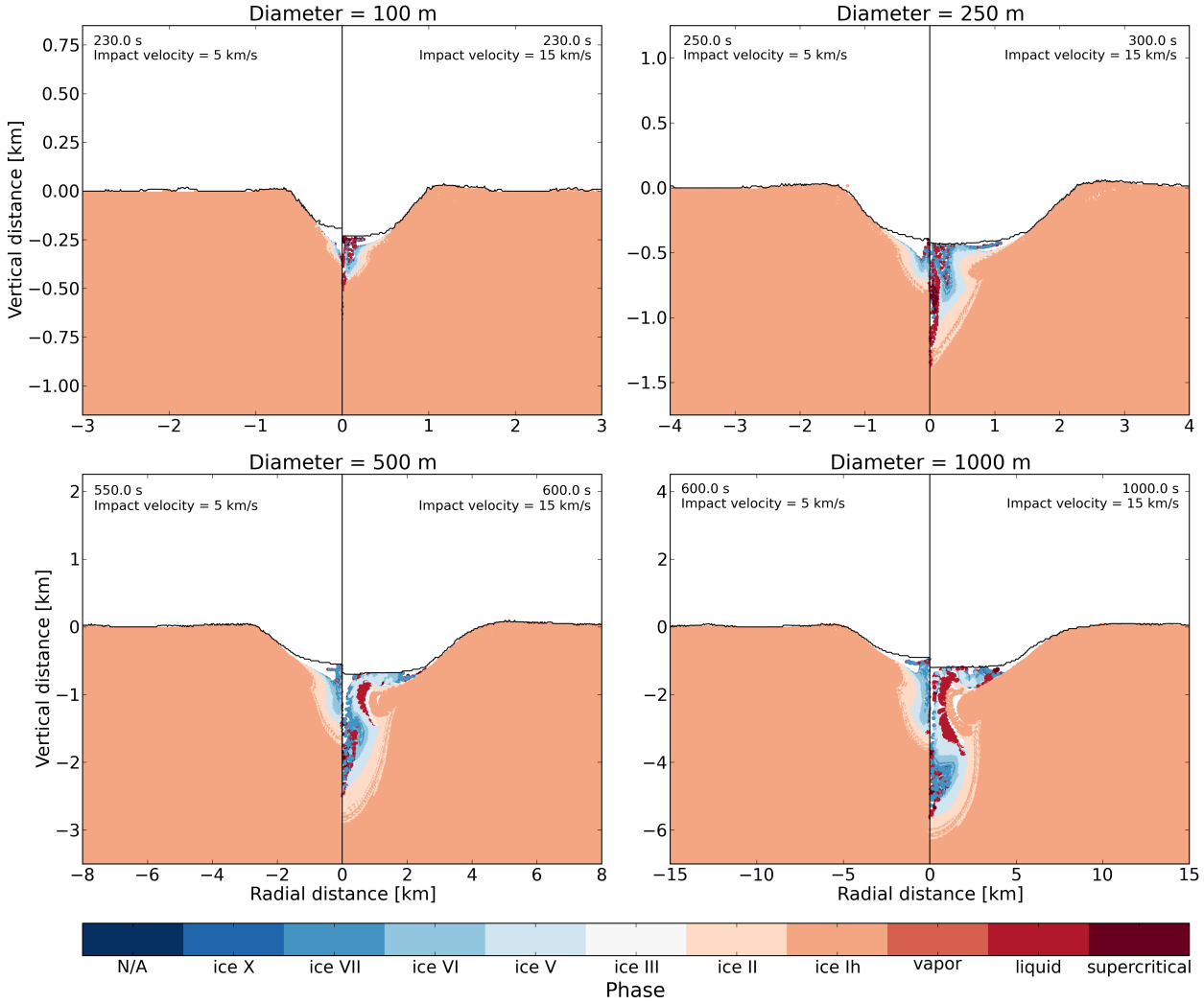

Figure 7.6: Ice phase plots for the Ganymede simulations. Note that different ice phases are primarily found in the same regions where high temperatures were found in Figure 7.5. Note that the plots were created at different time intervals. These were chosen such that no movement of material was detected.

Figure 7.6 shows that crystalline ice can be found in the same areas as Figure 7.5 indicated. Specifically, a

mixture of primarily ice III, ice V, ice VI, and ice VII can be found on the crater floor and partially along the crater walls for all simulations. This could be useful for observations, where correlations can be drawn based on the observed ice phases, and those found during simulations. However, the pressure at Ganymede's surface is near vacuum, and so high-pressure ice phases are not stable, and will eventually revert back to another stable form, that is ice Ih or amorphous ice. However, this amorphous ice can still transition to crystalline ice through sintering, as mentioned before. So, crystalline ice can still be observed in the craters, and a mix of crystalline and amorphous ice might even be indicative of a fresh crater.

8

Discussion

This chapter discusses the results from Chapter 7. In Section 8.1, the results on crater morphology, damage and fracturing, and temperature and ice phases are interpreted. Then, in Section 8.2 the results are compared to previous research, and links to observations are made. Finally, in Section 8.3 the limitations of the results are given.

8.1. Interpretation of the Results

The simulation data and results presented in Chapter 7 are interpreted in this section. The structure of this section is as follows: Subsection 8.1.1 discusses the influence of impactor size and velocity on the crater shape, Subsection 8.1.2 focuses on the crater damage, and Subsection 8.1.3 addresses the temperature.

8.1.1. Effect of Impactor Size and Velocity on the Crater Shape

The results from Subsection 7.2.1 are further analyzed here. Plots are created, relating the crater diameter and depth to each other and the impact energy, as shown in Figure 8.1. To avoid the usage of multiple identical legends, a global legend is given at the top of the plot. In the legend, the color black represents the data from the 5 km/s simulations, which applies here to all dark-colored data points and curves. Similarly gray represents the data from the 15 km/s simulations, applying to all lighter-colored data points and curves. Also, arrows are used to indicate the direction of increasing impactor size. Essentially, the leftmost data point corresponds to the results from the 100 m diameter impactor, and increases in the direction of the arrow up until 1000 m. The error bars given in the plot have been determined graphically from Figure 7.1.

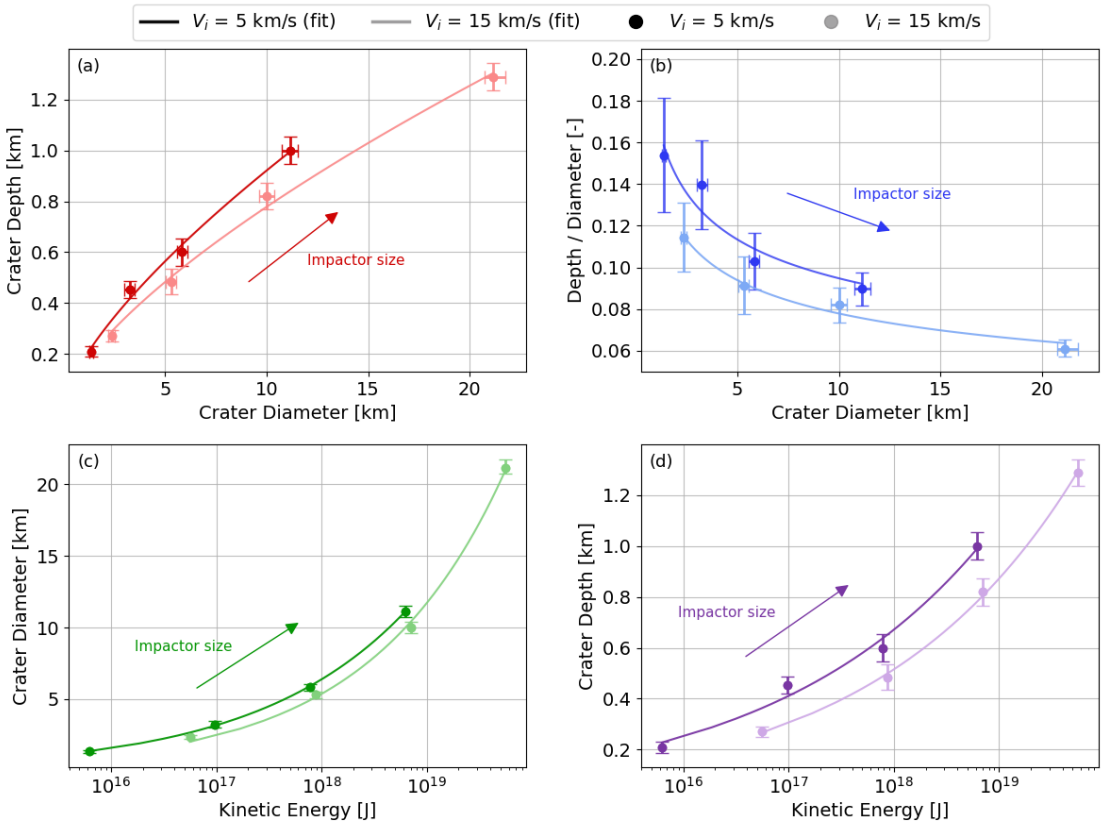

Figure 8.1: (a) Crater depth is plotted against the crater diameter. Error bars for both diameter and depth are given, and have been determined graphically. (b) Depth-to-diameter ratio is plotted against diameter. (c) Crater diameter and kinetic energy of the impactor are plotted for the different impactor sizes. (d) Similar to (c), the crater depth and the kinetic energy is plotted. The black color in the legend is there to indicate that all darker colored lines and points correspond to the data from the 5 km/s simulations. Similarly, the gray color indicates that the lighter colored lines and points correspond to the data from the 15 km/s simulations.

From Figure 8.1, it is evident that Figure 8.1(a) displays an increase in both crater diameter and depth, with a particularly large jump between the second-to-last and last data points for both the 5 km/s and 15 km/s simulations. This aligns with expectations, as an increase in impactor size, or kinetic energy, should result in larger craters. The significant increase in size is likely due to the impactor size doubling, from 500 m to 1000 m in diameter, thereby dramatically increasing the kinetic energy. In Figure 8.1b, the same x-axis is used in Figure 8.1a, but with the depth-to-diameter ratio on the y-axis. It becomes apparent that as the impactor size increases, the d/D ratio decreases. Initially, this trend might seem counterintuitive, as larger impacts are generally expected to produce larger craters in both diameter and depth. However, while the crater diameter increases with larger impacts, the depth increases only marginally. This discrepancy occurs because larger craters are more influenced by gravitational effects. Consequently, the rebound of material from the crater floor and the amount of material falling back into the crater are amplified, which reduces the final depth. As a result, the crater diameter increases more significantly than the crater depth, leading to a lower depth-to-diameter ratio. This effect is expected to be more pronounced at higher velocities, where material ejection and fallback are enhanced. This is reflected in the lower depth-to-diameter ratios for the 15 km/s simulations compared to the 5 km/s simulations. Additionally, the effects of the shock wave could explain this effect: at higher velocities, more energy might dissipate into heating or vaporization of material, rather than excavating it. Figure 8.1c and Figure 8.1d show that both crater diameter and depth exhibit trends with increasing kinetic energy that follow a power-law relationship. Expected is that the 15 km/s simulations would result in a much larger diameter than the 5 km/s simulations, however, this is not reflected in Figure 8.1c. One possible explanation could be the influence of the ACFL parameters. As discussed in Chapter 6, these parameters can significantly affect the crater shape. By using the same values for both the 5 km/s and 15 km/s simulations, it could have played a role in affecting the final crater diameter. As for the crater depth, Figure 8.1d shows a clear difference, with the 5 km/s simulations consistently producing greater depths for the same kinetic energy. This can again be attributed to the fact that higher velocities cause relatively more material ejection and fallback, which reduces the final depth.

8.1.2. Effect of Impactor Size and Velocity on the Crater Damage

For higher velocities, it is expected that the damage extends more radially and vertically compared to lower velocities. This is due more energy being delivered to the target, thereby propagating the shock wave further, which leads to increased excavation and fracturing of material. Similarly, larger impactor sizes contain more kinetic energy, which using the same reasoning will result in wider and deeper zones of damage. Given the lower cohesion of icy material, it can be expected that the rebound and collapse of material have an enhanced effect. However, these effects are also heavily influenced by the ACFL parameters, which play a critical role in shaping the final crater, hence discernment would be difficult.

The simulations from Figure 7.3 reveal that impacts at 15 km/s produce significantly larger damage zones, with extensive fracturing evident in the form of radial ”stripes”, as predicted. The difference in damage due to impactor size is also notable. For smaller impactors, the increase in damage is primarily reflected in a larger damage area, however, for larger impactors, the extent of fracturing becomes much more apparent with the appearance of stripes as well. Specifically, for the 1000 m impactor simulations, the area of damage increases tremendously, both radially and vertically. One possible explanation for this dramatic increase in damage area with the largest impactors is the thermal profile of the target. At greater depths, the relatively higher temperature of the ice likely weakens its structural integrity, making it more prone to fracturing. This weakening effect could explain why the damaged material extends farther and deeper in the simulations involving the larger impactors. Additionally, the energy delivered by these larger impactors amplifies these effects, resulting in significantly greater damage zones.

To further study the damage received by the target, plots can be made of the radial and vertical extend of the damage, against the impactor size and velocity. This could shed light on how the extent of damage scales with the size of the impactor, and whether the scaling differs between the lower and higher velocities. It might also show the relative importance of impactor size versus velocity in determining radial and vertical damage extent. The plot is shown in Figure 8.2, where in blue, data is given for the radius of the damaged area, and in red the data for the depth of the damaged area. Note that curves are plotted as well, which have been fitted through the data points. The radius and depth of the damaged area are determined by the damaged area that does not include the fractures. For instance, the 500 m and 15 km/s simulation in Figure 7.3 shows a lot of fractures that reach deep into the target, however, the depth of the damaged area is considered here to be

about 10 km, in essence, approximately where the rounded shape of damage ends.

Nevertheless, the fractures are important when considering the thickness of the lithosphere. The damage and fracturing observed for the 500 m and 15 km/s simulation, and both 1000 m simulations, is extensive and reaches into territory where material exhibits a relatively significantly larger temperature compared to the surface. As mentioned in Subsection 7.2.2, this can lead to the conduction and advection of warmer material through the fractures, causing local temperature rise, reducing ice strength and viscosity, resulting in an increased relaxation rate. However, the fractures can freeze shut over time, though the larger the impact, the greater the damage, and thus the longer it will take for this to happen. Fortunately, the ACFL parameters used account for all these processes. As mentioned in Subsection 6.3.5, the ACFL values have been determined by fitting observed crater data, such that the resulting crater shape would resemble observations. However, it is still important to keep in mind how fracturing can affect the craters. For instance, if warm material were to find its way to the surface, this might be observed through different albedo values. Or, warm material might contain different substances such as salts or minerals that are not found on the surface.

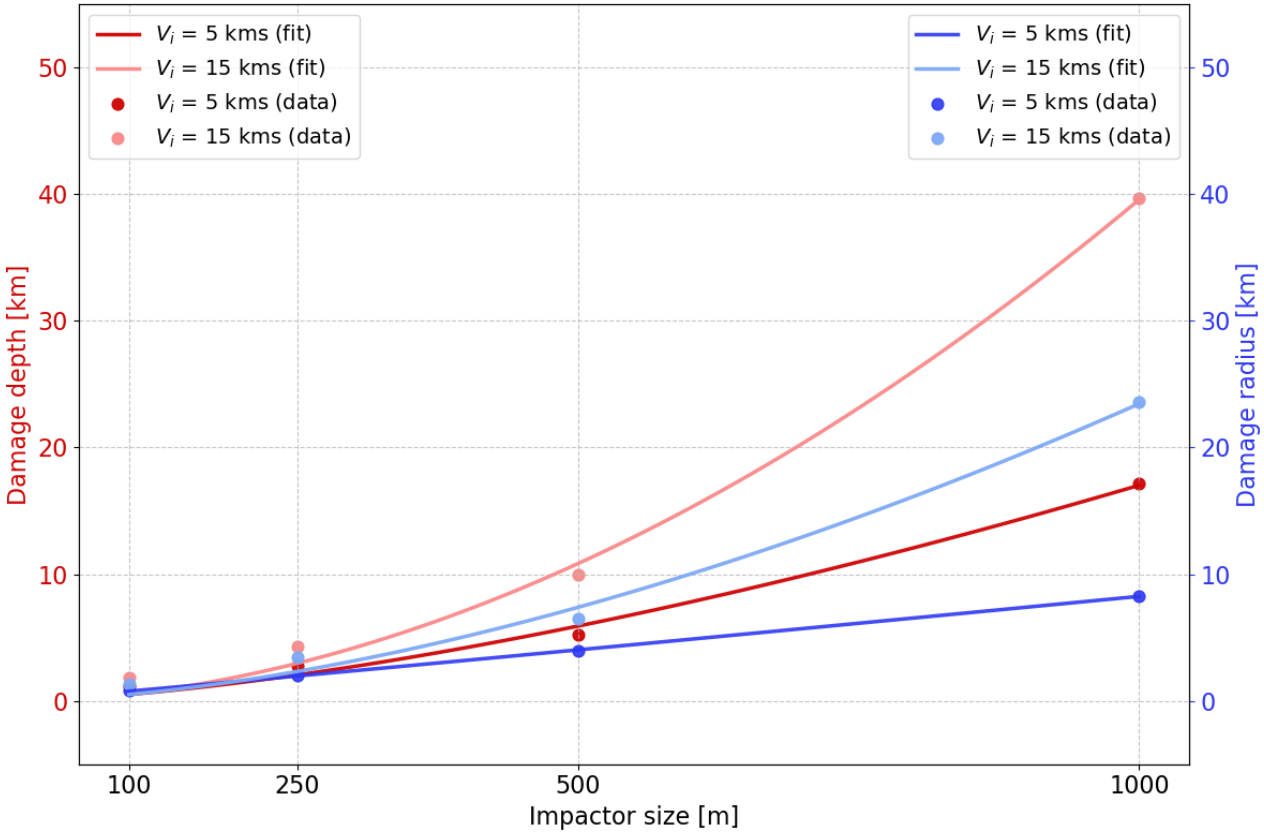

Figure 8.2: Radius and depth of the damaged area in the target against impactor size. The data points are the results from the simulations, and the curves are fitted to these data points.

From Figure 8.2, it can be observed that both the damage depth and damage radius increase with impactor size. This is consistent with the expectation that larger impactors carry more kinetic energy, which leads to more extensive material excavation, fracturing, and displacement. The non-linearity is especially noticeable for the 15 km/s simulation, meaning larger impactors appear to cause disproportionately larger damage zones. As for the 5 km/s simulations, slight non-linearity can be seen for the damage depth, though the damage radius seems to show a linear relationship. However, with an increased sample of impactor sizes, this could show a non-linearity as well.

At 15 km/s, both the damage depth and radius are consistently larger than those observed at 5 km/s for any given impactor size. This supports the expectation that the resulting shock wave propagates further into the target, creating larger damage zones. Additionally, enhanced material vaporization and melting at higher velocities could have contributed to the increased extend of the damage.

For both velocities, the damage depth increases more significantly compared to damage radius as the impactor size grows. This indicates that the energy from larger impacts propagates more efficiently vertically than radially. This may be attributed to thermal effects, which are enhanced with depth and could weaken the

ice significantly, facilitating deeper fracturing. Furthermore, in the 1000 m and 15 km/s simulation, the radial spread of damage occurs approximately around the depth where the thermal gradient is largest, which is the end of the lithosphere. Beyond this point, the material temperature is highest, which affects the amount of damage received at these depths. Additionally, if warmth of this material travels upwards to the surface, it can lead to enhanced post-impact relaxation effects. The influence of the ACFL parameters should also be considered, as they directly affect the vibration duration and strength.

Another plot was made displaying the damage depth against the damage radius. This can be useful to point out whether there is a proportional relationship between radial and vertical damage or if one parameter dominates under certain conditions, for instance higher velocities or larger impactors. Such a plot would also directly show whether increasing velocity skews the damage more radially than vertically. The plot is shown in Figure 8.3.

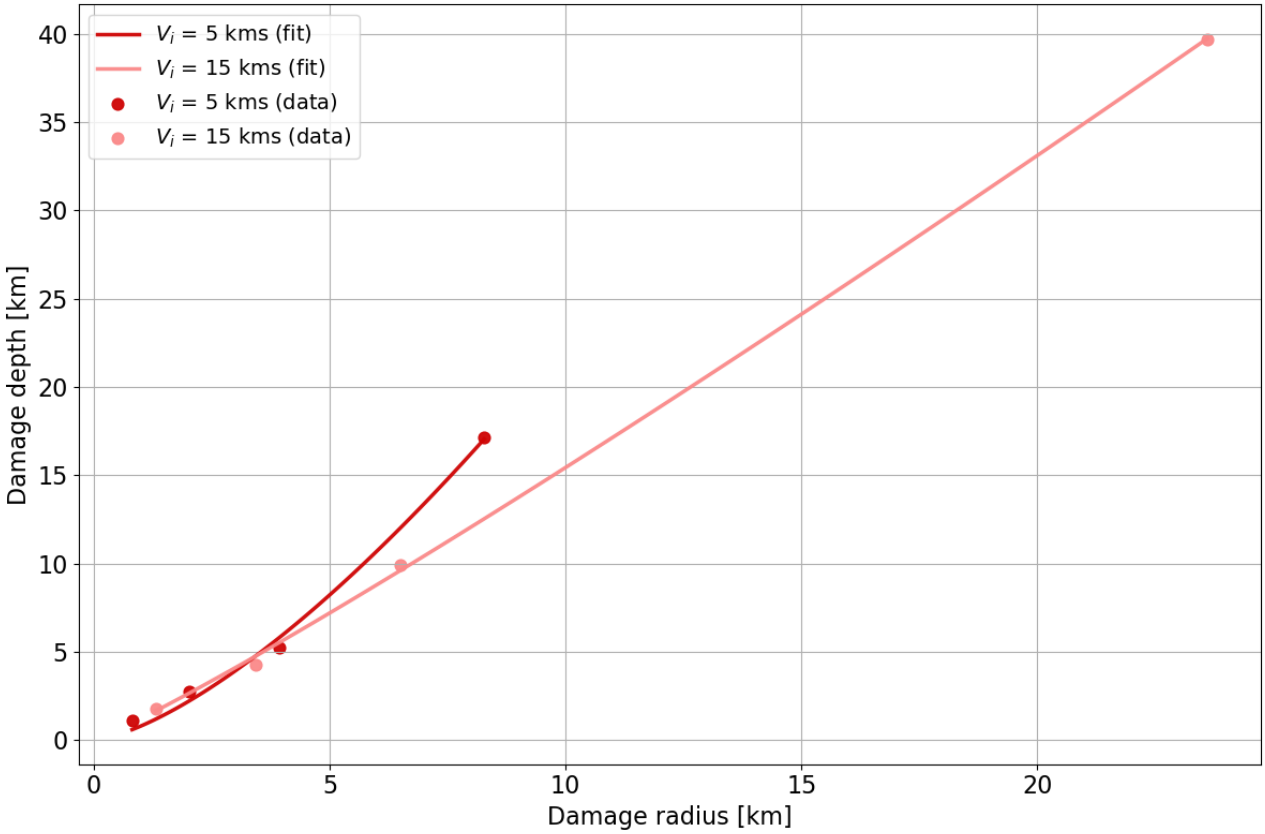

Figure 8.3: Damage depth against damage radius in the target, resulting from the Ganymede simulations. The data is shown for the 5 km/s (darker color) and 15 km/s (lighter color) simulations. The data points are given, as well as curves that are fitted to these data points.

Figure 8.3 shows that the 15 km/s simulation data exhibits a linear relationship. This suggests that both vertical and radial damage increases almost equally, although the damage depth is consistently higher than the damage radius.

For 5 km/s simulation, the relationship appears non-linear, with damage depth increasing more rapidly than the radius, as evident from the curvature of the data points. This indicates that at lower velocities, the energy is less efficiently distributed radially, potentially due to the thermal gradient discussed earlier. Another explanation is that the shock wave's amplitude decays more rapidly in the radial direction as it propagates outward.

8.1.3. Effect of Impactor Size and Velocity on the Crater Temperature

From Figure 7.5, it becomes clear that the main differences between the 5 km/s and 15 km/s simulations are the maximum value of the temperature and the location and spread of high-temperature material. The depth and shape of the high-temperature material can be considered atypical, although somewhat expected, as similar shapes were observed in the plots in Chapter 5. This behavior arises because of the use of different viscosity models. The unusual shape is caused by high-temperature material that rebounds during the excavation phase. After reaching its maximum height, this material falls back down, covering the lower-temperature material that

had settled into the crater while the high-temperature material was being ejected.

To investigate the high-temperature material further, it can be useful to plot the radial (or horizontal) extend of high-temperature material along the surface. This can provide information on how high-temperature material spreads inside the crater. This could shed light on the range of high temperature material and thus crystalline ice, which can be linked to observations. High-temperature material of ≥255 K was tracked along the surface, and the horizontal extend was measured along the x-axis. The results are presented in Figure 8.4.

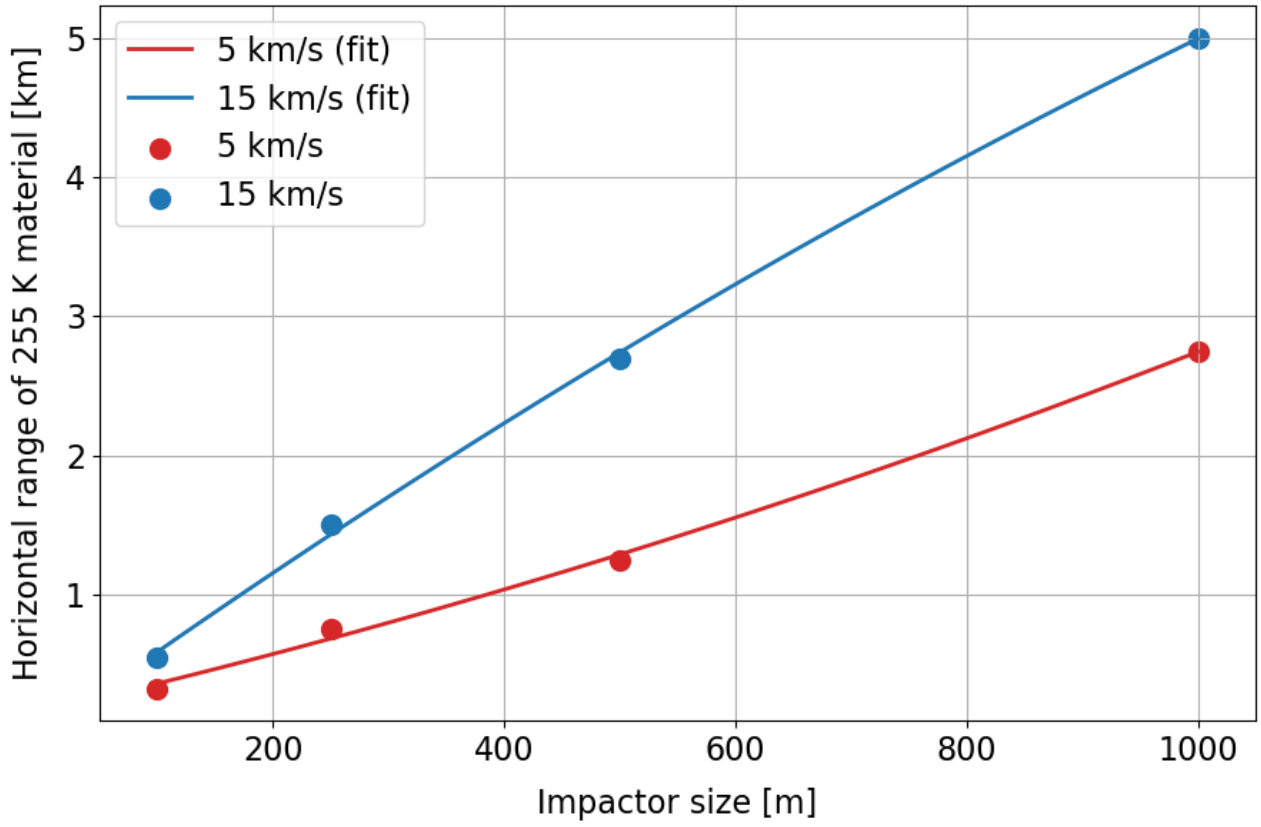

Figure 8.4: Horizontal extend of high-temperature (≥255 K) material against impactor size. The points represent the data extracted from Figure 7.5, and the curves are fitted through these points. A near-linear relationship can be observed for both 5 km/s and 15 km/s data.

Interestingly, Figure 8.4 shows almost a linear relationship between the horizontal extend of 255 K material, and the impactor size, for both the 5 km/s and 15 km/s simulations. Equally curious is that the slope for the curve for 15 km/s is approximately twice the slope for 5 km/s. This can be used as an additional method to compare with observations, providing added confidence for the determination of impactor origin. If observed horizontal crystalline extent of a crater lies near the 15 km/s curve and far from the 5 km/s curve, it can indicate heliocentric origin. If it falls closer to the 5 km/s curve, the origin might more likely be planetocentric.

8.2. Comparison of the Results

In this section, the results are compared with previous work. Subsection 8.2.1 discusses differences in crater shape, Subsection 8.2.2 compares the crater damage, and Subsection 8.2.3 focuses on the temperature. Finally, Subsection 8.2.4 provides a link between the findings and the observations.

8.2.1. Comparing the Crater Shape

To compare simulation results with observational data and best-fit curves from previous studies, Figure 8.5 was created. It is important to note that the best-fit curves from prior research were obtained under slightly different conditions. For example, Bjonnes et al. [1] performed simulations using the ice Tillotson EOS, a thermal profile capped at 250 K, and the PEIERLS viscosity model. Among these differences, the viscosity model likely has the most significant effect on the crater shape, as seen in Chapter 5, where the PEIERLS viscosity model

produced a shallower and slightly wider crater. Consequently, it is expected that the curve from Bjonnes et al. [1] is located below and to the right of the results from this study. In Figure 8.5, data taken from Bjonnes et al. [1] is indicated by a dark green color. However, note that the data points were initially sourced from Schenk [99]. Data from Bray et al. [24] corresponds to fresh craters on Ganymede, with the curve representing the best-fit through these points given in blue.

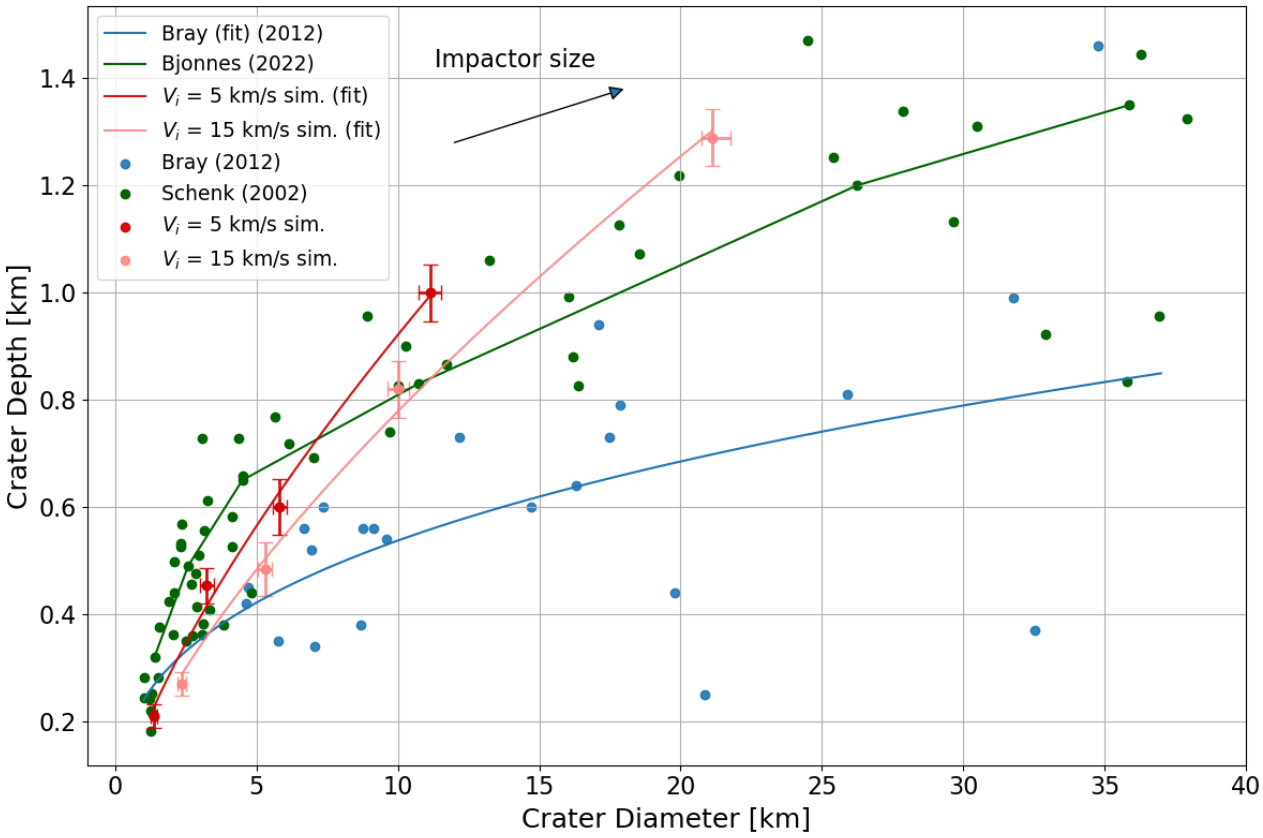

Figure 8.5: Crater depth and crater diameter of the Ganymede simulations. In addition, data from Bjonnes et al. [1], Bray et al. [24], and Schenk [99] is added for comparison. Note that points represent data obtained from different sources, as displayed by the legend. The curve from Bray was created by fitting a curve through the Bray (2012) data points. The curve from Bjonnes (2022) resulted from their simulations, and not from any particular fitting method.

From Figure 8.5, it can be seen that the simulation data aligns especially well with observations for smaller impactor sizes. This makes sense, because the effects of the viscosity model and other factors, such as the ACFL parameters, become more pronounced at higher impact energies. Hence, for larger impacts the differences becomes clearer. Between the 5 km/s and 15 km/s simulation data, it can be seen that the 15 km/s simulation data aligns better with observations, suggesting it is a better representative of the natural crater formation on Ganymede. Despite this, recall the fact that a change in the viscosity model and ACFL parameters could further improve the simulation data, though the 15 km/s data would likely remain a better fit.

Although the largest impacts (500 m and 1000 m) are within the range of observations, these simulations tend to overestimate the crater depth. This overestimation can be attributed to the viscosity model used, as they influence material strength and rebound, which become more pronounced with increasing impact size. The PEIERLS model showed a considerably shallower and slightly wider crater in Chapter 5, which compared to the results from the Ganymede simulations, resemble a lower viscosity model. In Figure 8.5, this is expressed by a primarily downward shift of the curve. Hence, the curve of Bjonnes et al. [1] is below the curves resulting from the simulations. To visualize the effects of viscosity on the crater shape, Figure 8.6 is created.

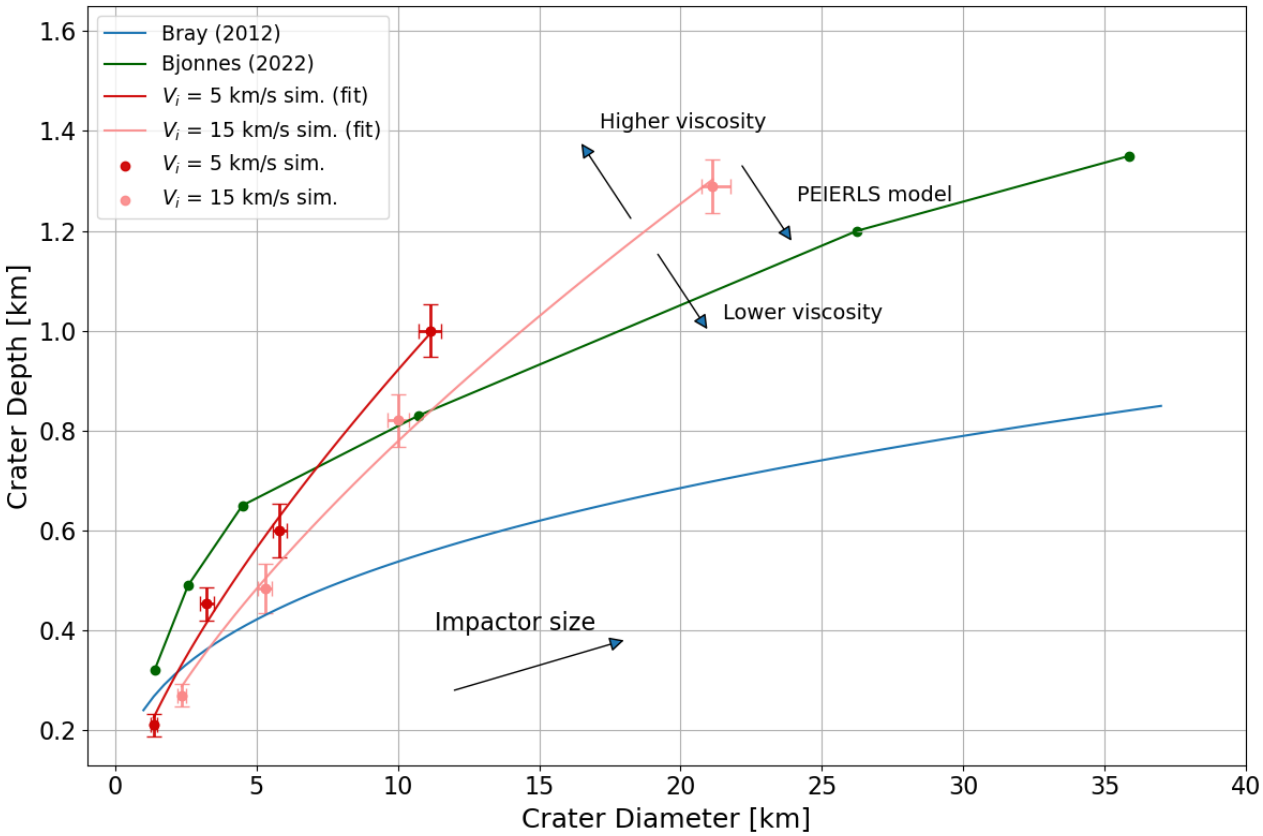

Figure 8.6: The best-fit curves for the crater depth and crater diameter obtained from the Ganymede simulations are given, as well as the curves from Bjonnes et al. [1] and Bray et al. [24]. Arrows are shown indicating the speculative shift of the curves from the Ganymede simulations, provided a lower, higher or PEIERLS viscosity model had been used.

In addition to the viscosity model, ACFL parameter values also have a sizable influence on the crater shape, as shown in Chapter 6. While equations were found to produce ACFL values that would result in crater shapes that matches observations, small changes in these parameters could easily alter the results. However, a detailed parameter study would be required to further fine-tune these ACFL parameter values.

Finally, the depth-to-diameter ratio can be compared with findings from previous studies. As observed in Figure 8.1b, the depth-to-diameter ratio was found to decrease with increasing impact size. This trend is consistent with the findings from Bray et al. [24] and Bland and Bray [100]. Depending on the crater type, depth-to-diameter ratios typically range between approximately 0.005-0.3 [1, 24, 65, 100]. From these numbers, it can be concluded that the ratios obtained from this study fall well within this range; however, as shown in Figure 8.5, the slope of the curves remains rather steep in comparison with the other curves.

8.2.2. Comparing the Crater Damage

Very little research has focused on the damage profile and fracturing in an icy target struck by an icy impactor. The limited studies that are available are mainly studying small-scale experiments, such as those performed by Sherbun and Horstemeyer [101]. However, these cannot be directly compared to the large-scale simulations conducted in this report.

Research from Collins et al. [4] does investigate target damage from large-scale impacts, though their focus is on rocky materials. Despite the difference in material, their results show some similarities with the results obtained in this report. Figure 8.7 shows a figure taken from Collins et al. [4], together with the 500 m and 1000 m impact simulations results taken from Subsection 7.2.2. As shown in Figure 8.7, fracturing patterns are evident in both cases, although the fractures have mostly propagated in a horizontal direction for Figure 8.7a, and more vertical for Figure 8.7b.

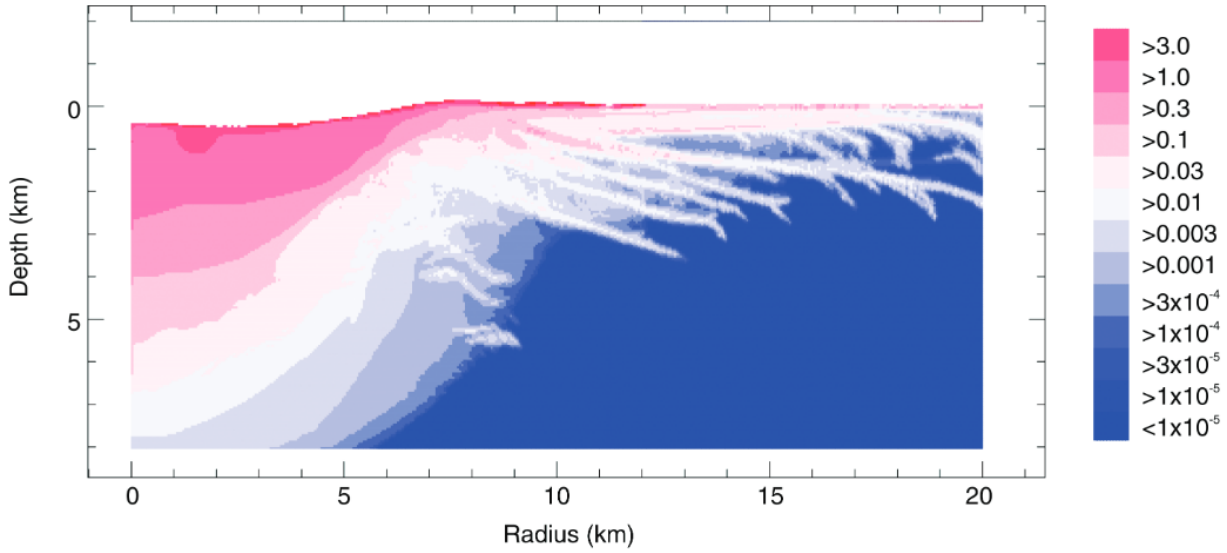

(a) Final total accumulated plastic strain contours resulting from a simulation of a 10 km diameter transient crater event, taken from Collins et al. [4].

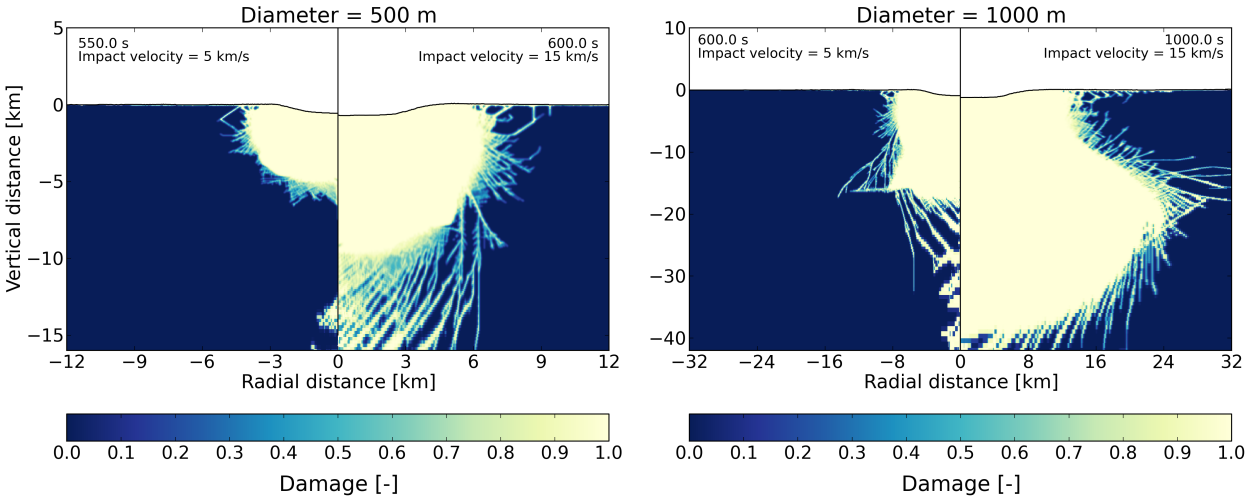

(b) Damage in the target resulting from the 500 m and 1000 m diameter impactor Ganymede simulations.

Figure 8.7: The damage in the target from the simulation performed by Collins et al. [4] can be seen in a). The 500 m and 1000 m impactor diameter simulation results can be seen in b).

Simulation results can also be compared to observations. The simulations show damage and fracturing on the crater floor and slightly beyond the crater rim, which could be used for comparison.

Looking at the surface of Ganymede, many fractures have been detected, however, observations show practically no signs of fracturing in the aforementioned areas. The fractures that are observed have mainly been produced by tectonic movements, and for craters with sizes similar to the ones from the simulations performed, observations show primarily smooth floors rather than fractures [94].

On the other side, an explanation can be devised on why fractures are not observed for these craters. For instance, fractures in the crust freeze shut over time, and post-relaxation effects and tectonic movements could contribute to erasing them from the surface. Only for craters equal to or larger than 50-80 km in diameter, does fracturing become more visible, although this is not always the case [94, 95]. According to Elder et al. [94], such craters exhibit signs of fracturing more often, and also show an additional surface feature caused by fracturing, namely central pits. Elder et al. [94] states that central pits can form due to drainage of impact melt through the produced fractures.

Thus, damage and fracturing are more useful to study for larger impacts than considered in this report. However, even then, fractures are not always visible, but the presence of a central pit can be used to identify craters where extensive fracturing occurred.

8.2.3. Comparing the Temperature

The temperature within and around the crater can provide valuable insight into the phase of the ice. As shown in Figure 7.5 and Figure 8.4, the majority of high-temperature material is concentrated near the impact site, particularly for larger impacts, where it covers a great part of the crater floor as well.

Comparisons with observations, and prior research by López [97], shows that for fresh craters on Rhea, crystalline ice is present not only within the crater, but also in surrounding areas, which can be seen in Figure 8.8. This phenomenon is also present on Ganymede, and is the result from heat generated during the impact, which triggers phase changes and re-crystallization of amorphous ice. Meanwhile, the vaporized material rapidly cools (flash-freeze) and falls back onto the surface. Figure 8.8b shows a plot of the grain size of these icy particles, with a notably large area outside the crater under the form of crystalline ice.

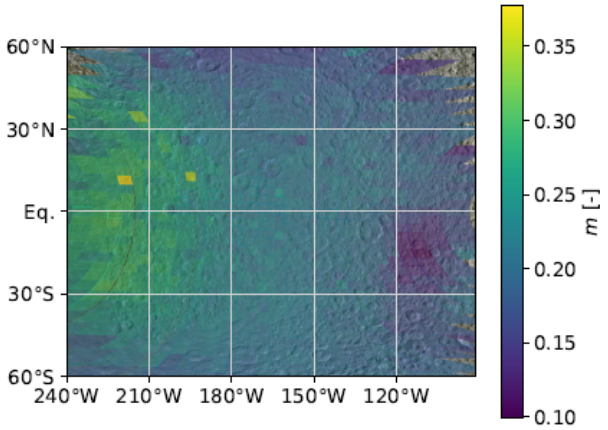

(a) Mass fraction of amorphous ice. The lower the value of m, the more crystalline ice is present. For the Inktomi crater, this leads up to 90% crystalline ice.

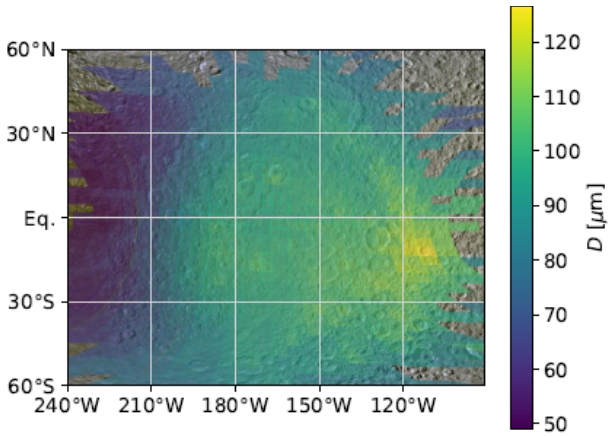

(b) Grain size of icy particles. It can be seen that for the Inktomi crater, there is a clear maximum in grain size, and even ray patterns can be seen.

Figure 8.8: Plots of the amorphous ice mass fraction and grain size from part of the terrain of Rhea, taken from López [97]. The Inktomi crater, located at 14.0°S and 112.0°W, can be seen as a prominent feature, where in Figure 8.8a it exhibits the lowest mass fraction, and in Figure 8.8b is displays the highest grain size.

Figure 8.8 shows that the smallest value of m and the largest value of D are located in the Inktomi crater. However, while the grain size remains large even outside the crater and over a large area, the amorphous ice mass fraction outside of the crater increases. According to López [97], this suggests that thermal energy transfer takes place upon contact between vaporized material, likely warmer than the surface, and the regolith, which triggers sintering. This increases the grain size in the surface layers, explaining the value of D. As for the ice mass fraction, the temperatures involved could simply be insufficient for the crystallization process to occur, but still high enough to create larger grains size. This would align with the findings from Figure 7.5, where crystalline ice is predominantly located in the crater. Furthermore, Figure 8.9 shows that the ejecta from the 1000 m and 15 km/s simulation exhibits a relatively high temperature, but not sufficiently so that it allows for full crystallization.

Such findings might be able to help and narrow down relationships between impact energy and the amount of (sintered) crystalline ice. Crystalline ice is created after an impact, and so a relation could be drawn between estimated impact energy and observed (sintered) crystalline ice.

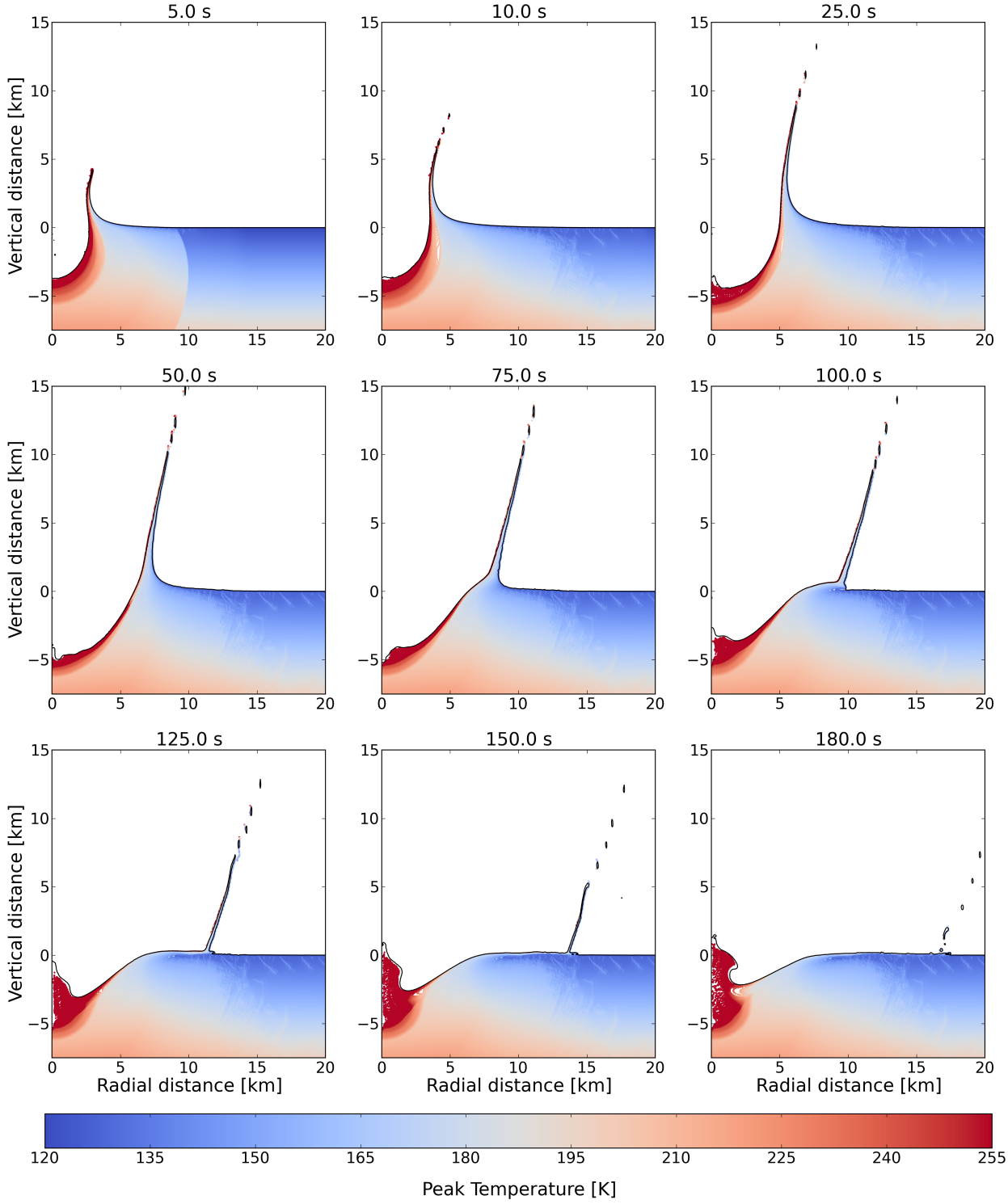

Figure 8.9: Peak temperature plot from the 1000 m impactor diameter and 15 km/s Ganymede simulation. A very thin part of the top layer of the ejecta shows a temperature equal to or higher than 255 K, however the majority of the material is cooler, yet still warmer than the surface temperature.

While the ejecta remains warm upon contact with the surface, it does only partially, and briefly, reach the threshold for full crystallization. As shown in Figure 7.4 considering larger timescales in the order of tens to hundreds of seconds, the crystallization temperature shifts to approximately 155 K. Ejecta that exhibits this temperature is mainly located near the crater. Although iSALE2D cannot simulate grain size, the temperature findings support the hypothesis proposed by López [97]: ejecta temperatures exceed the surface temperature but remain largely insufficient for crystallization. These observations, particularly for larger craters, suggest a potential distinction between low-velocity and high-velocity impacts, with the latter producing more pronounced thermal and phase-change effects. Thus, observations that show potential for distinguishing between plane-

tocentric and heliocentric impacts, would be related to a combination of temperature in and around the crater, mass fraction and grain size of particles.

8.2.4. Linking Findings to Observations

The simulations presented in Chapter 7 have been interpreted and compared to several sources of information. However, it is important to link the findings obtained throughout this report to observations, in order to uncover methods that can be used to provide a distinction between planetocentric and heliocentric impactors, which can ultimately address the research question.

From crater morphology results, the simulations showed a distinctly lower depth-to-diameter ratio for impacts at 15 km/s. This difference implies that crater depth and diameter measurements from observations could help locate where the observed craters belong along the modeled 5 km/s and 15 km/s curves. The outcome may indicate whether they are more consistent with lower- or higher-velocity impacts. In this way, the analysis could help infer whether an impactor was likely of planetocentric or heliocentric origin.

It was noticed that fracturing is more prominent for 15 km/s simulations, while the 5 km/s simulations exhibit fracturing to a lesser degree. Although small-scale fracturing does not significantly alter crater morphology, large or deep fractures could promote drainage of impact melt and the formation of central pits, which according to the fracturing patterns from the simulations, occurs mostly for the 15 km/s simulations. Consequently, the presence of central pits or drained melt deposits in large craters could point to higher-velocity (heliocentric) impacts. However, this is assuming that the response can be extrapolated to craters of larger sizes.

Regarding the temperature and ice phases, all simulations showed the formation of crystalline ice on the crater floor and partially on the crater wall. Also, a thin layer of warm, but not high-temperature material, can be observed closely surrounding the crater on the surface. It was noticed though, that for the 15 km/s simulations, the amount of crystalline ice covers a much larger area on the crater floor and along the surface than for the 5 km/s simulations, typically reaching halfway the crater wall. Additionally, the 15 km/s simulation results matched with the observations of grain sizes and amorphous ice mass fraction in Subsection 8.2.3, which could be used to find craters that are similar, and therefore are more probable to have been created by 15 km/s impacts rather than 5 km/s. Observations would look for craters that exhibit a low amorphous ice mass fraction in and around the crater, and have icy particles with large grain sizes.

8.3. Limitations of the Results

This section discusses the limitations associated with the crater impact simulations presented in Chapter 7. First, the assumptions stated in Subsection 7.1.2 are revisited in Subsection 8.3.1 to highlight the limitations they impose on the results. Subsection 8.3.2 then covers the limitations resulting from the inability to use the PEIERLS viscosity model. Finally, limitations regarding post-impact effects are discussed in Subsection 8.3.3.

8.3.1. Effect of the Assumptions

Assumptions are used to simplify the problem while ensuring sufficiently accurate results. However, this introduces inherent constraints that limit the scope of the simulations. Here, the limitations that are involved with the assumptions made in Subsection 7.1.2 are discussed.

The first assumption assumes a perfectly vertical impact, in essence, an impact angle of 90 degrees relative to the target surface. In reality, this is an unrealistic scenario, which limits the applicability of the results. However, according to Michikami et al. [102], impacts that occur at an impact angle greater than approximately 20 degrees still create a circular crater and a similar shape as craters striking a target head-on. Moreover, approximately the same amount of heated material is produced. Collins et al. [103] even state impact angles as low as 10 degrees would have this effect. Combining this with the fact that most impacts have been determined to occur at impact angles of 45 degrees, and approximately 90% of all impacts occur at angles smaller than 70 degrees, this assumption is viable and can be used for the vast majority of impact events [104]. The actual limitation here lies with impacts that strike a target with angles lower than 10-20 degrees, which will create a crater shaped as a butterfly, where most of the material shoots out to the sides and a more oval-shaped and shallow crater is left behind [103]. In short, due to this assumption, impacts at very low angles cannot with

sufficient accuracy be simulated, thus the results are limited to impacts at angles larger than 10-20 degrees.

The second assumption is with respect to undifferentiated materials. In reality, impactors are composed of a mixture of materials, such as ice, silicates, and metals. Creating an accurate EOS for such complicated compositions is practically impossible. Hence, the simulations are limited to the usage of homogeneous materials, which in this case is pure ice. Nevertheless, Ganymede's surface has been determined to be composed of primarily water ice [105]. Therefore, this assumption is still valid in this scenario.

The final assumption is the usage of a linear thermal gradient. In reality, the thermal gradient can vary depending on location, the presence of a subsurface and its composition, and several geological processes. This is virtually impossible to recreate, which limits the accuracy the results can provide compared to real scenarios. However, based on the findings from Subsection 6.2.6 and Chapter 7, it was observed that the effect of the thermal profile does not significantly influence the cratering process. Therefore, despite this limitation, the results remain useful to answer the research question.

8.3.2. iSALE2D Viscosity Model

From Chapter 5, a notable difference was observed between the default viscosity model used by iSALE2D and the PEIERLS model. The PEIERLS model results in slightly larger crater diameters, shallower depths, and reduced high-temperature areas, which are more spherical in shape. Moreover, material behavior differs as well; for the default model, the material is lifted up after the contact phase, and then turns over and falls back on the surface, allowing for surrounding low-temperature material to slide in between high-temperature material. Additionally, it increases the depth of high-temperature material, which was also explained in Subsection 8.1.3.

Since a part of the previously conducted research worked with the PEIERLS viscosity model, there are limitations as to how the results from this report can be compared. However, even with the differences between the viscosity models, Chapter 5 showed that the final crater dimensions and final crater shape deviate only slightly in comparison to results employing the PEIERLS model. Therefore, if differences in diameter, depth, shape, and temperature are taken into consideration, a comparison can be made.

8.3.3. Post-Impact Effects

The simulations show the immediate post-impact results, excluding long-term effects such as crater relaxation and cooling. While computational limitations are an obvious factor, the ACFL parameters partially address crater relaxation by shaping the crater to align with observations, which inherently incorporates these relaxation effects, as described in Subsection 6.3.5. Cooling effects, however, remain unmodeled. Nevertheless, temperature changes can have long-lasting effects on the surface, partially due to ice's low thermal conductivity [106]. Additionally, studies by Turtle et al. [107] and Silber and Johnson [2] suggest that thermal anomalies in icy crusts could persist for thousands to millions of years, depending on the impact scale and local environmental conditions. Furthermore, Kattenhorn and Prockter [108] notes that impact-induced fracturing and deformation can allow warmer subsurface material to rise, thereby prolonging localized thermal effects.

9
Conclusion and Recommendations

In this chapter, conclusions are drawn in Section 9.1, which are based on the results obtained throughout this report. Additionally, the research question and sub-questions are answered. Finally, recommendations are given in Section 9.2, to point out potential research directions.

9.1. Conclusions

In order to help answer the main research question, multiple sub-questions were proposed in Section 2.8, and will now be answered based on the knowledge and findings obtained in this report.

1. **Is the resolution of the different equations of state in iSALE2D high enough to be able to distinguish different ice phases?**
   The EOSs were examined in Chapter 3 by plotting a heatmap with pressure on the y-axis, temperature on the x-axis, and varying density. A clear difference in resolution and quality was observed between the two available ANEOS EOSs for water. The water_ice EOS, compared to the h2o_ice EOS, has very low resolution, making it nearly impossible to distinguish between different ice phases. Conversely, the h2o_ice EOS showed much more promise due to a much higher resolution, allowing most ice phases to be identified in the plot of the heatmap. However, near the boundary between solid, liquid and gas phases, the resolution remains considerably low.

2. **Are there other promising equations of state outside of the ones present in iSALE2D?**
   Alternative EOSs for water have been developed by various researchers and research groups, and could offer improved results. For example, the 5-phase EOS by Senft and Stewart [74] is suitable for impact cratering. However, consultation with the creator Professor Sarah T. Stewart, revealed that it is only viable for low pressures and low energy impacts, making it unsuitable for the simulations planned in this report.

   Another promising option is the AQUA EOS from Haldemann et al. [3], which is used in planetary modeling and can be used for impact cratering. Additionally, it was also recommended by Professor Stewart. This EOS proved very promising due to the resolution being the highest encountered so far, with data provided in a very clear and understandable manner. The data provides information not only on the pressure, temperature and density, but also the ice phases themselves directly. The plotted heatmap confirmed the superior resolution compared to the water_ice and h2o_ice EOSs. A downside, however, is that the minimum temperature of AQUA is limited to 100 K.

   Comparing the h2o_ice and AQUA EOSs in simulations revealed noticeable, though relatively small, differences. A clear distinction can be made during the impact. For h2o_ice, material that was excavated showed a violent or chaotic response, with material scattering and forming many small clumps of material. On the other side, AQUA simulations displayed smoother and more organized material behavior, resembling somewhat of a wave of material during excavation. All things considered, AQUA was selected as the best EOS for this study.

3. **How can the iSALE2D hydrocode be verified and validated?**
   The iSALE2D software is widely used in impact research and naturally has undergone verification and validation. However, to ensure correct installation and functionality, additional verification and validation was performed by recreating example problems provided by iSALE2D, which have been created precisely for this purpose. These tests showed no significant deviations, with only minor differences in a few cases.

   Besides the example problems, figures from two different research papers were also recreated. While small differences were observed, these were attributed to variations in iSALE2D version. Some versions include the PEIERLS viscosity model, which was unavailable for this study. Co-creator of iSALE2D Professor Collins pointed out that this caused the observed deviations in the final plots. These differences are henceforth acknowledged in the results and discussion.

4. **How can the diameter and depth be determined from the simulations?**
   Crater diameter and depth are critical features of a crater, but are not directly output by iSALE2D. To avoid inaccuracies and the inefficiency of reading every plot, a Python script was written that calculates the diameter and depth using the iSALE2D output file. The script analyzes the material density in each cell to determine the location of the surface contour, from which the location of the rim and the crater floor can be identified. From this, the crater diameter and depth easily follow.

5. **What are the effects of a sensitivity analysis of the input parameters on the final crater and the impact process?**
   There are numerous input parameters in iSALE2D that could influence the simulation. In order to determine the most sensitive parameters, a sensitivity analysis was performed in Chapter 6. Here, the effects on crater diameter and crater depth by varying input parameters one-at-a-time is investigated. After comparing the results against a control simulation and quantifying the sensitivity, it was concluded that the parameters with the greatest effects on the crater shape and impact process were the surface gravity, impact velocity, impactor size, the friction coefficient of damaged material, the poisson ratio, and the thermal softening parameter. A special importance was placed on the ACFL parameters, which proved to be not as sensitive, but are highly variable in their range of values, with limited information on how to determine them.

6. **What is the influence of impact velocity and impactor size on the resulting crater morphology in impact simulations under Ganymede-like conditions?**
   The simulations showed that crater diameter and depth increased with impact energy. Comparing the 5 km/s and 15 km/s simulations, it was observed that depth does not change significantly for the 100 m, 250 m and 500 m impactor sizes. However, a more obvious distinction can be made for the crater diameter. Distinguishing these differences is easy when taking into account only the impactor size. However, considering the combination of impactor size and impact velocity, it remains difficult to make a clear distinction, as craters can have similar shapes for different combinations of impactor size and impact velocity.

   The depth-to-diameter ratio was found to decrease for larger impacts, which aligns with other research that simulated impacts in ice. This is primarily due to increase material fluidity in larger impacts, causing material to spread out under gravity and creating a shallower and flatter crater floor. Consequently, the diameter increases more than the depth, reducing the depth-to-diameter ratio.

   Plotting crater diameter and depth, alongside observational data and other research results, revealed that the Ganymede simulations performed in this report produced relatively small diameters for their corresponding depths. It was concluded from this that the fitted curves tend to overestimate the data. Nonetheless, the data itself does not consist of outliers, and falls within observations. Explanations are highly likely related to the viscosity model, as mentioned in Chapter 5. It showed that a smaller diameter and greater depth should be expected when comparing results with other research. In fact, this is evident from the location of the curve from Bjonnes et al. [1], which used the PEIERLS viscosity model. It was expected that this curve had a lower depth and larger diameters, which were indeed observed from the plot.

7. **What is the influence of impact velocity and impactor size on the resulting crater damage in impact simulations under Ganymede-like conditions?**
   The crater damage was also analyzed for various impact velocities and impactor sizes. For the 5 km/s simulations, damage is minimal beyond the radius from the center of the crater to the rim. However, in the 15 km/s simulations, damage is also evident near the surface, likely due to ejecta deposition. Fractures in the target are especially prominent in the 15 km/s cases compared to 5 km/s.

   Regarding the impactor size, damage depth increases significantly for the 500 m and 1000 m simulations compared to the damage in the radial direction, particularly for the 15 km/s simulations. This could be related to the relatively warmer, and therefore weaker, material at those depths, allowing the pressure wave to penetrate further while retaining sufficient energy to afflict extensive damage. Another factor could be the ACFL parameters, as they directly influence vibration duration and strength.

Comparing the damage to observations, it becomes apparent that smaller craters show primarily smooth crater floors, with practically no visible fracturing. This could be explained by that fact that fractures in the crust freeze shut over time, which would happen more quickly for craters were fracturing is limited, and post-relaxation effects and tectonic movements could contribute to erasing them from the surface. Only for craters equal to or larger than 50-80 km in diameter does fracturing become more visible. Even then, fracturing might not be observable. However, such craters can exhibit other signs of fracturing in the form of central pits, which can form due to drainage of impact melt through the produced fractures [94–96].

Thus, damage and fracturing are more useful to study for larger impacts than considered in this report. However, even then, fractures are not always visible, but the presence of a central pit can be used to identify craters where extensive fracturing occurred.

8. **What is the influence of impact velocity and impactor size on the resulting crater temperature and ice phases in impact simulations under Ganymede-like conditions?**
Logically, the crater temperature was found to increase with higher impact energy. For the 15 km/s simulations, the crater floor was largely covered by high-temperature material, and heated material was found at considerably greater depths. Additionally, substantial temperature increases were noted further from the impact site, particularly in the 500 m and 1000 m simulations. For the 15 km/s cases, high-temperature material was found beneath the surface over a wide horizontal extend.

   Plots were created highlighting high-temperature ($\geq$ 255 K) material, or crystalline ice. Results showed a distinct difference in the amount present inside and surrounding the crater. For 15 km/s simulations, the amount of high-temperature material in the crater was found to be almost double that for 5 km/s, and mainly located on the crater floor and crater walls.

   Research by López [97] was used for comparison. They show that observations of amorphous ice mass fraction and grain size can be used to determine the state of icy material. Typically, high-temperature crystalline ice will have a low amorphous mass fraction, and high grain size due to the increased temperature clumping together icy particles. From fresh crater observations on Rhea, crystalline ice was observed mainly inside the crater, and partially surrounding the crater, whereas large grain sizes remained even outside of the crater and over a large area.

   Since the 1000 m and 15 km/s simulation produced a similarly sized crater, it was used for the comparison. For this simulation, high-temperature crystalline ice is primarily located within the crater. Outside of the crater, temperatures were found too low for crystallization, but sufficient for larger grains to grow. Since these findings were also observed by López [97], the 1000 m and 15 km/s simulation shows good agreement with the results. Thus, craters that exhibit similar amorphous ice mass fractions and grain sizes might be useful to indicate craters with a high-velocity impactor origin.

With the sub-questions answered, the main research question, originally stated in Chapter 2, can now be addressed. However, this question requires modification. Initially, the focus was partially on performing impacts on Enceladus-like targets, however, due to unknown ACFL parameters, which can significantly influence the crater shape, these simulations were eventually excluded. Therefore, the main research question is revised to: *"Can crater morphology, target damage, target temperature, and different ice phases be used to identify whether the impactor had a heliocentric or planetocentric origin in craters on icy moons?"*

To answer the research question, this report investigated the effects of different impact velocities and impactor sizes on crater shape, target damage, and temperature distributions through impact simulations.

Crater morphology results revealed notable differences between the 5 km/s and 15 km/s simulations. Although best-fit curves for crater diameter and depth slightly overestimate the crater depth, primarily due to the difference in the viscosity model of the hydrocode, it still shows a distinct difference in the depth-to-diameter ratio. Therefore, knowing the crater diameter and depth could lead to an indication of whether they are more consistent with lower- or higher-velocity impacts, based on its location with respect to the best-fit curves of depth-to-diameter ratio.

Damage analysis showed that 15 km/s impacts caused significant fracturing deep within the target, unlike the limited fracturing observed in the 5 km/s simulations, even at larger impactor sizes. However, observations for craters with similar sizes show limited to no impact-induced fracturing, and only for craters $\geq$ 50-80 km does

it more noticeable. Although, even then fractures remain difficult to observe. This can be related to fractures that freeze shut and erode over time due to post-impact relaxation and tectonic movements. However, before this happens, when fracturing is extensive, central pits can be formed. This means that for large crater, such observations could indicate that they were created by high-velocity impactors, as only the results from the 15 km/s simulations show this extensive fracturing pattern. However, this is assuming the outcome is linear, and can be extrapolated to such large crater sizes.

Regarding the temperature and ice phases, crystalline ice is formed on the crater floor and crater walls upon impact, and a thin warm layer of material was observed surrounding the crater for larger impacts. These features were observed more significantly for the 15 km/s simulations, especially the distribution of high-temperature (or crystalline ice) inside the crater, which was found to be double the amount compared to the 5 km/s simulations. Additionally, from comparisons with research by López [97], it was determined that the 1000 m and 15 km/s simulation matches the observations of low amorphous ice mass fractions in combination of large grain sizes in and around the researched crater. This could indicate that observed craters in a similar situation were also created by a high-velocity impactor with a heliocentric origin.

Combining the findings above, observations of crater diameter, crater depth, presence of fracturing and/or central pit, crystalline ice, amorphous ice mass fraction, and icy particle grain size, can give a good first indication of what the origin of the impactor was. However, many uncertainties remain, and several adjustments and improvements could be made to attain a more concrete answer. Therefore, recommendations are given in Section 9.2 for future research.

9.2. Recommendations

In this section, recommendations are given to improve upon the research performed in this report. Different or additional options, methods, and approaches will be discussed that have not been used in this research, which can explore new possibilities in this field. Subsection 9.2.1 describes how the ACFL parameters can be improved, and looks at other icy moons. In Subsection 9.2.2, the usage of the PEIERLS viscosity model is discussed. Then, in Subsection 9.2.3, recommendations regarding increasing the range of impactor sizes and the number of simulations is discussed. Finally, recommendations related to 3D simulations are given in Subsection 9.2.4.

9.2.1. ACFL Parameters and Other Moons

From Subsection 6.3.5, it was concluded that the ACFL parameters are important to the impact dynamics. As a result, specific equations from Bray et al. [65] were utilized to achieve crater morphologies that are consistent with observations. However, these equations are valid only under specific conditions, such as Ganymede-like and Europa-like environments, and cannot reliably be applied to other icy moons. The reason is the lack of best-fit ACFL values, which could lead to crater morphologies that deviate significantly from observations.

To address this, a dedicated ACFL parameter study is recommended. By systematically varying γ_β and γ_η and analyzing the resulting crater morphologies, best-fit equations can be derived, similar to the approach used by Bray et al. [65]. This approach could also include different impact velocities, which could prove useful as the 5 km/s simulations in this study relied on the ACFL values originally determined for the 15 km/s impacts.

Expanding the scope to other icy moons, such as Enceladus, could offer valuable insights. With large parts of the surface being covered in snow, and with a substantial subsurface ocean, it presents unique conditions for crater formation. Simulating these factors may reveal unexpected differences or correlations when compared to Jovian and Saturnian moons.

9.2.2. Different Viscosity Models

As noted in Section 5.2, the choice of viscosity model showed a distinguishable impact on the simulation outcome. A comparison between the default viscosity model in iSALE2D and the PEIERLS viscosity model revealed small differences in crater dimensions, but particularly notable changes in the distribution of high-temperature material. Future studies should systematically explore the effects of different viscosity models. For instance, the trends observed in Figure 8.6 suggest that utilizing the PEIERLS viscosity model could align the simulation results more closely with observational data and previous research. Using the PEIERLS viscosity model may also provide clearer distinctions between simulations at different velocities and impactor sizes,

which can help identify impact conditions.

9.2.3. Increase Range of Impactor Sizes and Number of Simulations

The impactor sizes used in this study ranged from 100 m to 1000 m, but expanding this range, and increasing the number of simulation, could enhance the dataset and improve accuracy. A greater variety of size would aid in the challenge of distinguishing craters created by lower velocities and larger sizes, from those caused by higher velocities and smaller sizes. Intermediate sizes within the current range could provide enhanced insights, while smaller impactor sizes would be particularly relevant for simulating planetocentric impactors, which are typically on the smaller side and especially relevant when simulating impacts on bodies such as Enceladus.

Simulating different velocities could also provide a different perspective. By introducing intermediate values between 5 km/s and 15 km/s, this could help bridge the gap in current datasets and identify finer trends in the results.

Additionally, increasing the number of simulations allows for the usage of a more advanced sensitivity analysis such as Morris's method, which can provide a more complete overview of the sensitivity of the input parameters.

9.2.4. 3D Simulations

The simulations conducted in this study were two-dimensional, which inherently limited the diversity of impact scenarios and the detail of the results. Transitioning to 3D simulations could address these limitations by enabling the ability to simulate oblique impacts, which would provide a new perspective. Additionally, features such as central peaks and ejecta distributions are better resolved in 3D simulations. An example of an impact simulation in iSALE3D is shown in Figure 9.1, which provides a top view of an impact crater one second after impact. Material located underneath surface level is depicted in a blue or purple color, while uplifted material is shown in orange and red.

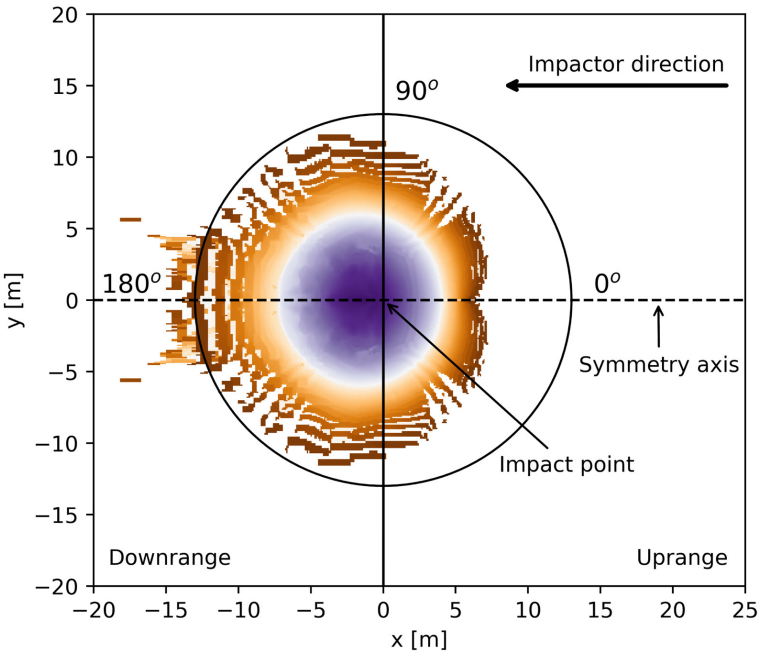

Figure 9.1: Top view of an impact crater resulting from a 3D simulation in iSALE3D at a 45 degree impact angle, one second after impact. Material located underneath the surface level is shown in a blue and purple color, while uplifted material is represented by orange and red [109].

Figure 9.1 provides a clear overview of the crater and ejecta pattern. Central peaks, if present, could also be identified in this way. These features are critical for understanding their relation regarding impact energy. Improved resolution in 3D simulations could also clarify velocity-dependent variations in ejecta patterns, which could be independent of impactor size.

Bibliography

[1] Bjonnes, E., Johnson, B., Silber, E., Singer, K., and Evans, A., "Ice shell structure of Ganymede and Callisto based on impact crater morphology," *Journal of Geophysical Research: Planets*, Vol. 127, No. 4, 2022, p. e2021JE007028. doi: https://doi.org/10.1029/2021JE007028.

[2] Silber, E. A., and Johnson, B. C., "Impact Crater Morphology and the Structure of Europa's Ice Shell," *Journal of Geophysical Research: Planets*, Vol. 122, No. 12, 2017, pp. 2685–2701. doi: https://doi.org/10.1002/2017JE005456.

[3] Haldemann, J., Alibert, Y., Mordasini, C., and Benz, W., "AQUA: A Collection of H2O Equations of State for Planetary Models," *Astronomy & Astrophysics*, Vol. 643, 2020, p. A105. doi: 10.1051/0004-6361/202038367.

[4] Collins, G. S., Melosh, H. J., and Ivanov, B. A., "Modeling damage and deformation in impact simulations," *Meteoritics & Planetary Science*, Vol. 39, No. 2, 2004, pp. 217–231. doi: https://doi.org/10.1111/j.1945-5100.2004.tb00337.x.

[5] Bell, S. W., "Relative Crater Scaling Between the Major Moons of Saturn: Implications for Planetocentric Cratering and the Surface Age of Titan," *Journal of Geophysical Research*, Vol. 125, 2020, p. e2020JE006392. doi: https://doi.org/10.1029/2020JE006392.

[6] Colzi, L., *Isotopic fractionation study towards massive star-forming regions across the Galaxy*, Firenze University Press, 2021. doi: 10.36253/978-88-5518-380-2.

[7] Casasola, V., "The Small Scale Physical Evolution of Molecular Gas in Nearby Galaxies," Phd thesis, Université Pierre et Marie Curie - Paris VI, 2008. url: https://theses.hal.science/tel-00608597.

[8] Lissauer, J. J., and de Pater, I., *Fundamental Planetary Science: Physics, Chemistry and Habitability*, Cambridge Univerity Press, 2019.

[9] James, D. J., Aarnio, A. N., Richert, A. J. W., Cargile, P. A., Santos, N. C., Melo, C. H. F., and Bouvier, J., "Fundamental stellar parameters for selected T-Tauri stars in the Chamaeleon and Rho Ophiuchus star-forming regions," *Monthly Notices of the Royal Astronomical Society*, Vol. 459, No. 2, 2016, pp. 1363–1392. doi: 10.1093/mnras/stw481.

[10] Matsuo, T., Shibai, H., Ootsubo, T., and Tamura, M., "Planetary Formation Scenarios Revisited: Core-Accretion versus Disk Instability," *The Astrophysical Journal*, Vol. 662, No. 2, 2007. doi: 10.1086/517964.

[11] Rice, K., "Planet Formation Through Gravitational Instabilities," , 01 2023. doi: 10.1093/acrefore/9780190647926.013.250.

[12] Boss, A., "Giant Planet Formation by Gravitational Instability," *Science*, Vol. 276, No. 5320, 1997, pp. 1836–1839. doi: 10.1126/science.276.5320.1836.

[13] Kratter, K., and Lodato, G., "Gravitational Instabilities in Circumstellar Disks," *Annual Review of Astronomy and Astrophysics*, Vol. 54, 2016, pp. 271–311. doi: https://doi.org/10.1146/annurev-astro-081915-023307.

[14] Helled, R., and Schubert, G., "HEAVY-ELEMENT ENRICHMENT OF A JUPITER-MASS PROTOPLANET AS A FUNCTION OF ORBITAL LOCATION," *The Astrophysical Journal*, Vol. 697, No. 2, 2009, p. 1256. doi: 10.1088/0004-637X/697/2/1256.

[15] Canup, R. M., and Ward, W. R., "Origin of Europa and the Galilean Satellites," , 2008. url: https://arxiv.org/abs/0812.4995.

[16] Asphaug, E., and Reufer, A., "Late origin of the Saturn system," *Icarus*, Vol. 223, No. 1, 2013, p. 544–565. doi: https://doi.org/10.1016/j.icarus.2012.12.009.

[17] Anderson, S. E., Mousis, O., and Ronnet, T., "Formation conditions of Titan and Enceladus' building blocks in Saturn's circumplanetary disk," *The Planetary Science Journal*, Vol. 2, No. 2, 2021, p. 50–57. doi: https://doi.org/10.3847/PSJ/abe0ba.

[18] Crida, A., and Charnoz, S., “Formation of Regular Satellites from Ancient Massive Rings in the Solar System,” *Science*, Vol. 338, 2012, p. 1196–1199. doi: 10.1126/science.1226477.

[19] Canup, R., and Ward, W., “A common mass scaling for satellite systems of gaseous planets,” *Nature*, Vol. 441, 2006, pp. 834–839. doi: https://doi.org/10.1038/nature04860.

[20] DLR, “Asteroids – the remains of planetary building materials,” https://www.dlr.de/en/research-and-transfer/projects-and-missions/hayabusa2/asteroids-the-remains-of-planetary-building-materials, 2024. Accessed October 10, 2025.

[21] Kurokawa, H., Shibuya, T., Sekine, Y., Ehlmann, B. L., Usui, F., Kikuchi, S., and Yoda, M., “Distant Formation and Differentiation of Outer Main Belt Asteroids and Carbonaceous Chondrite Parent Bodies,” *AGU Advances*, Vol. 3, No. 1, 2022, p. e2021AV000568. doi: https://doi.org/10.1029/2021AV000568.

[22] Marchi, S., McSween, H. Y., O’Brien, D. P., Schenk, P., Sanctis, M. C. D., Gaskell, R., Jaumann, R., Mottola, S., Preusker, F., Raymond, C. A., Roatsch, T., and Russell, C. T., “The Violent Collisional History of Asteroid 4 Vesta,” *Science*, Vol. 336, No. 6082, 2012, pp. 690–694. doi: 10.1126/science.1218757.

[23] Davis, D. R., Chapman, C. R., Weidenschilling, S. J., and Greenberg, R., “Collisional history of asteroids: Evidence from Vesta and the Hirayama families,” *Icarus*, Vol. 62, No. 1, 1985, pp. 30–53. doi: https://doi.org/10.1016/0019-1035(85)90170-8.

[24] Bray, V. J., Schenk, P. M., Melosh, H. J., Morgan, J. V., and Collins, G. S., “Ganymede crater dimensions – Implications for central peak and central pit formation and development,” *Icarus*, Vol. 217, No. 1, 2012, pp. 115–129. doi: https://doi.org/10.1016/j.icarus.2011.10.004.

[25] Hargitai, H., and Watters, W. A., *Encyclopedia of Planetary Landforms*, Springer New York, 2021. doi: 10.1007/978-1-4614-9213-9_348-1.

[26] Kiefer, W. S., “Impact Craters in the Solar System,” 2003. url: https://www.lpi.usra.edu/science/kiefer/Education/SSRG2-Craters/craterstructure.html, Accessed March 2, 2023.

[27] Melosh, H. J., *Impact Cratering: A Geologic Process*, Oxford University Press, 1989.

[28] Plescia, J. B., *Transitional Crater (Simple/Complex)*, Springer New York, New York, NY, 2021, pp. 1–5. doi: 10.1007/978-1-4614-9213-9_407-2.

[29] Patterson, G. W., Collins, G. C., Head, J. W., Pappalardo, R. T., Prockter, L. M., Lucchitta, B. K., and Kay, J. P., “Global geological mapping of Ganymede,” *Icarus*, Vol. 207, No. 2, 2010, p. 845–867. doi: https://doi.org/10.1016/j.icarus.2009.11.035.

[30] Lunar and Planetary Institute (LPI), “Callisto,” , 1997. url: https://www.lpi.usra.edu/resources/outerp/call.html, Accessed March 3, 2023.

[31] Schenk, P. M., Chapman, C. R., Zahnle, K., and Moore, J. M., “Ages and interiors: The cratering record of the Galilean satellites,” *Cambridge University Press*, 2004, p. 427–456.

[32] Holsapple, K. A., “The Scaling of Impact Processes in Planetary Sciences,” *Annual Review of Earth and Planetary Sciences*, Vol. 21, 1993, pp. 333–373. doi: https://doi.org/10.1146/annurev.ea.21.050193.002001.

[33] Croft, S. K., “Crater Depth/Diameter/Morphology Relationships on the Icy Satellites: Implications for Ice Rheology,” https://ui.adsabs.harvard.edu/abs/1988LPI....19..219C/abstract, 1988. Accessed September 26, 2025.

[34] Kring, D., “Formation of a simple crater,” https://www.lpi.usra.edu/exploration/training/illustrations/craterFormation/, 2006. Accessed March 6, 2023.

[35] Prieur, N. C., Rolf, T., Luther, R., Wünnemann, K., Xiao, Z., and Werner, S. C., “The effect of target properties on transient crater scaling for simple craters,” *Journal of Geophysical Research: Planets*, Vol. 122, No. 8, 2017, pp. 1704–1726. doi: https://doi.org/10.1002/2017JE005283.

[36] McKinnon, W. B., “Galileo at Jupiter - meetings with remarkable moons,” *Nature*, Vol. 390, 1997, p. 23–26. doi: https://doi.org/10.1038/36222.

[37] Bierhaus, E. B., and Schenk, P. M., “Constraints on Europa’s surface properties from primary

and secondary crater morphology," *Journal of Geophysical Research*, Vol. 115, 2010. doi: https://doi.org/10.1029/2009JE003451.

[38] King, O., Fletcher, L. N., and Ligier, N., "Compositional Mapping of Europa Using MCMC Modeling of Near-IR VLT/SPHERE and Galileo/NIMS Observations," *The Planetary Science Journal*, Vol. 3, No. 3, 2022, p. 72. doi: 10.3847/psj/ac596d.

[39] Institute, N.-C., "Europa's Stunning Surface," https://www.jpl.nasa.gov/images/pia19048-europas-stunning-surface, 2014. Accessed October 24, 2023.

[40] Pappalardo, R. T., "Seeking Europa's Ocean," *Proceedings of the International Astronomical Union*, Vol. 6, No. S269, 2010, p. 101–114. doi: 10.1017/S1743921310007325.

[41] Canup, R., and Ward, W., "Formation of the Galilean Satellites: Conditions of Accretion," *The Astronomical Journal*, Vol. 124, 2002, pp. 3404–3423. doi: https://doi.org/10.1086/344684.

[42] Lunar and Planetary Institute (LPI), "Ganymede," https://www.lpi.usra.edu/resources/outerp/gany.html, 1997. Accessed March 16, 2023.

[43] Pappalardo, R. T., Collins, G. C., Head, J. W., III, Helfenstein, P., McCord, T. B., Moore, J. M., Prockter, L. M., Schenk, P. M., and Spencer, J. R., "Geology of Ganymede," *Cambridge University Press*, 2004, p. 363–396.

[44] Greely, R., Klemaszewski, J. E., and Wagner, R., "Galileo views of the geology of Callisto," *Icarus*, Vol. 48, No. 9, 2000, p. 829–853. doi: https://doi.org/10.1016/S0032-0633(00)00050-7.

[45] Schenk, P. M., "The geology of Callisto," *Journal of Geophysical Research: Planets*, Vol. 100, No. E9, 1995, pp. 19023–19040. doi: https://doi.org/10.1029/95JE01855.

[46] Wood, C. A., Lorenz, R., Kirk, R., Lopes, R., Mitchell, K., and Stofan, E., "Impact craters on Titan," *Icarus*, Vol. 206, No. 1, 2010, pp. 334–344. doi: https://doi.org/10.1016/j.icarus.2009.08.021.

[47] Artemieva, N., and Lunine, J., "Cratering on Titan: impact melt, ejecta, and the fate of surface organics," *Icarus*, Vol. 164, No. 2, 2003, pp. 471–480. doi: https://doi.org/10.1016/S0019-1035(03)00148-9.

[48] Kirchoff, M. R., and Schenk, P. M., "Crater modification and geologic activity in Enceladus' heavily cratered plains: Evidence from the impact crater distribution," *Icarus*, Vol. 202, No. 2, 2009, pp. 656–668. doi: https://doi.org/10.1016/j.icarus.2009.03.034.

[49] Bland, M. T., Singer, K. N., McKinnon, W. B., and Schenk, P. M., "Enceladus' extreme heat flux as revealed by its relaxed craters," *Geophysical Research Letters*, Vol. 39, No. 17, 2012. doi: https://doi.org/10.1029/2012GL052736.

[50] Schenk, P. M., and Seddio, S., "Geologic and cratering history of Enceladus," American Astronomical Society, DPS meeting #38, 2006. Bulletin of the American Astronomical Society, Vol. 38, p.513.

[51] Bray, V. J., Smith, D. E., Turtle, E. P., Perry, J. E., Rathbun, J. A., Barnash, A. N., Helfenstein, P., and Porco, C. C., "Impact Crater Morphology Variations on Enceladus," 38th Lunar and Planetary Science Conference, (Lunar and Planetary Science XXXVIII), 2007. Held in League City, Texas. LPI Contribution No. 1338, p.1873.

[52] Zahnle, K., Schenk, P., Sobieszczyk, S., Dones, L., and Levison, H. F., "Differential Cratering of Synchronously Rotating Satellites by Ecliptic Comets," *Icarus*, Vol. 153, 2001, pp. 111–129. doi: 10.1006/icar.2001.6668.

[53] Öpik, E. J., "Collision Probabilities with the Planets and the Distribution of Interplanetary Matter," *Proceedings of the Royal Irish Academy. Section A: Mathematical and Physical Sciences*, Vol. 54, 1951, pp. 165–199. url: http://www.jstor.org/stable/20488532.

[54] Zimbelman, J. R., "Planetary impact probabilities for long-period comets," *Icarus*, Vol. 57, No. 1, 1984, pp. 48–54. doi: https://doi.org/10.1016/0019-1035(84)90006-X.

[55] Zahnle, K., Schenk, P., Levison, H., and Dones, L., "Cratering rates in the outer Solar System," *Icarus*, Vol. 163, No. 2, 2003, p. 263–289. doi: https://doi.org/10.1016/S0019-1035(03)00048-4.

[56] Baez, J., "Phase diagram of water," http://math.ucr.edu/home/baez/chemical/725px-Phase_diagram_of_

water.svg.png, 2012. Accessed October 24, 2023.

[57] Limmer, D. T., and Chandler, D., "Theory of amorphous ices," *Proceedings of the National Academy of Sciences*, Vol. 111, No. 26, 2014, pp. 9413–9418. doi: 10.1073/pnas.1407277111.

[58] Stewart, S. T., and Ahrens, T. J., "Shock properties of H2O ice," *Journal of Geophysical Research: Planets*, Vol. 110, No. E3, 2005. doi: https://doi.org/10.1029/2004JE002305.

[59] Anderson, C., "An overview of the theory of hydrocodes," *International Journal of Impact Engineering*, Vol. 5, No. 1, 1987, pp. 33–59. doi: https://doi.org/10.1016/0734-743X(87)90029-7.

[60] Pierazzo, E., Artemieva, N., Asphaug, E., Baldwin, E. C., Cazamias, J., Coker, R., Collins, G. S., Crawford, D. A., Davison, T., Elbeshausen, D., Holsapple, K. A., Housen, K. R., Korycansky, D. G., and Wünnenmann, K., "Validation of numerical codes for impact and explosion cratering: Impacts on strengthless and metal targets," *Meteorites & Planetary Science*, Vol. 43, No. 12, 2008, pp. 1917–1938. doi: https://doi.org/10.1111/j.1945-5100.2008.tb00653.x.

[61] Souli, M., Ouahsine, A., and Lewin, L., "ALE formulation for fluid–structure interaction problems," *Computer Methods in Applied Mechanics and Engineering*, Vol. 190, No. 5, 2000, pp. 659–675. doi: https://doi.org/10.1016/S0045-7825(99)00432-6.

[62] Pierazzo, E., "Numerical Modeling of Impact Cratering," 2006.

[63] Wang, G., Cheng, A. H.-D., Ostoja-Starzewski, M., Al-Ostaz, A., and Radziszewski, P., "Hybrid Lattice Particle Modelling Approach for Polymeric Materials Subject to High Strain Rate Loads," *Polymers*, Vol. 2, No. 1, 2010, pp. 3–30. doi: 10.3390/polym2010003.

[64] Senft, L. E., and Stewart, S. T., "Modeling the morphological diversity of impact craters on icy satellites," *Icarus*, Vol. 214, No. 1, 2011, pp. 67–81. doi: https://doi.org/10.1016/j.icarus.2011.04.015.

[65] Bray, V. J., Collins, G. S., Morgan, J. V., Melosh, H. J., and Schenk, P. M., "Hydrocode simulation of Ganymede and Europa cratering trends – How thick is Europa's crust?" *Icarus*, Vol. 231, 2014, pp. 394–406. doi: https://doi.org/10.1016/j.icarus.2013.12.009.

[66] Bray, V. J., "Impact Crater Formation on the Icy Galilean Satellites," Ph.D. thesis, Imperial College London, 2009.

[67] Crósta, A., Silber, E., Lopes, R., Johnson, B., Bjonnes, E., Malaska, M., Vance, S., Sotin, C., Solomonidou, A., and Soderblom, J., "Modeling the formation of Menrva impact crater on Titan: Implications for habitability," *Icarus*, Vol. 370, 2021, p. 114679. doi: https://doi.org/10.1016/j.icarus.2021.114679.

[68] Roberts, J., and Stickle, A., "Breaking the symmetry by breaking the ice shell: An impact origin for the south polar terrain of Enceladus," *Icarus*, Vol. 359, 2021, p. 114302. doi: https://doi.org/10.1016/j.icarus.2021.114302.

[69] Wissing, R., and Hobbs, D., "A new equation of state applied to planetary impacts - I. Models of planetary interiors," *Astronomy & Astrophysics*, Vol. 635, 2020, p. A21. doi: 10.1051/0004-6361/201935814.

[70] Tillotson, J., "Metallic Equations of State For Hypervelocity Impact," General Atomic Report GA-3216. 1962. Technical Report, jul 1962. url: https://ui.adsabs.harvard.edu/abs/1962geat.rept.3216T, provided by the SAO/NASA Astrophysics Data System.

[71] Collins, G. S., Elbeshausen, D., Davison, T. M., Wünnemann, K., Ivanov, B., and Melosh, H. J., "iSALE-Dellen manual," 2016. doi: 10.6084/m9.figshare.3473690.v2.

[72] Melosh, H. J., "A hydrocode equation of state for SiO2," *Meteoritics & Planetary Science*, Vol. 42, No. 12, 2007, pp. 2079–2098. doi: https://doi.org/10.1111/j.1945-5100.2007.tb01009.x.

[73] Linstrom, P. J., and Mallard, W. G., "NIST Chemistry WebBook," NIST Standard Reference Database Number 69, National Institute of Standards and Technology, Gaithersburg MD, 20899, 1996. doi: https://doi.org/10.18434/T4D303, Accessed August 7, 2023.

[74] Senft, L., and Stewart, S., "Impact crater formation in icy layered terrains on Mars," *Meteoritics & Planetary Science*, Vol. 43, No. 12, 2008, pp. 1993–2013. doi: https://doi.org/10.1111/j.1945-5100.2008.tb00657.x.

[75] Ebnesajjad, S., "Properties of Tetrafluoroethylene Homopolymers," *Fluoroplastics (Second Edition)*,

Vol. 1, edited by S. Ebnesajjad, William Andrew Publishing, Oxford, 2015, second edition ed., pp. 396–440. doi: https://doi.org/10.1016/B978-1-4557-3199-2.00018-5.

[76] Hunter, J. D., "Matplotlib: A 2D graphics environment," *Computing in Science & Engineering*, Vol. 9, No. 3, 2007, pp. 90–95. doi: 10.1109/MCSE.2007.55.

[77] Bradski, G., "The OpenCV Library," *Dr. Dobb's Journal of Software Tools*, 2000.

[78] Davidson, T., "isale-code," Github repository, 2021. url: https://github.com/isale-code/isale-wiki.

[79] Parmentier, E. M., and Head, J. W., "Viscous relaxation of impact craters on icy planetary surfaces: Determination of viscosity variation with depth," *Icarus*, Vol. 47, No. 1, 1981, pp. 100–111. doi: https://doi.org/10.1016/0019-1035(81)90095-6.

[80] JPL, N., "Solar System Small Worlds Fact Sheet," https://nssdc.gsfc.nasa.gov/planetary/factsheet/galileanfact_table.html, 2016. Accessed June 22, 2023.

[81] Zhang, Y., Qian, Z., Lv, S., Huang, W., Ren, J., Fang, Z., and Chen, X., "Experimental Investigation of Uniaxial Compressive Strength of Distilled Water Ice at Different Growth Temperatures," *Water*, Vol. 14, No. 24, 2022. doi: 10.3390/w14244079.

[82] Vallis, G., *Atmospheric and Oceanic Fluid Dynamics: Fundamentals and Large-scale Circulation*, Cambridge University Press, 2006. url: https://books.google.nl/books?id=cC0Kye7nHEEC.

[83] OpenStax, *University Physics Volume 1*, UCF PRESSBOOKS, 2016. url: https://pressbooks.online.ucf.edu/osuniversityphysics/chapter/7-2-kinetic-energy/.

[84] Hughes, D. W., "The approximate ratios between the diameters of terrestrial impact craters and the causative incident asteroids," *Monthly Notices of the Royal Astronomical Society*, Vol. 338, No. 4, 2003, pp. 999–1003. doi: 10.1046/j.1365-8711.2003.06157.x.

[85] Sinha, N. K., "Effective Poisson's ratio of isotropic ice," *NRC Publications Archive*, Vol. 4, 1987, pp. 189–195. url: https://nrc-publications.canada.ca/eng/view/object/?id=1fd98838-9a90-4148-9860-28e8e6e63394.

[86] Silber, E. A., Osinski, G. R., Johnson, B. C., and Grieve, R. A. F., "Effect of impact velocity and acoustic fluidization on the simple-to-complex transition of lunar craters," *Journal of Geophysical Research: Planets*, Vol. 122, No. 5, 2017, pp. 800–821. doi: https://doi.org/10.1002/2016JE005236.

[87] Rae, A. S. P., Collins, G. S., Grieve, R. A. F., Osinski, G. R., and Morgan, J. V., "Complex crater formation: Insights from combining observations of shock pressure distribution with numerical models at the West Clearwater Lake impact structure," *Meteoritics & Planetary Science*, Vol. 52, No. 7, 2017, pp. 1330–1350. doi: https://doi.org/10.1111/maps.12825.

[88] Wünnemann, K., and Ivanov, B., "Numerical modelling of the impact crater depth–diameter dependence in an acoustically fluidized target," *Planetary and Space Science*, Vol. 51, No. 13, 2003, pp. 831–845. doi: https://doi.org/10.1016/j.pss.2003.08.001.

[89] Saltelli, A., Ratto, M., Andres, T., Campolongo, F., Cariboni, J., Gatelli, D., Saisana, M., and Tarantola, S., *Global Sensitivity Analysis: The Primer*, Wiley, 2008. url: https://books.google.nl/books?id=wAssmt2vumgC.

[90] Campolongo, F., Cariboni, J., and Saltelli, A., "An effective screening design for sensitivity analysis of large models," *Environmental Modelling & Software*, Vol. 22, No. 10, 2007, pp. 1509–1518. doi: https://doi.org/10.1016/j.envsoft.2006.10.004.

[91] Hamby, D., "A review of techniques for parameter sensitivity analysis of environmental models," *Environ Monit Assess*, Vol. 32, 1994, pp. 135–154. doi: https://doi.org/10.1007/BF00547132.

[92] McKinnon, W. B., "On convection in ice I shells of outer Solar System bodies, with detailed application to Callisto," *Icarus*, Vol. 183, No. 2, 2006, pp. 435–450. doi: https://doi.org/10.1016/j.icarus.2006.03.004.

[93] NASA, 2023. url: https://science.nasa.gov/solar-system/asteroids/facts/, Accessed December 12, 2023.

[94] Elder, C. M., Bray, V. J., and Melosh, H. J., "The theoretical plausibility of central pit crater formation via melt drainage," *Icarus*, Vol. 221, No. 2, 2012, pp. 831–843. doi:

https://doi.org/10.1016/j.icarus.2012.09.014.

[95] Dombard, A. J., and McKinnon, W. B., "Elastoviscoplastic relaxation of impact crater topography with application to Ganymede and Callisto," *Journal of Geophysical Research: Planets*, Vol. 111, No. E1, 2006. doi: https://doi.org/10.1029/2005JE002445.

[96] Pappalardo, R. T., and Collins, G. C., "Strained craters on Ganymede," *Journal of Structural Geology*, Vol. 27, No. 5, 2005, pp. 827–838. doi: https://doi.org/10.1016/j.jsg.2004.11.010.

[97] López, M. R., "Spectral Modeling of Rhea, Dione, and Enceladus," , 2023. Available at https://repository.tudelft.nl/record/uuid:6b9363b7-d6ee-4c4b-ad9a-c72a12537ca8.

[98] Boshuizen, I., "James Webb Space Telescope observations to study Ganymede's surface properties," , 2023. Available at https://repository.tudelft.nl/record/uuid:b7fc36a6-7300-4290-80ca-e0a4291e9ff4.

[99] Schenk, P., "Thickness constraints on the icy shells of the galilean satellites from a comparison of crater shapes," *Nature*, Vol. 417, 2002, pp. 419–421. doi: https://doi.org/10.1038/417419a.

[100] Bland, M. T., and Bray, V. J., "The inevitability of large shallow craters on Callisto and Ganymede: Implications for crater depth-diameter trends," *Icarus*, Vol. 408, 2024, p. 115811. doi: https://doi.org/10.1016/j.icarus.2023.115811.

[101] Sherbun, J. A., and Horstemeyer, M. F., "Hydrodynamic modeling of impact craters in ice," *International Journal of Impact Engineering*, Vol. 37, No. 1, 2010, pp. 27–36. doi: https://doi.org/10.1016/j.ijimpeng.2009.07.001.

[102] Michikami, T., Hagermann, A., Morota, T., Haruyama, J., and Hasegawa, S., "Oblique impact cratering experiments in brittle targets: Implications for elliptical craters on the Moon," *Planetary and Space Science*, Vol. 135, 2017, pp. 27–36. doi: https://doi.org/10.1016/j.pss.2016.11.004.

[103] Collins, G., Elbeshausen, D., Davison, T., Robbins, S., and Hynek, B., "The size-frequency distribution of elliptical impact craters," *Earth and Planetary Science Letters*, Vol. 310, No. 1, 2011, pp. 1–8. doi: https://doi.org/10.1016/j.epsl.2011.07.023.

[104] Shoemaker, E. M., "Interpretation of lunar craters: Physics and astronomy of the Moon," *Z. Kopal*, 1962, pp. 283–359.

[105] Ligier, N., Paranicas, C., Carter, J., Poulet, F., Calvin, W., Nordheim, T., Snodgrass, C., and Ferellec, L., "Surface composition and properties of Ganymede: Updates from ground-based observations with the near-infrared imaging spectrometer SINFONI/VLT/ESO," *Icarus*, Vol. 333, 2019, pp. 496–515. doi: https://doi.org/10.1016/j.icarus.2019.06.013.

[106] The Engineering ToolBox, "Ice - Thermal Properties," https://www.engineeringtoolbox.com/ice-thermal-properties-d_576.html, 2004. Accessed November 12, 2024.

[107] Turtle, E. P., Pierazzo, E., and O'Brien, D. P., "Numerical modeling of impact heating and cooling of the Vredefort impact structure," *Meteoritics & Planetary Science*, Vol. 38, No. 2, 2003, pp. 293–303. doi: https://doi.org/10.1111/j.1945-5100.2003.tb00265.x.

[108] Kattenhorn, S., and Prockter, L., "Evidence for subduction in the ice shell of Europa," *Nature Geosci*, Vol. 7, 2014, pp. 762–767. doi: https://doi.org/10.1038/ngeo2245.

[109] Raducan, S., Davison, T., and Collins, G., "Ejecta distribution and momentum transfer from oblique impacts on asteroid surfaces," *Icarus*, Vol. 374, 2022, p. 114793. doi: https://doi.org/10.1016/j.icarus.2021.114793.

[110] The Engineering ToolBox, "Poisson's Ratio," https://www.engineeringtoolbox.com/poissons-ratio-d_1224.html, 2008. Accessed June 22, 2023.

[111] The Engineering ToolBox, "Ice and Water - Melting Points vs. Pressure," https://www.engineeringtoolbox.com/water-melting-temperature-point-pressure-d_2005.html, 2017. Accessed June 22, 2023.

A

Supplementary Figures

In this chapter, additional figures can be found. Section A.1 shows supplementary figures from Chapter 2, and Section A.2 provides extra figures related to Chapter 3. Then, Section A.3 provides additional figures from Chapter 4, followed by Section A.4, which shows additional figures from Chapter 5. Then, Section A.5 provides additional sensitivity simulation results from Chapter 6, and finally, Section A.6 provides supplementary figures from Chapter 7.

A.1. Scientific Background Figures — Different Types of Craters on Ganymede

This section provides an additional figure, displaying the wide variety of crater types that can be found on Ganymede, which can be seen in Figure A.1.

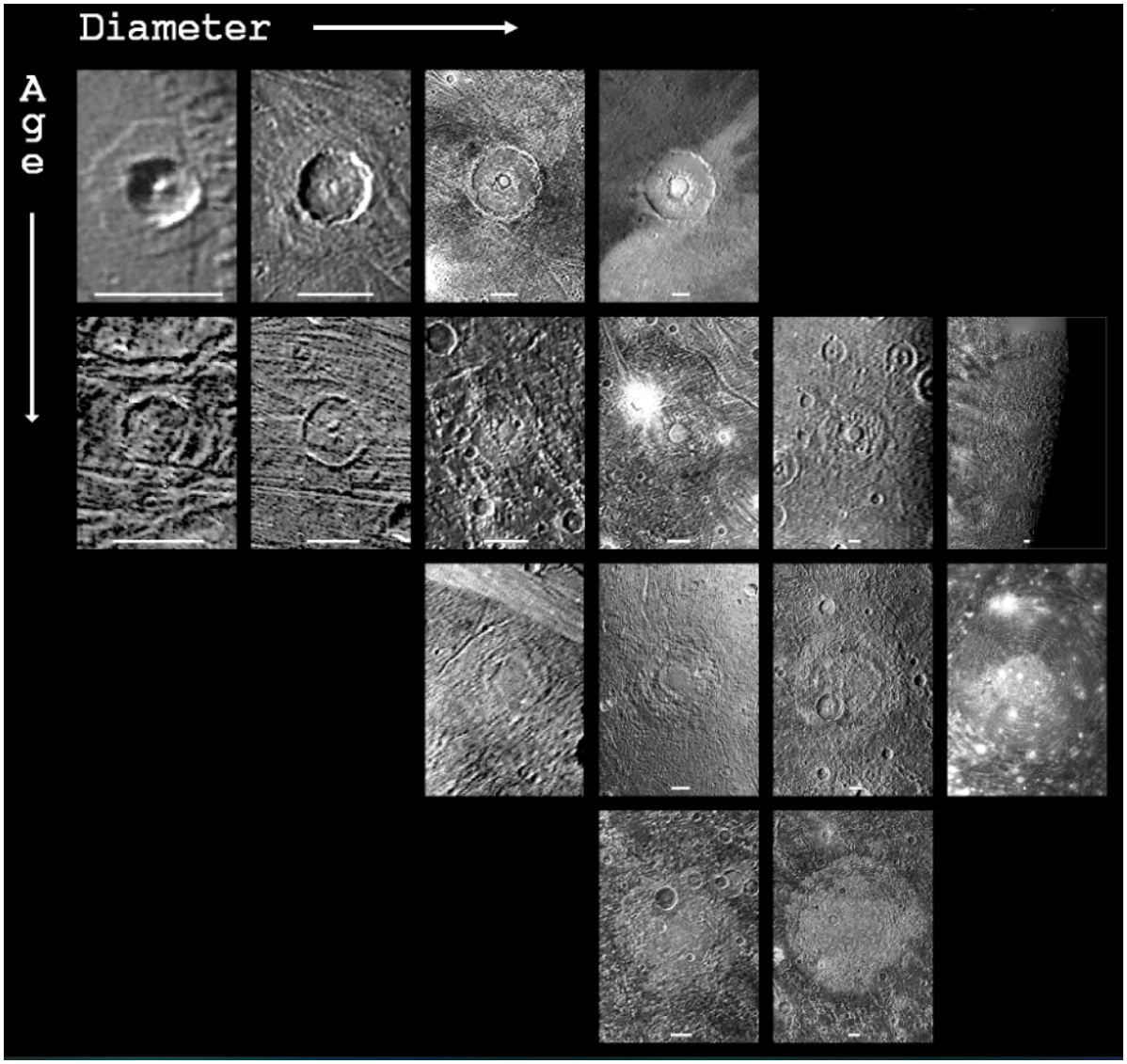

Figure A.1: Examples of some of the different types of craters that can be found on Ganymede. They are arranged by increasing diameter and estimated age. Column 1 contains complex central peak craters. Column 2 shows central pit craters. Column 3-4 and row 1-2 show dome craters. Row 3-4 show palimpsests. Palimpsests are relatively bright, circular impact scars and are very different in appearance from normal craters. Column 5 contains a dome crater in row 2, and palimpsests in row 3-4. Lastly, column 6 shows multi-ringed basins [42].

A.2. Equation of State Figures

Enhanced Plot of Pressure Against Density During Interpolation

In Figure A.2, an enhanced plot of the pressure against the density, based on Figure 3.1, can be seen.

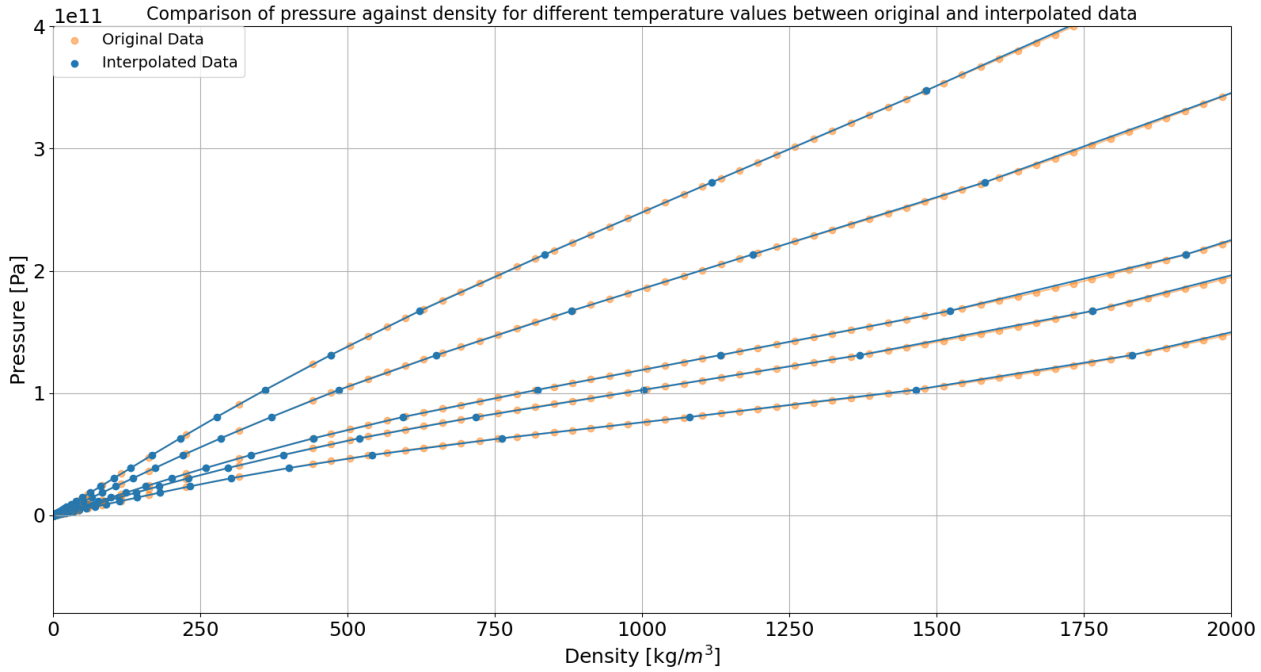

Figure A.2: Pressure against density for different temperatures. The original data is displayed by the orange colored dots, and the interpolated data is given by blue dots and lines.

Water_ice Negative Pressure Plots

Negative pressures were discovered in the water_ice EOS ANEOS file. Upon plotting the pressure against the density for the first seven temperature nodes, this became visually notable. The plot is given by Figure A.3.

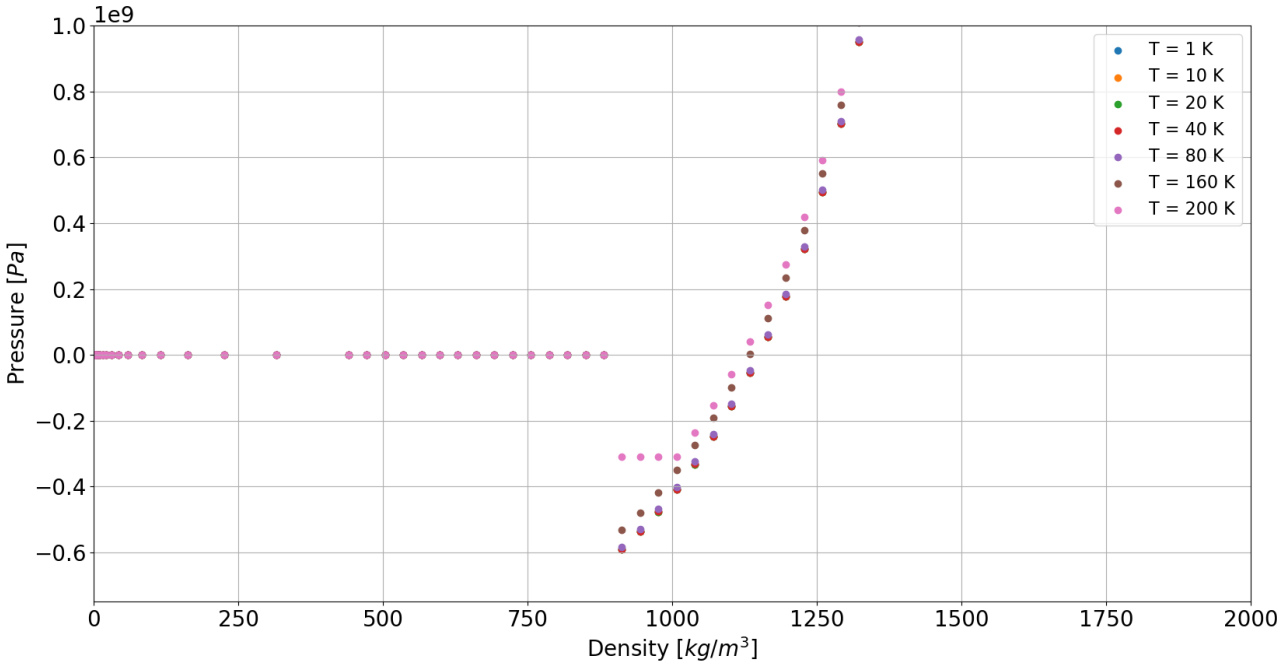

Figure A.3: Data from the water_ice EOS shows that the pressure is negative between a density of 875 kg/m^3 and 1125 kg/m^3 for the first seven temperature nodes.

By manually removing the negative pressures from the dataset, another plot was created to confirm that the negative pressures were removed. This plot can be seen in Figure A.4.

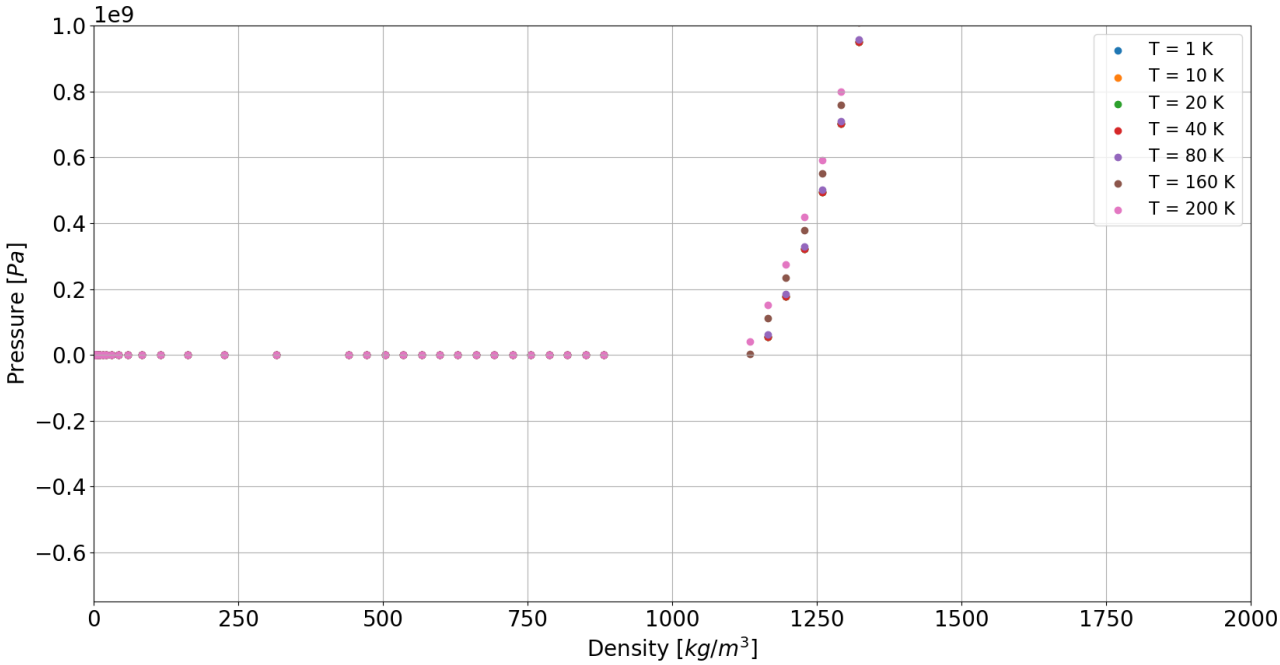

Figure A.4: Data from the water_ice EOS showing the pressure and density for the first seven temperatures with the negative pressures removed.

Simulation Plots of AQUA for Different Number of Nodes

The simulation results for the AQUA EOS, employing different number of temperature and density nodes, is shown in Figure A.5 at different time steps.

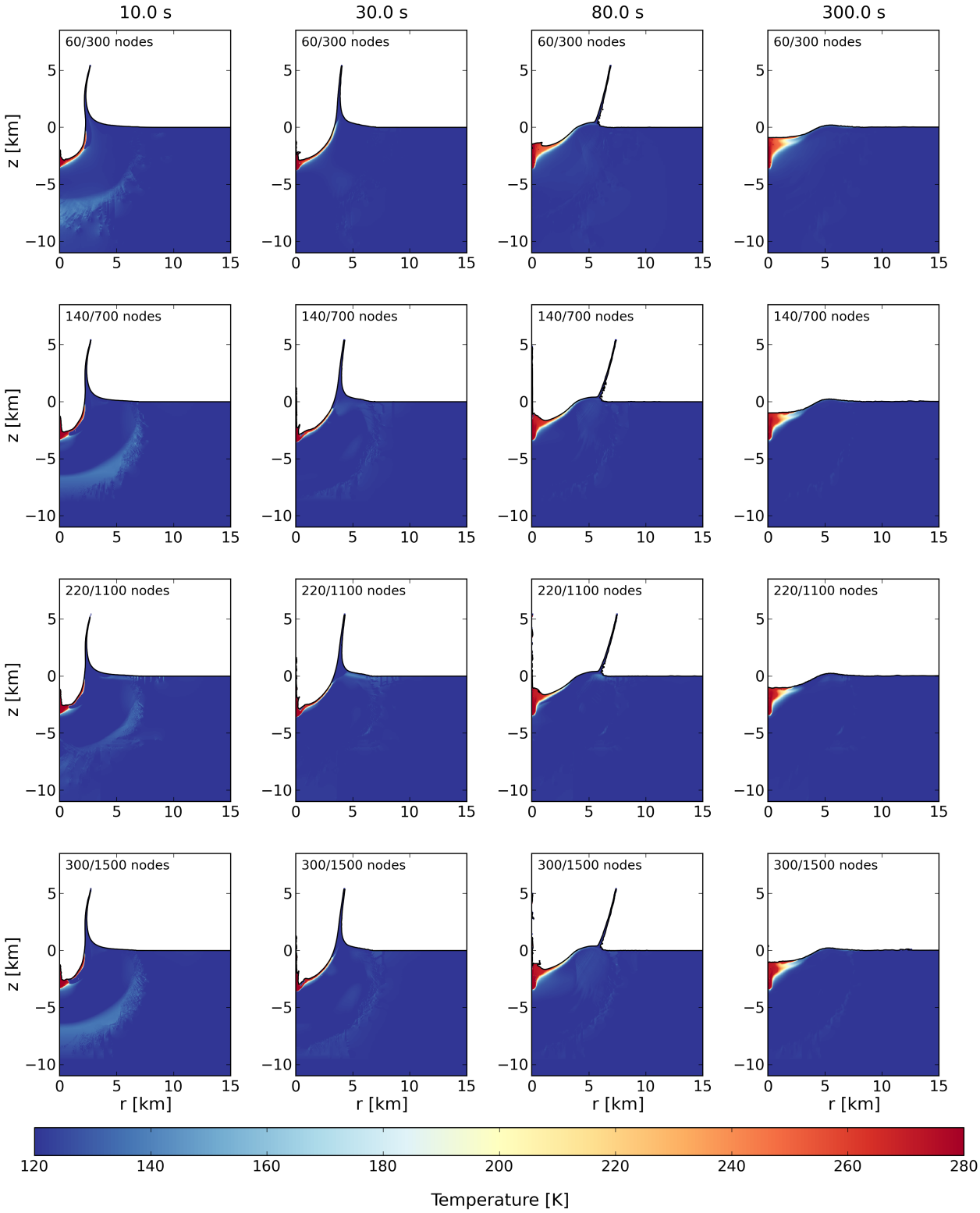

Figure A.5: The simulation results of the temperature for the different AQUA EOS that employ different number of temperature and density nodes. The simulation uses a granite impactor with a size of 500 m in diameter, striking an icy target at 10 km/s.

A.3. Experimental Setup and Method Figures

Grid Parameters from the Asteroid Input File

In the asteroid file, the first few parameters are related to the grid or mesh. In this grid, consisting of many individual cells, the simulation takes place. An example of a grid with an ocean layer on top of a layer of rocky material, is shown in Figure A.6 [71]. Note that the grid only shows the right side of the impact. This is, because a perfectly vertical impact is symmetrical, so only one half is required, reducing the simulation runtime.

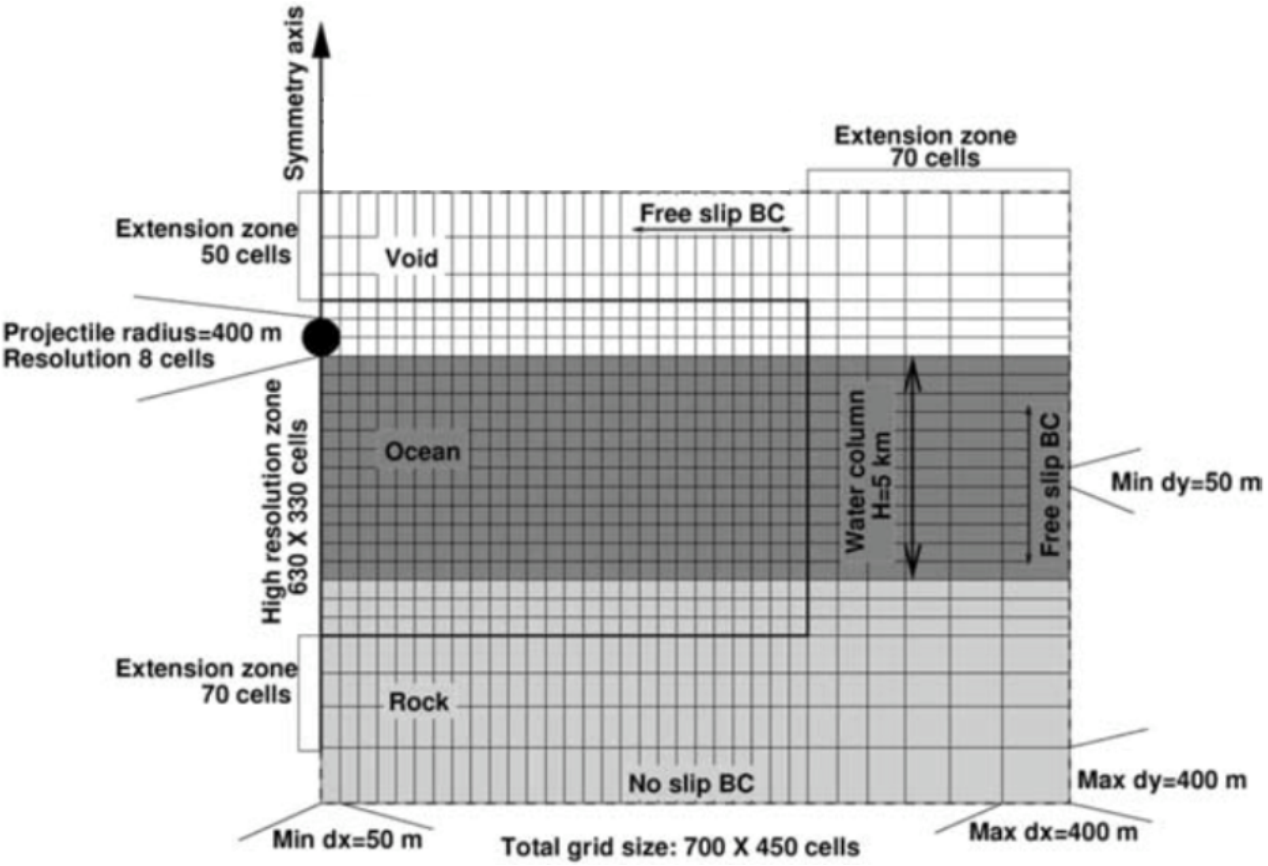

Figure A.6: Example of a simulation grid, where an ocean layer (dark gray area) rests on top of a rock layer (gray area). The area inside the black lines in the center, and left of the grid, is the high-resolution zone. The cell spacing is smallest in this part of the grid. Directly above, to the right, and below the high-resolution zone are the extension zones. These areas have a lower resolution. The resolution is at its lowest in the areas located in the top right and bottom right of the grid [71].

As shown in Figure A.6, the grid consists of multiple rows and columns of cells. The number of row is defined by the parameter GRIDV, and the number of columns by GRIDH. These parameters specify the number of cells in both the high-resolution and the extension zones. The spacing between cells in the high-resolution zone is controlled by GRIDSPC, representing the value of ”min dy” and ”min dx” in Figure A.6. In the extension zone, cell spacing increases progressively up to a maximum value defined by GRIDSPCM, which in Figure A.6 is equal to ”max dy” and ”max dx”. The rate by which the spacing increases after each cell in the extension zone is determined by the GRIDEXT parameter.

iSALE2D Terminal Simulation Overview

In Figure A.7, an example of the overview given by iSALE2D is given upon starting a simulation.

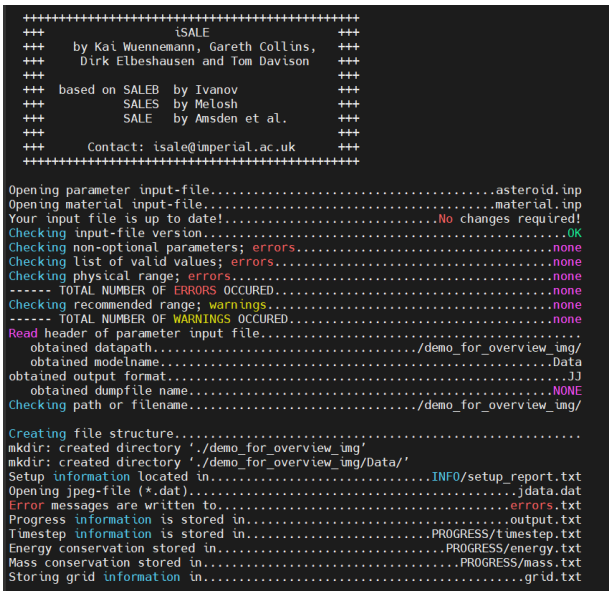

(a) Checks are performed first, allowing the user to confirm whether the setup is free of errors. The file structure is also displayed, showing the paths where specific files will be stored.

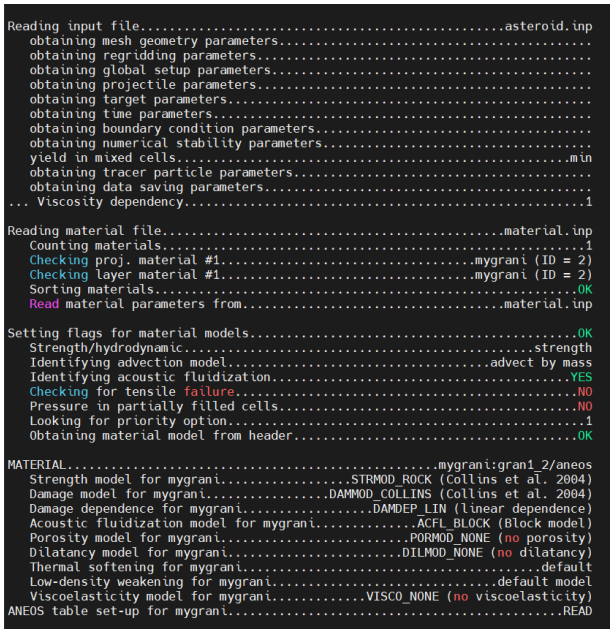

(b) Next, the material input file is read. iSALE2D then returns information about the details of the material used and the parameters that were defined in the input file.

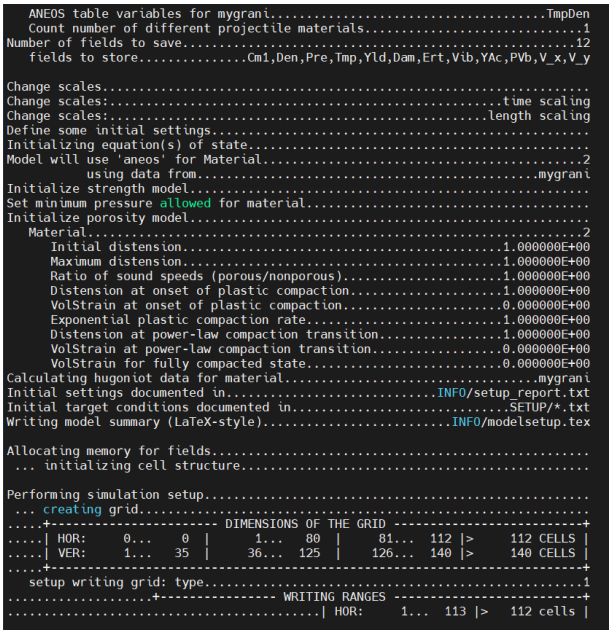

(c) Continuing from b), initialization occurs of the EOS, strength model, porosity model, and target conditions amongst other things. An overview of the dimensions of the grid is given as well.

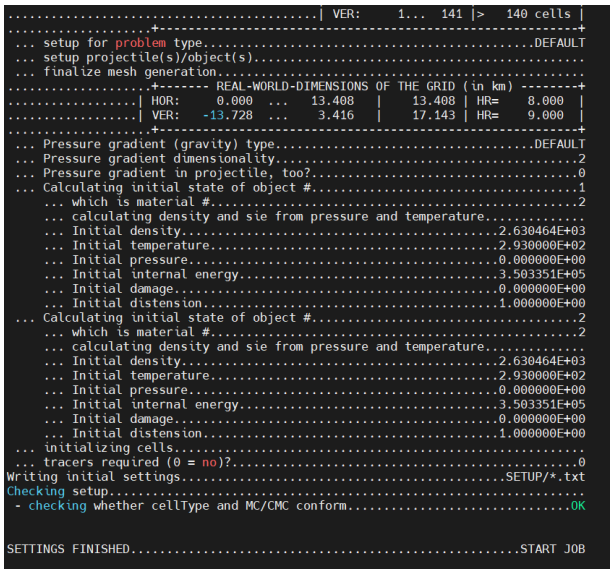

(d) Finally, the grid is generated and the pressure gradient is calculated. Then, the initial state of the impactor and target are determined. A final check to see whether the setup has no issues is performed last.

Figure A.7: An overview of general information and parameter inputs regarding an example simulation that has been started in iSALE2D.

A.4. Verification and Validation Figures

In this section, the example problems provided by the iSALE2D Github, that were not presented in Chapter 5, are shown.

Planet2D Example Problem

The planet2D example problem is shown in Figure A.8. Very minor deviations were observed, which were considered small enough to ignore.

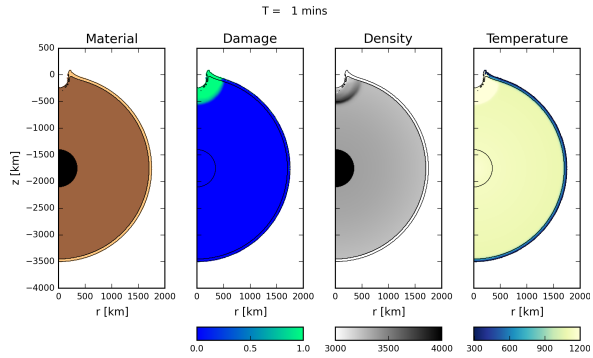

(a) Plot from iSALE2D Github at t = 1 min

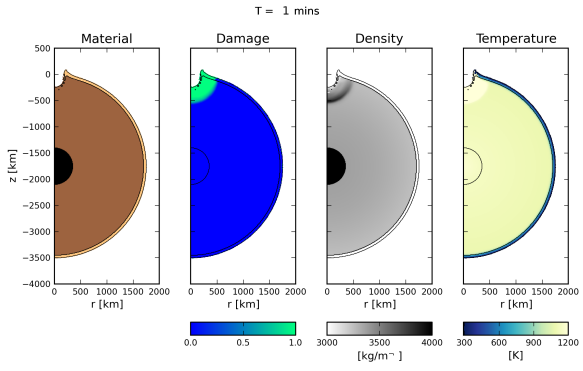

(b) Recreated plot from simulation at t = 1 min

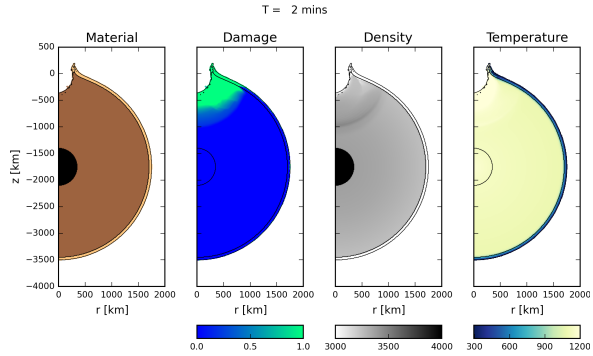

(c) Plot from iSALE2D Github at t = 2 min

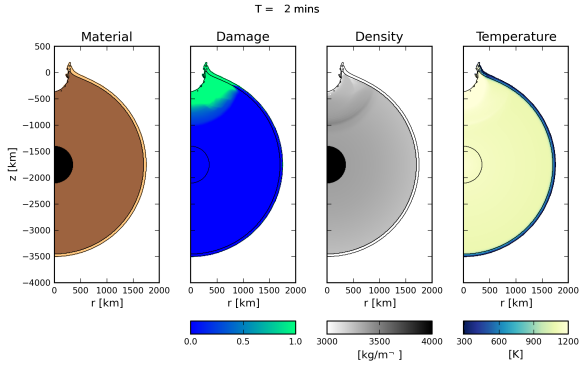

(d) Recreated plot from simulation at t = 2 min

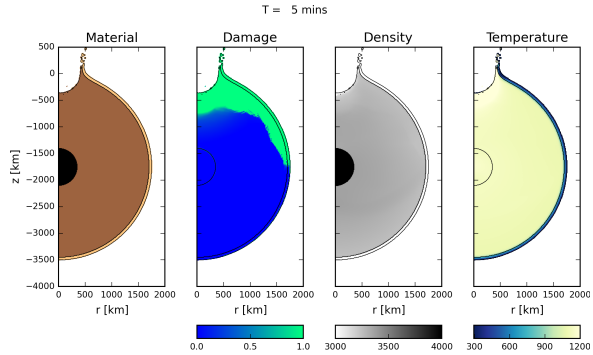

(e) Plot from iSALE2D Github at t = 5 min

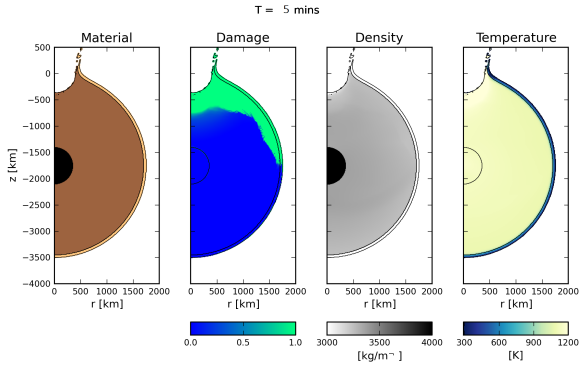

(f) Recreated plot from simulation at t = 5 min

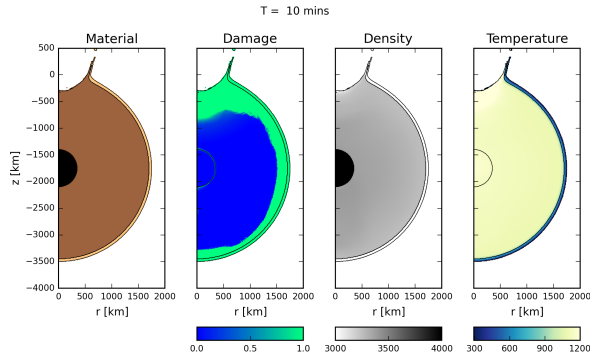

(g) Plot from iSALE2D Github at t = 10 min

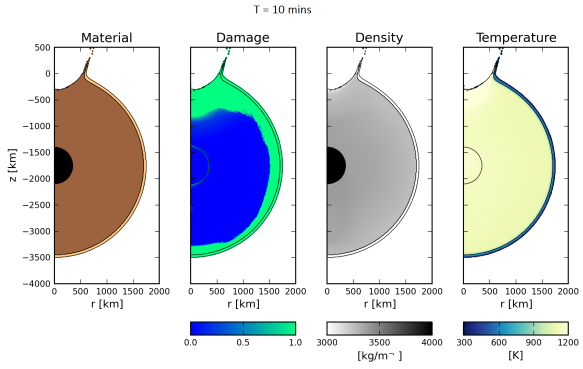

(h) Recreated plot from simulation at t = 10 min

Figure A.8: Comparison of the planet2D example problem results between the iSALE2D Github and the outcome obtained from running the simulation. The simulation simulates a 200 km diameter asteroid striking the Moon at 12 km/s. The impactor and the mantle of the Moon are represented using a dunite material, the lunar crust is represented by a basalt material model, and the lunar core is represented by an iron material model [78].

Dilatency Example Problem

The simulation plots of the dilatency example problem are given in Figure A.9. Similar to Section A.4, very small differences can be seen, which were deemed negligible.

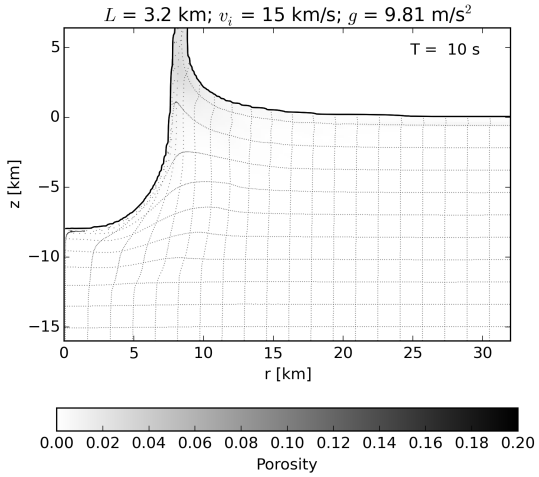

(a) Plot from iSALE2D Github at t = 10 sec

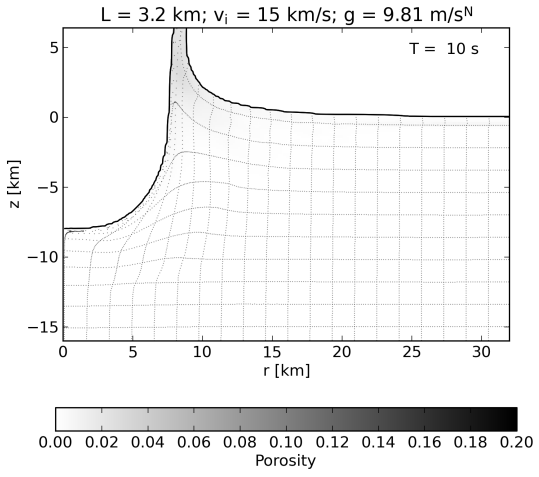

(b) Recreated plot from simulation at t = 10 sec

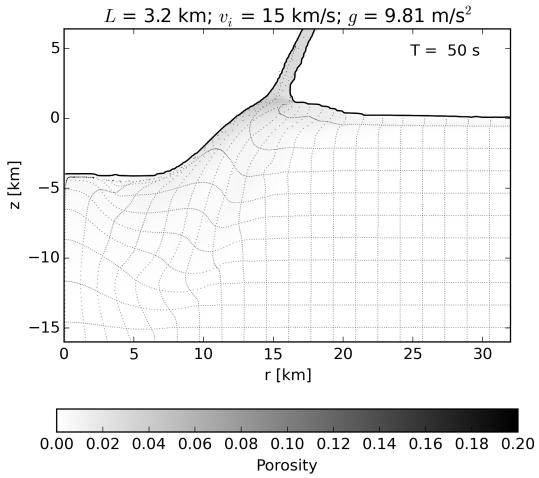

(c) Plot from iSALE2D Github at t = 50 sec

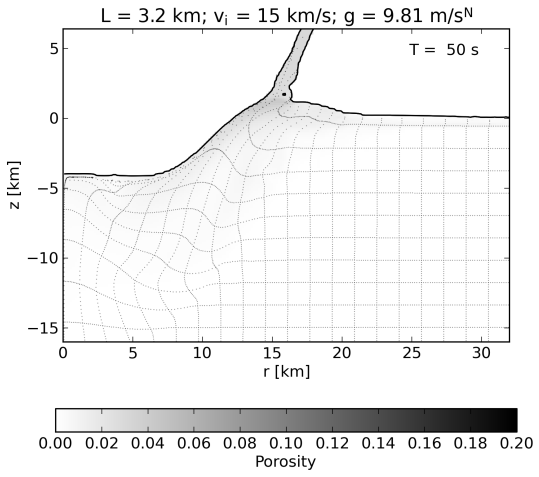

(d) Recreated plot from simulation at t = 50 sec

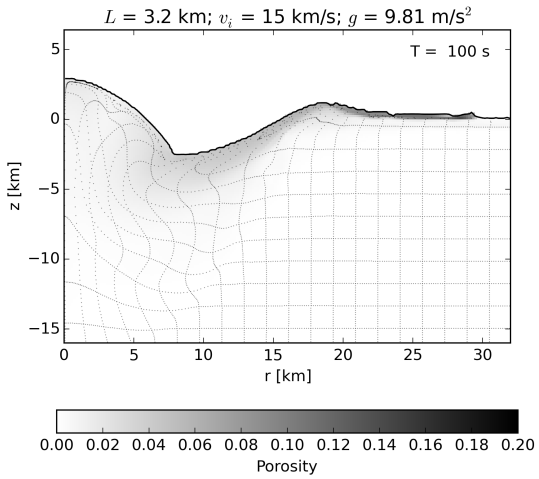

(e) Plot from iSALE2D Github at t = 100 sec

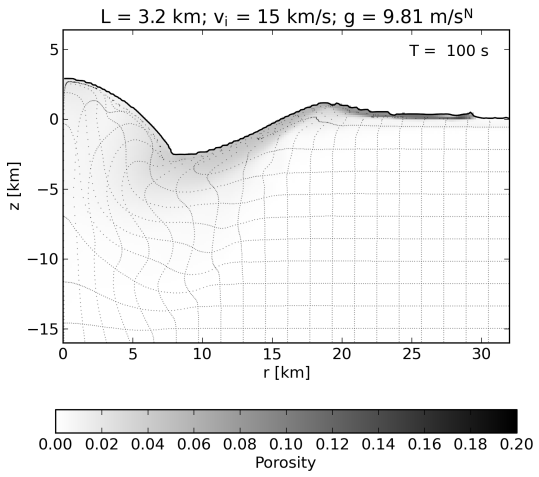

(f) Recreated plot from simulation at t = 100 sec

Figure A.9: Comparison of the dilatency example problem results between the iSALE2D Github and the outcome obtained from running the simulation. The simulation simulates an impact of a 3.2 km diameter impactor striking a target at 15 km/s. Both impactor and target consist of a granite-like material [78].

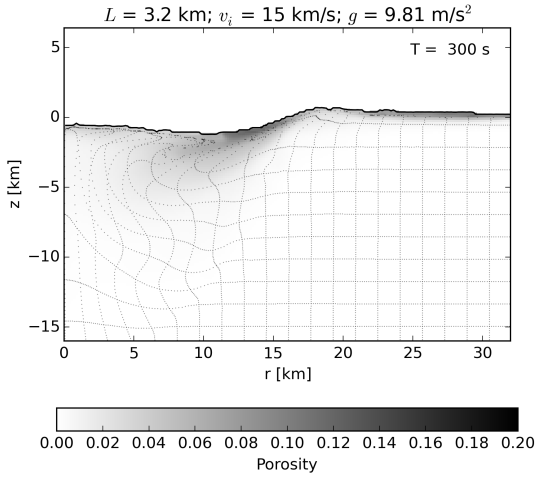

(g) Plot from iSALE2D Github at t = 300 sec

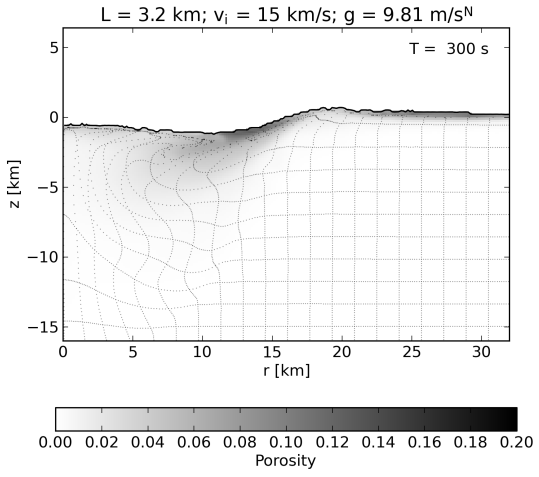

(h) Recreated plot from simulation at t = 300 sec

Figure A.9: Continued from previous page.

Planetsimal2D Example Problem

The planetsimal2D example problem is given by Figure A.10. Once more, minor differences in the order of a few pixels can be observed. Hence, these distinctions are ignored.

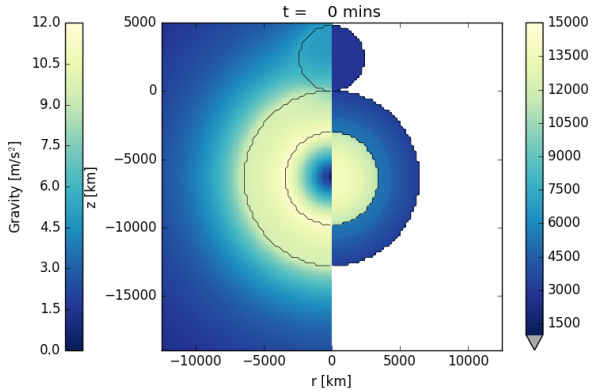

(a) Plot from iSALE2D Github at t = 0 min

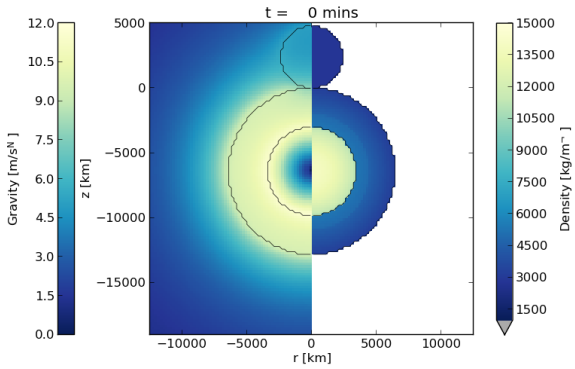

(b) Recreated plot from simulation at t = 0 min

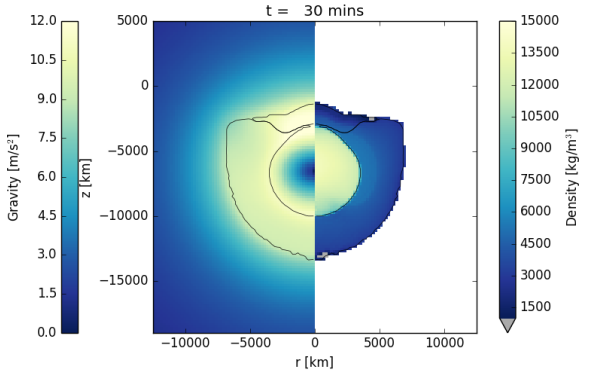

(c) Plot from iSALE2D Github at t = 30 min

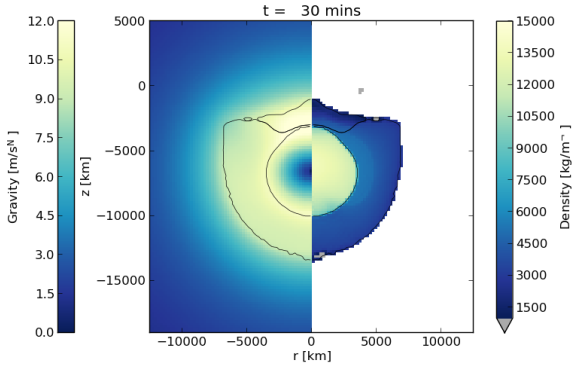

(d) Recreated plot from simulation at t = 30 min

Figure A.10: Comparison of the planetsimal2D example problem results between the iSALE2D Github and the outcome obtained from running the simulation. The simulation simulates an impact of a 4800 km diameter proto-planet striking an Earth-like planet at 12 km/s. The mantle of the planet is represented by a dunite material, the impactor is based on a basalt material, and the planet's core is made of iron [78].

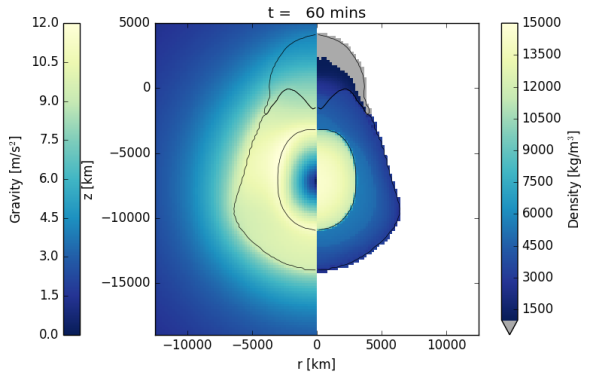

(e) Plot from iSALE2D Github at t = 60 min

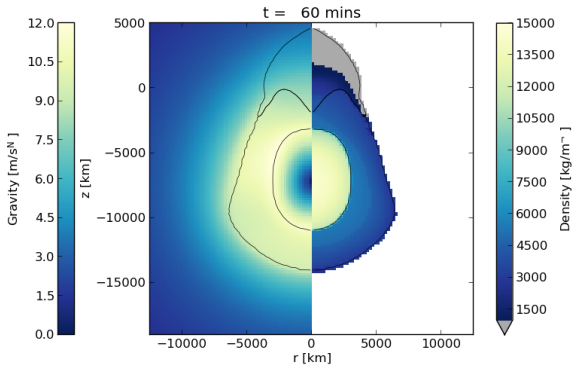

(f) Recreated plot from simulation at t = 60 min

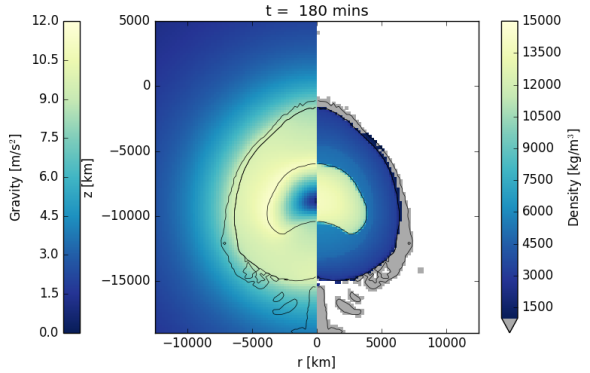

(g) Plot from iSALE2D Github at t = 180 min

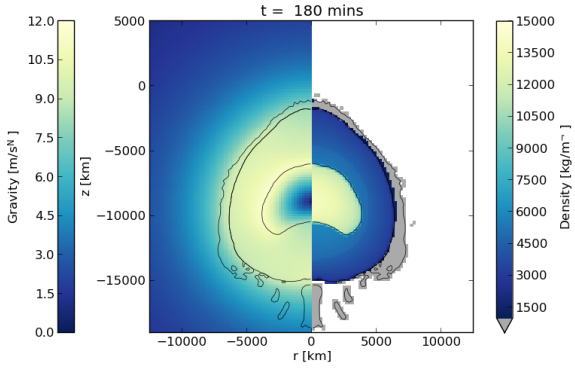

(h) Recreated plot from simulation at t = 180 min

Figure A.10: Continued from previous page.

Aluminium 1100 2D Example Problem

In Figure A.11, the plots for the aluminium 1100 example problem can be seen. Pixel-sized differences were observed that are considered small enough to be neglected.

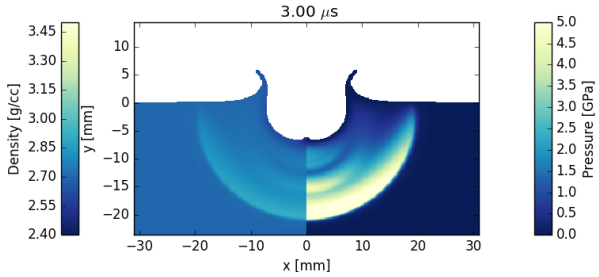

(a) Plot from iSALE2D Github at t = 3 µs

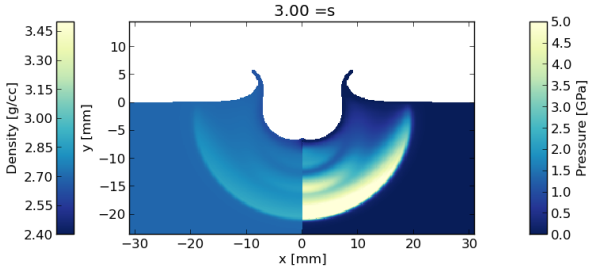

(b) Plot from simulation results at t = 3 µs

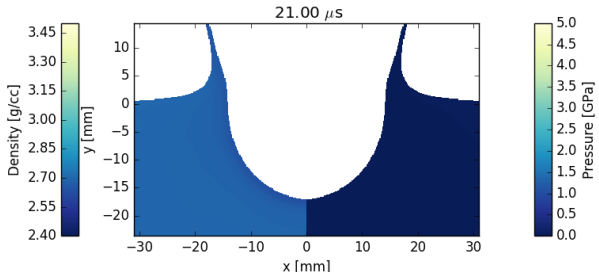

(c) Plot from iSALE2D Github at t = 21 µs

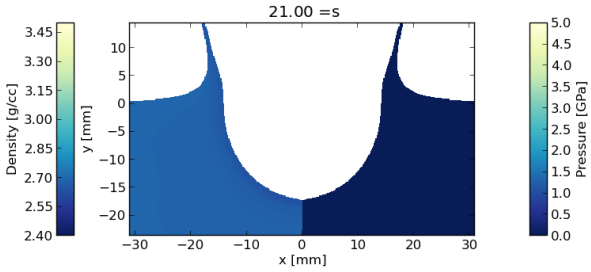

(d) Plot from simulation results at t = 21 µs

Figure A.11: Comparison of the aluminium 1100 example problem results between the iSALE2D Github and the outcome obtained from running the simulation. The impact consist of a 6.35-mm diameter aluminium sphere impacting an aluminium target at 7 km/s. The target has a constant temperature of 293 K [78].

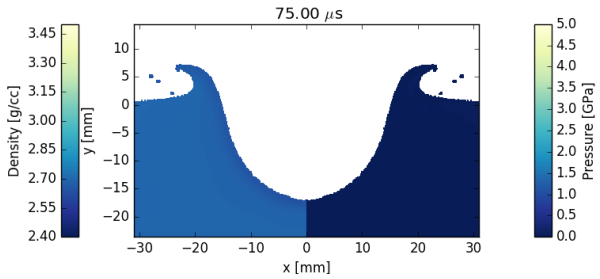

(e) Plot from iSALE2D Github at t = 75 µs

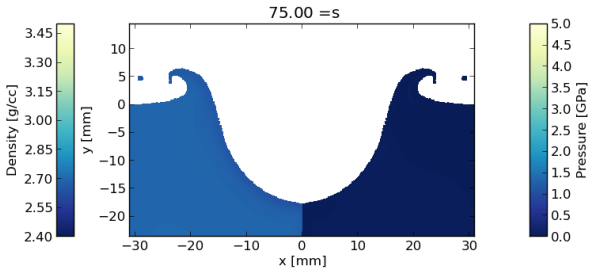

(f) Plot from simulation results at t = 75 µs

Figure A.11: Continued from previous page.

Airburst Example Problem

Given in Figure A.12 are the plots created by the iSALE2D code for an Airburst example problem. No differences between the plots from the iSALE2D Github and the recreated plots were observed.

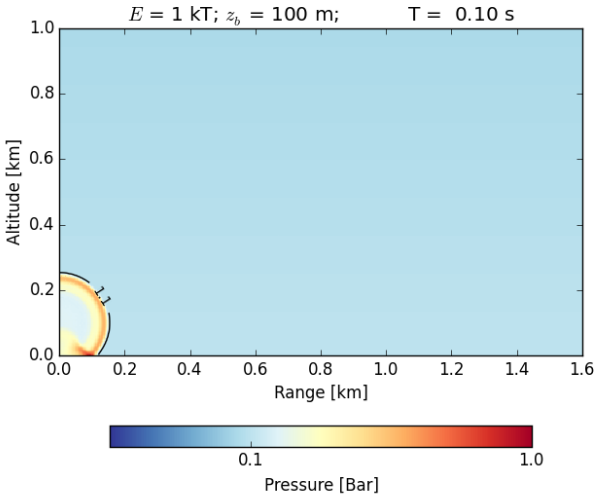

(a) Plot from iSALE2D Github at t = 0.1 s

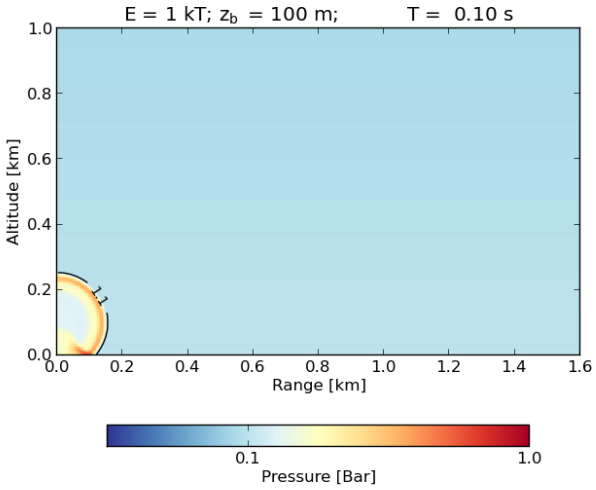

(b) Plot from simulation results at t = 0.1 s

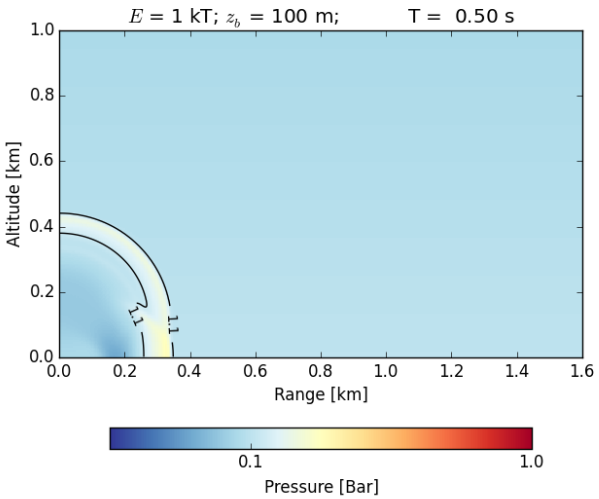

(c) Plot from iSALE2D Github at t = 0.5 s

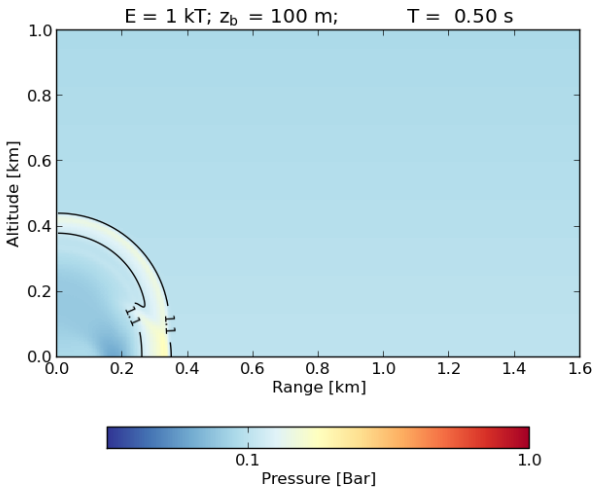

(d) Plot from simulation results at t = 0.5 s

Figure A.12: Comparison of the planet2D example problem results between the iSALE2D Github and the outcome obtained from running the simulation. The simulation simulates a 1kT (TNT energy equivalent) airburst at 100m altitude. The air is represented by a material model with an ideal gas Tillotson equation of state and an inviscid constitutive model [78].

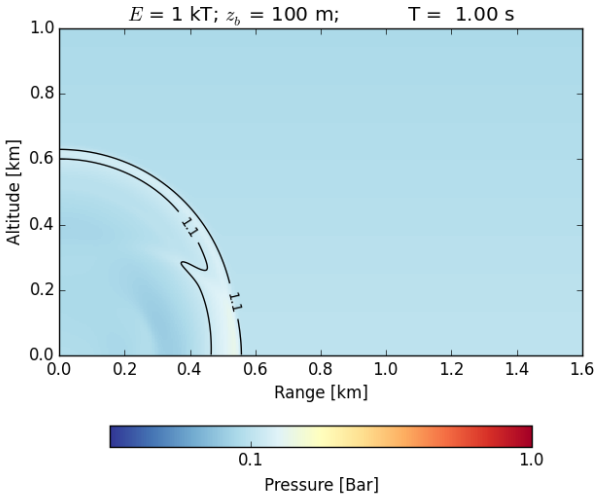

(e) Plot from iSALE2D Github at t = 1 s

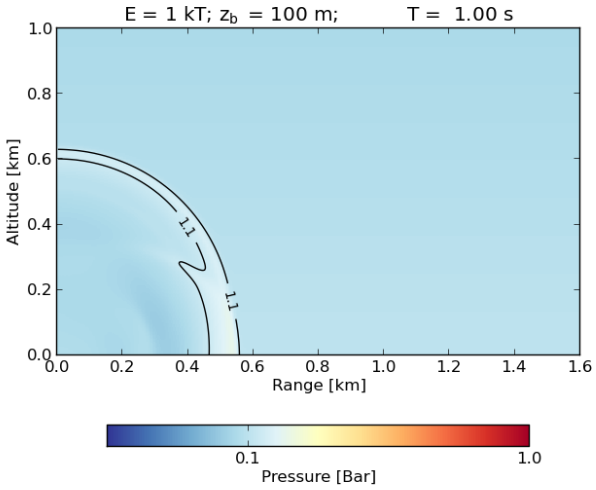

(f) Plot from simulation results at t = 1 s

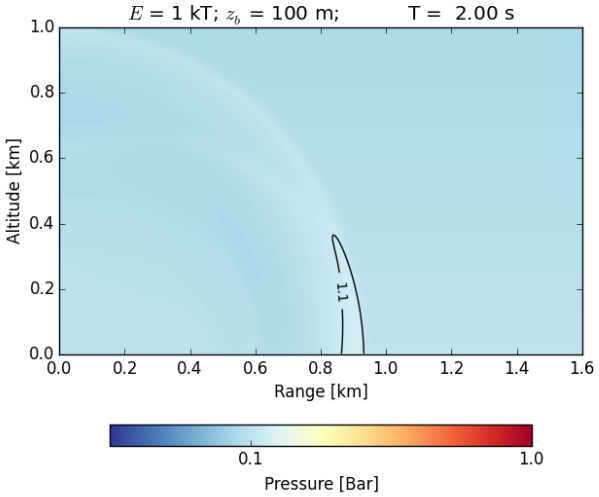

(g) Plot from iSALE2D Github at t = 2 s

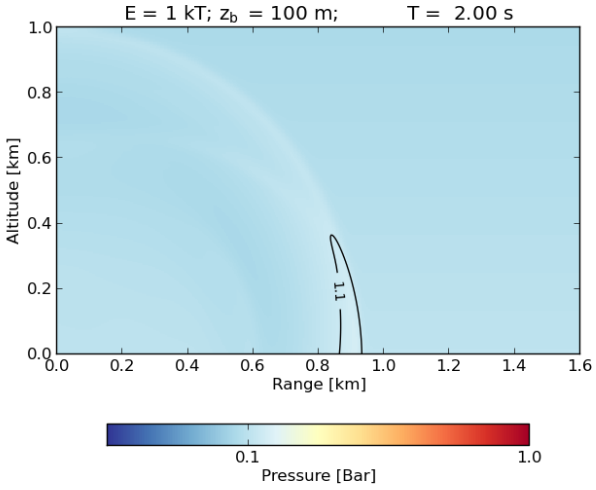

(h) Plot from simulation results at t = 2 s

Figure A.12: Continued from previous page.

Chicxulub Example Problem

Given in Figure A.13 are the plots created by the iSALE2D code for the Chicxulub example problem. No substantial differences between the plots were observed here.

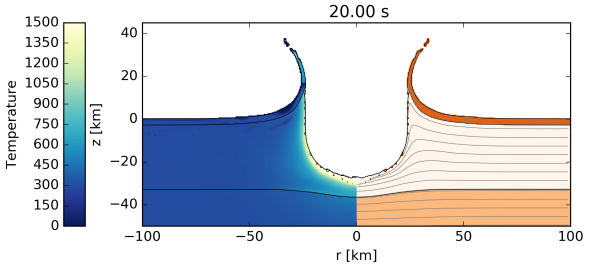

(a) Plot from iSALE2D Github at t = 20 s

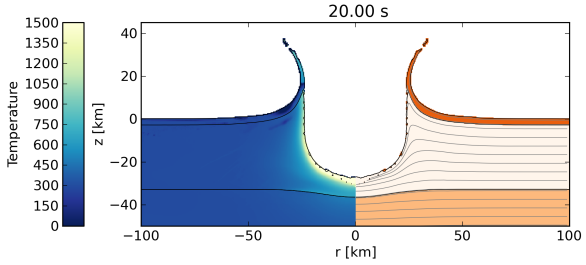

(b) Plot from simulation results at t = 20 s

Figure A.13: Comparison of the Chicxulub example problem results between the iSALE2D Github and the outcome obtained from running the simulation. The simulation attempts to reproduce the Chicxulub crater. The impactor is a 14.4 km diameter asteroid striking a layered target at 12 km/s. The EOS used for the impactor is the ANEOS-derived EOS for granite. The target has a surface gravity of 9.81 m/s^2 and has a 2.8 km layer of calcite above 30 km crust made of granite, which in turn is above a mantle made of dunite material, which all employ an ANEOS EOS [78].

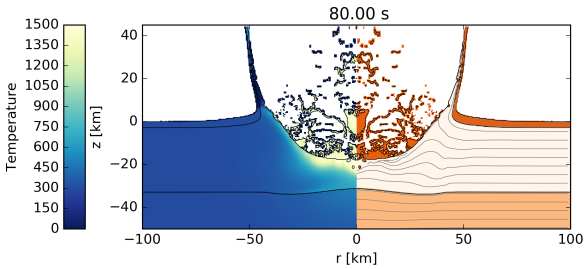

(c) Plot from iSALE2D Github at t = 80 s

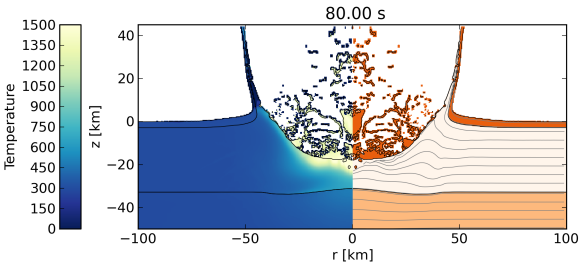

(d) Plot from simulation results at t = 80 s

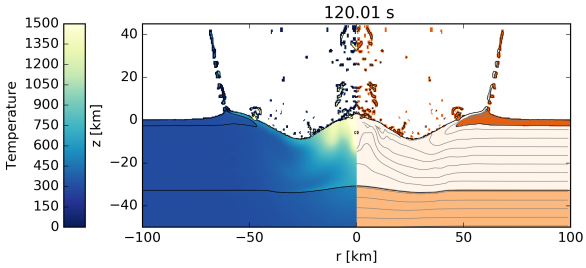

(e) Plot from iSALE2D Github at t = 120 s

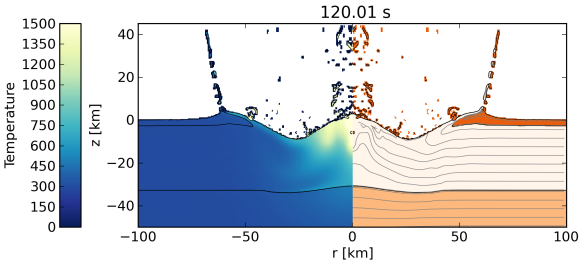

(f) Plot from simulation results at t = 120 s

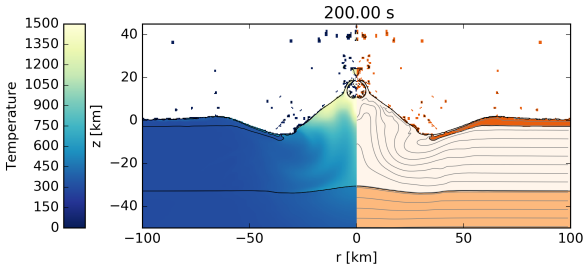

(g) Plot from iSALE2D Github at t = 200 s

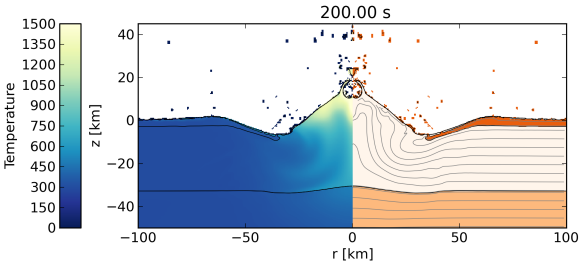

(h) Plot from simulation results at t = 200 s

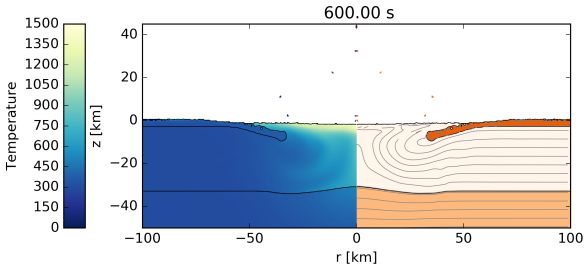

(i) Plot from iSALE2D Github at t = 600 s

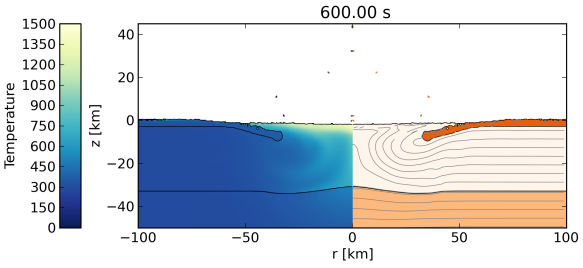

(j) Plot from simulation results at t = 600 s

Figure A.13: Continued from previous page.

Collision2D Example Problem

Given in Figure A.14 are the plots created by the iSALE2D code for a collision2D example problem. Practically no differences were observed between the recreated plots and the iSALE2D Github plots.

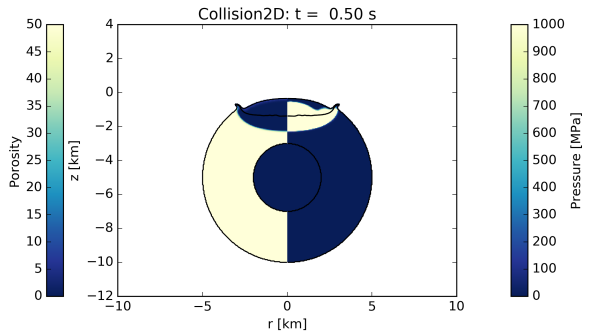

(a) Plot from iSALE2D Github at t = 0.5 s

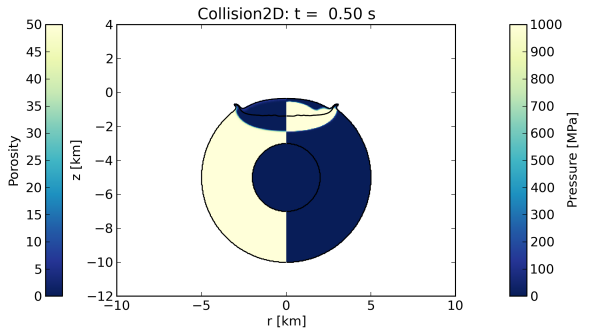

(b) Plot from simulation results at t = 0.5 s

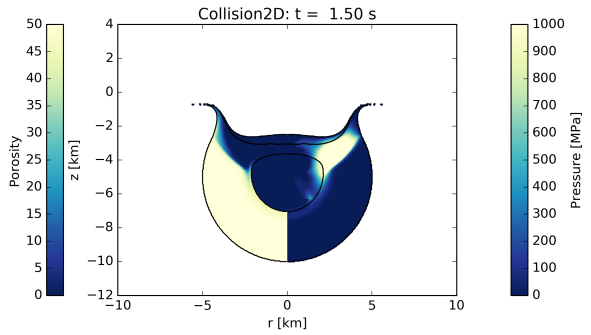

(c) Plot from iSALE2D Github at t = 1.5 s

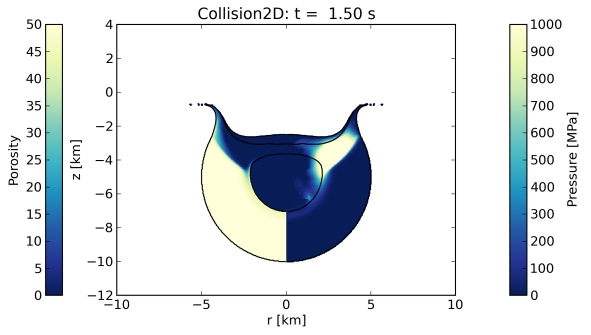

(d) Plot from simulation results at t = 1.5 s

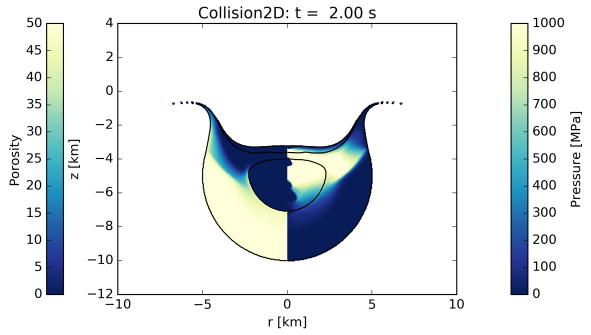

(e) Plot from iSALE2D Github at t = 2 s

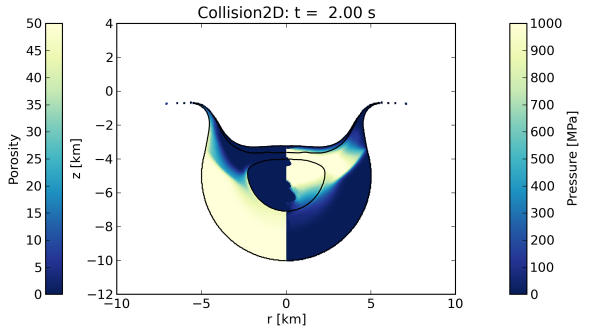

(f) Plot from simulation results at t = 2 s

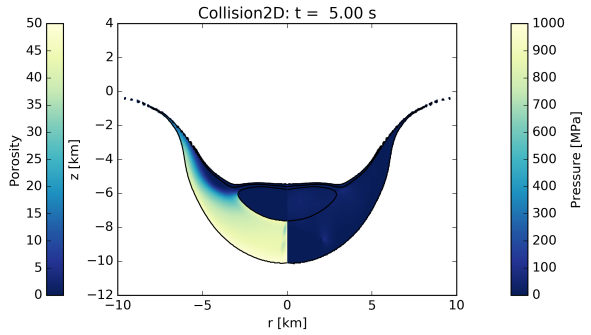

(g) Plot from iSALE2D Github at t = 5 s

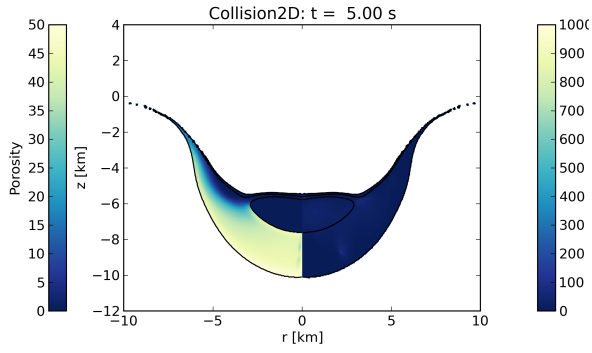

(h) Plot from simulation results at t = 5 s

Figure A.14: Comparison of the collision2D example problem results between the iSALE2D Github and the outcome obtained from running the simulation. The simulation simulates an impactor with a semi-major axis of 2.4 km and a semi-minor axis of 1 km. The impact velocity is 5 km/s. The impactor has a porosity of 40%. The target body is spherical with a radius of 5 km. There is a central core of non-porous dunite 2 km in radius. The outer shell is composed of 50% porosity dunite. The dunite in both bodies is represented by the ANEOS EOS. Both bodies have a constant initial temperature of 293 K. [78].

Sand2D Example Problem

In Figure A.15, the results for the sand2D example problem are shown. No distinctions were made between the recreated plots and the ones from the iSALE2D Github.

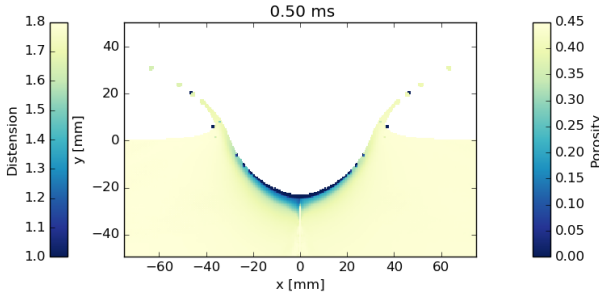

(a) Plot from iSALE2D Github at t = 0.5 ms

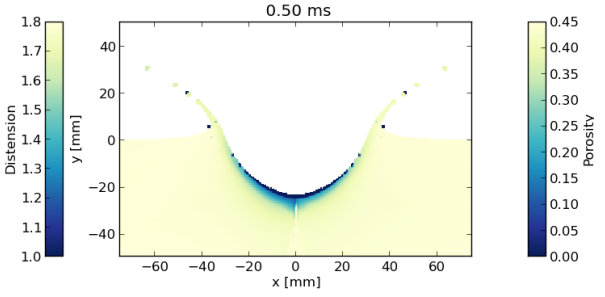

(b) Plot from simulation results at t = 0.5 ms

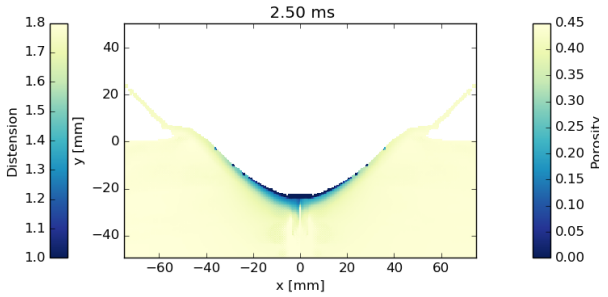

(c) Plot from iSALE2D Github at t = 2.5 ms

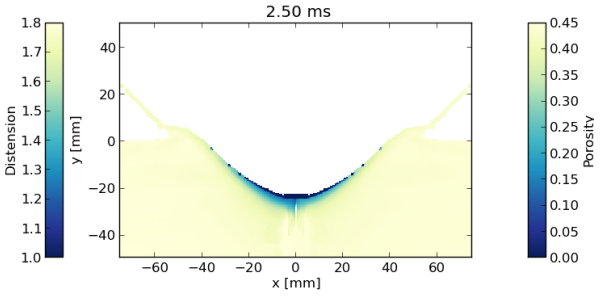

(d) Plot from simulation results at t = 2.5 ms

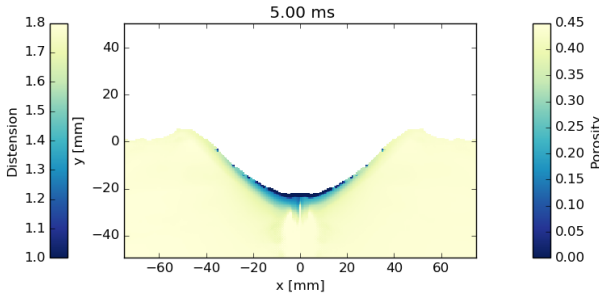

(e) Plot from iSALE2D Github at t = 5 ms

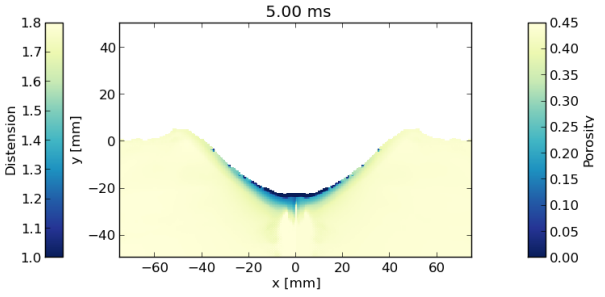

(f) Plot from simulation results at t = 5 ms

Figure A.15: Comparison of the sand2D example problem results between the iSALE2D Github and the outcome obtained from running the simulation. The simulation simulates an impact under very high gravity (500 G). The impactor is made of polyethylene and has a diameter of 13 mm. The impact velocity is 1.9 km/s and the target is sand, which is represented in the model as 44% porous fused silica [78].

A.5. Sensitivity Analysis Figures

This section provides additional sensitivity simulation results for the parameters discussed in Chapter 6. The results show the simulation of an icy impactor with a diameter of 500 m, striking an icy target at 10 km/s.

TSURF Parameter

In Figure A.16, the results of the control simulation can be seen in the second column, the results for a lower surface temperature of 100 K in the first column, and the results for a higher surface temperature of 140 K in the third column.

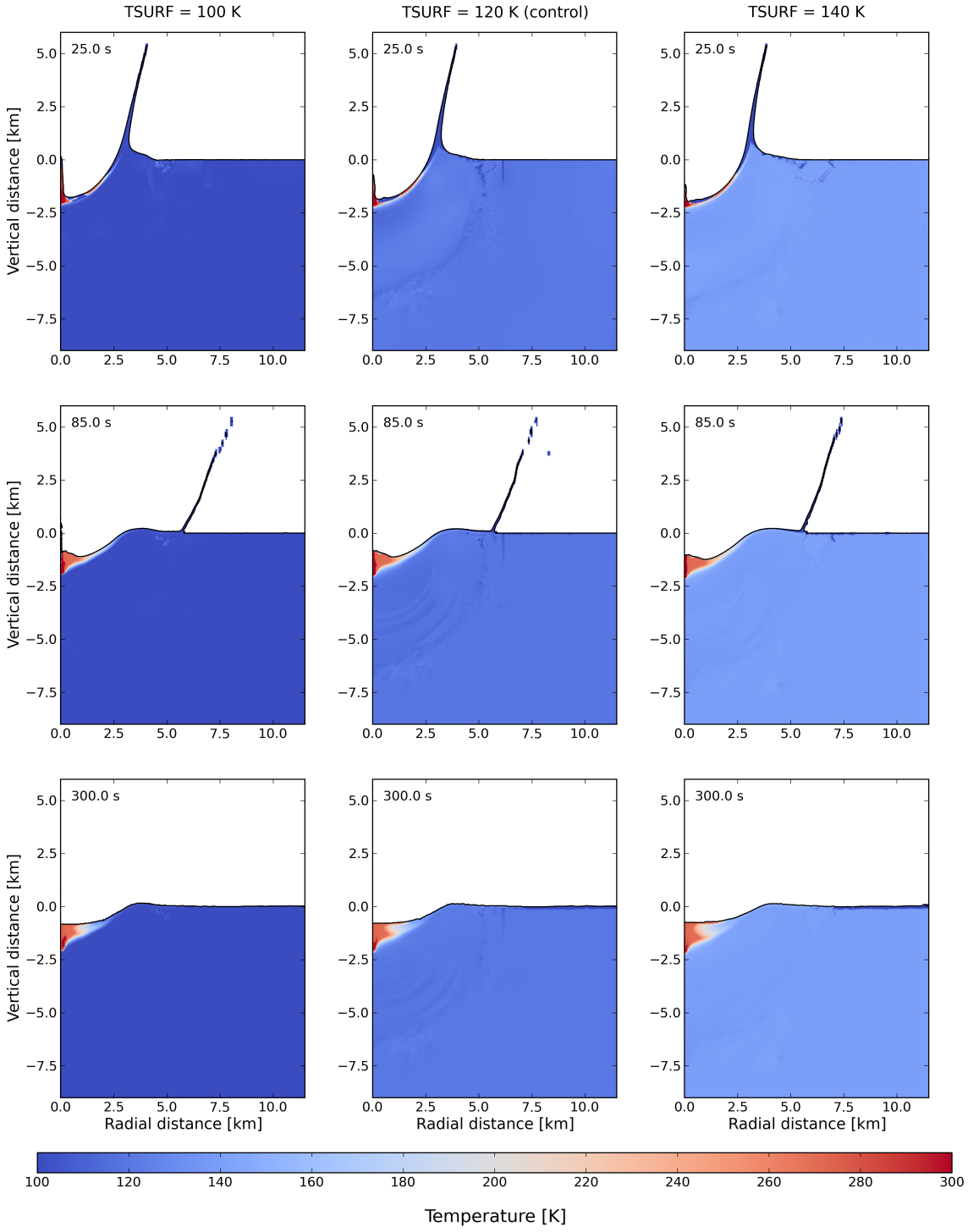

Figure A.16: Sensitivity simulation results of the surface temperature. Two simulations are compared to the control simulation, one with a lower surface temperature of 100 K, and the other with a higher surface temperature of 140 K.

LAYTPROF Parameter

In Figure A.17, the results of the control simulation can be seen in the first row. The second row shows the results of the simulation using the conductive thermal profile, whereas the third row shows results of the simulation using the conductive and convective thermal profile. Finally, the fourth row shows the results of the simulation using the conductive and convective thermal profile with a temperature cap.

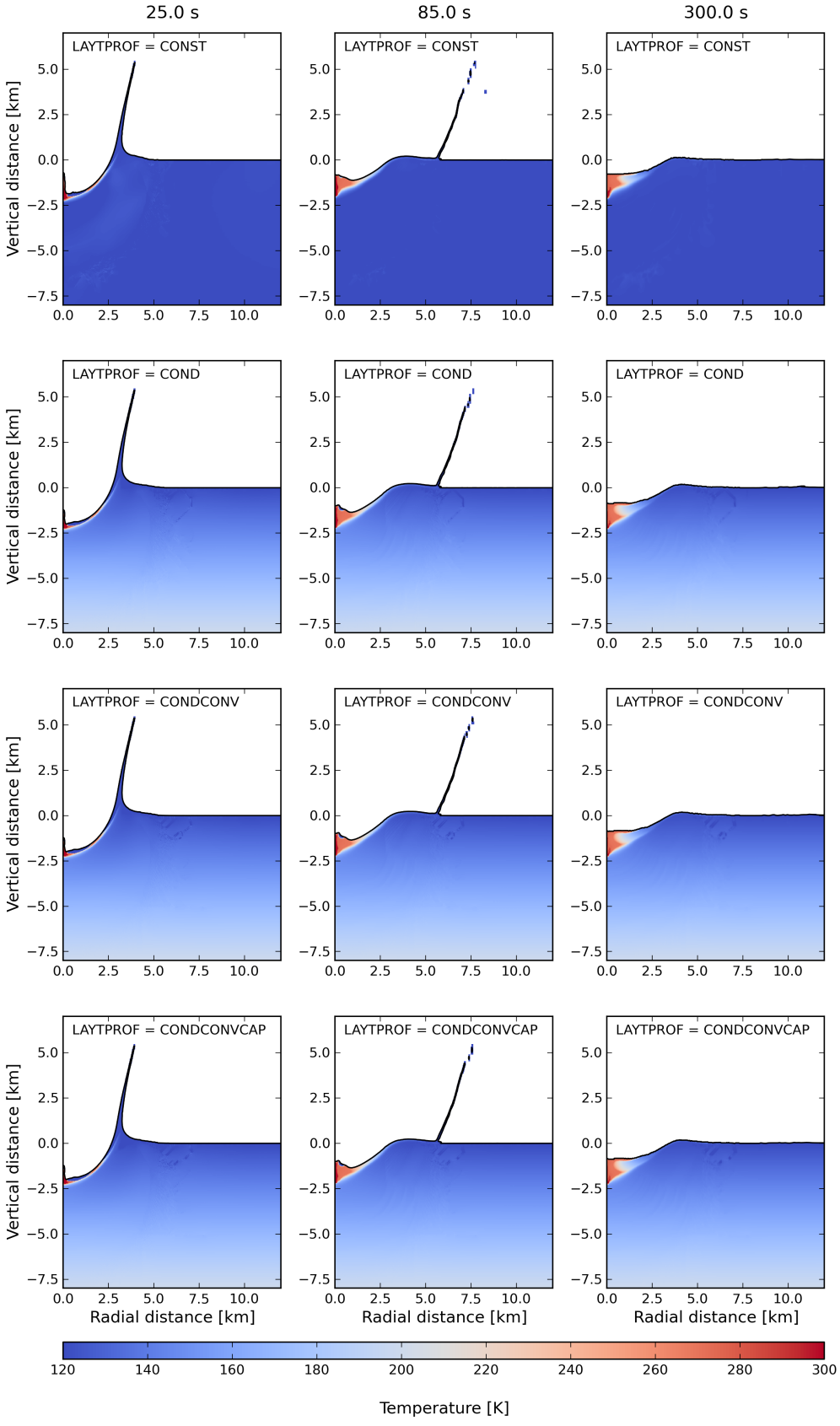

Figure A.17: Sensitivity simulation results of the thermal profile of the target layer. Different thermal profiles are compared to the control simulation.

POIS Parameter

In Figure A.18, the results of the control simulation can be seen in the second column. The first column displays the simulation using a lower poisson ratio, and in the third column the simulation using a higher poisson ratio is shown.

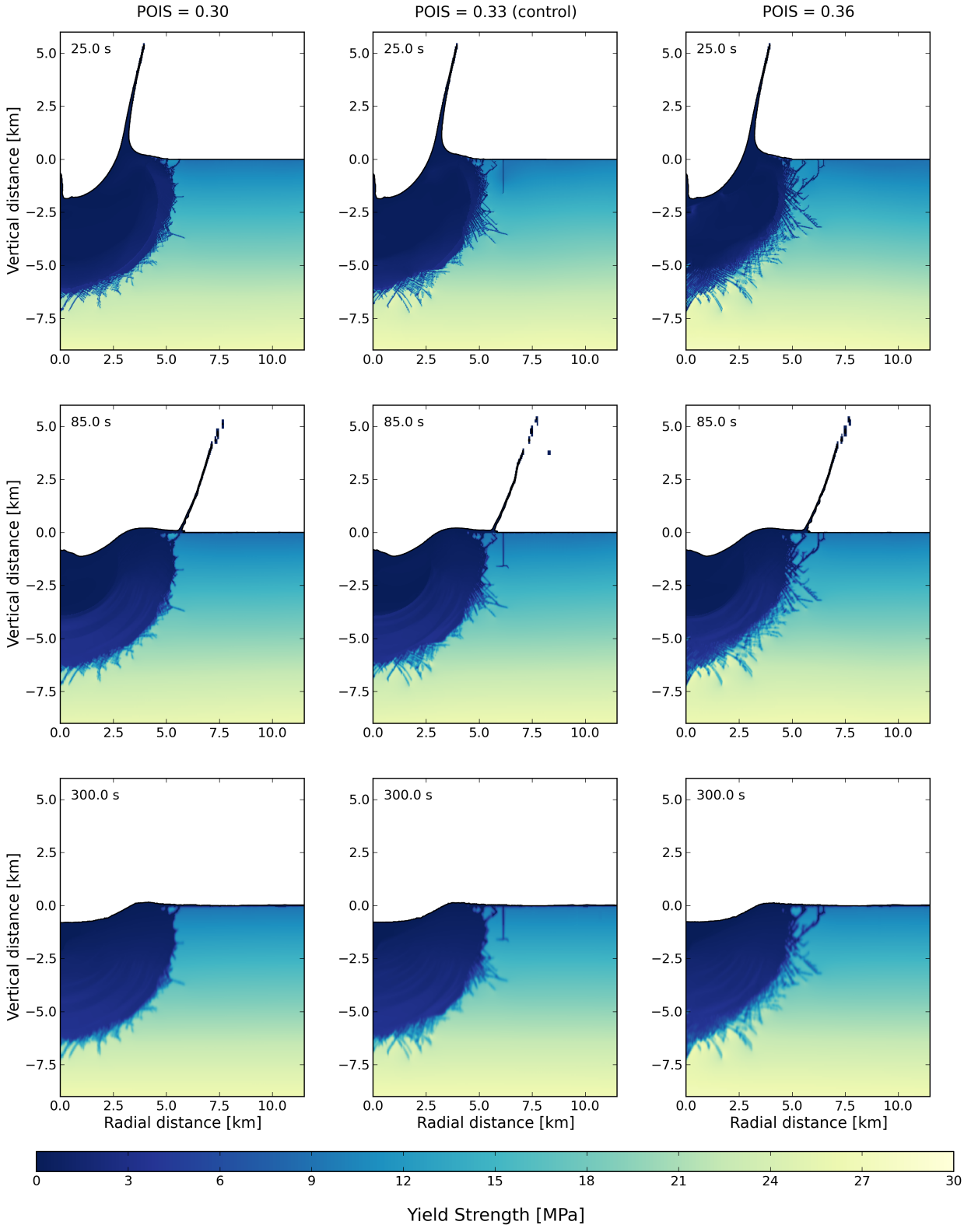

Figure A.18: Sensitivity simulation results of the poisson ratio, comparing different poisson ratios to the control simulation by looking at the yield strength in the target over three time steps.

TMELT0 Parameter

In Figure A.19, the comparison of the temperature in the target between the control simulation, and the simulations employing a different melting temperature at zero pressure, can be seen at three different time steps.

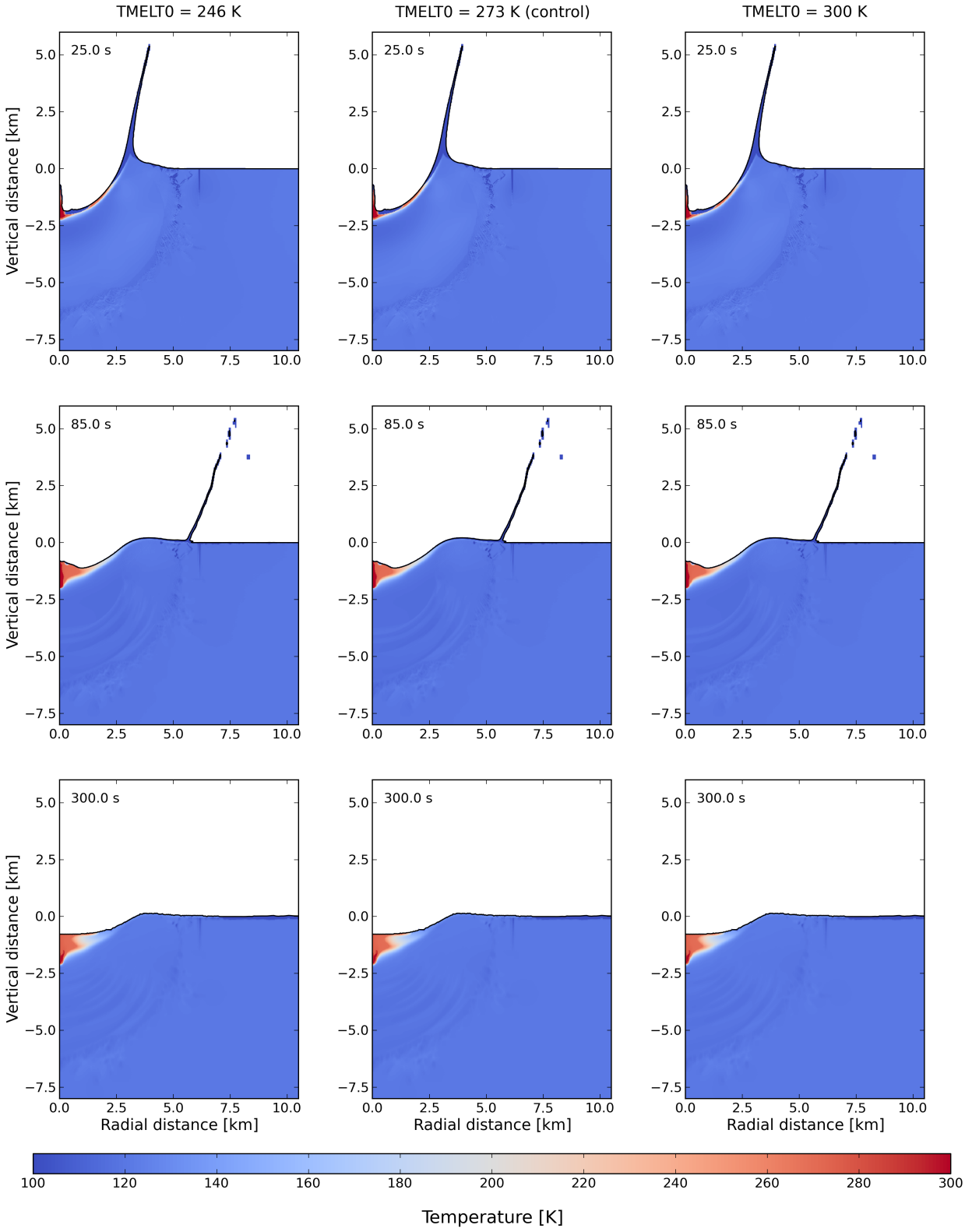

Figure A.19: Sensitivity simulation results of the melting temperature at zero pressure parameter, by comparing the temperatures in the target from using different values to the control simulation.

ASIMON Parameter

In Figure A.20, the comparison of the temperature in the target between the control simulation, and the simulations employing a different value of the ASIMON parameter, can be seen at three different time steps.

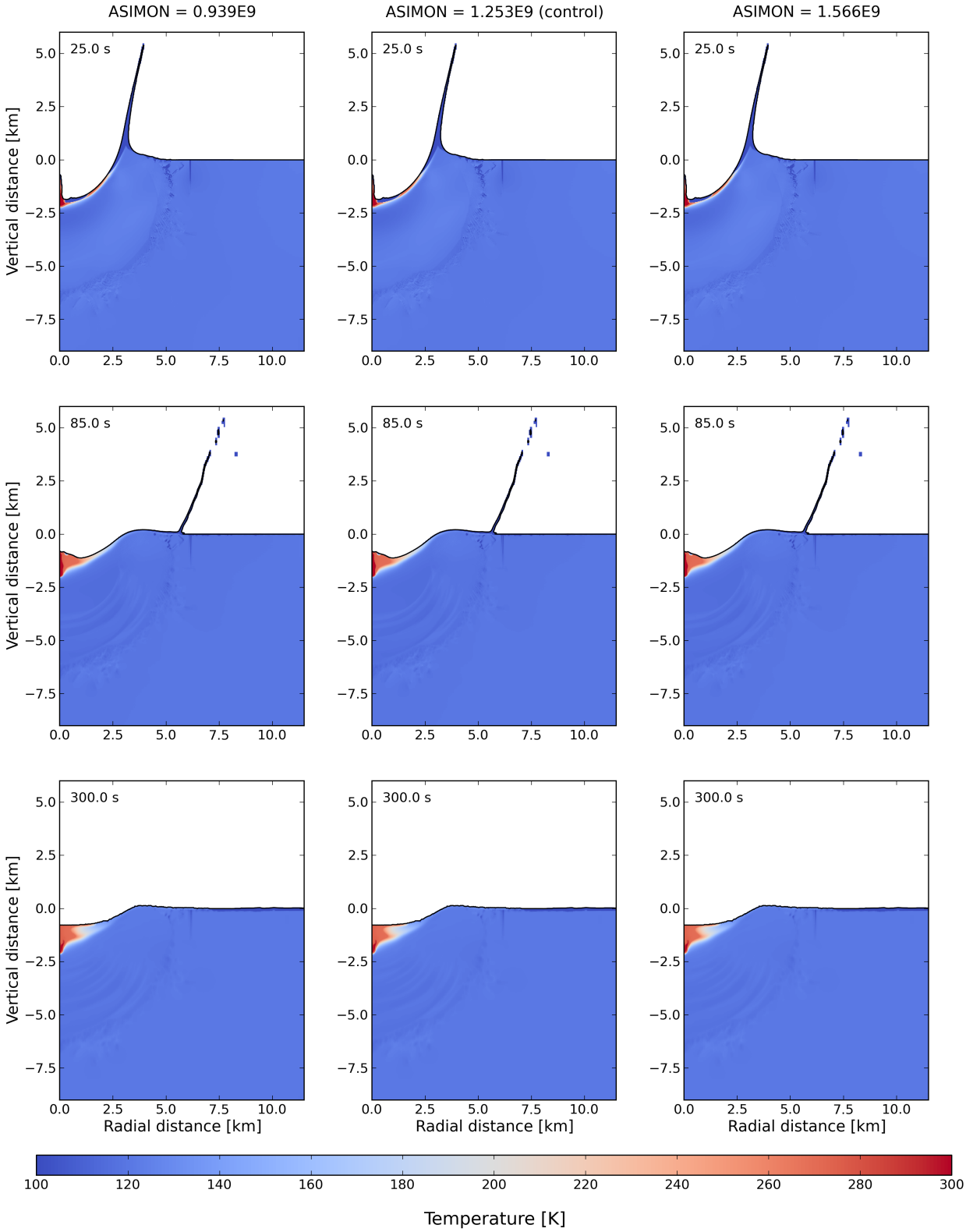

Figure A.20: Sensitivity simulation results of the ASIMON parameter. Comparisons are made between different ASIMON values to the control simulation by looking at the changes in temperature in the target.

CSIMON Parameter

In Figure A.21, the comparison of the temperature in the target between the control simulation, and the simulations employing a different value of the CSIMON parameter, can be seen at three different time steps.

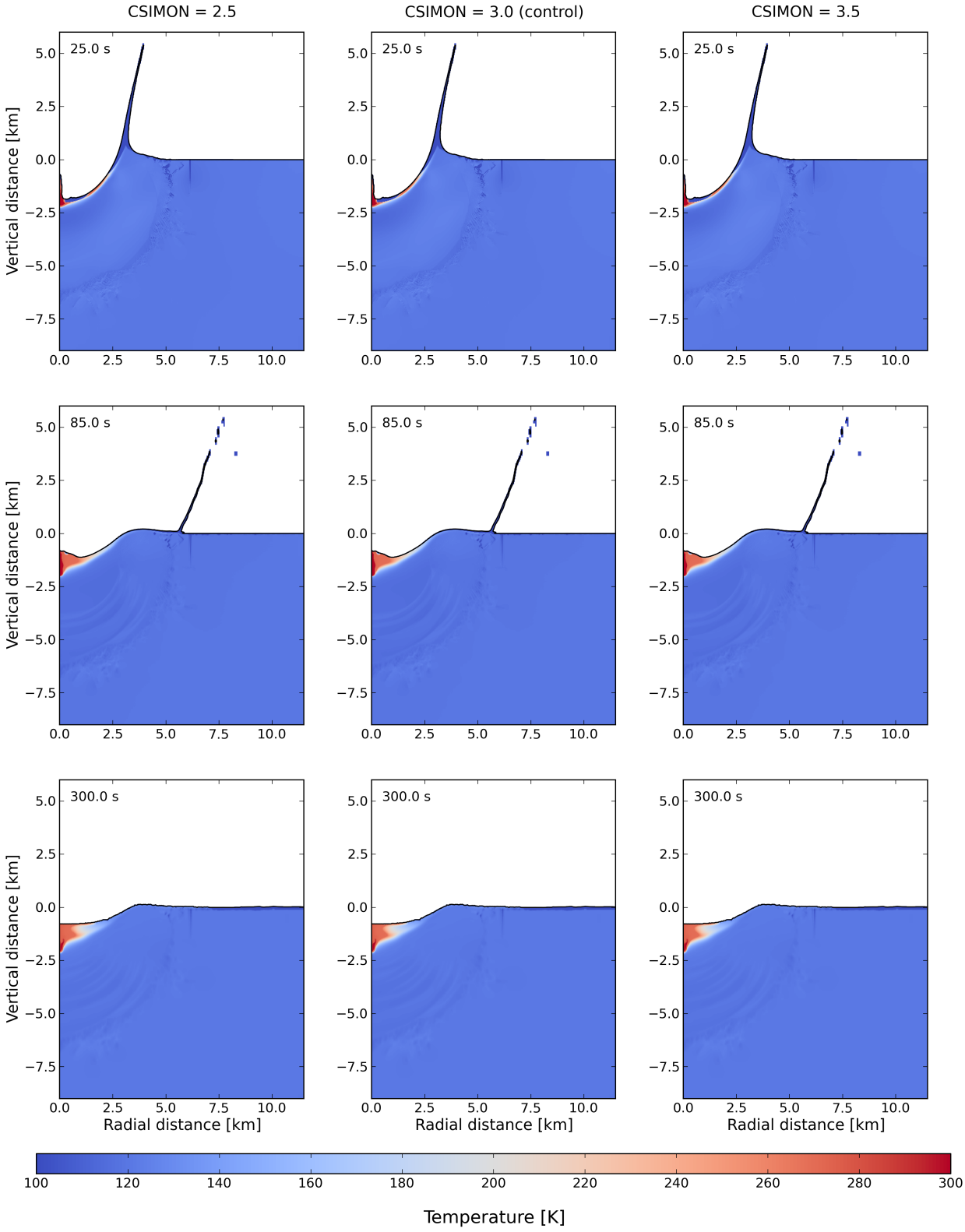

Figure A.21: Sensitivity simulation results of the CSIMON parameter. Comparisons are made between different CSIMON values to the control simulation by looking at the changes in temperature in the target.

YINT0 Parameter

In Figure A.22, the results of the control simulation can be seen in the second column. The first column displays the simulation using a lower YINT0, and in the third column the simulation using a higher YINT0.

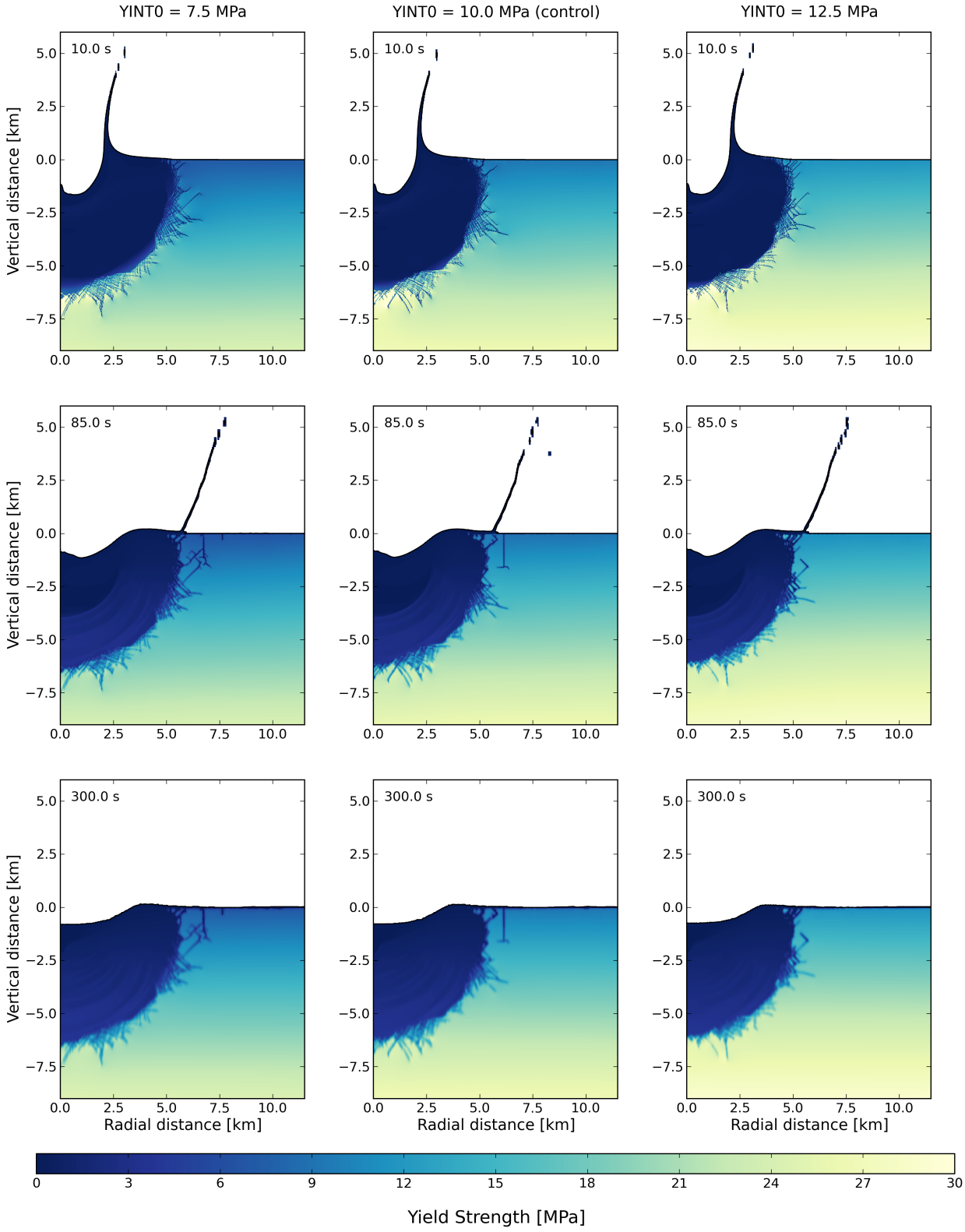

Figure A.22: Sensitivity simulation results of the cohesion at zero pressure of intact material, comparing two simulations to the control simulation.

FRICINT Parameter

In Figure A.23, the results of the control simulation can be seen in the second column. The first column displays the simulation using a lower FRICINT, and in the third column the simulation using a higher FRICINT.

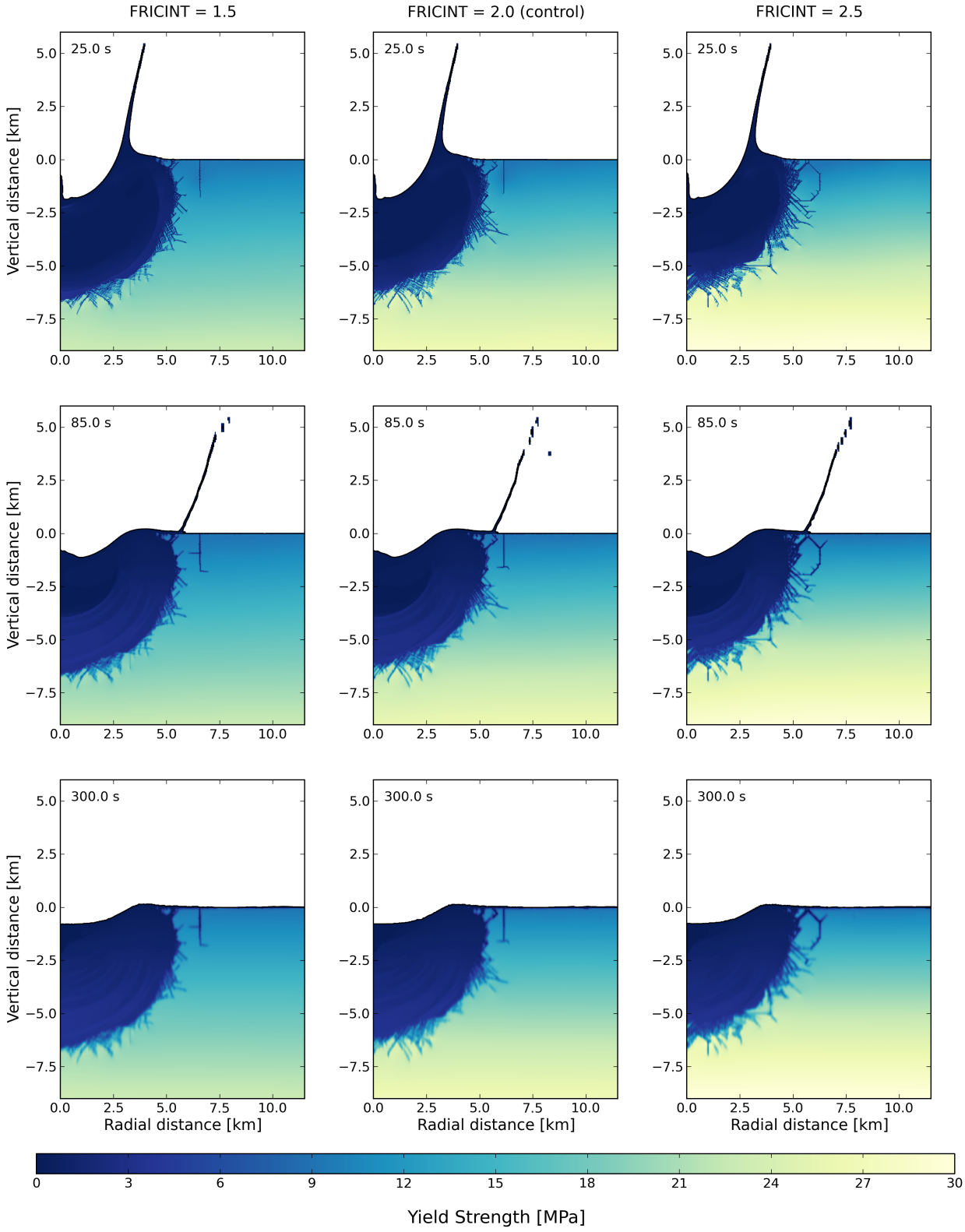

Figure A.23: Sensitivity simulation results of the coefficient of internal friction for intact material, comparing two simulations with a lower and higher value, to the control simulation.

YLIMINT Parameter

In Figure A.24, the results of the control simulation can be seen in the second column. The first column displays the simulation using a lower YLIMINT, and in the third column the simulation using a higher YLIMINT.

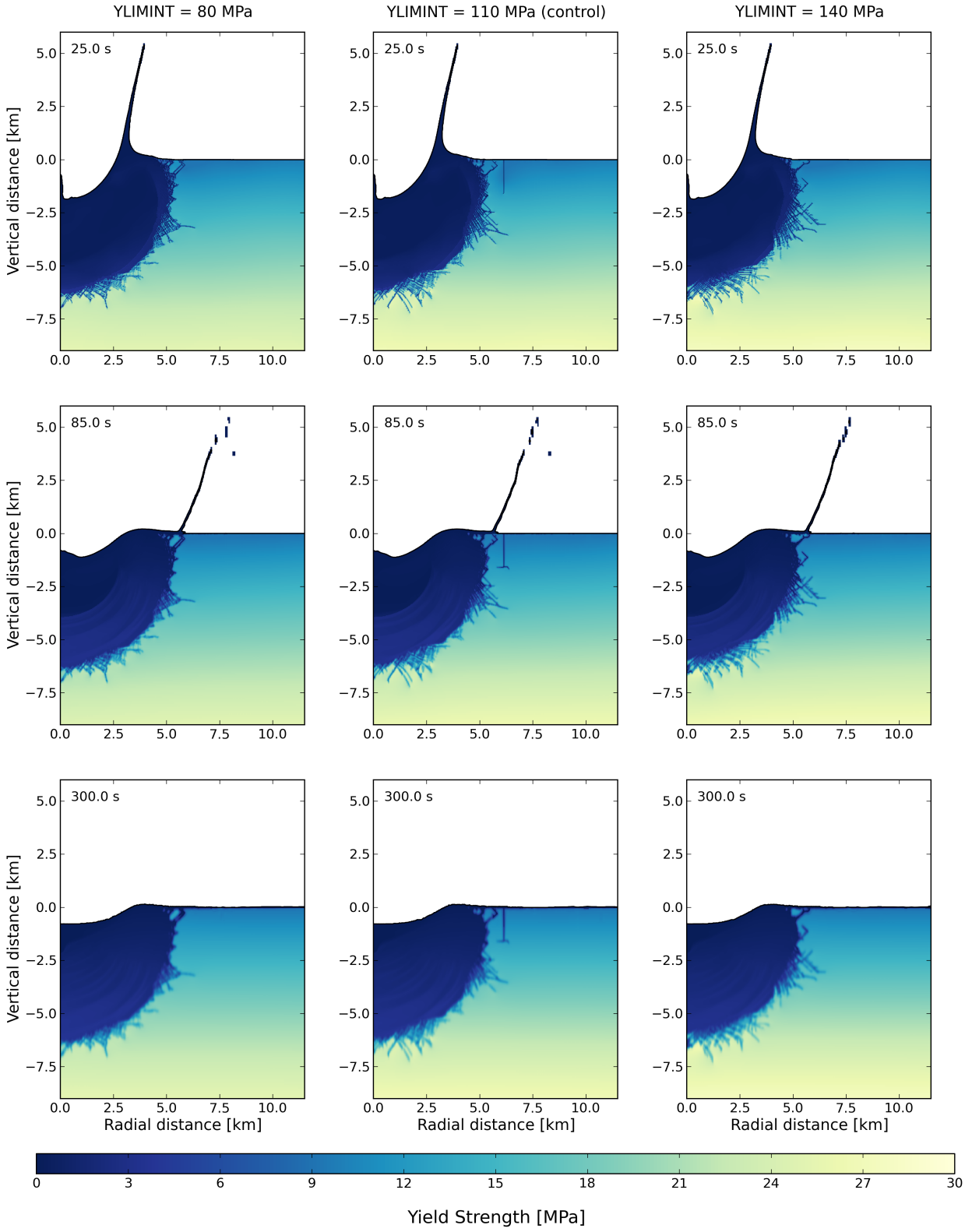

Figure A.24: Sensitivity simulation results of the limit strength of intact material at high pressures, comparing simulations with a lower and higher value, to the control simulation.

YDAM0 Parameter

In Figure A.25, the results of the control simulation can be seen in the second column. The first column displays the simulation using a lower YDAM0, and in the third column the simulation using a higher YDAM0.

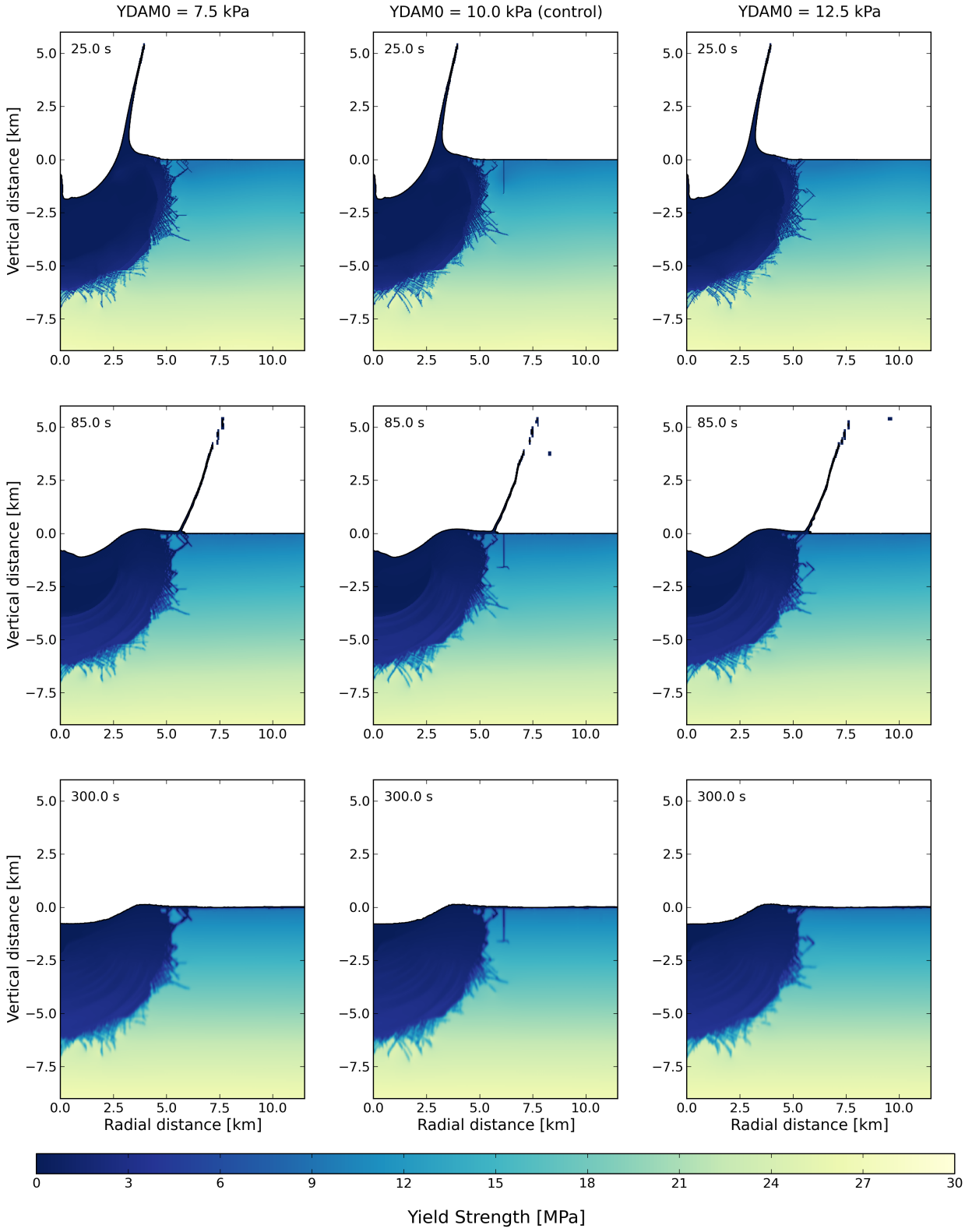

Figure A.25: Sensitivity simulation results of the cohesion of damaged material at zero pressure, comparing simulations with a lower and higher value to the control simulation.

YLIMDAM Parameter

In Figure A.26, the results of the control simulation can be seen in the second column. The first column displays the simulation using a lower YLIMDAM, and in the third column the simulation using a higher YLIMDAM.

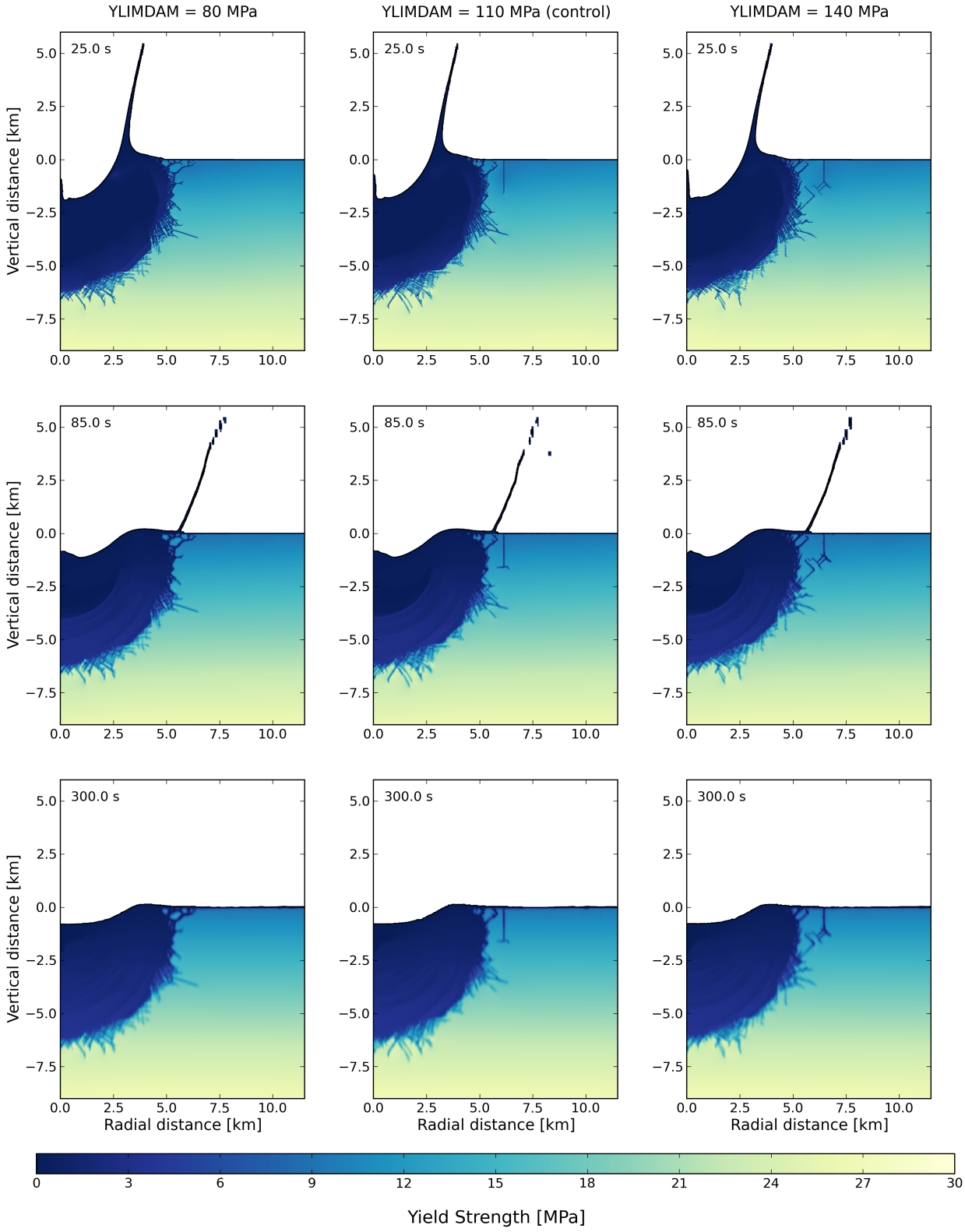

Figure A.26: Sensitivity simulation results of the limit strength of damaged material at high pressures, comparing simulations with a lower and higher value to the control simulation.

IVANOV_A Parameter

In Figure A.27, the results of the control simulation can be seen in the second column. The first column displays the simulation using a lower IVANOV_A, and in the third column the simulation using a higher IVANOV_A.

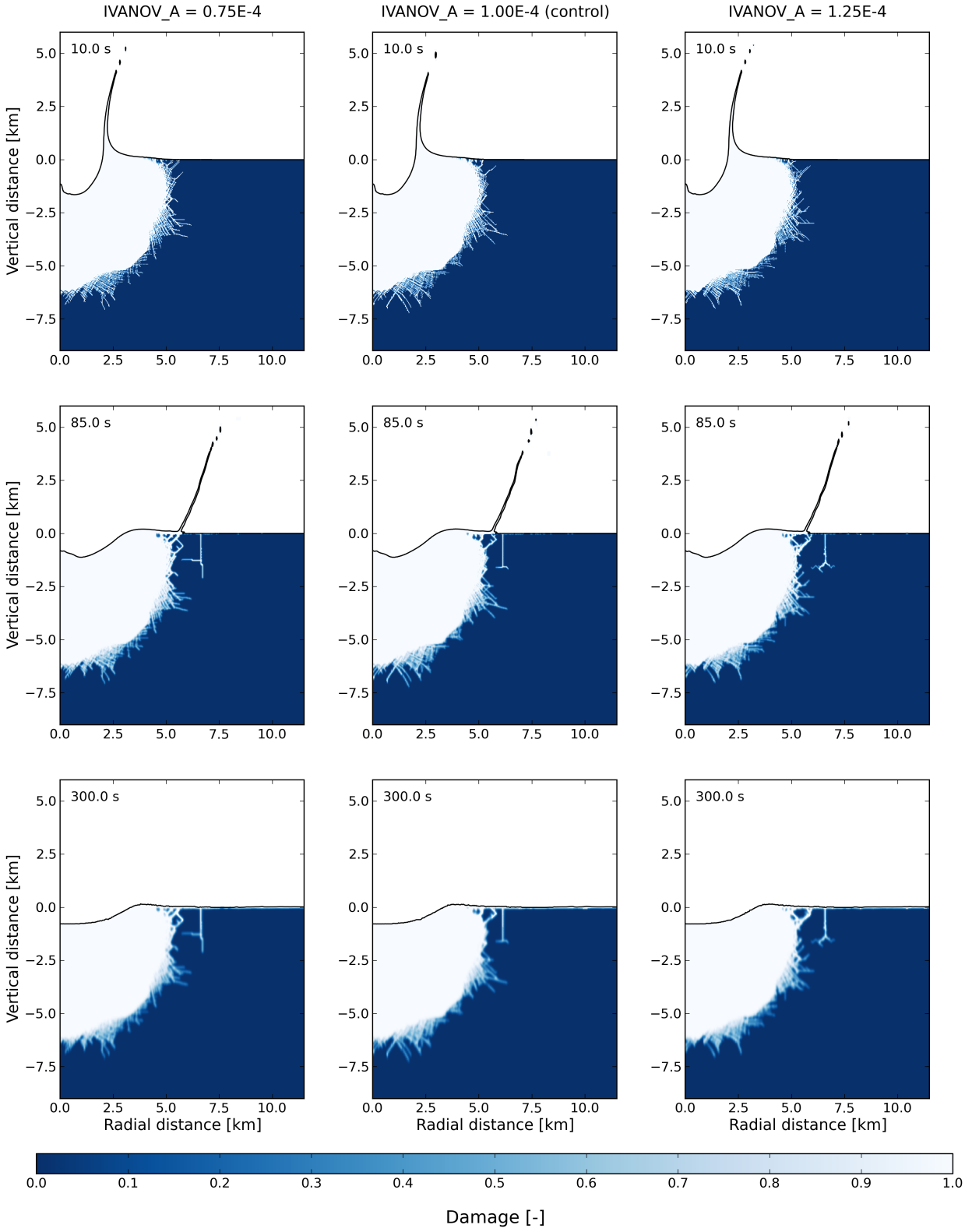

Figure A.27: Sensitivity simulation results of the IVANOV_A parameter, comparing simulations with a lower and higher value to the control simulation.

IVANOV_B Parameter

In Figure A.28, the results of the control simulation can be seen in the second column. The first column displays the simulation using a lower IVANOV_B, and in the third column the simulation using a higher IVANOV_B.

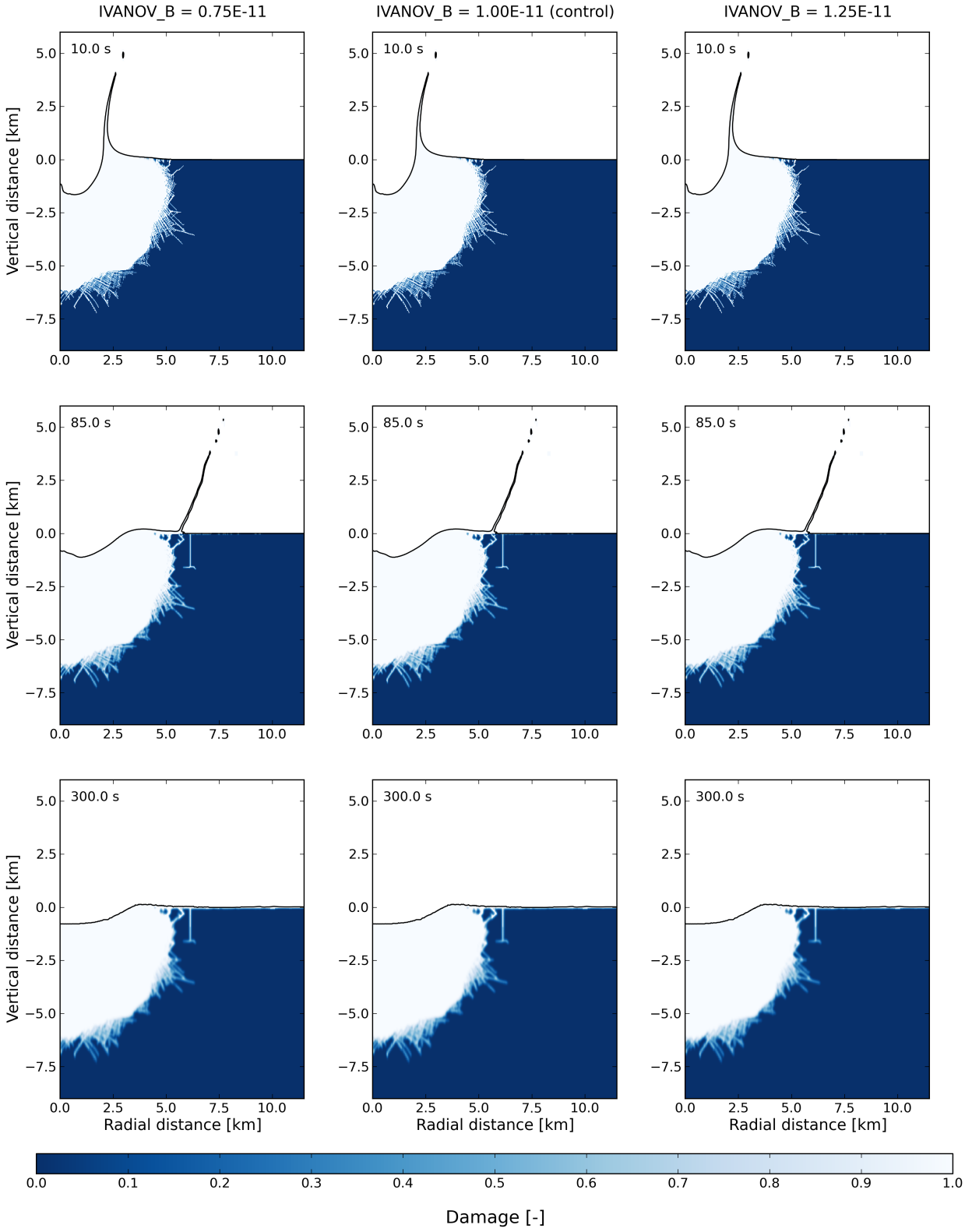

Figure A.28: Sensitivity simulation results of the IVANOV_B parameter, comparing simulations with a lower and higher value to the control simulation.

IVANOV_C Parameter

In Figure A.29, the results of the control simulation can be seen in the second column. The first column displays the simulation using a lower IVANOV_C, and in the third column the simulation using a higher IVANOV_C.

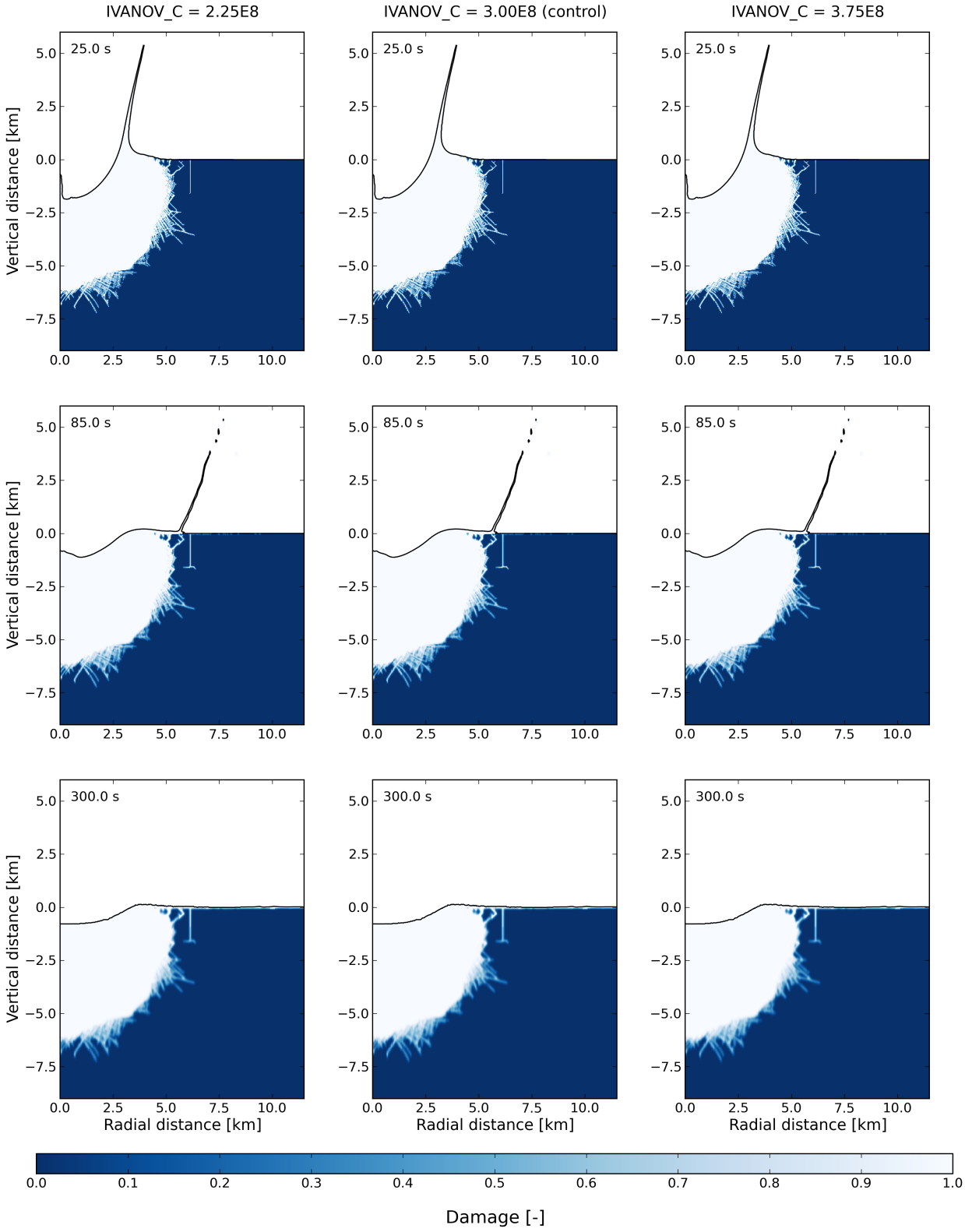

Figure A.29: Sensitivity simulation results of the IVANOV_C parameter, comparing simulations with a lower and higher value to the control simulation.

TFRAC Parameter

In Figure A.30, the results of the control simulation can be seen in the second column. The first column displays the simulation using a lower TFRAC, and in the third column the simulation using a higher TFRAC.

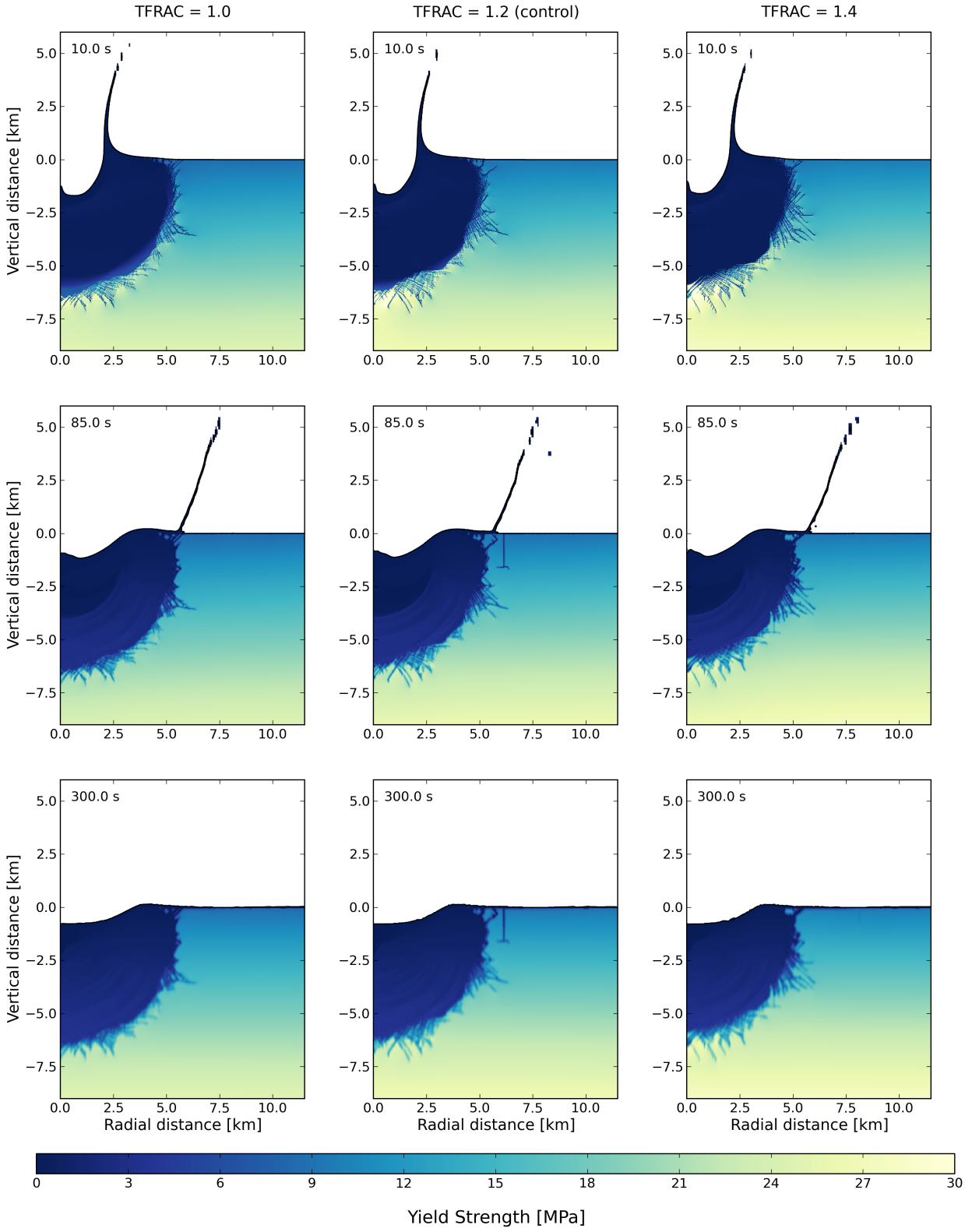

Figure A.30: Sensitivity simulation results of the thermal softening parameter, comparing simulations with a lower and higher value to the control simulation.

A.6. Ganymede Simulations Figures

Given in Figure A.31-Figure A.38 are the eight simulations that have been performed in Chapter 7. The figures show the resulting plots, where the pressure can be seen at nine different time steps for each simulation.

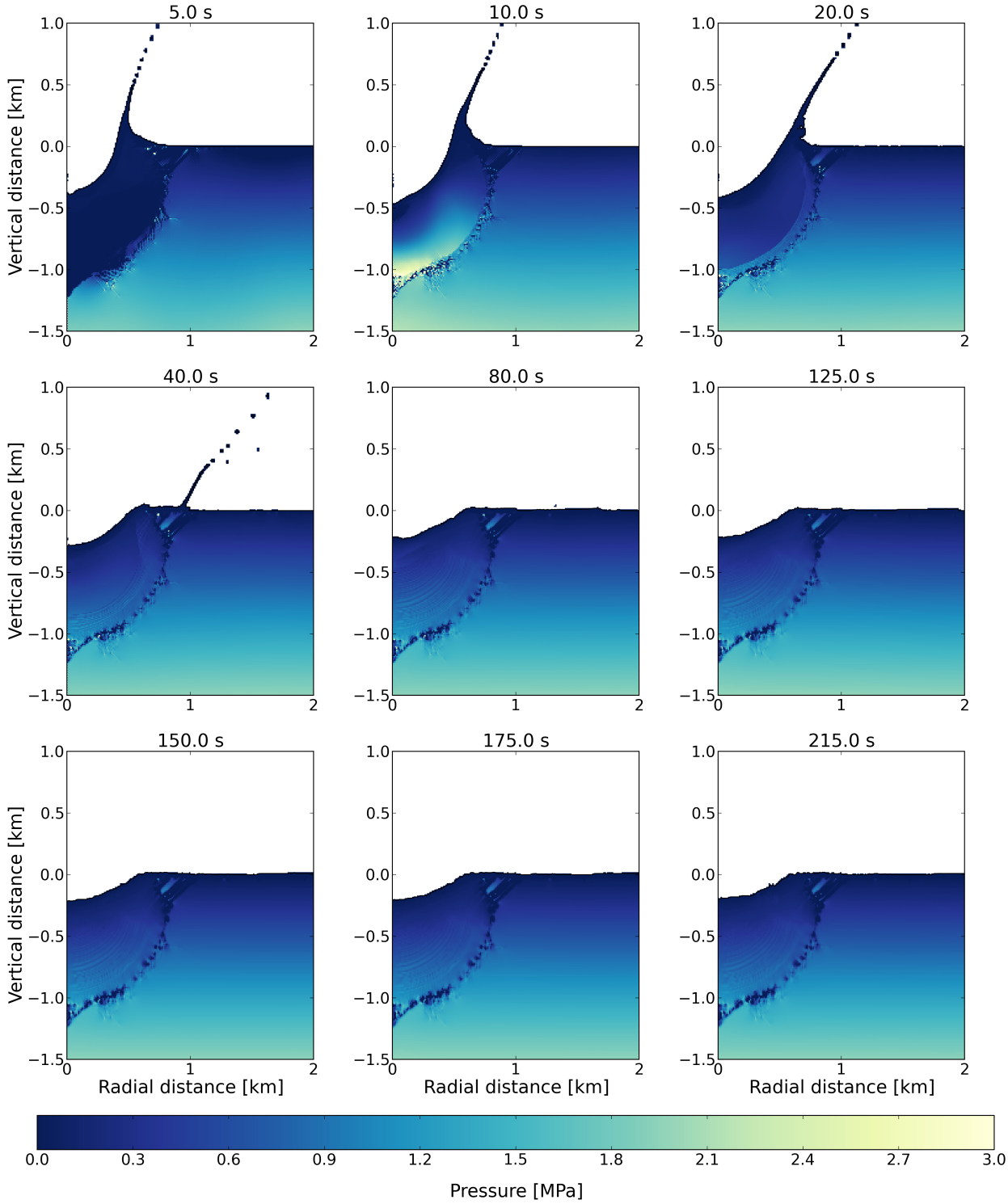

Figure A.31: Pressure for the Ganymede simulation. The results show the impact of an icy impactor, with a diameter of 100 m, striking an icy target at 5 km/s.

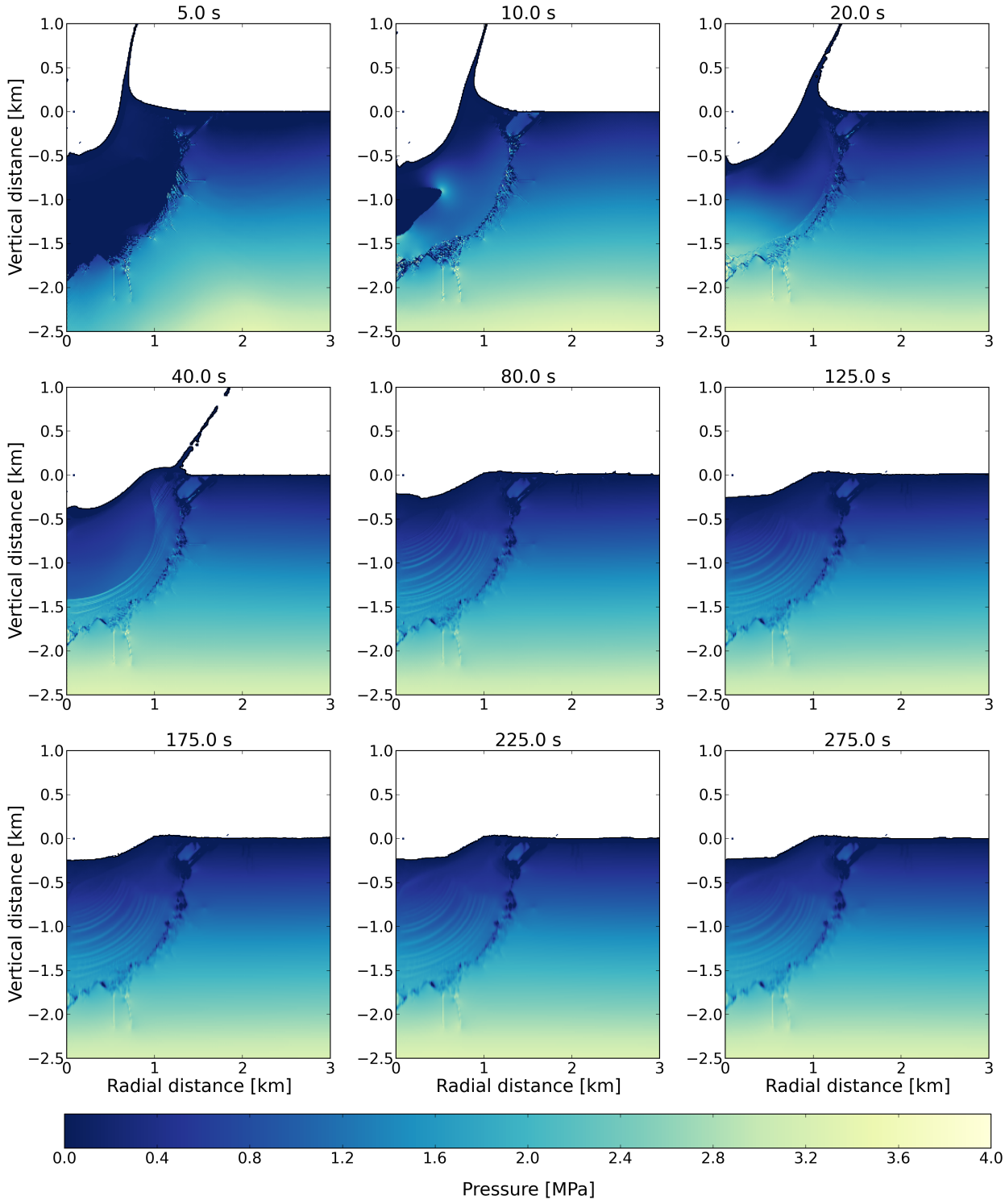

Figure A.32: Pressure for the Ganymede simulation. The results show the impact of an icy impactor, with a diameter of 100 m, striking an icy target at 15 km/s.

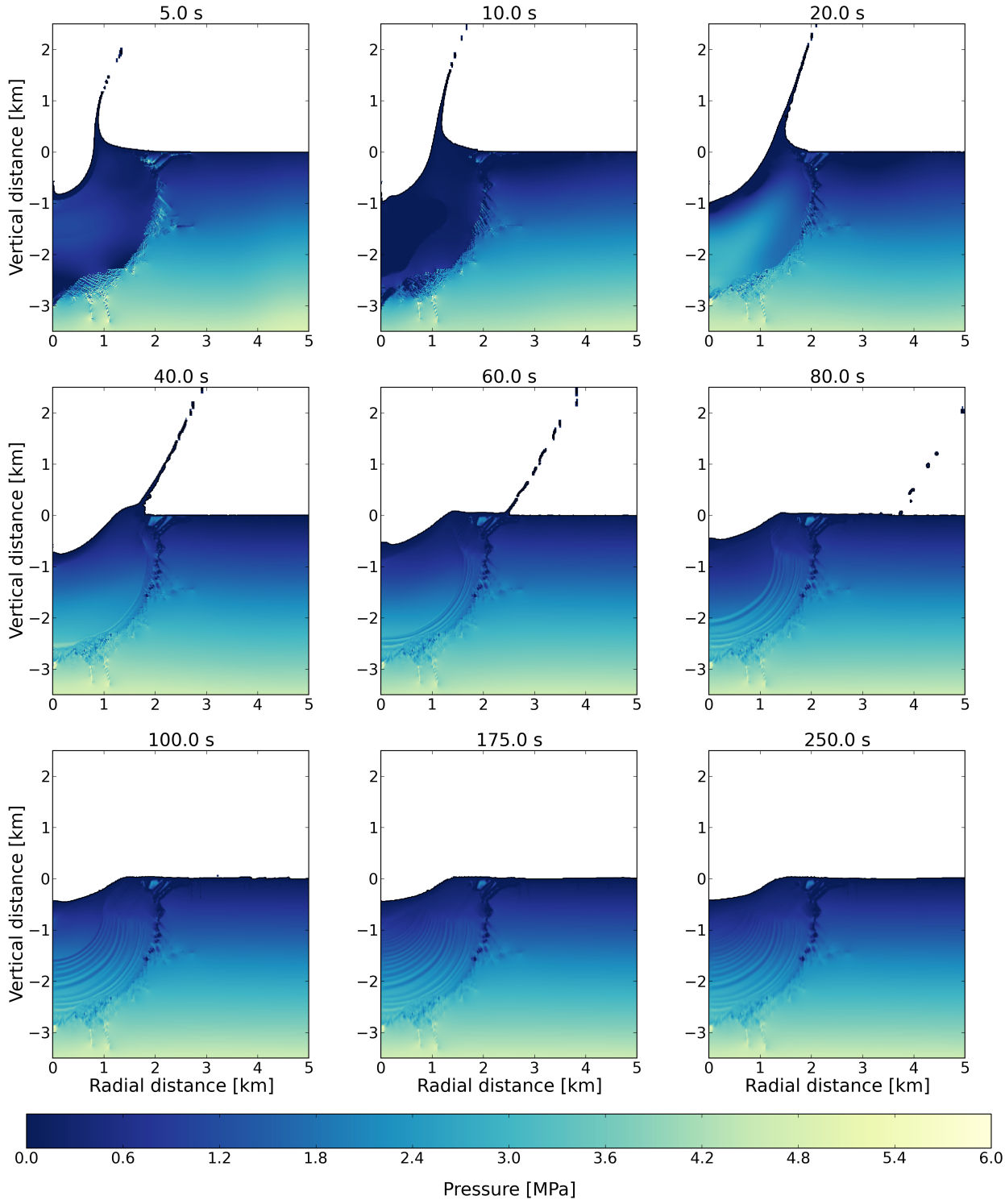

Figure A.33: Pressure for the Ganymede simulation. The results show the impact of an icy impactor, with a diameter of 250 m, striking an icy target at 5 km/s.

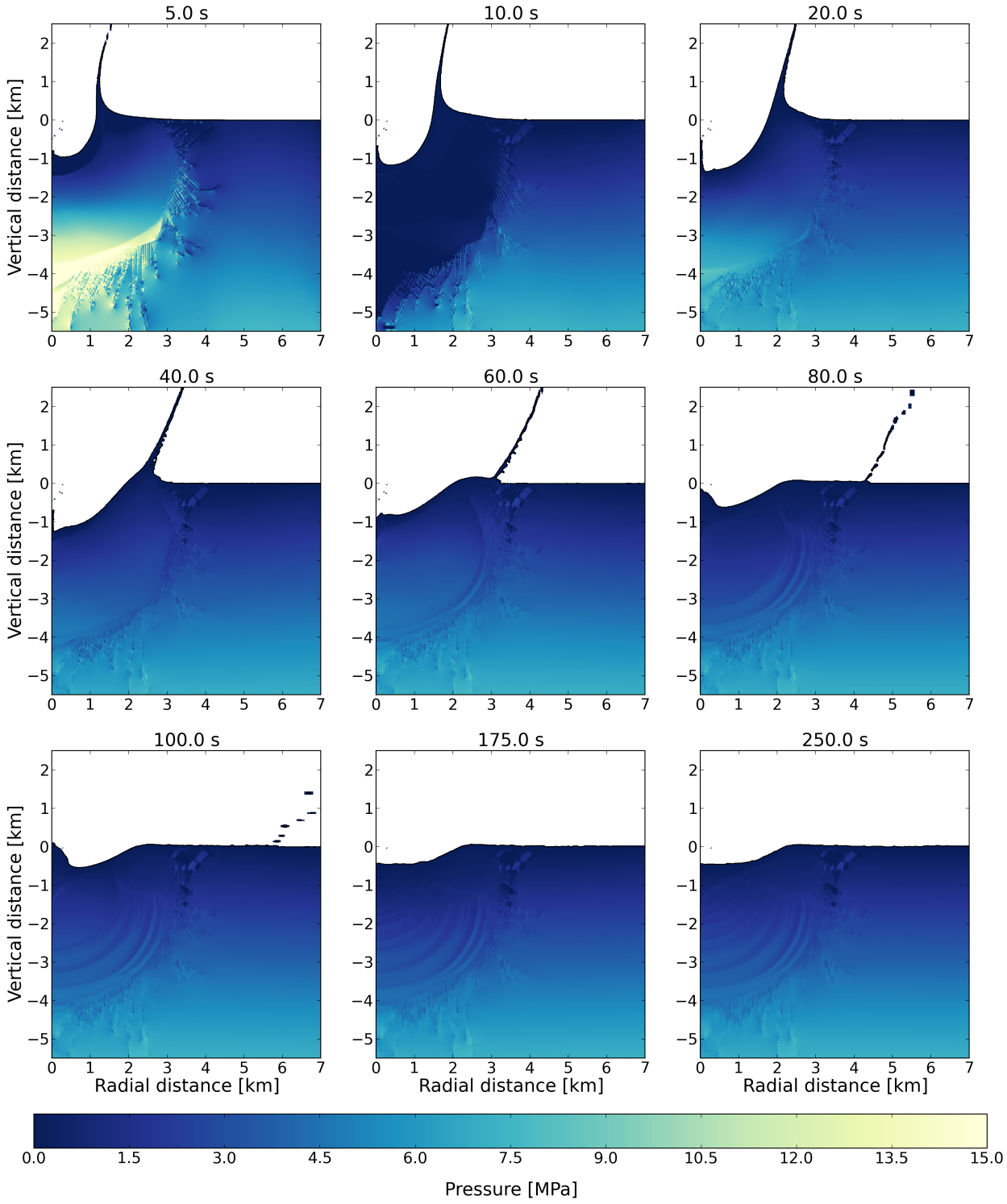

Figure A.34: Pressure for the Ganymede simulation. The results show the impact of an icy impactor, with a diameter of 250 m, striking an icy target at 15 km/s.

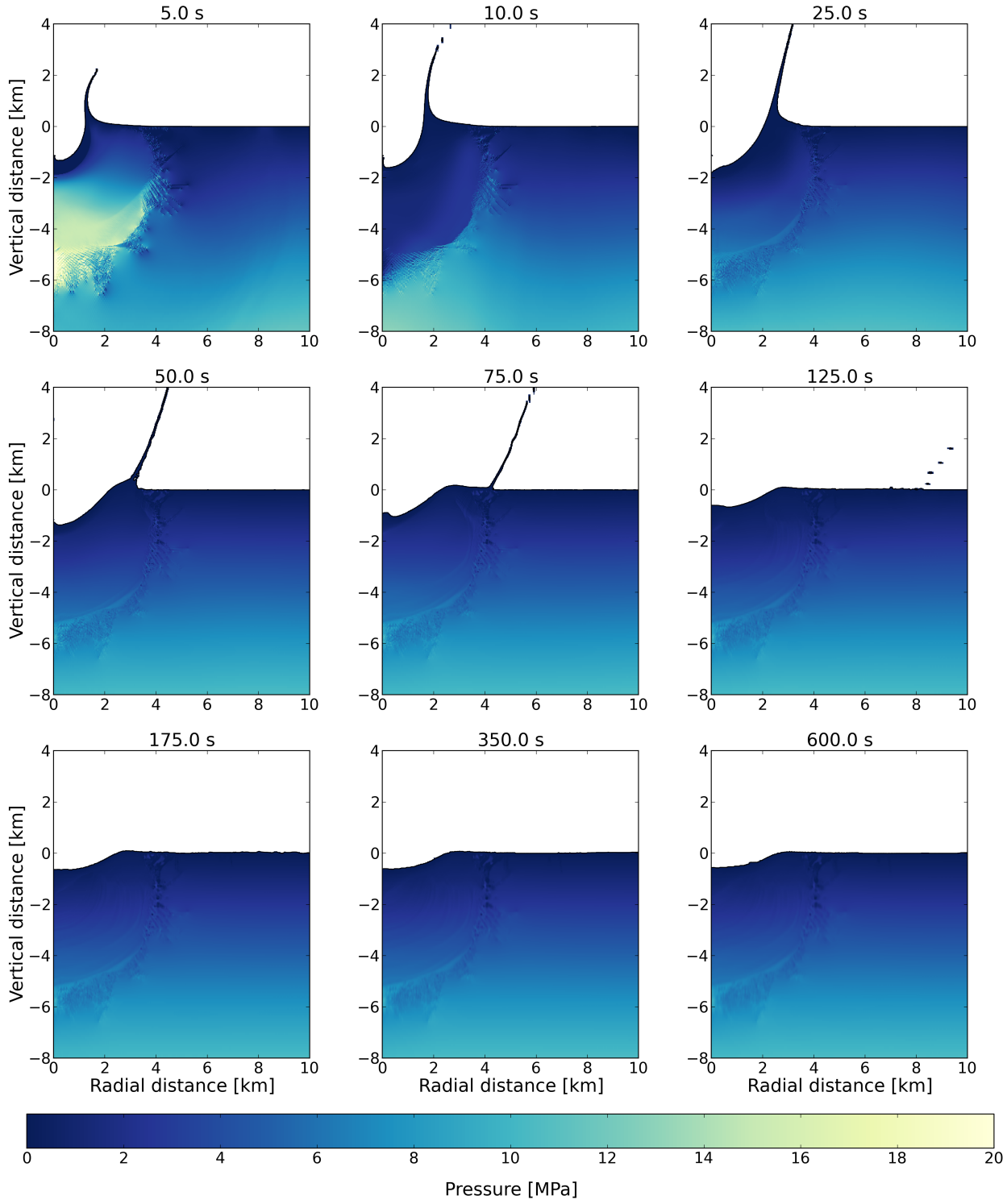

Figure A.35: Pressure for the Ganymede simulation. The results show the impact of an icy impactor, with a diameter of 500 m, striking an icy target at 5 km/s.

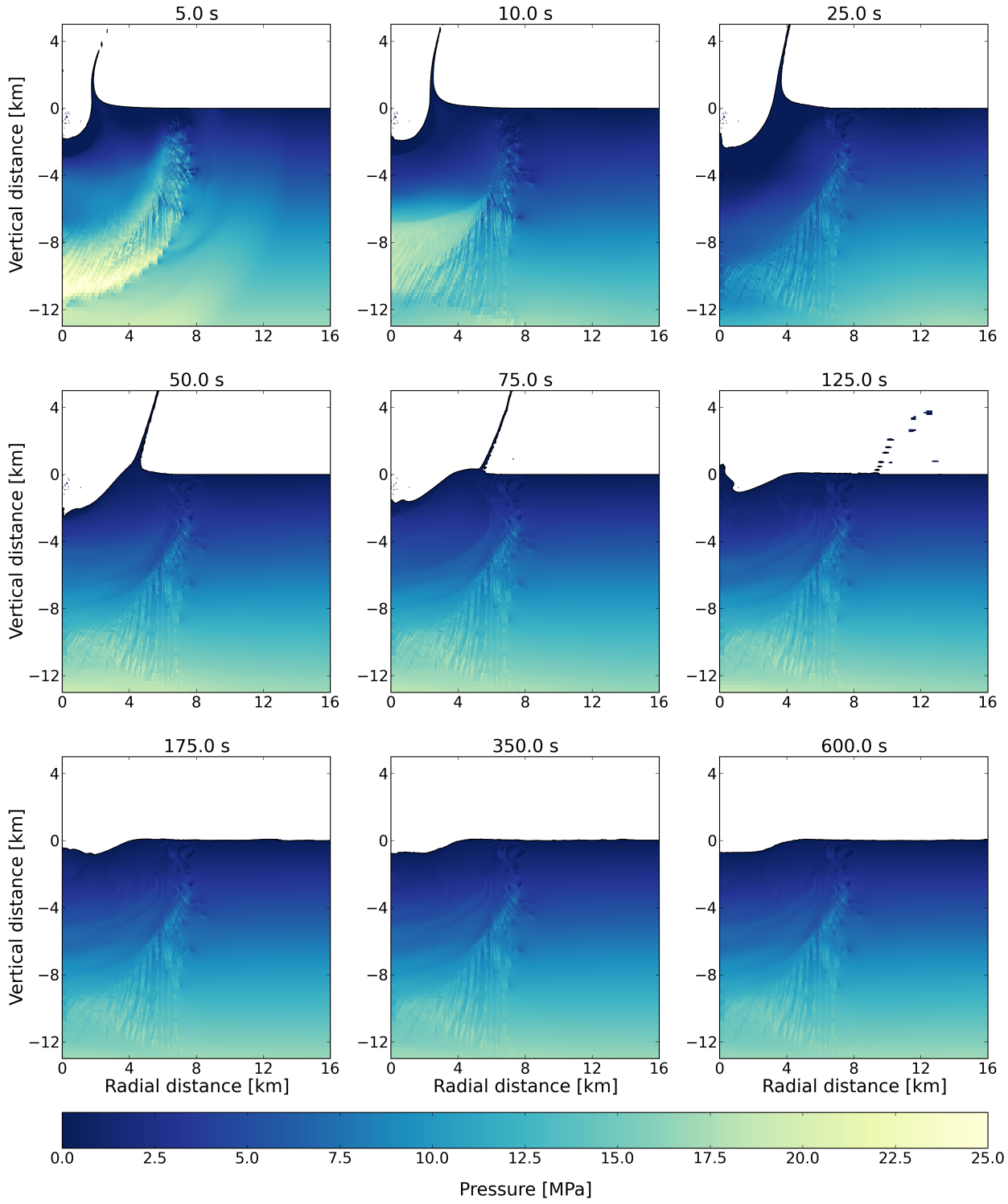

Figure A.36: Pressure for the Ganymede simulation. The results show the impact of an icy impactor, with a diameter of 500 m, striking an icy target at 15 km/s.

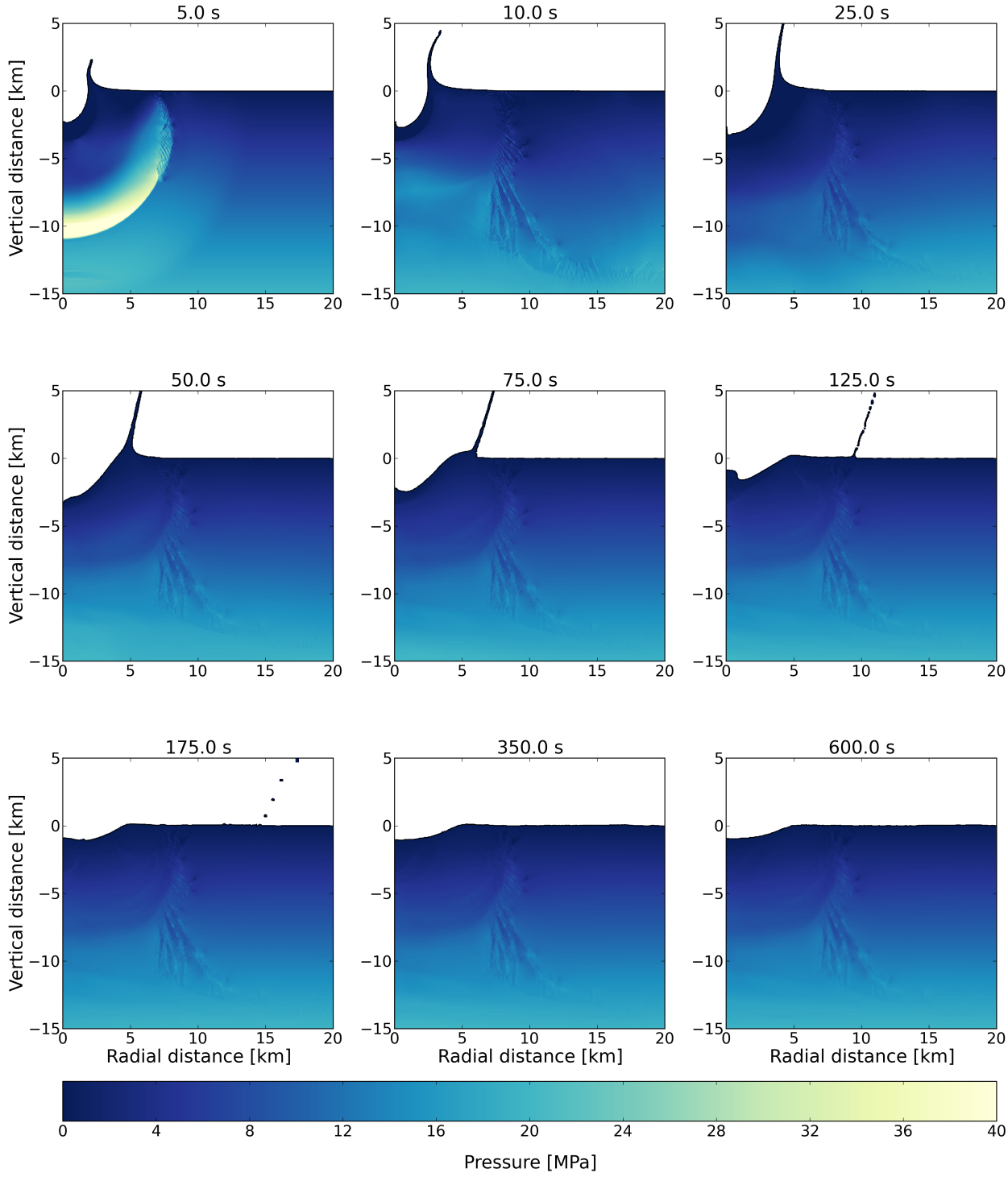

Figure A.37: Pressure for the Ganymede simulation. The results show the impact of an icy impactor, with a diameter of 1000 m, striking an icy target at 5 km/s.

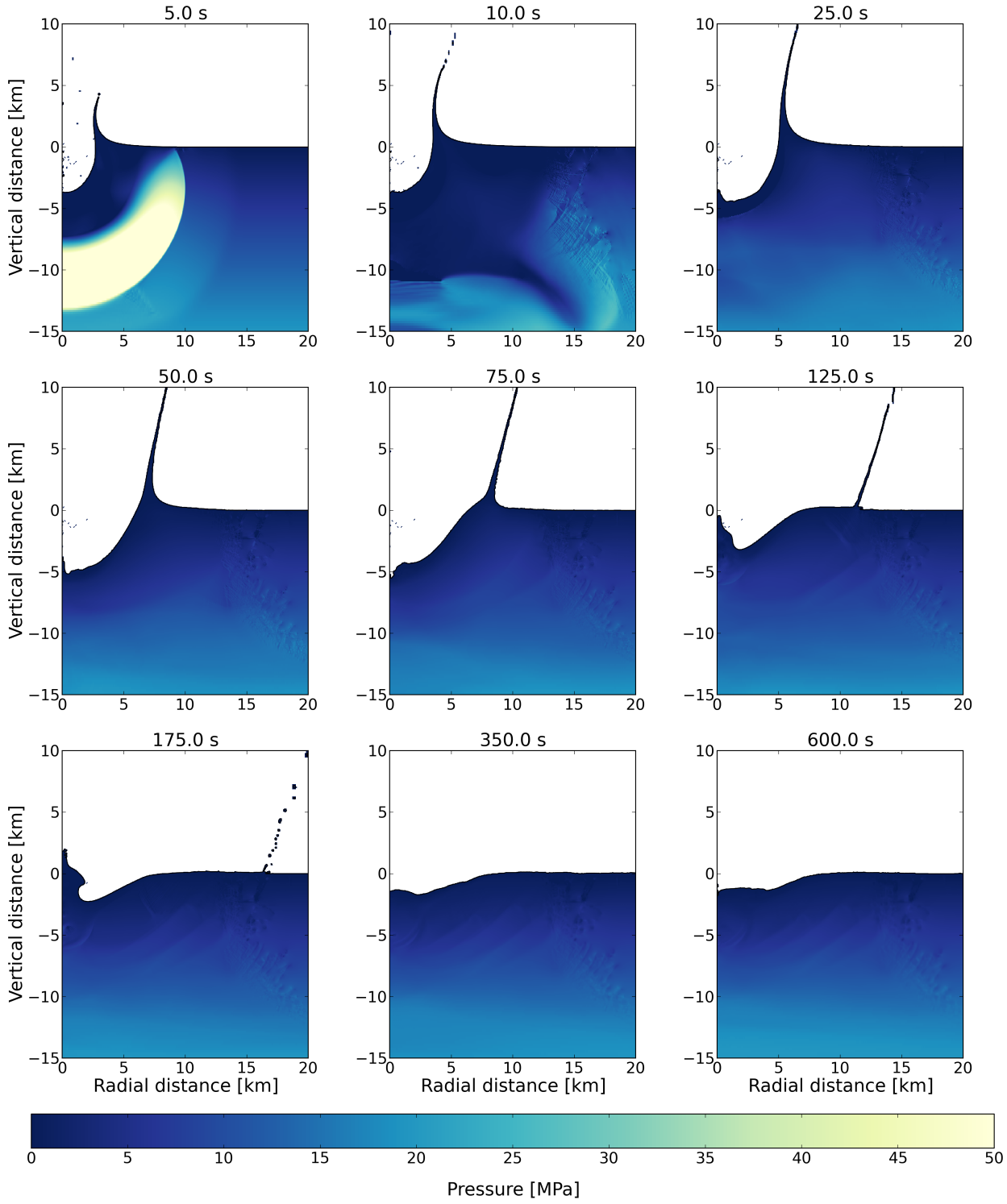

Figure A.38: Pressure for the Ganymede simulation. The results show the impact of an icy impactor, with a diameter of 1000 m, striking an icy target at 15 km/s.

B

Detailed List of Control Simulation Inputs

This appendix provides a detailed list of information regarding the inputs used for the control simulation in Chapter 6. In Table B.1, all the inputs from the input files used in iSALE2D for the control simulation can be seen.

Table B.1: All input parameters from the input files used for the control simulation in iSALE2D. The letter D that can be seen for some numbers, is practically a metric affix used by iSALE2D, which can be considered similar to the letter E (or e) that is more commonly used. In essence, 1D3 is equivalent to 1E3, which is identical to 1000. Parameter values that have been taken from other research are cited accordingly.

Asteroid Input File Parameters		
Parameter	**Value**	**unit**
GRIDH	0 : 275 : 100	[cells]
GRIDV	100 : 300 : 60	[cells]
GRIDEXT	1.03	[-]
GRIDSPC	25	[m]
GRIDSPCM	-20	[-]
S_TYPE	Default	[-]
TSURF	120	[K]
GRAV_V	−1.428	[m/s^2]
OBJNUM	1	[-]
OBJRESH	10	[cells]
OBJVEL	-10D3	[m/s]
OBJMAT	H2O_ice	[-]
LAYNUM	1	[-]
LAYPOS	350	[cells]
LAYMAT	H2O_ice	[-]
LAYTPROF	CONST	[-]
DT	1D-03	[s]
DTMAX	5	[s]
T_END	300	[s]
DTSAVE	2.5	[s]
TOFF	16	[s]
CVIB	0.1	[-]
VIBMAX	200	[m/s]
BND_L	FREESLIP	[-]
BND_R	NOSLIP	[-]
BND_B	NOSLIP	[-]
BND_T	OUTFLOW	[-]
AVIS	0.24	[-]
AVIS2	1.2	[-]
STRESS	1	[-]

Table B.1: continued from previous page

Asteroid Input File Parameters		
QUALITY	-50	[-]
VARLIST	#Den-Pre-Tmp-Yld-Dam#	[-]
Material Input File Parameters		
Parameter	**Value**	**unit**
MATNAME	H2O_ice	[-]
EOSNAME	aqua___	[-]
EOSTYPE	aneos	[-]
STRMOD	ICE	[-]
DAMMOD	IVANOV	[-]
ACFL	BLOCK	[-]
PORMOD	NONE	[-]
THSOFT	OHNAKA	[-]
LDWEAK	POLY	[-]
POIS [110]	0.33	[-]
TMELT0 [111]	273	[K]
TFRAC [1, 65]	1.2	[-]
ASIMON [1]	1.253D9	[-]
CSIMON [1]	3	[-]
YINT0 [1, 65, 66]	1D7	[Pa]
FRICINT [1, 65, 66]	2	[-]
YLIMINT [1, 65, 66]	1.1D8	[Pa]
YDAM0 [1, 65, 66]	1D4	[Pa]
FRICDAM [1, 65, 66]	0.6	[-]
YLIMDAM [1, 65, 66]	1.1D8	[Pa]
IVANOV_A [1, 2]	1D-4	[-]
IVANOV_B [1, 2]	1D-11	[-]
IVANOV_C [1, 2]	3D8	[-]
GAMETA	1.1D3	[-]
GAMBETA	6.92D-02	[-]

C
Additional Equations

This appendix provides additional information about the equations used throughout the report. Section C.1 discusses the equations related to the Tillotson equation of state. Then, Section C.2 provides additional equations regarding the ANEOS equation of state. Finally, Section C.3 briefly discusses linear interpolation theory and the associated equations.

C.1. Tillotson Equation of State

The equations in this section have been taken from Collins et al. [71]. Only the most fundamental and relevant equations are provided here.

The Tillotson equation of state has two forms. One applies when the material is compressed to a higher density than its zero-pressure form, while the other is used when the material expands to a lower density form. In cases of compression where the energy density remains below the energy of incipient vaporization (cold expanded states), the appropriate form that is used is given by Equation C.1.

$$P_c = \left[a + \frac{b}{(E/(E_0\eta^2) + 1)}\right]\rho E + A\mu + B\mu^2 \tag{C.1}$$

Where $\eta = \rho/\rho_0$, $\mu = \eta - 1$, and a, b, A, B and E_0 are Tillotson parameters with a constant value, which need to be defined by the user.

For the expended state, $\eta \leq 1$, in essence when the internal energy exceeds the energy of complete vaporization, the pressure is given by Equation C.2.

$$P_h = a\rho E + \left[\frac{b\rho E}{(E/(E_0\eta^2) + 1)} + A\mu e^{-\beta\mu}\right]e^{-\alpha\mu^2} \tag{C.2}$$

Where α and β are constants that control the rate of convergence of this equation to the perfect gas law.

To make the transition between these two forms smooth, the pressure can best be computed using Equation C.3, which is a hybrid formula.

$$P_m = \left(\frac{E - E_{iv}}{E_{cv} - E_{iv}}\right)P_h + \left(\frac{E_{cv} - E}{E_{cv} - E_{iv}}\right)P_c \tag{C.3}$$

Where P_h is computed from Equation C.2 and P_c from Equation C.1.

C.2. ANEOS Equation of State

The equations in this section have been taken from Collins et al. [71]. Only the most fundamental and relevant equations are provided here.

The ANEOS equation of state is a semi-analytical model in which pressures, temperatures, and densities are derived from the Helmholtz free energy (F), and are therefore thermodynamically consistent. The pressure, specific internal energy, and energy can be computed using Equation C.4, Equation C.5, and Equation C.6.

$$p = \rho^2\frac{\partial F}{\partial \rho} \tag{C.4}$$

$$S = -\frac{\partial F}{\partial T} \tag{C.5}$$

$$E = F + TS \tag{C.6}$$

Where p is the pressure, F is the Helmholtz free energy, ρ is the density, S is the entropy, T is the temperature, and E is the specific internal energy.

The Helmholtz free energy has three parts, the cold part (F_c), the thermal part (F_t), and the electronic part (F_e). In essence, the Helmholtz free energy can be given by Equation C.7.

$$F = F_c(\rho) + F_t(\rho, T) + F_e(\rho, T) \tag{C.7}$$

Consequently, the pressure and specific internal energy can also be written as a sum of their cold, thermal and electronic terms, as shown in Equation C.8 and Equation C.9, respectively.

$$p = p_c(\rho) + p_t(\rho, T) + p_e(\rho, T) \tag{C.8}$$

$$E = E_c(\rho) + E_t(\rho, T) + E_e(\rho, T) \tag{C.9}$$

The relation between the cold pressure and energy is given by Equation C.10.

$$p_c = \rho^2 \frac{\partial E_c}{\partial \rho} \tag{C.10}$$

It has to be stated that for pressures under 100 GPa, the electronic part is not very important.

C.3. Linear Interpolation Theory

To linearly interpolate a single point, for instance point P, two reference points are required: one with a lower x-value, and another with a higher x-value. A linear equation is established using these points, and point P is located on this line. With the x-coordinate of point P known, its y-value is calculated using Equation C.11. The slope (a) is determined via Equation C.12, and the bias (b) via Equation C.13, employing coordinates of the reference points. Substituting these values into Equation C.11 yields the y-value of point P.

$$y = ax + b \tag{C.11}$$

$$a = \frac{y_2 - y1}{x_2 - x_1} \tag{C.12}$$

$$b = y_1 - ax_1 \tag{C.13}$$

In this report, interpolation is repeated multiple times, and occurs between density and pressure for all temperature nodes. This requires a nested ”for loop”, where the outer loop iterates over the temperature nodes, reducing the pressure from a 2D matrix to a 1D list. The inner loop identifies the two closest pressure points and creates the linear equation through which the new density value can be calculated. These values are then stored in a list. The process continues until all density points for each temperature node are interpolated, resulting in a 1D pressure list and 2D density list.